

VAN HEERDEN, STEPHANUS PHILIPUS

CHARACTERIZATION OF WAVEGUIDES, BEAM  
COUPLING AND PROPAGATION FOR STIMULATED  
RAMAN CONVERSION

PhD

UP

1993

*Characterization of waveguides, beam coupling and  
propagation for stimulated Raman conversion*

by

**STEPHANUS PHILIPUS VAN HEERDEN**

Submitted in partial fulfilment of the requirements for the degree

**PHILOSOPHIAE DOCTOR**

in the

**FACULTY OF SCIENCE  
UNIVERSITY OF PRETORIA**

Supervisors: Dr T.B. Scheffler and Dr E. Ronander

**DECEMBER 1993**

## ***ABSTRACT***

The Raman conversion of a 10  $\mu\text{m}$  CO<sub>2</sub> laser beam in parahydrogen is an integral part of the <sup>235</sup>UF<sub>6</sub> laser isotope enrichment process. The nonlinear Raman process depends strongly on the input laser power density. Lasers providing such high power (> 2 J in 80 ns pulsed) in a Gaussian mode are complex and sensitive items.

To achieve high power (> 150 mJ in 40 ns pulsed), high repetition rate (> 1 kHz) 16  $\mu\text{m}$  output, two beam confinement schemes filled with cold (77 K) parahydrogen were investigated: A novel multimirror multipass (35 passes) Raman cell and a hollow metal waveguide. A rate equation model was developed and verified using experimental results obtained from the conventional multipass (25 passes) Raman experiments.

The parameters investigated for the waveguide confinement scheme are:

- the manufacture of minimum loss metal waveguides with an inner germanium layer,
- the effective coupling of the free space laser mode (TEM<sub>00</sub>) to the minimum loss HE<sub>11</sub> waveguide mode,
- the power transmission (experimental) through the waveguide, and
- the effect the waveguide has on the input laser beam polarization.

The actual (non-ideal) laser beam propagation parameters differ from the ideal Gaussian parameters ( $\omega_0$  and  $z_0$ ). It is characterized by three parameters:  $W_0$  (minimum beam radius or "waist"),  $z_0$  (position of the "waist" along the propagation axis), and the beam quality parameter ( $M^2$ ). Knowing these parameters the master-oscillator-power-amplifier chain can be optimized for maximum amplifier extraction with as little possible interference from the finite apertures on the propagation path.

The characterization of the high repetition rate CO<sub>2</sub> oscillator includes the following:

- the size and position of the intracavity aperture for optimum output beam quality, and
- the effect of gas lifetime and high pulse rates on the output laser beam quality.

Some experimental results obtained from 16  $\mu\text{m}$  line width measurements, Raman threshold measurements (for 10P20 and 10R18 lines), and the influence of the beam quality ( $M^2$ ) on the 16  $\mu\text{m}$  output will be given.

## *SAMEVATTING*

Die Raman omskakeling van 'n  $10\ \mu\text{m}$   $\text{CO}_2$  laserstraal in parawaterstof is 'n integrale komponent van die  $^{235}\text{UF}_6$  laser verrykingsproses. Die nie-liniêre Raman proses hang sterk af van die inset laser drywing. Die hoë drywing laser (pulse  $> 2\ \text{J}$  in  $80\ \text{ns}$ ) wat hiervoor nodig is, is kompleks en sensitief.

Twee tipes Ramanselle is ondersoek vir die verkryging van hoë drywing (pulse  $> 150\ \text{mJ}$  in  $40\ \text{ns}$ ), hoë pulse tempo ( $> 1\ \text{kHz}$ )  $16\ \mu\text{m}$  uitset: 'n nuwe multispieël multideurgang (35 deurgange) Ramansel en 'n hol metaal golfgeleier beide gevul met koue ( $77\ \text{K}$ ) parawaterstof. 'n Tempovergelyking model is gebruik nadat die resultate van die model vergelyk is met die eksperimentele resultate verkry vanaf die konvensionele multideurgang (25 deurgange) Ramansel eksperimente.

Die volgende parameters vir die golfgeleiers Ramansel is ondersoek:

- die vervaardiging van minimum verlies metaal golfgeleiers met 'n germanium lagie aan die binne oppervlakte van die geleier,
- die effektiewe koppeling van die vrye laser mode ( $\text{TEM}_{00}$ ) na die minimum verlies  $\text{HE}_{11}$  golfgeleier mode,
- die drywingstransmissie (eksperimenteel) van die golfgeleiers, en
- die invloed van die golfgeleier op die polarisasie van die intree laserstraal.

Die werklike (nie-ideale) laserstraal se voortplantingsparameters verskil van die ideale Gaussparameters ( $\omega_0$  en  $z_0$ ). Dit word deur drie parameters bepaal:  $W_0$  (minimum radius van die bundel),  $z_0$  (posisie van  $W_0$  langs die voortplantingsas) en die straalkwaliteitparameter ( $M^2$ ). Indien die parameters bekend is, kan die ossillator-versterker ketting geoptimeer word vir maksimale versterking sonder te veel benadeling deur die eindige openinge langs die straalpad.

Die karakterisering van die hoë pulstempo  $\text{CO}_2$  ossillator sluit die volgende in:

- die grootte en posisie van die intra-resonator opening vir optimum straalkwaliteit, en
- die invloed van gasleef tyd en hoë pulstempos op die uitset straalkwaliteit.

Eksperimentele resultate waarvan verslag gedoen word, sluit in:  $16\ \mu\text{m}$  lynwydte metings, Raman drumpel metings (vir die 10P20 en 10R18  $\text{CO}_2$  lyne) en die invloed van die straalkwaliteit ( $M^2$ ) op die  $16\ \mu\text{m}$  uitset.

***To my dad:***

***" I am sure you would have liked to see this!! "***

## ***ACKNOWLEDGEMENTS***

I am greatly indebted to

- my supervisors Dr. T. B. Scheffler and Dr. E. Ronander for their able and valued assistance and guidance,
- my colleagues (T. Salamon, Dr L.R. Botha and F.J. Prinsloo) for their assistance and fruitful discussions,
- the technicians (M. Venter, K. Delpont, M. Botha and C. de Swardt) for all their hard work,
- M. Botha for the drawings,
- my wife, Kathy for her help, support and encouragement,
- the Atomic Energy Corporation of South Africa for the opportunity to use their facilities and funding of this project, and
- finally the Lord without whom this would not have been possible!!

# TABLE OF CONTENTS

	page no
<b>ABSTRACT</b>	ii
<b>SAMEVATTING</b>	iii
<b>ACKNOWLEDGEMENTS</b>	v
<b>1. INTRODUCTION AND BACKGROUND</b>	1.1
1.1 Stimulated Raman conversion	1.2
1.2 Infrared waveguides	1.4
1.3 Laser beam quality parameter - $M^2$	1.7
1.4 References: Chapter 1	1.8
List of symbols: Chapter 1	1.9
<b>2. INFRARED WAVEGUIDES</b>	
2.1 Introduction	2.1
2.2 Theoretical analysis	2.2
2.2.1 Coupling into a hollow waveguide	2.5
2.2.2 Attenuation coefficients of hybrid modes for hollow metal waveguides with an inner dielectric layer	2.9
2.2.3 Dielectric layer thickness for minimum loss	2.13
2.3 Waveguide manufacture	2.14
2.4 Measurement of parameters relevant to efficient Raman conversion	2.17
2.4.1 Coupling condition measurements	2.18
2.4.2 Transmission measurements	2.19
2.4.3 Polarization measurements	2.22
2.4.4 Conclusions	2.23
2.5 References: Chapter 2	2.24
Appendix 2.A Brewster stack polarizer	2.27
List of symbols: Chapter 2	2.29
<b>3. ROTATIONAL RAMAN GAIN CALCULATIONS</b>	
3.1 Introduction	3.1
3.2 Energy levels and population difference $\Delta N$ for parahydrogen	3.1
3.3 Raman line width $\Delta\nu_R$	3.4

3.4	Differential scattering cross section $d\sigma/d\Omega$ and polarization effects	3.7
3.5	Gain calculations	3.9
3.6	References: Chapter 3	3.11
	List of symbols: Chapter 3	3.13
<b>4.</b>	<b>THEORETICAL ANALYSIS OF THE STIMULATED ROTATIONAL RAMAN CONVERSION</b>	
4.1	Introduction	4.1
4.2	Theoretical Model	4.2
4.3	Model for the Raman conversion in a multipass cell	4.4
	4.3.1 Gain enhancement due to ray crossings in the multipass cell	4.6
	4.3.2 Calculation of the Stokes seed	4.8
	4.3.3 Calculation of Raman conversion in a multipass cell	4.10
	4.3.4 Discussion of multipass cell calculation results	4.12
4.4	Model for waveguide Raman cell	4.16
	4.4.1 Discussion of calculation results	4.18
	4.4.2 Experimental results	4.20
4.5	References: Chapter 4	4.21
Appendix 4.A	Multipass Raman cell and waveguide Raman cell Turbo Pascal code	4.24
	List of symbols: Chapter 4	4.33
<b>5.</b>	<b>LASER BEAM PROPAGATION</b>	
5.1	Introduction	5.1
5.2	Resonators and modes	5.1
	5.2.1 Stable resonator geometry	5.2
	5.2.2 Transverse modes	5.4
5.3	The paraxial wave equation and the complex beam parameter	5.5
5.4	Gaussian beam propagation	5.8
5.5	Gaussian beam propagation through a thin-lens system	5.9
5.6	Mode matching of Gaussian beams	5.11
5.7	Beam parameters of non-ideal laser beams	5.12
5.8	Beam parameter measurements	5.15
5.9	Beam-width measurement methods	5.18
	5.9.1 Scanning slit method	5.18



5.9.2	Scanning knife edge	5.19
5.9.3	Variable aperture method	5.20
5.9.4	Beam width measurement using the beam variances	
	theory ( $W=2\sigma_x$ )	5.21
5.9.4.1	Scanning pinhole devices	5.22
5.9.4.2	Single shot devices	5.22
5.10	Raman threshold in cold parahydrogen for non-ideal Gaussian beams	5.23
5.11	Characterization of the CO <sub>2</sub> beam for optimum Raman output	5.24
5.12	References: Chapter 5	5.31
Appendix 5.A	ABCD matrix method for beam propagation through an optical system	5.34
Appendix 5.B	Second-order least-squares fit for the extraction of propagation parameters	5.36
Appendix 5.C	Error calculation for scanning slit method	5.36
Appendix 5.D	Clip level calculation for the knife-edge method	5.37
Appendix 5.E	Power content calculations for the variable aperture method	5.39
	List of symbols: Chapter 5	5.40
<b>6.</b>	<b>RAMAN CONVERSION RESULTS AND CONCLUSIONS</b>	
6.1	Introduction	6.1
6.1.1	Master oscillator power amplifier chain description	6.2
6.1.2	Wavelength calibration	6.7
6.1.3	Detectors	6.9
6.2	Results	6.12
6.2.1	Bandwidth measurement	6.12
6.2.2	Raman threshold measurements	6.22
6.2.3	Raman output as a function of parahydrogen pressure	6.24
6.3	Conclusions and future projects	6.25
6.4	References: Chapter 6	6.27
	List of symbols: Chapter 6	6.28

# 1. INTRODUCTION AND BACKGROUND

One often needs a specific laser wavelength, which may not be directly available. There are a number of laser lines available (Figure 1.1) between 0.1  $\mu\text{m}$  and 20  $\mu\text{m}$ , and techniques to change these to the specific lines needed. These techniques for generating new wavelengths are normally based on nonlinear effects (stimulated Raman conversion [1,2], four-wave mixing [1,3], the optical mixing of frequencies in crystals [2], etc).

The aim of this thesis is the theoretical and experimental characterization of the efficient Raman conversion of an amplified pulsed ( $>25$  MW per pulse)  $\text{CO}_2$  laser beam in parahydrogen. This is the process used for generating the wavelengths needed for the selective excitation in  $^{235}\text{UF}_6$ . The molecular laser isotope enrichment process (MLIS) of  $^{235}\text{UF}_6$  makes use of an infrared excitation in the 16  $\mu\text{m}$  region which is accessible through the Raman conversion of  $\text{CO}_2$  wavelengths in parahydrogen. The characterization includes the following:

- Raman gain (Chapters 3 and 4),
- confining the (pump and Raman) laser beams inside a hollow metallic waveguide (Chapters 2 and 4),
- $\text{CO}_2$  laser beam characterization for optimum amplifier extraction and master-oscillator-power-amplifier chain propagation. Thus knowing the beam parameters optimum coupling into a (multipass or waveguide) Raman cell can be achieved (Chapter 5), and
- experimental results of the Raman output bandwidth and Raman thresholds (Chapter 6).

The pump beam was a  $\text{CO}_2$  laser at 10.2  $\mu\text{m}$  ( $980\text{ cm}^{-1}$ ) which generates the first Stokes at 16  $\mu\text{m}$  ( $626\text{ cm}^{-1}$ ) i.e.  $\omega_S = \omega_L - \omega_R$  where  $\omega_R$  is the Raman transition frequency ( $S_0(0) \approx 354\text{ cm}^{-1}$ ). The Raman cell was cooled to between 77 K and 100 K and the polarization of the amplified  $\text{CO}_2$  laser beam was circular for maximum Raman gain. A general rate equation model for the Raman conversion was constructed. The model was tested against results obtained from multipass Raman cell experiments. With this verification of the model, waveguide Raman cell parameters are specified in terms of waveguide length and input  $\text{CO}_2$  power. Further, a theoretical description for minimum loss waveguides at 10  $\mu\text{m}$  will

be given. This includes the design criteria and the coupling conditions for efficient  $TEM_{00}$  coupling.

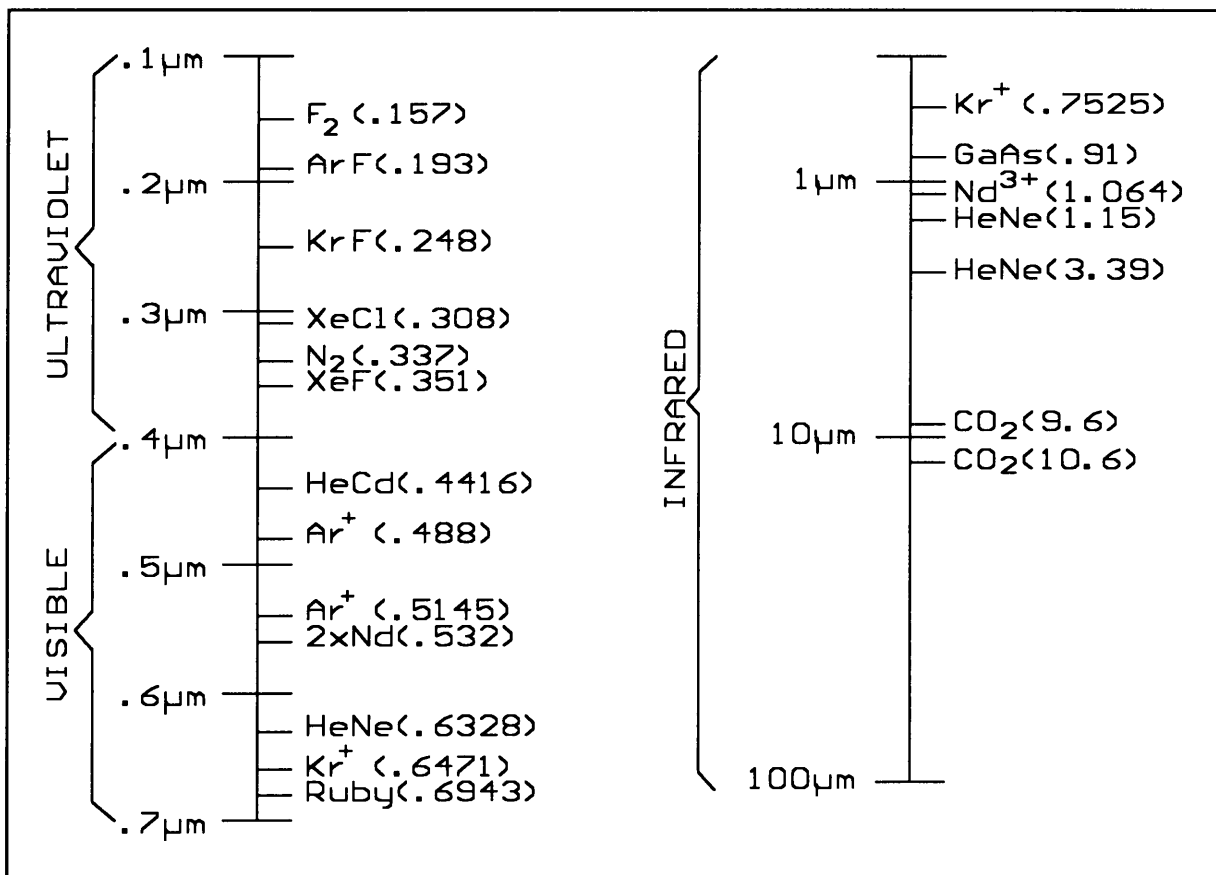


Figure 1.1 A few laser lines available between 0.1 μm and 20 μm

## 1.1 STIMULATED RAMAN CONVERSION

Stimulated Raman scattering (SRS) is a process in which a laser beam, called the pump, generates optical gain collinear with itself. This can be in a down-shifted frequency, called the Stokes frequency, or in an up-shifted frequency called the anti-Stokes frequency. These frequency shifts are equal to an energy level transition frequency of the Raman medium. The Stokes signals are normally generated from amplified blackbody and/or spontaneous Raman emission noise. Since the noise signal is quite small ( $\approx 5 \times 10^{-10}$  Watt), large gains ( $\approx e^{36}$ ) are required to generate useful signals. The anti-Stokes frequencies are somewhat weaker than their counterparts, the Stokes frequencies.

There are several advantages using stimulated rotational Raman scattering (SRRS) in hydrogen

with a CO<sub>2</sub> laser, namely:

- CO<sub>2</sub> laser technology is well developed, efficient and also scalable to high peak and average power,
- stimulated Raman conversion is a well known and also an efficient method for optical frequency conversion, and
- since most CO<sub>2</sub> lasers are tunable, the Raman shifted frequencies are also tunable.

In hydrogen, two convenient rotational Stokes frequency shifts are available, the 354 cm<sup>-1</sup> S(0) transition in parahydrogen and the 586 cm<sup>-1</sup> S(1) transition in orthohydrogen. By using a continuously tunable high pressure CO<sub>2</sub> laser around 9 - 10 μm one can tune the Stokes Raman-shifted frequencies around 13 - 16 μm for parahydrogen and 19 μm and 24 μm for orthohydrogen. Keeping in mind that the 16 μm region is needed for selective <sup>235</sup>UF<sub>6</sub> excitation it is thus clear that the parahydrogen shift is extremely useful in the uranium enrichment process [molecular laser isotope separation (MLIS)].

Any material which is efficient in spontaneous Raman scattering may also be efficient for stimulated Raman scattering. Usually the spontaneous Raman spectrum consists of a few lines, some of them often having nearly equal intensities. In such a case, the line having the highest intensity with the smallest line width will be the first to appear in the stimulated Raman spectrum.

There are a number of distinct differences between spontaneous and stimulated Raman scattering (Figure 1.2 shows some of the spontaneous and stimulated Raman characteristics). They are:

- The spontaneous Raman spectrum consists of many lines corresponding to various allowed vibrational/rotational transitions, whereas the stimulated Raman spectrum typically consists of one or two vibrational/rotational transitions. When the threshold of the stimulated Raman process is reached, the intensity of the line increases, and therefore the

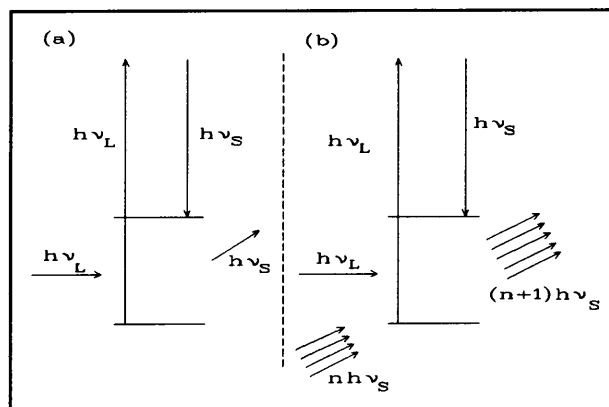


Figure 1.2 Diagram of (a) spontaneous and (b) stimulated Raman scattering

probability of scattering by that line increases rapidly compared to the other lines. However, with increasing intensity of the first Raman line, this generates its own Raman line, which results in a succession of lines of higher order. This means that the Raman spectrum normally consists of several orders of Stokes and/or anti-Stokes lines of one or two vibrational/rotational transitions.

- While the spontaneous Raman scattering is incoherent, the stimulated Raman scattering is coherent.
- Another feature is the directionality of the stimulated Raman scattering. This is the result of the momentum-matching condition in a dispersive medium. Both energy and momentum are conserved in an interaction between radiation and matter. If a single photon is scattered by a single molecule, the molecule recoils suitably to conserve the momentum, but when a coherent beam interacts with the molecules constituting a medium, the difference of momentum is taken up by the frequency shifted photon.
- The stimulated Raman process is a far more efficient process, with photon-to-photon conversion efficiencies of up to 80% .
- As in ordinary lasers there is also a narrowing of the Raman lines for stimulated Raman scattering, although it is not as spectacular as with ordinary lasers.
- In the spontaneous process the rate of production of Stokes photons of energy  $h\nu_s$  is independent of the number of Stokes photons already present in the mode. In the stimulated process this rate is proportional to the number of Stokes photons present.

## ***1.2 INFRARED WAVEGUIDES***

In the beginning of the 1970's the development of infrared fibre optics accelerated as applications emerged in medicine, industry, military and communications. These include:

- flexible delivery of infrared laser power to a work site for surgery,
- flexible transmission of infrared radiation for remote sensing, and
- ultralow loss (less than 0.001 to 0.0001 dB/km) telecommunications.

For applications involving high energy lasers the absorption in the fibre at the laser wavelength must be taken into account since too high an absorption could cause the fibre to overheat and be damaged.

infrared MATERIAL	FIBRE TYPE	ATTENUATION (dB/km)	THEORETICAL ATTENUATION (dB/km)
AgBr	Single-crystal uncladded	~9000 @ 10.6 $\mu$ m	10 <sup>-3</sup> @ 5 $\mu$ m
AgCl	Polycrystalline uncladded	~6000 @ 14 $\mu$ m	10 <sup>-3</sup> @ 5 $\mu$ m
KRS-5	Polycrystalline uncladded	~300 @ 10.6 $\mu$ m	10 <sup>-3</sup> @ 7 $\mu$ m
TlBr	Polycrystalline uncladded	~400 @ 10.6 $\mu$ m	10 <sup>-4</sup> @ 7 $\mu$ m
KCl	Polycrystalline uncladded	~4000 @ 10.6 $\mu$ m	10 <sup>-4</sup> @ 5 $\mu$ m
Fluorohafnate & fluoro-zirconate	Glass	~300 @ 3.6 $\mu$ m	10 <sup>-3</sup> @ 3.5 $\mu$ m
Heavy metal fluoride	Glass	~2000 @ 3.5 $\mu$ m	10 <sup>-3</sup> @ 3.5 $\mu$ m
Chalcogenide	Glass	~10000 @ 6.5 $\mu$ m	10 <sup>-2</sup> @ 4.5 $\mu$ m

**Table 1.1 Attenuation data for infrared fibres**

Fibres are attractive as power guides because of their flexibility and low losses. Unfortunately there are but a few useful fibres, as is shown in Table 1.1 and Figure 1.3 [4,5]. The need for flexible waveguides at 10.6  $\mu$ m has arisen because of the prevalent use of the CO<sub>2</sub> laser for surgery as well as for cutting, welding and heat treatment, which requires a convenient method for getting the laser power to the target. At the present time it is done with a system of articulated arms and a bulky and awkward series of mirrors, because there are no suitable optical fibres sufficiently transparent at 10.6  $\mu$ m. The development of flexible infrared waveguides will allow infrared power to be delivered to targets as easily as optical fibres guide visible light [6].

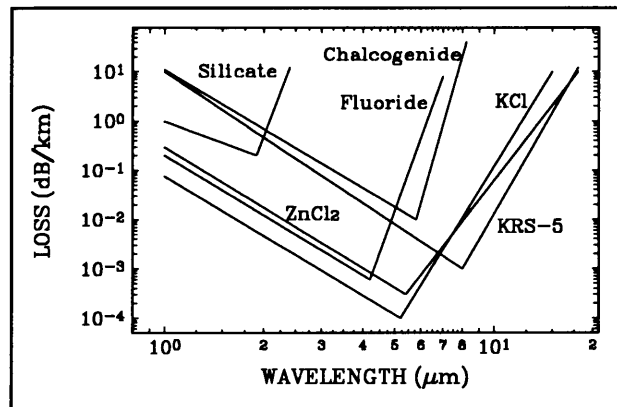


**Figure 1.3 Theoretical attenuation for a number of infrared fibre materials [4]**

Hollow waveguides provide a simpler approach to solve the laser power delivery problem. Hollow waveguides of square, rectangular and circular cross section have been developed for use at 10.6  $\mu$ m. Square and circular guides of about 2 mm in diameter are flexible enough to be used in endoscopic (medical) applications. The main advantage of these guides is their ability to carry high laser power - more than 800 Watt of CW-CO<sub>2</sub> power has been transmitted in rectangular guides measured by Elsa Garmire and co-workers [6], and 1 kW CW-CO<sub>2</sub> transmission through a 1.5 mm circular hollow guide was reported by Hongo *et al.* [7].

The five dominant factors that will influence the attenuation through a waveguide are:

- the diameter of the waveguide (inverse cube dependence),
- the wavelength of the transmitted light (square dependence),
- bends (losses will increase with a smaller radius of curvature bend),
- the materials used, and
- the optical finish of the waveguide.

As seen, the only effective waveguides in the  $10\ \mu\text{m}$  region are hollow waveguides. These waveguides can be of silica, metal or some combination of metal and dielectric materials (multilayer structure of infrared materials). Hollow dielectric waveguides have been used for  $10\ \mu\text{m}$  radiation but have extremely large transmission losses, called bending losses [8]. On the other hand losses below 1 dB per meter for a bent metal waveguide were observed (90° bend with a 50 cm radius of curvature)[6]. Surprisingly, the measured losses are far larger than one would expect from calculations of Marcatili and Schmeltzer [8] for cylindrical waveguides. Coupling from the low order waveguide modes to higher order high loss modes takes place in a bent hollow waveguide. It is then clear that high losses are expected for bent waveguides.

A difficulty in dealing with metallic waveguides in the infrared region is that this region of the EM spectrum is intermediate between the visible and microwave regions. In this region the index of refraction can be near unity or very large. This leads to the existence of different families of modes [9]. The azimuthally symmetric  $\text{TE}_{0q}$  and  $\text{TM}_{0q}$  modes are by symmetry required to exist throughout the entire wavelength range. The rest of the modes change markedly from one end of the spectrum to the other. For example the azimuthally non-symmetric transverse modes in the microwave region ( $\text{TE}_{pq}$ ,  $\text{TM}_{pq}$ ,  $p \neq 0$ ) are replaced by  $\text{HE}_{pq}$  ( $p \neq 0$ ) modes in the visible range [8].

The present reason for looking at hollow infrared waveguides is the need for a more compact Raman cell for converting infrared ( $\text{CO}_2$  laser) wavelengths to the first Stokes in a medium of parahydrogen at low pressure ( $< 1\ \text{atm}$ ). Due to the fact that the Raman process is an intensity effect it is possible to get away with a very compact and reasonably short Raman amplifier (between 5 and 15 meters). Pulsed power densities should be kept below  $1\ \text{GW}/\text{cm}^2$  to avoid gas breakdown, but high enough (above  $0.4\ \text{GW}/\text{cm}^2$ ) for efficient frequency conversion. Furthermore, a gaseous medium will be used in the waveguide. Thus it must be hollow with a diameter between 1.5 mm and 2.5 mm.

## ***1.3 LASER BEAM QUALITY PARAMETER- $M^2$***

In practice, the propagation of a laser beam is difficult to predict. There are many exterior influences which will result in unpredicted behaviour. For example:

- aberrations introduced to a beam by the optical system,
- high order resonator modes in the case of large aperture high power lasers, and
- unstable resonator modes which are highly diffracted beams in the near-field and have a Gaussian-like centre spot in the far-field.

A beam can focus at an unexpected position and size due to the above-mentioned reasons. In Chapter 5 the propagation of a "real" laser beam will be discussed. It will be shown that relationships derived for Gaussian beam propagation, mode-matching, etc. can be used with the introduction of a beam quality parameter called the  $M^2$ . Using this parameter and Gaussian relationships the beam propagation (coherent, partially coherent and incoherent) can be described using the transformation  $\lambda' = M^2\lambda$ .

It will be shown that the laser beam parameters, i.e. minimum beam radius  $W_0$ , position of the minimum radius  $z_0$  and the beam quality parameter  $M^2$  are extremely important for optimization of the amplifier extraction and Raman cell transmission. In this thesis all beam radii referred to will be the radius at  $1/e^2$  of the peak intensity. If any other definition is used this will be pointed out.



## **1.4 REFERENCES: CHAPTER 1**

1. Generation of 16  $\mu\text{m}$  radiation using stimulated Raman scattering in  $\text{H}_2$ .  
W.R. Trutna  
PhD Dissertation, Stanford University (1979)
2. Nonlinear infrared generation  
Ed: Y -R Shen  
Springer-Verlag Berlin, Heidelberg, New York (1977)
3. Parametric four-wave mixing processes in sodium vapour  
Y Shevy, M Rosenbluh  
Opt Lett **12**(4),257,(April 1987)
4. Infrared fibre optics  
P. Klocek  
Lasers & Applications **43**, (Oct 1982)
5. Infrared fibres: An overview of prospective materials, fabrication methods and applications  
B. Bendow, H. Rast, O.H. El-Bayoumi  
Opt Eng **24**(6),1072,(Nov/Des 1985)
6. Flexible infrared-transmissive metal waveguides  
E. Garmire, T. McMahon, M. Bass  
Appl Phys Lett **29**(4),254,(Aug 1976)
7. Transmission of 1 kW - class  $\text{CO}_2$  laser light through circular hollow waveguides for material processing  
A. Hongo, K. Morosawa, T. Shista  
Appl Phys Lett **58**(15),1582,(April 1991)
8. Hollow metallic and dielectric waveguides for long distance optical transmission and lasers  
E.A.J. Marcatili, R.A. Schmelzter  
Bell Syst Tech J **43**,1783,(1964)
9. Mode-coupling analysis of bending losses in infrared metallic waveguides  
M.E. Marhic  
Appl Opt **20**(19),3436,(Jan 1981)

## ***LIST OF SYMBOLS: CHAPTER 1***

- $M^2$  : beam quality parameter
- $W_0$  : minimum beam radius of a nonideal laser beam (this compares with the minimum radius  $\omega_0$  of a Gaussian beam)
- $z_0$  : the position of  $W_0$  along the propagation axis
- $\lambda$  : free space wavelength
- $\lambda'$  : the effective wavelength used for beam propagation calculations
- $\omega_P$  : input pump frequency
- $\omega_R$  : Raman transition frequency
- $\omega_S$  : output Stokes frequency

## 2. INFRARED WAVEGUIDES

### 2.1 INTRODUCTION

Hollow waveguides of appropriate geometry and material composition can be used to transmit infrared light in the same way as microwaves. The ideal hollow guide would consist of a perfectly reflecting metal tube. However, in practice all guides have finite losses that limit their useful transmission distance. Another type of hollow reflection guide might employ a multilayer dielectric coating (electro-formed [1,2,3] or rf-sputtered [4]) on the inside of the hollow guide. Alternatively, it would be possible to transmit light in the anomalous dispersion regime of hollow dielectric guides[5]. In addition to small but finite absorption losses, hollow guides also have much higher bending losses than solid fibres. Hollow waveguides appear better suited for applications involving power delivery over short distances of 1 to 10 metres.

For a hollow-glass fibre, the glass acts as the cladding and the air is essentially the fibre core, in analogy to step index fibres. Clearly, to achieve a condition of total internal reflection, and thus a high transmission, the glass cladding must have a refractive index of less than unity at the wavelength of interest. In hollow core waveguides there are virtually no core losses. However, these losses are now replaced by waveguide wall losses. Hollow core waveguides are manufactured of different types of glasses. Hidaka *et al.* [5] worked on  $\text{GeO}_2\text{-ZnO-K}_2\text{O}$  glasses as the cladding material for a hollow-core waveguide for  $10.6 \mu\text{m}$ . The same approach was followed by Worrell and Skarda [6] whose results suggested that glasses with low oxide additions ( $<10\%$ /mole) to  $\text{GeO}_2$  are preferable when waveguide transmission and

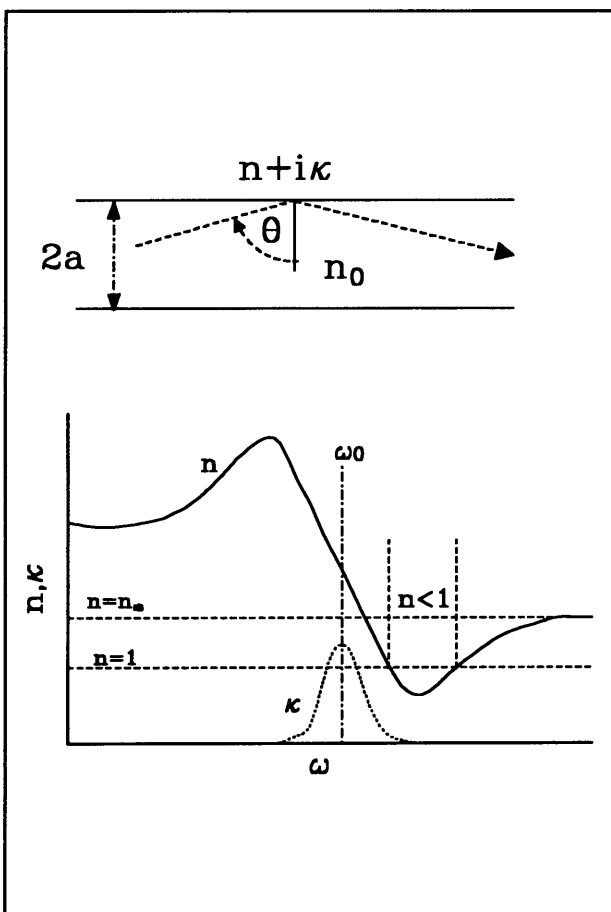


**Figure 2.1** Complex refractive index,  $n + iK$ . When  $K$  is large enough,  $n$  may have a value less than unity [5].

fibre fabrication are taken into account. The basic idea behind this type of waveguide is to design a glass that maintains a refractive index of less than unity at CO<sub>2</sub> laser wavelengths (see Figure 2.1).

There are a number of different fibres available on the market, especially for the near to mid-infrared region, and a few lossy fibres at 10.6 μm. For the infrared region of 10.6 μm the only useful glass fibres/waveguides are GeO<sub>2</sub>-based glasses and TiO<sub>2</sub>-SiO<sub>2</sub> based glasses which might be superior to GeO<sub>2</sub> glasses in environmental durability[7].

Other polycrystalline materials with good infrared transmission can be used, these are the silver halides (AgCl and AgBr) and the alkali-halides (KCl) and ZnSe. These materials are all extremely difficult to use because of their ductility (AgCl), surface cracking and tearing (KCl) and their susceptibility to weakening from bending. For a 1 mm fibre, the radius of curvature has to be more than 12 cm to avoid permanent deformation. It is therefore clear that poor mechanical behaviour is a disadvantage of these types of fibres.

For the above-mentioned reasons and because of the available technology, it was decided to use the metal waveguide for Raman scattering. Most of the work presented in this chapter will then focus on metal waveguides with a dielectric coating on the inner surface. A short discussion on the manufacturing and difficulties experienced will also be given.

## 2.2 THEORETICAL ANALYSIS

This analysis deals with the design of a low-loss hollow metallic waveguide with a single dielectric layer on the inner surface of a metal guide. The theoretical analysis of the glass hollow-core waveguides is formally the same. Furthermore it is important to know the condition for efficiently coupling the laser's TEM<sub>00</sub> mode to the low-loss mode of a waveguide. The coupling coefficients  $\eta_{1m}$  will be calculated and experimentally verified.

The notation used by Snitzer [8] and Degnan [9] is followed in this analysis. The notation differs in the hybrid mode identification where the dominant waveguide mode characterized by a single intensity peak is referred to as the EH<sub>11</sub> in the work by Marcatili *et al.* [10] whereas Snitzer describes this as the HE<sub>11</sub> mode. This section is based on work by Marcatili and Schmeltzer [10] and Snitzer [8] and is restricted to a mode description and the

analysis of the mode excitation for a straight circular waveguide using a  $TEM_{00}$  laser beam. Consider a circular guide (Figure 2.2) of radius  $a$  and free space dielectric constant  $\epsilon_0$  embedded in another medium of dielectric or metal having a complex dielectric constant  $\epsilon$ .

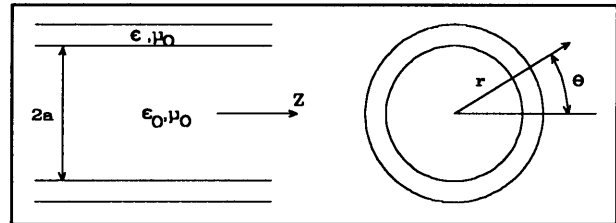


Figure 2.2 Hollow waveguides

Using the assumptions

$$ka = \frac{2\pi a}{\lambda} \gg |v| u_{nm}, \quad \left| \left( \frac{\gamma}{k} \right) - 1 \right| \ll 1, \quad (2.1)$$

where  $k = \omega \sqrt{\epsilon_0 \mu_0} = 2\pi/\lambda$  is the free-space propagation constant,  $u_{nm}$  is the  $m$ -th root of the equation  $J_{n-1}(u) = 0$  with  $n$  and  $m$  integers that characterize the propagating mode,  $v = (\epsilon/\epsilon_0)^{1/2} = n + ik$  is the complex refractive index of the external medium and  $\gamma$  is the axial propagation constant of the mode under consideration. The first inequality states that the radius  $a$  is much larger than the free space wavelength  $\lambda$ . In the case of metallization of the external medium,  $|v|$  may be quite large but still finite at optical frequencies. The second inequality restricts the analysis to low-loss modes, which are those whose propagation constants  $\gamma$  are nearly equal to that of free space. This guide supports three types of modes, i.e. transverse circular electric modes whose only field components are  $E_\theta$ ,  $H_r$  and  $H_z$ , transverse circular magnetic modes whose components are  $H_\theta$ ,  $E_r$  and  $E_z$  and the third are the hybrid modes with all the electric and magnetic components present. The field components for the different modes are given below. Only the mode equations for the internal medium are shown [10]:

a. Circular electric  $TE_{0m}(n=0)$

$$\left. \begin{aligned} E_{\theta 0m} &= J_1(u_{0m} \frac{r}{a}) \\ H_{r 0m} &= -\sqrt{\frac{\epsilon_0}{\mu_0}} J_1(u_{0m} \frac{r}{a}) \\ H_{z 0m} &= -i \sqrt{\frac{\epsilon_0}{\mu_0}} \frac{u_{0m}}{ka} J_0(u_{0m} \frac{r}{a}) \end{aligned} \right\} \exp[i(\gamma z - \omega t)], \quad (2.2a)$$

b. Circular magnetic modes  $TM_{0m}$  ( $n=0$ )

$$\left. \begin{aligned} E_{r0m} &= J_1(u_{0m} \frac{r}{a}) \\ E_{z0m} &= i \frac{u_{0m}}{ka} J_0(u_{0m} \frac{r}{a}) \\ H_{\theta 0m} &= \sqrt{\frac{\epsilon_0}{\mu_0}} J_1(u_{0m} \frac{r}{a}) \end{aligned} \right\} \exp[i(\gamma z - \omega t)] , \quad (2.2b)$$

c. Hybrid modes  $HE_{nm}$  ( $n \neq 0$ )

$$\left. \begin{aligned} E_{\theta nm} &= \left[ J_{n-1}(u_{nm} \frac{r}{a}) + \frac{i u_{nm}^2}{2nka} \sqrt{v^2 - 1} J_n'(u_{nm} \frac{r}{a}) \right] \cos[n(\theta + \theta_0)] \\ E_{rnm} &= \left[ J_{n-1}(u_{nm} \frac{r}{a}) + \frac{i u_{nm}}{2kr} \sqrt{v^2 - 1} J_n(u_{nm} \frac{r}{a}) \right] \sin[n(\theta + \theta_0)] \\ E_{znm} &= -i \frac{u_{nm}}{ka} J_n(u_{nm} \frac{r}{a}) \sin[n(\theta + \theta_0)] \end{aligned} \right\} \exp[i(\gamma z - \omega t)] , \quad (2.2c)$$

$$\left. \begin{aligned} H_{\theta nm} &= \sqrt{\frac{\epsilon_0}{\mu_0}} E_{rnm} \\ H_{rnm} &= -\sqrt{\frac{\epsilon_0}{\mu_0}} E_{\theta nm} \\ H_{znm} &= -\sqrt{\frac{\epsilon_0}{\mu_0}} E_{znm} \cot(n(\theta + \theta_0)) \end{aligned} \right\} , \quad (2.2d)$$

with  $u_{um}$  the  $m$ -th root of

$$J_{n-1}(u_{nm}) = 0 . \quad (2.3)$$

As usual,  $|n|$  is the number of periods of each field component in the  $\theta$  direction, and  $m$  is both the order of the root of equation (2.3) and the number of maxima and minima of each component counted in the radial direction within the internal medium.

For  $n=0$ , the modes are either transverse electric  $TE_{0m}$  or transverse magnetic  $TM_{0m}$ . The lines of the electric field of the  $TE_{0m}$  modes are transverse concentric circles centred on the  $z$ -axis. The lines of the magnetic field are in planes containing the  $z$ -axis. Similarly, the lines of the magnetic field  $TM_{0m}$  modes are transverse concentric circles centred on the  $z$ -axis with the electric field contained in radial planes. For  $n \neq 0$ , the modes are hybrid,  $HE_{nm}$ , i.e. the magnetic and electric fields are three-dimensional with relative small axial field components in the internal medium. Thus the hybrid modes are almost transverse. See Figure 2.3 for a graphical representation of some of the waveguide modes.

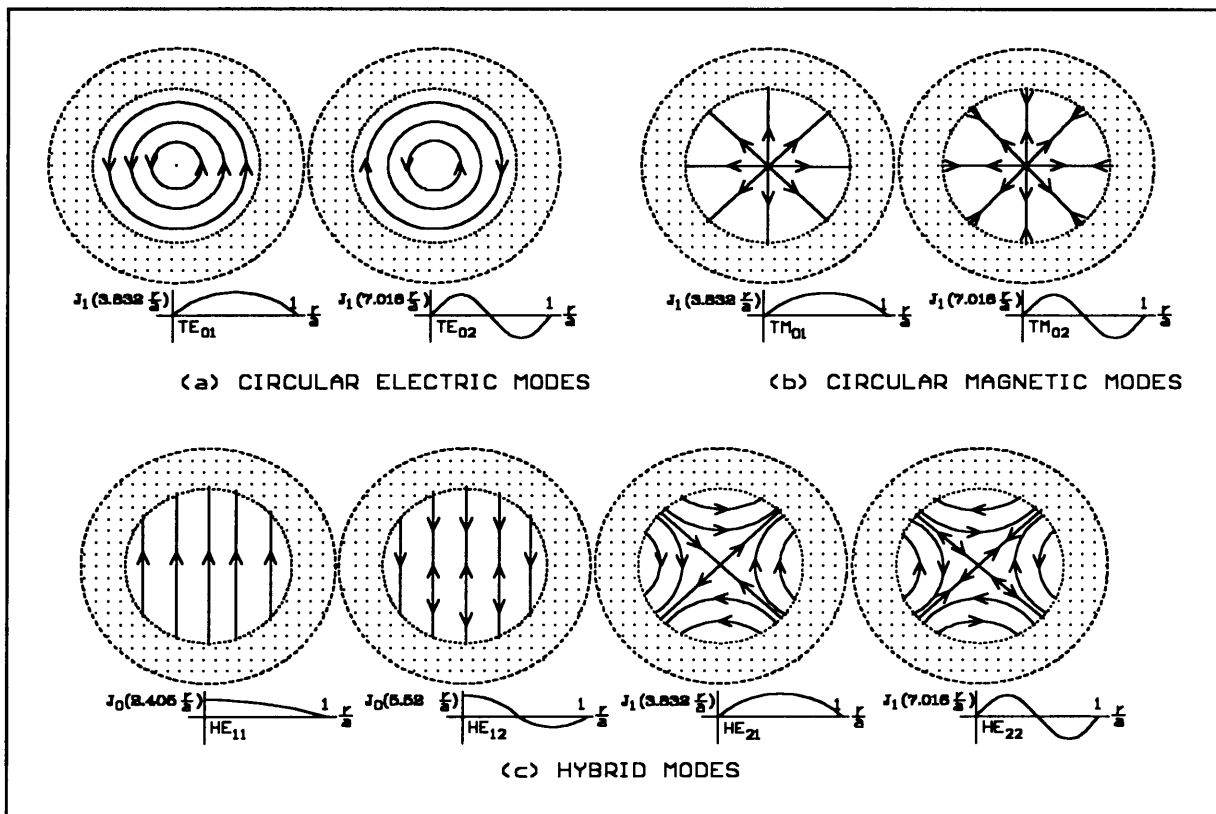


**Figure 2.3** Electric field lines of modes in hollow waveguides: (a) circular electric modes, (b) circular magnetic modes and (c) hybrid modes [10]

It is clear from Figure 2.3 that the  $HE_{1m}$  waveguide modes are linearly polarized. As shown in the figure the polarization is vertical. However owing to symmetry the horizontal polarization can also exist. Clearly a superposition of these components will allow a circular polarization to exist in the waveguide. This is confirmed by the measurement shown in Figure 2.20.

### 2.2.1 COUPLING INTO A HOLLOW WAVEGUIDE

The coupling of the laser energy into different waveguide modes is one of the fundamental aspects of the waveguide Raman experiment. It gives the relationship between the low-loss transverse laser mode ( $TEM_{00}$ ) and the low-loss waveguide mode ( $HE_{11}$ ) and is therefore of importance for the nonlinear optical processes taking place in the waveguide. The properties of the  $HE_{1m}$  waveguide modes and the extent of this excitation by the incoming laser field will thus be discussed.

There is a transition from the free-space (Gaussian electromagnetic wave) to a hollow

dielectric metallic waveguide. This transition is associated with the creation of a new wave front shape. The wave front propagation is now restricted by a different set of boundary conditions. A further requirement is that the electric and magnetic field amplitudes in the boundary (including the entrance aperture of the waveguide) must be continuous. Thus at the entrance the incoming field has to satisfy the wave equation describing the propagation inside the waveguide.

The coupling of the laser beam to the waveguide is important since the higher order waveguide modes have high transmission losses. It is therefore necessary that the low-loss  $HE_{11}$  should be, as far as possible, the only mode excited by the incoming  $TEM_{00}$  beam. Multimode coupling causes large losses - called coupling losses.

The coefficients  $\eta_{lm}$  describe the coupling of the free wave to the waveguide modes. Their values depend not only on the mode available, but also on the shape of the waveguide opening and on the direction of the incoming field relative to the guide axis.

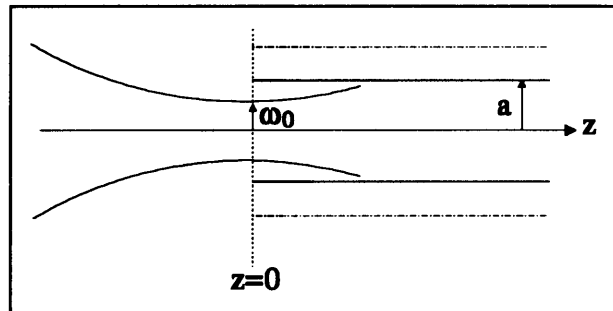


**Figure 2.4** Coupling of a laser beam to a waveguide

The discussion will be restricted to straight guides in which the direction of the incoming wave is parallel to the axis of the waveguide. Figure 2.4 shows the coupling scheme with the beam focused at the waveguide aperture (at  $z=0$ ). The incoming electric field is given by (Chapter 5)

$$E_{n,m} = E_0 H_n \left( \sqrt{2} \frac{x}{\omega_0} \right) H_m \left( \sqrt{2} \frac{y}{\omega_0} \right) e^{\left( -\frac{(x^2+y^2)}{\omega_0^2} \right)}, \quad (2.4)$$

where  $H_n$  and  $H_m$  are Hermite polynomials and  $\omega_0$  is the radius at  $1/e^2$  of the peak intensity - that is, at  $1/e$  of the peak field. It is shown by Heuer *et al.* [11] that Hermite Gaussian beams will only couple to the  $HE_{1m}$  waveguide modes which are linearly polarized. The coupling coefficients are given by [11,12,13]



$$\eta_{1m} = \frac{\left| \int_0^a e^{-\frac{r^2}{\omega_0^2}} J_0\left(u_m \frac{r}{a}\right) r dr \right|^2}{\int_0^\infty e^{-\frac{2r^2}{\omega_0^2}} r dr \int_0^a J_0^2\left(u_m \frac{r'}{a}\right) r' dr'} \quad (2.5)$$

for the  $TEM_{00}$  free-space beam coupled to the  $HE_{1m}$ , where  $r^2 = x^2 + y^2$  and  $u_m = u_{0m}$  (equation 2.3) is the  $m$ -th root of  $J_0(u) = 0$ . Figure 2.5 shows that there is an  $\omega_0/a$  ratio for which optimum  $HE_{11}$  mode coupling can be achieved. Near single mode excitation is possible for  $\omega_0/a \approx 0.66$  using a  $TEM_{00}$  input laser beam. Evidently, weak focusing will lead to excitation of only the lowest waveguide mode  $HE_{11}$ . At this coupling condition 98% of the power/energy is coupled to the waveguide. The 2% power loss is due to the truncation of the Gaussian beam. At  $\omega_0/a \sim 0.5$ , virtually 100% of the energy is coupled to the waveguide with about 10% to the high loss  $HE_{12}$  mode so that this energy will be lost after some propagation in the waveguide (see Section 2.2.2).

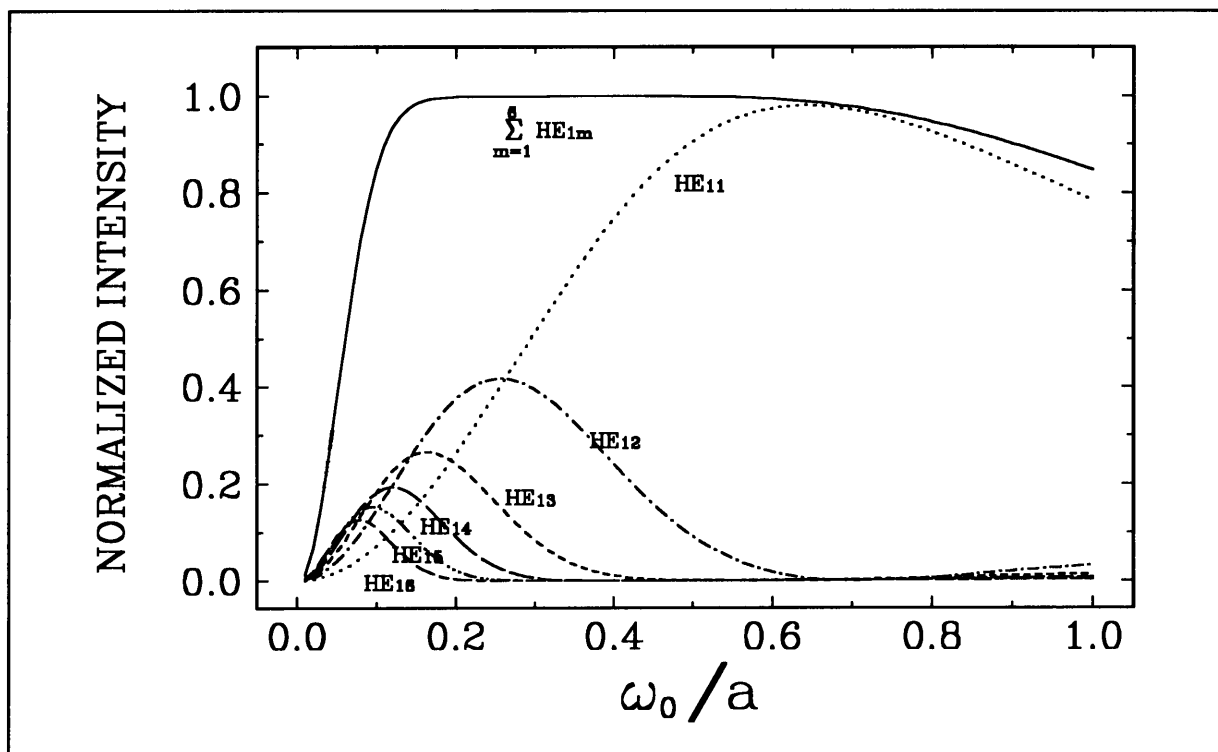


**Figure 2.5** Excitation of the  $HE_{1m}$  ( $m=1,2,3,4,5,6$ ) mode for a cylindrical hollow waveguide of radius  $a$  by a  $TEM_{00}$  laser beam

Figure 2.6 shows the field pattern, about a half a metre beyond the exit aperture of the waveguide, for two different launching conditions for the  $TEM_{00}$  to a nickel-germanium waveguide of 1.6 m in length with a core diameter of 2.3 mm. A CW- $CO_2$  laser delivering 30 Watt in a  $TEM_{00}$  mode was used for these measurements.

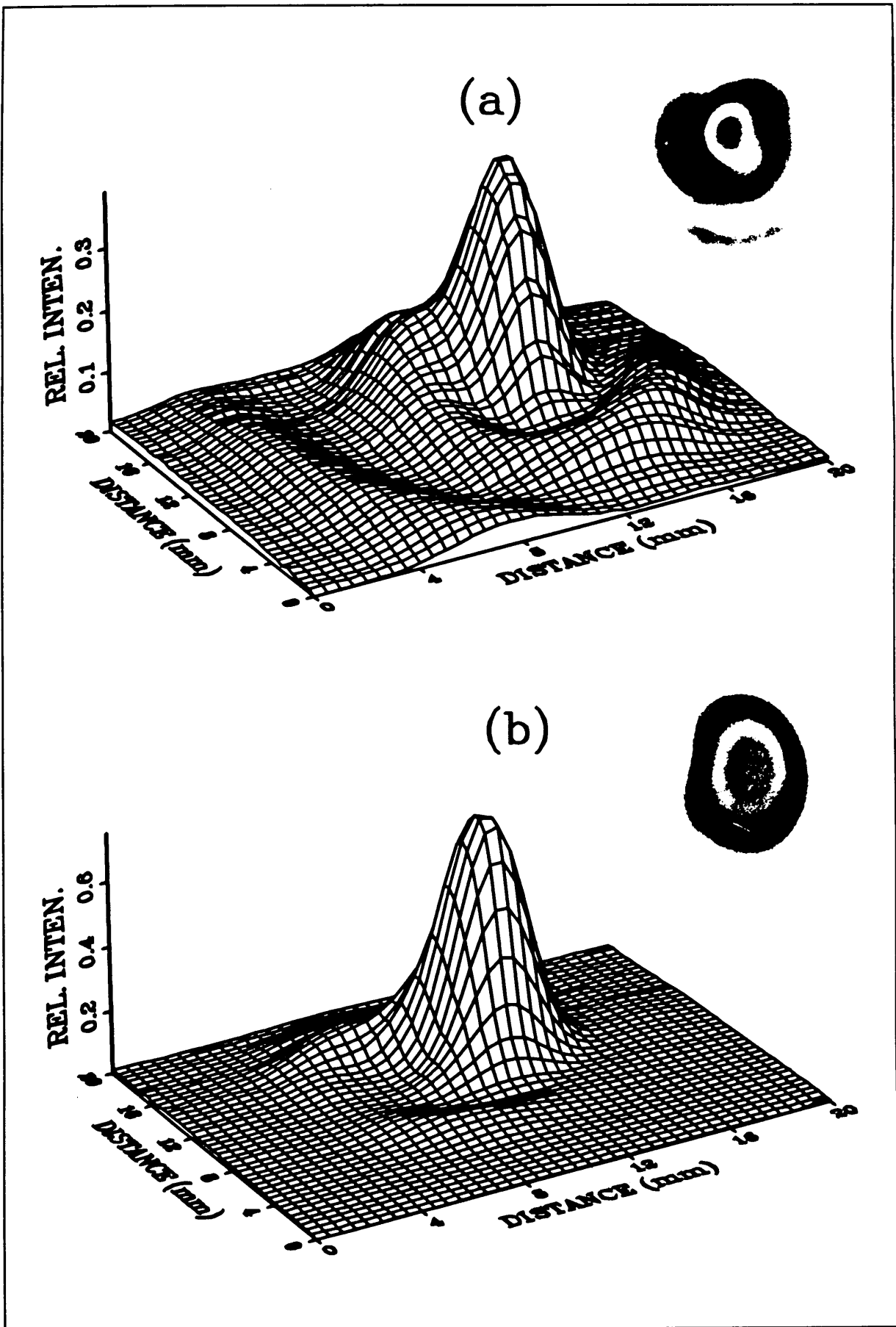


**Figure 2.6** Measured mode output for a 1.6 m nickel-germanium waveguide: (a)  $\omega_0/a \approx 0.16$  and (b)  $\omega_0/a \approx 0.45$  ( $2a = 2.3$  mm) at  $\lambda = 10.6$   $\mu\text{m}$

In Figure 2.6(a) a coupling condition  $\omega_0/a \approx 0.16$  was used. It is clear that higher order modes are excited, which resulted in this varying intensity distribution. Also shown are the burn patterns on thermal paper at the scanning position. A different distribution is found with a coupling condition of  $\omega_0/a \approx 0.45$  at exactly the same position along the propagation path. Clearly, less coupling into higher order modes was achieved with most of the energy in the  $HE_{11}$  and  $HE_{12}$  waveguide modes. From the relative intensity scale (on Figure 2.6) it is clear that the tighter focusing option introduced higher order modes that have higher losses than with using a weaker focus.

### 2.2.2 ATTENUATION COEFFICIENTS OF HYBRID MODES FOR HOLLOW METAL WAVEGUIDES WITH AN INNER DIELECTRIC LAYER

In this section only the  $HE_{1m}$  losses will be discussed. These are the only waveguide modes excited by the  $TEM_{00}$  laser mode. Consider a metal guide with refractive index  $n+i\kappa$ , core radius  $a$  and refractive index  $n_0$  and an inner dielectric layer of thickness  $\delta a$  and refractive index  $n_d$  (see Figure 2.7). Without the dielectric layer the attenuation coefficients  $\alpha_m$  of the hybrid  $HE_{1m}$  modes are expressed as [14]

$$\alpha_m = n_0 k \frac{u_m^2}{(n_0 k a)^3} \frac{n}{2}, \quad (2.6)$$

where  $u_m$  is the  $m$ -th root of  $J_0(u)=0$  and  $k=2\pi/\lambda$ . These are the attenuation coefficients for a pure metal guide.

For the guide in Figure 2.7 with a dielectric layer of thickness  $\delta a$  and refractive index  $n_d$ , the attenuation constants are given by [14]

$$\alpha_m = n_0 k \frac{u_m^2}{(n_0 k a)^3} \alpha_{metal} \alpha_{diel} = n_0 k \frac{u_m^2}{(n_0 k a)^3} F, \quad (2.7)$$

where

$$\alpha_{metal} = \frac{n}{n^2 + \kappa^2}, \quad \alpha_{diel} = \frac{1}{2} \left[ 1 + \frac{n_d^2}{(n_d^2 - 1)^{1/2}} \right]^2, \quad F = \alpha_{metal} \alpha_{diel} \quad (2.8)$$

when  $\delta a$  is chosen optimally in accordance with equation (2.11).

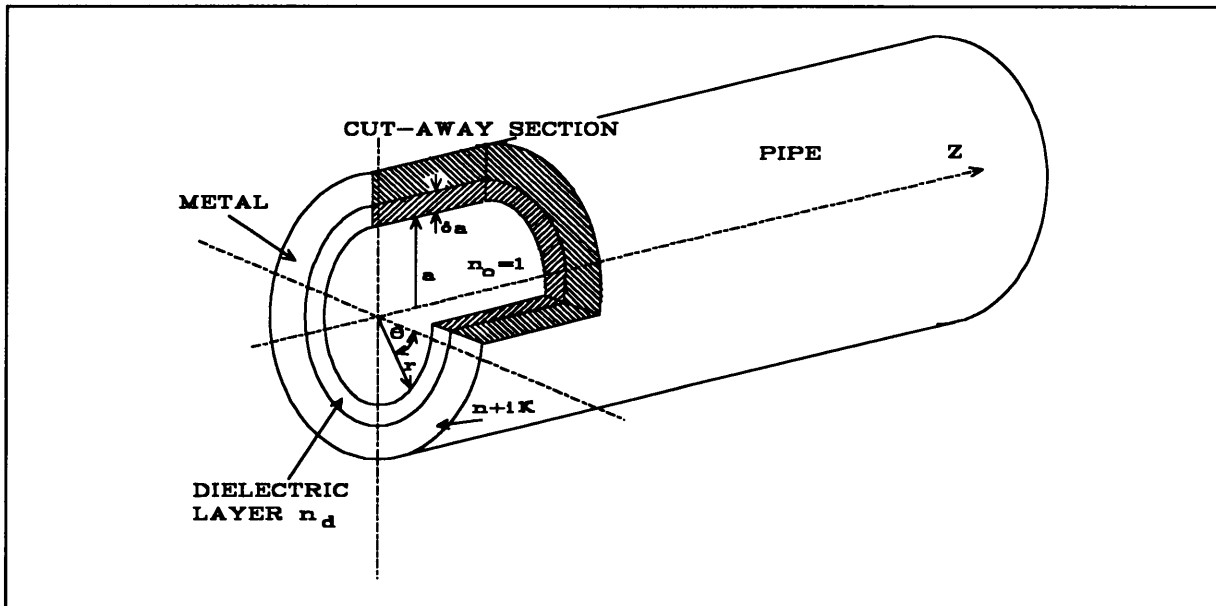


**Figure 2.7** Metal waveguide with an inner dielectric layer for improved waveguide transmission

Assuming no absorption losses in the dielectric layer material, the relative power output from a waveguide of length  $L$  can be calculated. Using the orthogonality<sup>[1]</sup> of the guided modes in a straight guide the output  $P$  can be written as

$$P = \sum_{m=1}^N \eta_m e^{-\alpha_m L}, \quad (2.9)$$

where  $N$  is the number of propagating modes. For these calculations only the first six modes [ $HE_{1m}$  ( $m=1,2,3,4,5,6$ )] will be considered.

<i>METAL [14]</i>				<i>DIELECTRIC [15]</i>	
Type	$n$	$\kappa$	$\alpha_{\text{metal}}$ ( $\times 10^{-3}$ )	Type	$n_d$
Ag	15.5	75.3	2.31	KCl	1.454
Cu	14.1	64.3	3.27	AgCl	1.98
Au	17.1	55.9	5.02	ZnSe	2.4
Ni	9.08	34.8	7.03	Ge	4

**Table 2.1** Input values for minimum loss calculations for the  $TEM_{00}$  laser mode excited  $HE_{1m}$  waveguide modes

The input values used for the calculations are shown in Table 2.1. Most of the calculations were performed for the 10P20  $CO_2$  laser line ( $\lambda = 10.6 \mu\text{m}$ ). From Figure 2.8 it is clear that the transmission losses can be reduced considerably if a correctly designed dielectric layer (see

<sup>[1]</sup> This implies that modes do not couple into other modes.

Section 2.2.3) is used on the inner surface of the metal waveguide. Furthermore, from Table 2.1 and Figure 2.9 it is evident that silver waveguides with a KCl layer will be the optimum guide if only the transmission of a guide is considered (see Figure 2.10). As it is expensive to manufacture pure silver waveguides, combinations of metal layers can be used as shown in Figure 2.11. Due to the availability of a germanium-plating technique and the low mechanical strength of the other dielectric materials, germanium was selected for further investigation (see Section 2.3 for the manufacture of waveguides).

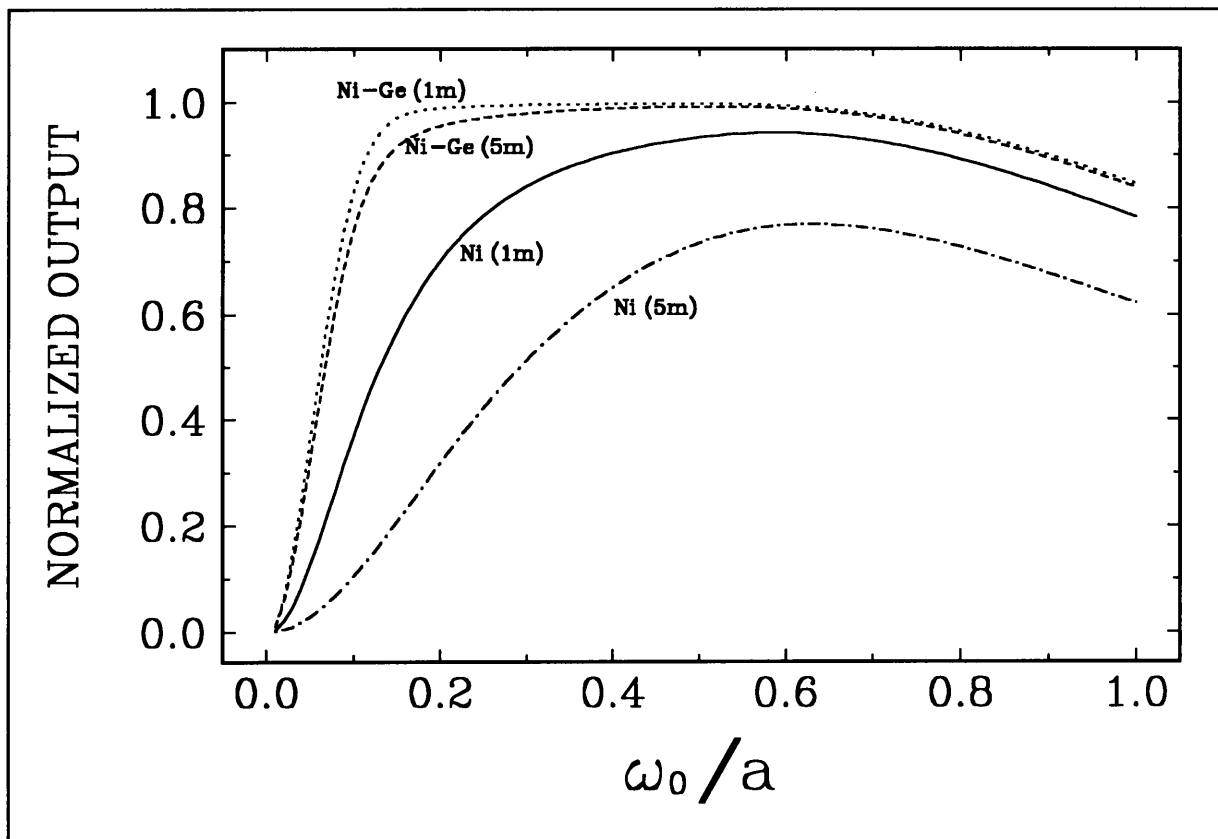


**Figure 2.8** Theoretical transmission ( $P$ ) of a nickel guide with and without a germanium layer for 1 m and 5 m guides of  $2a=2.3$  mm as a function of  $\omega_0/a$

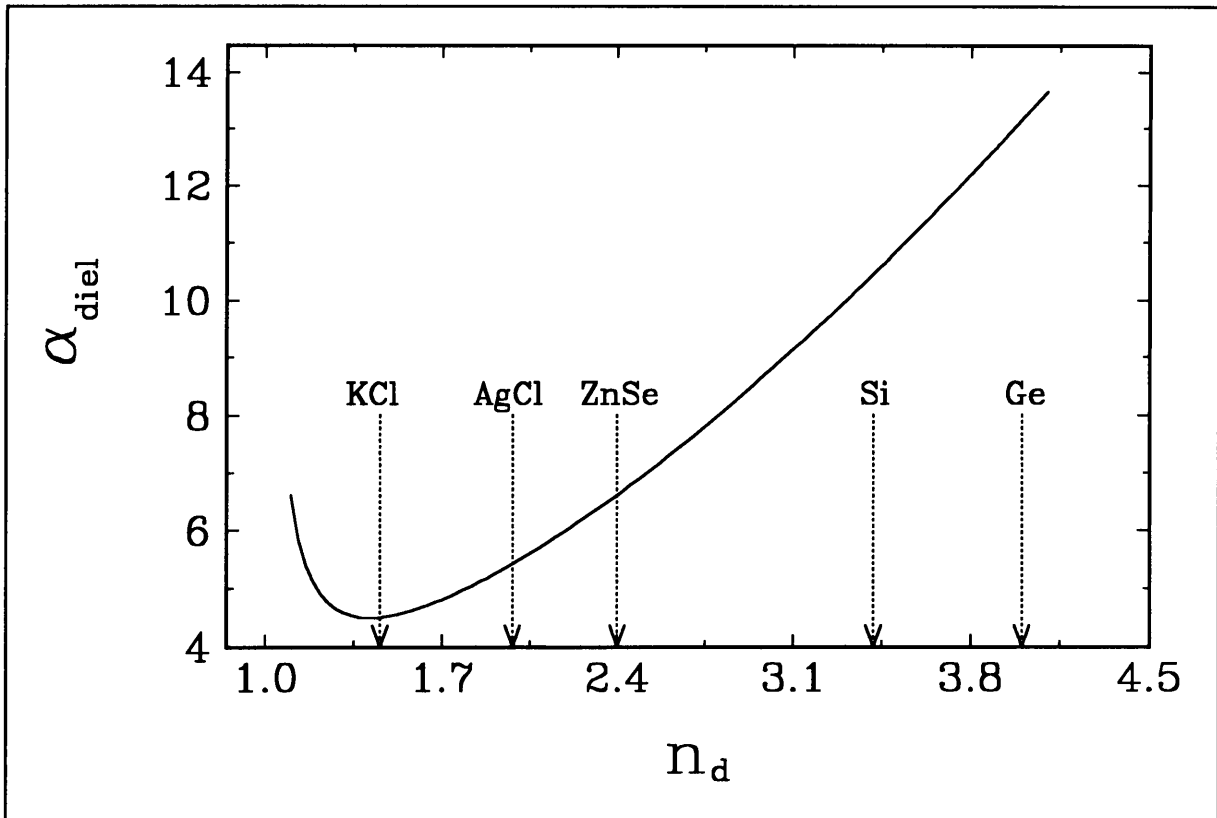


Figure 2.9  $\alpha_{diel}$  as a function of dielectric refractive index

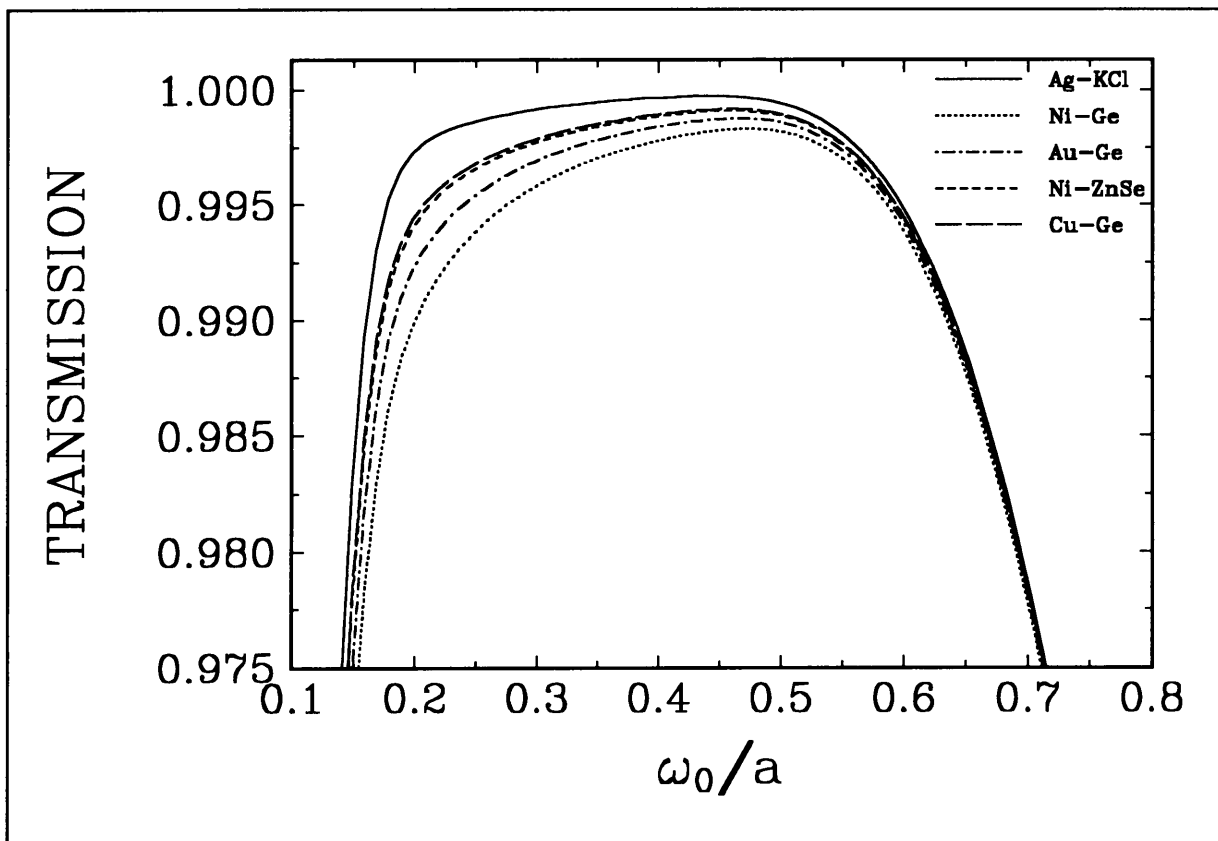
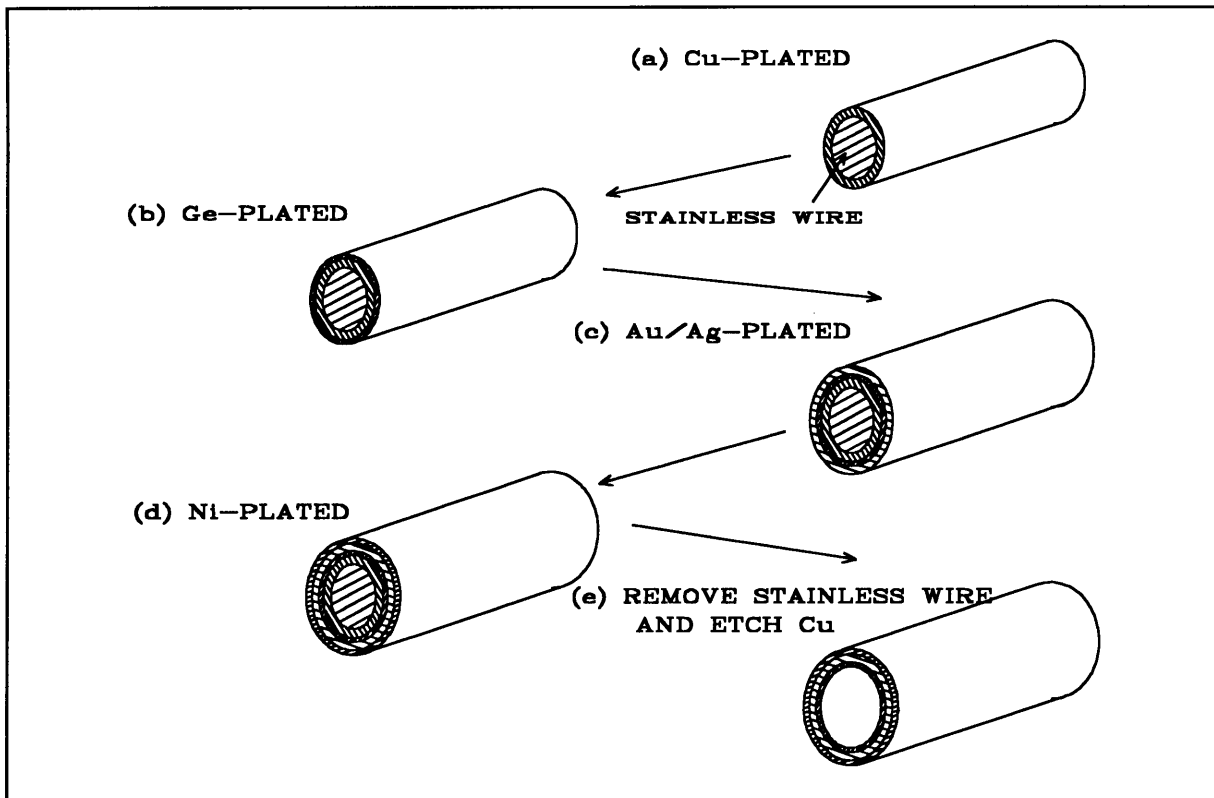


Figure 2.10 Theoretical transmission ( $P$ ) of various hollow waveguides (core diameter - 2.3 mm and length 1 m) as a function of  $\omega_0/a$



**Figure 2.11** Manufacturing technique of waveguides using high-value metals

### 2.2.3 DIELECTRIC LAYER THICKNESS FOR MINIMUM LOSS

From the work of Miyagi *et al.* [14] it is clear that there are discrete layer thicknesses for which the attenuation constants are minimized. For the layer depicted in Figure 2.7, the attenuation constants are minimized for

$$F = \alpha_{metal} \alpha_{diel} = \left[ \frac{1}{(1+\cos 2x)} + \frac{c^2}{(1-\cos 2x)} \right] \frac{n}{n^2 + \kappa^2}, \quad (2.10)$$

where  $c = \frac{n_d^2}{(n_d^2 - 1)^{1/2}}$  at

$$x \equiv \delta a (n_d^2 - 1)^{1/2} n_0 k a = \pm \arctan \left[ \frac{n_d}{(n_d^2 - 1)^{1/4}} \right] + s\pi \quad s=0,1,2,\dots \quad (2.11)$$

The waveguide has to be designed for use as a Raman amplifier which implies that the pump wavelength  $\lambda_p$ , and the Stokes wavelength  $\lambda_s$ , must both have low loss on propagation through the waveguide. Assuming  $\lambda_p = 10.2 \mu\text{m}$  then the Stokes wavelength will be  $\lambda_s = 16 \mu\text{m}$ .

Figure 2.12 shows the parameter  $F$  (defined in equation (2.10)) as a function of (a) wavelength and (b) layer thickness. It is clear that one can specify a layer thickness that will allow good transmission for both the wavelengths.

The thicknesses for  $s=0$  and 1 are selected as the values for the designed layer thickness. With these layers the absorption is minimised because of the thin layer ( $\delta a < 1 \mu\text{m}$ ). For the waveguides that were manufactured, a layer thickness of  $0.52 \mu\text{m}$  ( $s=0$ ) was specified which is the thickness for minimum losses at  $10.6 \mu\text{m}$ . At this stage only the  $10.6 \mu\text{m}$  transmission was of interest and not the  $16 \mu\text{m}$ .

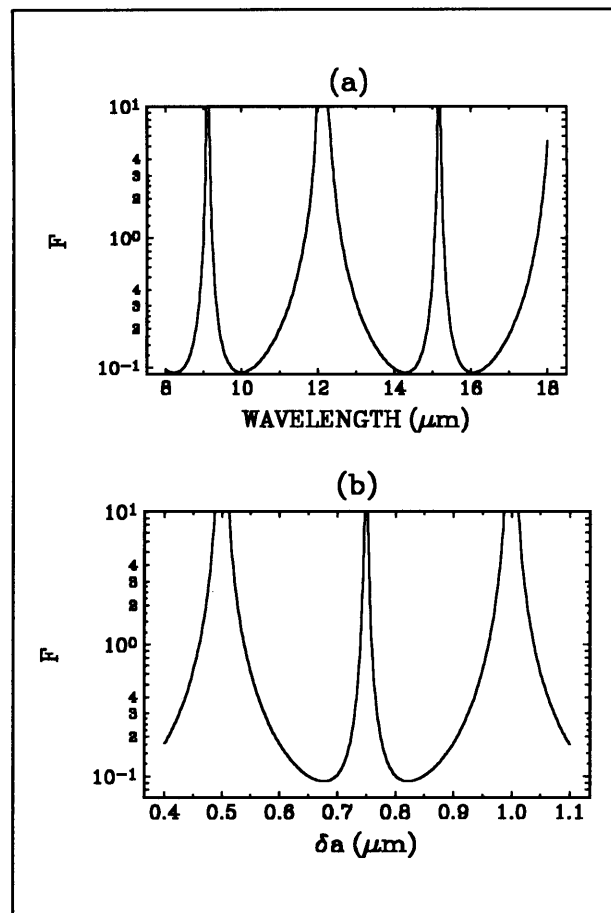


**Figure 2.12**  $F$  vs (a)  $\lambda$  for  $\delta a = 0.83 \mu\text{m}$  and (b)  $\delta a$  for  $\lambda_p = 10.2 \mu\text{m}$  using a Ni-Ge waveguide

## 2.3 WAVEGUIDE MANUFACTURE

Manufacture of the waveguides is beyond the scope of this project. However, a brief discussion will be given. The procedure is shown in Figure 2.13. Specialized plating techniques are needed for the production of useful guides. Initially, nickel-germanium waveguides of 1 m were manufactured. From the validated Raman model (Section 4.4) it became clear that waveguides longer than 10 m were needed for sufficient single-pass gain. This would entail unacceptably high cost. From the literature it appears that the manufacture of such waveguides has not yet been achieved. The idea was then to use the already available 2.2 m waveguides as Raman amplifiers (see Section 4.4) and terminate the production of longer nickel-germanium waveguides.



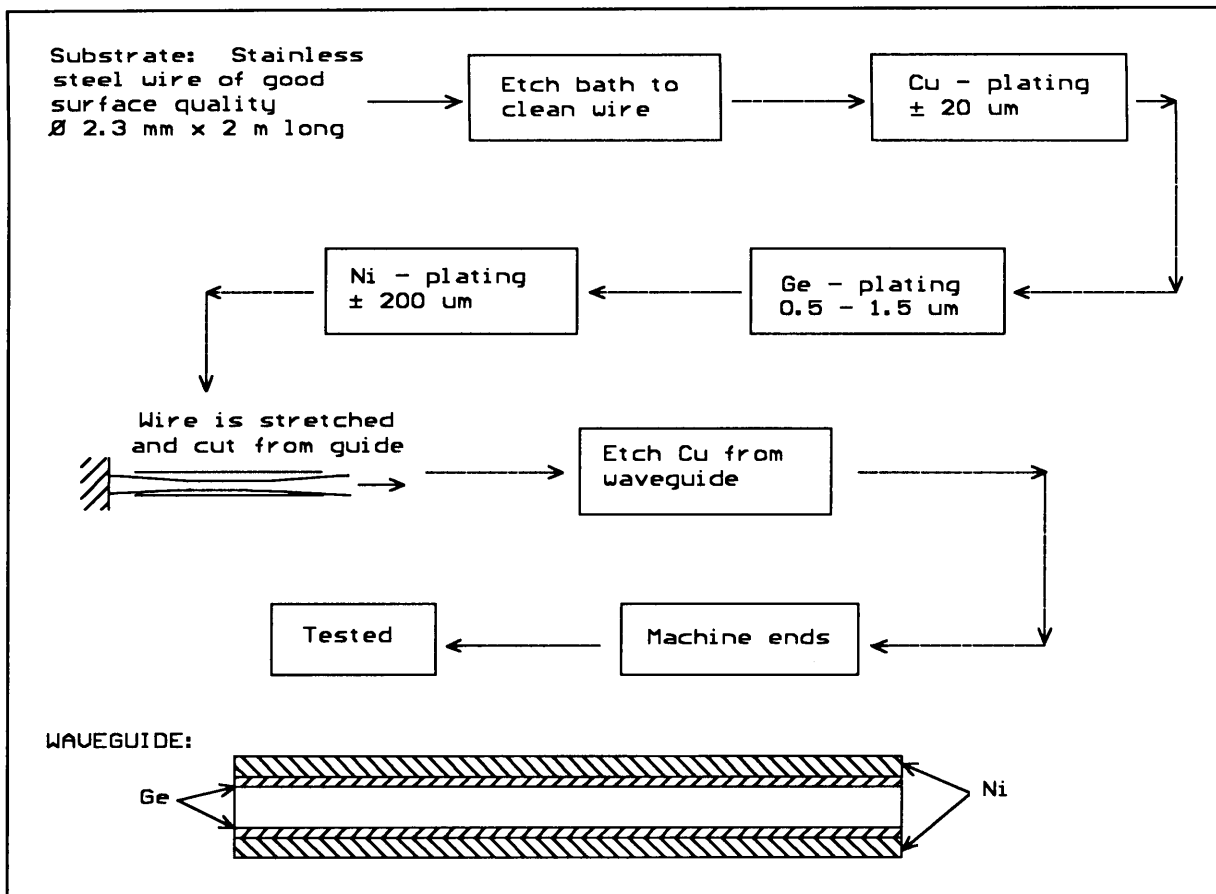


**Figure 2.13** Manufacturing process

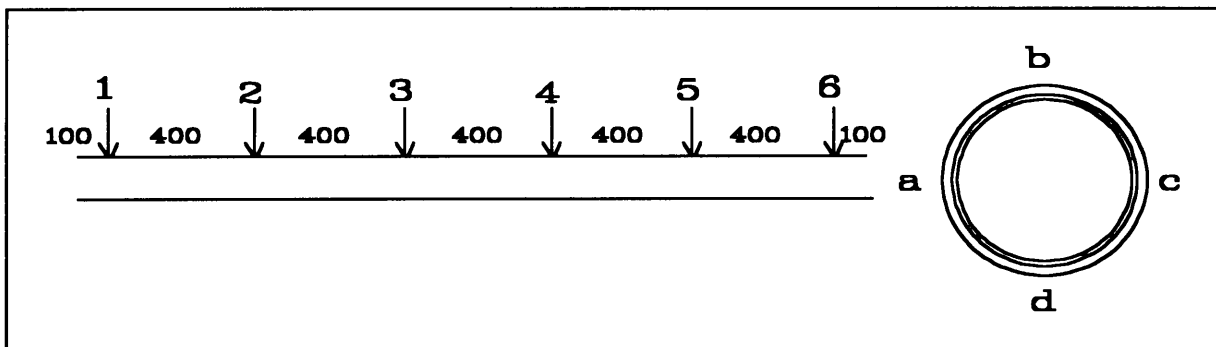


**Figure 2.14** Explanation of  $\delta a$  measurements shown in Table 2.2. The sizes are given in millimeters.

The technology for the plating of copper and nickel is well known. The only new technology was the plating of germanium. Two plating schemes were used as shown in Figure 2.15. The horizontal technique (Figure 2.15a) gave layers of fairly uniform<sup>[2]</sup> thickness  $\delta a$  - see Table 2.2. In the (destructive) measurement samples of the waveguides were cut at the

<sup>[2]</sup> The uniformity is insufficient for the wavelength matching shown in Figure 2.12. It is, however, considered to be excellent in the context of electroplating technology. This indicates that electroplating is not an appropriate technology for the manufacture of high transmission dielectric coated waveguides in this wavelength region.

positions shown in Figure 2.14. However, it was clear from transmission measurements and microscopic investigation that the optical quality of the waveguide surface is a key property needed for good transmission. The germanium surface roughness is due to the cathode contacts to the copper plated stainless steel wire.

A number of transmission experiments were performed using the vertical plating technique (Figure 2.15b) which employs two contact points at the ends of the wire. A layer thickness that is a function of the voltage drop over the length of the wire was expected. This was also confirmed by

microscopic measurements of the layer thickness as shown in Table 2.3. Better transmissions were measured with these guides. This suggests that at the present level of manufacturing expertise, the surface finish is more important than the layer uniformity.

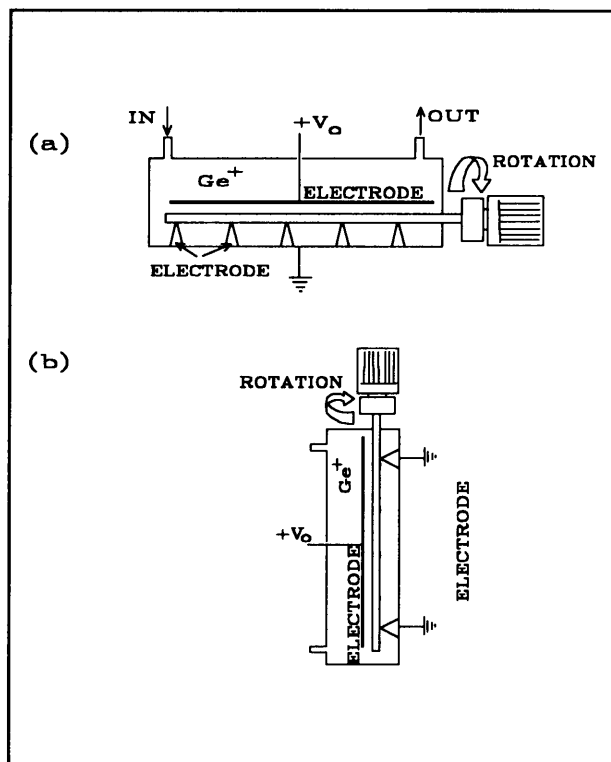


Figure 2.15 Ge plating techniques

Cross section #	Position on waveguide perimeter				Average ( $\mu\text{m}$ )
	<i>a</i>	<i>b</i>	<i>c</i>	<i>d</i>	
1	0.9	0.9	0.8	0.8	$0.85 \pm 0.05$
2	1.1	1.0	1.1	1.0	$1.05 \pm 0.05$
3	1.1	1.1	1.1	1.1	1.1
4	1.1	1.1	1.2	1.1	$1.125 \pm 0.04$
5	1.2	1.2	1.1	1.2	$1.175 \pm 0.04$
6	1.1	1.2	1.3	1.2	$1.2 \pm 0.07$

Table 2.2  $\delta a$  measurements (in microns) for the horizontal plating technique described in Figure 2.15(a). The positions at which the  $\delta a$ 's were measured are shown in Figure 2.14 [16].

Figure 2.15b also suggests an improvement of the plating technique. If an anode of the same resistance per unit length as the copper plated steel wire is used, the voltage drop across the

anode - cathode should be fairly constant. Thus, better uniformity of the germanium layer  $\delta a$  can be expected [17].

Cross Section #	Position on waveguide perimeter				Average ( $\mu\text{m}$ )
	<i>a</i>	<i>b</i>	<i>c</i>	<i>d</i>	
1	0	0	0	0	0
2	0	0	0	0	0
3	3.7	3.8	3.8	3.8	$3.78 \pm 0.04$
4	4.2	3.9	3.8	3.8	$3.85 \pm 0.14$
5	3.6	3.5	2	3.2	$3.08 \pm 0.64$
6	2.2	2.8	2.1	2.3	$2.35 \pm 0.27$
7	3.0	2.8	3.2	3.0	$3.0 \pm 0.14$
8	2.8	3.0	2.4	2.6	$2.7 \pm 0.22$
9	2.5	2.4	3.6	3.2	$2.93 \pm 0.5$
10	1.5	1.4	1.5	1.7	$1.53 \pm 0.11$
11	3.8	4.5	3.5	4.2	$4.0 \pm 0.4$
12	4.6	5.0	5.1	5.0	$4.93 \pm 0.2$
13	6.2	5.0	5.2	5.0	$5.35 \pm 0.5$
<b>Overall Average</b>					$3.41 \pm 1.12$

**Table 2.3**  $\delta a$  measurements (in microns and on a single waveguide) for the vertical plating technique described in Figure 2.15(b). The positions at which the  $\delta a$ 's were measured are shown in Figure 2.14, except that the measurement spacing is now 100 mm and not 400 mm [18].

## 2.4 MEASUREMENT OF PARAMETERS RELEVANT TO EFFICIENT RAMAN CONVERSION

From Chapters 3 and 4 it will be clear that the following parameters determine the nett Raman gain in the waveguide Raman cell. They are:

- (a) The degree of power coupling from the  $\text{TEM}_{00}$  free space laser mode to the  $\text{HE}_{11}$  waveguide mode. Inefficient coupling can also shorten the waveguide lifetime and promote gas breakdown in parahydrogen.

- (b) The transmission through the waveguide. If good transmission is not achieved, the losses introduced will increase the threshold for Raman action. This will probably result in impractical lengths of waveguides needed (see Section 4.4 ).
- (c) The pump laser beam must be circularly polarized.

### 2.4.1 COUPLING CONDITION MEASUREMENTS

We now describe the measurement of the coupling condition (the value for  $\omega_0/a$ ) for the excitation of the  $HE_{11}$  waveguide mode. In order to do this, the propagation of this fundamental mode that exits from the waveguide is measured.

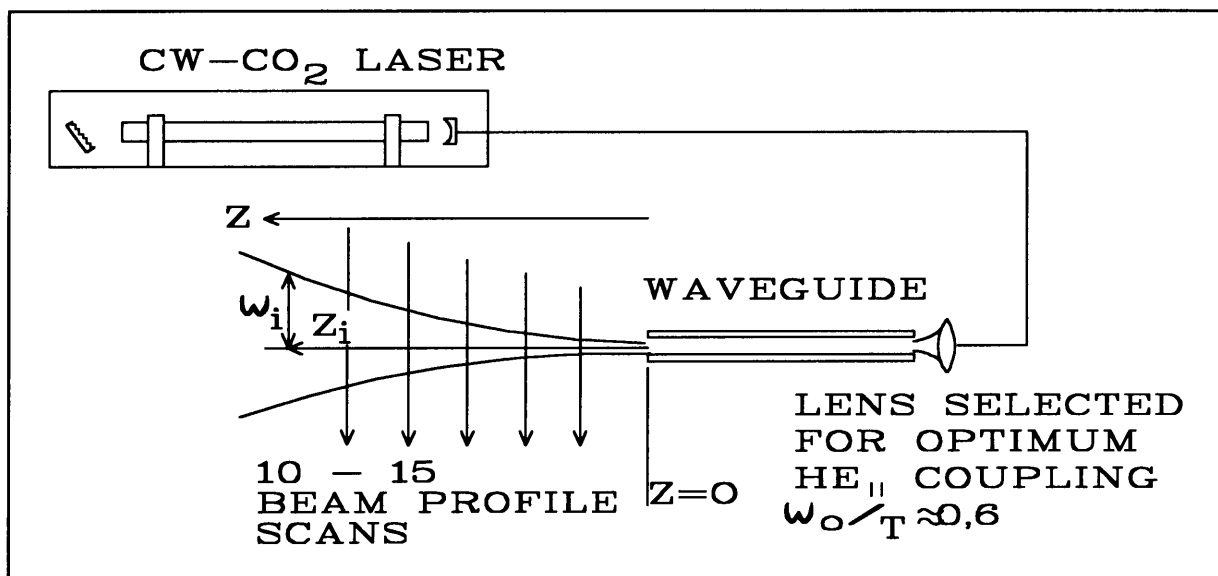


Figure 2.16  $\omega_0/a$  - ratio measurement layout

Assume that this  $HE_{11}$  waveguide mode can be approximated by a Gaussian distribution. This is a good approximation - see Bennett *et al.* [19]. The measurement procedure is shown in Figure 2.16. This procedure is also followed in Chapter 5 for the characterization of a laser beam, except here  $M^2$  is taken as 1. The propagation of an ideal Gaussian beam is given by (see Chapter 5):

$$\omega^2(z) = \omega_0^2 \left( 1 + \left( \frac{z-z_0}{z_R} \right)^2 \right)$$

with the Rayleigh range  $z_R = \pi\omega_0^2/\lambda$  and  $\omega_0$  the effective minimum beam radius at the exit aperture of the waveguide. The  $z$ -axis origin ( $z=0$ ) is taken as the position of the exit aperture. A typical result of a least-squares fit is shown in Figure 2.17.

Table 2.4 shows a number of waveguides measured for the fundamental mode  $HE_{11}$  propagation. These values compare well with the maximum coupling conditions calculated by Bennet *et al.* [19] and the values reported by Belland *et al.* [20]. The discrepancy with the value 0.644 calculated in Section 2.2.1 is probably due to the assumption that  $M^2 = 1$ . Thus the  $HE_{11}$  mode does not propagate as an ideal Gaussian beam. If the definition followed by Johnston [21] is used, an  $M^2 \equiv W_0^2/\omega_0^2 = 1.3$  can be calculated.

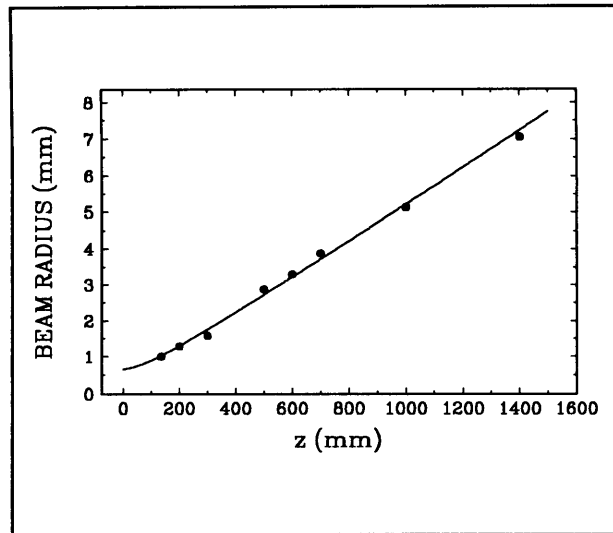


Figure 2.17 Typical  $\omega_0/a$  measurement

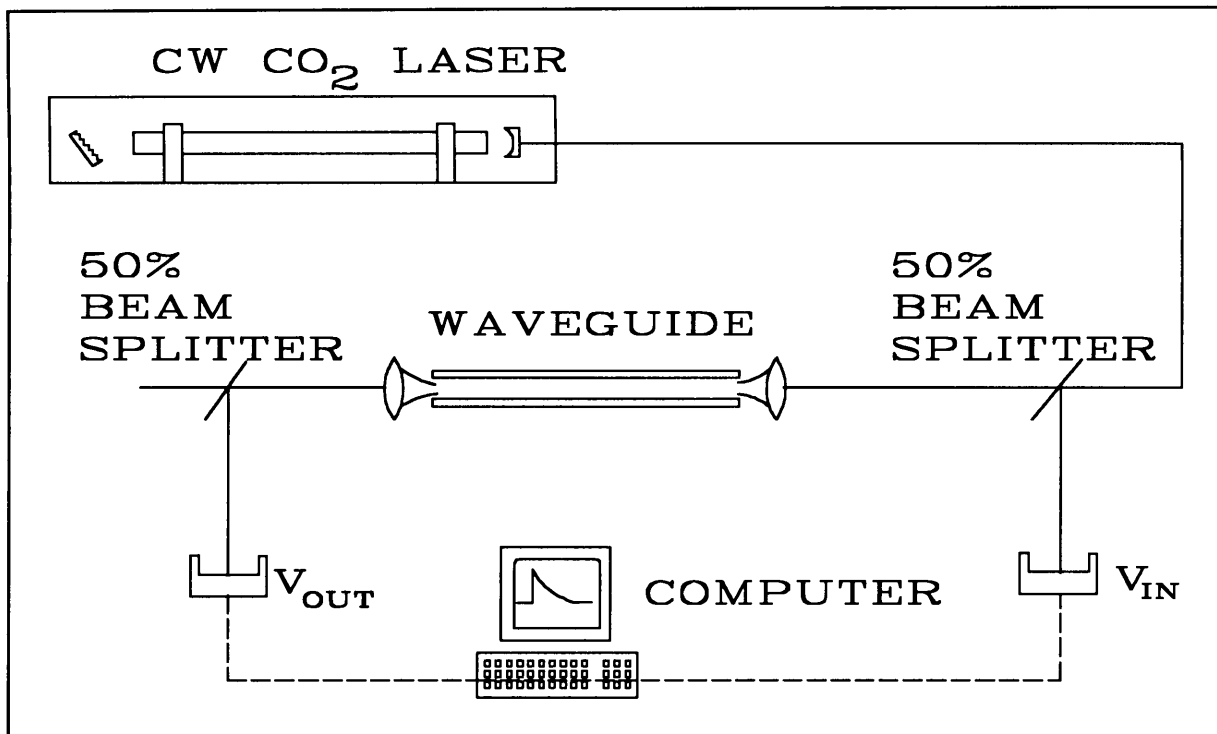
Waveguide no.	$z_0$ (mm)	$\omega_0$ (mm)	$\omega_0/a$
1	$8 \pm 10$	$0.63 \pm 0.03$	$0.55 \pm 0.03$
2	$-11 \pm 15$	$0.66 \pm 0.03$	$0.57 \pm 0.03$
3	$-16 \pm 10$	$0.66 \pm 0.06$	$0.57 \pm 0.04$
4	$-23 \pm 31$	$0.65 \pm 0.06$	$0.57 \pm 0.04$
5	$9 \pm 16$	$0.62 \pm 0.03$	$0.54 \pm 0.03$
<b>Average</b>	$-6.5 \pm 21$	$0.64 \pm 0.05$	$0.56 \pm 0.04$

Table 2.4  $\omega_0/a$ -ratio measurements for the  $HE_{11}$  waveguide mode and a number of different waveguides

### 2.4.2 TRANSMISSION MEASUREMENTS

The experimental setup is shown in Figure 2.18. It is clear from the figure that the power transmission, described by equation (2.9), is measured. The measurement therefore includes the coupling efficiency and the attenuation losses owing to

- the waveguide mode coupled, and
- the optical quality and layer thickness of the germanium layer.



**Figure 2.18** Experimental layout for transmission measurements

There are two methods to accurately measure the attenuation coefficient for the  $HE_{11}$  waveguide mode. They are:

- (a) The experimental verification of Figure 2.8 can be used. In this case a number of  $\omega_0/a$  ratios can be used which will allow one to extract the attenuation constants for the different waveguide modes.
- (b) The second method described by Matsuura *et al.* [22] employs an incoherent source with a large divergence angle ( $7^\circ$  FWHM) and a high loss coupler. Using this configuration many higher order modes are excited and relatively large transmission losses can be measured on short waveguides ( $< 1$  m).

As already mentioned only the power transmission was measured (Figure 2.18). We were unable to measure attenuation coefficients. All the measurements were taken with the same lens system and the ratio  $\omega_0/a$  was therefore constant. It was not possible at the time to determine this ratio precisely, but it was between 0.4 and 0.6 (see Figure 2.8).

Table 2.5 shows the transmission measurements for a number of the better 1.1 m waveguides. The guides were manufactured using the technique described in Figure 2.15(a). From Figure 2.12, it is clear that a uniform thickness is needed for good transmission. The results

<i>Length (m)</i>	<i>Transmission</i>	
	<i>%</i>	<i>dB/m</i>
1.1	90	0.42
1.1	91	0.37
1.1	93	0.29
1.1	95	0.2
1.1	95	0.2
1.1	96	0.16
1.1	98	0.09

**Table 2.5** *Transmission measurements for waveguides manufactured using the technique shown in Figure 2.15(a)*

in Table 2.5 and the measurements shown in Table 2.2, show a large variance which can probably be explained by:

- High loss due to the variation in germanium-layer thickness (Figure 2.12)
- Optical quality of the germanium layer. It was found that the optical quality of the layers is adversely affected by defects in the form of holes ( $> 1 \mu\text{m}$ ) and cracks ( $> 10 \mu\text{m}$  in length) in the electro-formed germanium layer - see the report by Mudde[23]. In this report it was also shown that some waveguides have excellent surface quality - better than  $1 \mu\text{m}$ . This appears to be the reason for the large variances in the output beam quality and transmissions measured.

<i>Length (m)</i>	<i>Transmission</i>	
	<i>%</i>	<i>dB/m</i>
2.0	76	0.6
2.0	81	0.46
1.8	80	0.54
1.8	86	0.36
1.6	90	0.29

**Table 2.6** *Transmission measurements for waveguides manufactured using the technique shown in Figure 2.15(b)*

The second set of measurements was obtained from guides that were manufactured by the technique shown in Figure 2.15(b). As shown in Table 2.3 the wall thickness varies between  $1.4 \mu\text{m}$  and  $6.2 \mu\text{m}$  on a single waveguide. This and again the surface quality are probable causes for the poor transmissions measured (Table 2.6) as transmissions of better than 99% ( $< 0.025 \text{ dB/m}$ ) were expected .

The coupling efficiencies were obtained by measuring the output for a short waveguide. It was found that the quality of the launching aperture (in terms of surface finish and aperture obstructions) is most important. It appears from these measurements and the results obtained in Section 4.4 that the manufacture of high quality infrared waveguides needs much more attention before these waveguides can be used as single-pass Raman amplifiers.

### 2.4.3 POLARIZATION MEASUREMENTS

Heuer *et al.* showed that the fundamental modes  $\text{HE}_{1m}$  are the only modes that are linearly polarized[11] (see also Figure 2.3). From symmetry, both horizontal and vertical linear polarizations must be permitted. Hence also superpositions of these linear polarizations. We now determine whether the linear and circular polarization of the laser beam launched into the waveguide is indeed retained on transmission through the waveguide. Figure 2.19 shows the experimental arrangement used for this measurement.

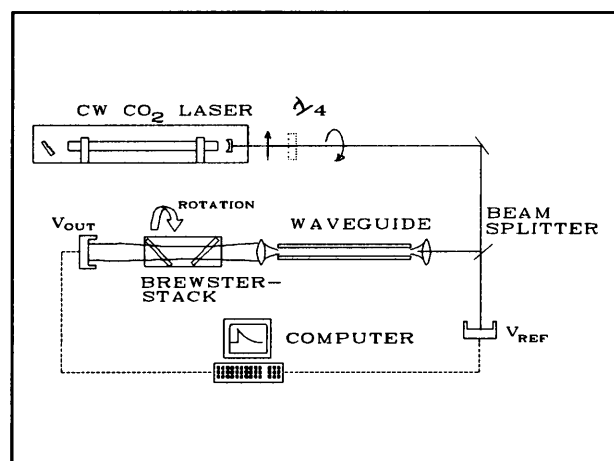


**Figure 2.19** *The experimental layout for the polarization measurement*

A germanium Brewster stack was used as polarizer with a 250:1 polarization ratio (see Appendix 2.A). Figure 2.20 shows the results for a 1 m nickel-germanium waveguide. It was again not possible at the time to determine the  $\omega_0/a$  ratio precisely, but it was between 0.4 and 0.6. It appears that the polarization of the laser beam is retained on propagation through a short waveguide ( $L \approx 1 \text{ m}$ ). It would then be possible to achieve maximum Raman gain in the waveguide with a circularly polarized beam launched into the guide.



## 2.4.4 CONCLUSIONS

A waveguide can be used as a laser beam confinement for an infrared Raman conversion. However only short waveguides (<2 m) were used for 10  $\mu\text{m}$  measurements because of the manufacturing limitations. Longer waveguides (>2 m) can be used if the manufacturing problems are solved. Two aspects of the nickel-germanium waveguides need improvement:

- the optical finish of the germanium layer, and
- the uniformity of the germanium-layer thickness.

If these conditions are met, high quality waveguides with a power transmission of better than 98% per meter for the  $\text{HE}_{11}$  mode, can be manufactured.

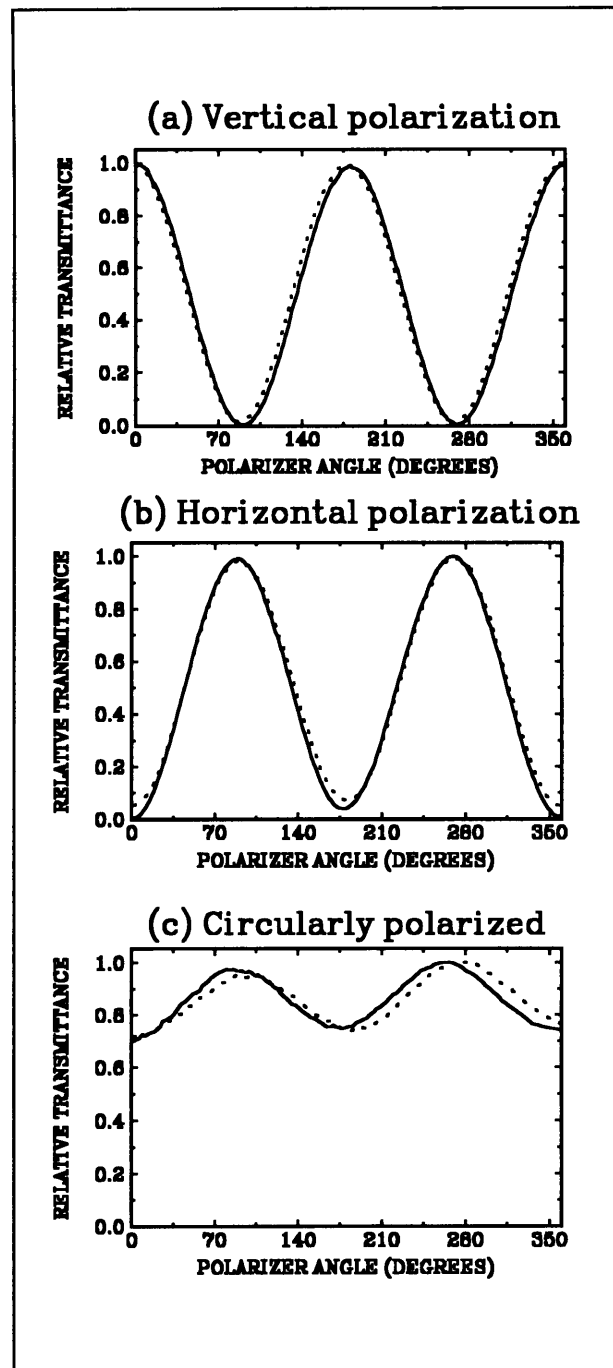


**Figure 2.20** Polarization measurements. Solid line - laser beam (waveguide removed in Figure 2.19). Dashed line - waveguide output.

## 2.5 REFERENCES: CHAPTER 2

1. Fabrication of dielectric-coated metallic, hollow waveguides for infra-red radiation by the electro-deposition of germanium  
M. Miyagi, Y. Shimada, S. Nishida  
*Opt & Laser Tech*, 197,(Aug 1985)
2. Electro-formed Ni-Ge waveguides (Afrikaans)  
F.R. Strydom  
AEC quarterly report of chemical surface treatment technology, (April 1989)
3. Fabrication and transmission properties of electrically deposited germanium-coated waveguides for infrared radiation  
M. Miyagi, Y. Shimada, A. Hongo, K. Sakamoto, S. Nishida  
*J Appl Phys* **60**(1),454, (July 1986)
4. Fabrication of germanium coated nickel hollow waveguides for infrared transmission  
M. Miyagi, Y. Shimada, A. Hongo, K. Sakamoto, S. Nishida  
*Appl Phys Lett* **43**(5),431, (Sept 1983)
5. GeO<sub>2</sub>-ZnO-K<sub>2</sub>O glass as the cladding material of 940 cm<sup>-1</sup> CO<sub>2</sub> laser light transmitting hollow-core waveguide  
T. Hidaka, K. Kumada, J. Shimada, T. Morikawa  
*J Appl Phys* **53**(8), 5484,(Aug 1982)
6. CO<sub>2</sub> laser waveguides from germania-based glasses  
C.A. Worrel, V. Skarda  
*J Phys D: Appl Phys* **22**, 535,(1989)
7. TiO<sub>2</sub>-SiO<sub>2</sub> based glasses for IR hollow waveguides  
N. Nagano, M. Saito, M. Miyagi, N. Baba, N. Sawanobori  
*Appl Opt* **30**(9), 1074, (20 March 1991)
8. Cylindrical dielectric waveguide modes  
E. Snitzer  
*J Opt Soc of Amer* **51**,491,(1961)
9. Waveguide laser mode patterns in the near and far field  
JJ Degnan  
*Appl Opt* **12**(5), 1026, (May 1973)

10. Hollow metallic and dielectric waveguides for long distance optical transmission of laser  
E.A.J. Marcatili, R.A. Schmelzter  
Bell System Tech Journal, 1783, (July 1964)
11. Stimulated Raman effect and four-wave mixing in a hollow waveguide  
W. Heuer, H. Zacharias  
IEEE J Quantum Elect **24**(10),2087,(October 1988)
12. Excitation dependent losses and temperature increase in various hollow waveguides at 10.6  $\mu\text{m}$   
A. Hongo, M. Miyagi, K. Sakamoto, S. Karasawa, S. Nishida  
Opt & Laser Tech **19**(4),214,(August 1987)
13. Mode-coupling analysis of bending losses in IR metallic waveguides  
M.E. Marhic  
Appl Opt **20**(19),3436,(October 1981)
14. Design theory of dielectric-coated circular metallic waveguides for infrared transmission  
M. Miyagi, S. Kamakami  
J of Lightwave Technology, **LT-2**(2), 116,(April 1984)
15. Handbook on materials data  
BDH CRYSTRAN
16. SEM evaluation of Ge layers (Afrikaans)  
P. Mudde  
AEC report BMW/160/5(8) (MF-2094),(03-09-1987)
17. Private discussions  
T.B. Scheffler  
University of Pretoria, Pretoria,(1993)
18. Thickness of the Cu, Ge and Ni layers (Afrikaans)  
M v Reenen  
AEC report BMF/160/(5) VTF-0122, (05-07-1989)
19. Far field propagation of the truncated  $\text{EH}_{11}$  dielectric waveguide mode  
C.A. Bennett, D.P. Hutchinson  
Appl Opt **28**(13),2581,(July 1989)
20. Gaussian approximation of the waveguide  $\text{EH}_{11}$  mode patterns in the far field  
P. Belland, J.P. Crenn  
Opt Comm **45**(3), 165,(April 1983)

21.  $M^2$  concept characterizes beam quality  
T.F. Johnston, Jr.  
Laser focus world, 173, (May 1990)
22. Loss reduction of dielectric-coated metallic hollow waveguides for CO<sub>2</sub> laser light transmission  
Y. Matsuura, M. Miyagi, A. Hongo  
Opt & Laser Tech **22**(2),141,(1990)
23. Surface finish and thickness of Ge-layer on the inner surface of a Nickel pipe  
P. Mudde  
AEC report BMF/160/5/VTF-0146, (24-07-1989)

## APPENDIX 2.A BREWSTER STACK POLARIZER

The Brewster stack is an effective polarizer, especially using dielectric materials of large index of refraction. Figure 2.A.1 shows the multiple reflection of the polarized component perpendicular to the plane of incidence. The question is then: "How many plates are needed to obtain a polarization ratio ( $T_{\parallel} / T_{\perp}$ ) of at least 250:1 on transmittance of the Brewster stack?"

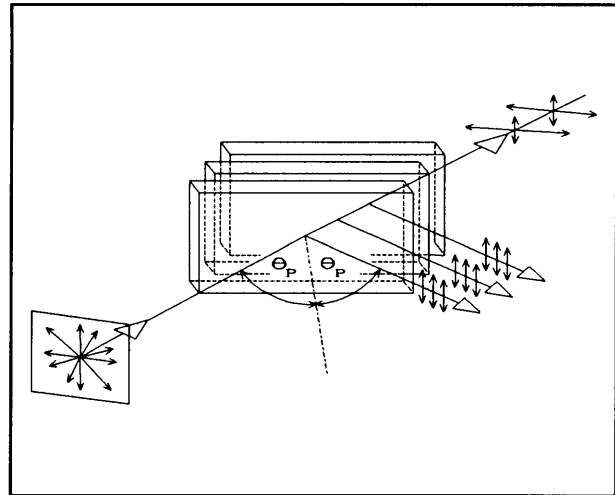


Figure 2.A.1 Brewster stack polarizer

The Fresnel equations<sup>[3]</sup> for the reflection of the parallel  $R_{\parallel}$  and perpendicular  $R_{\perp}$ , components are

$$R_{\parallel} = \frac{\tan^2(\theta_i - \theta_t)}{\tan^2(\theta_i + \theta_t)}, \quad R_{\perp} = \frac{\sin^2(\theta_i - \theta_t)}{\sin^2(\theta_i + \theta_t)}, \quad (2.A.1)$$

with  $\theta_i$ ,  $\theta_t$  defined in Figure 2.A.2. When  $\theta_i + \theta_t = 90^\circ$ ,  $R_{\parallel}$  becomes zero and

$$R_{\perp} = \sin^2(\theta_i - \theta_t) = 1 - T_{\perp}. \quad (2.A.2)$$

The  $\theta_i$  which corresponds to this case is the Brewster angle  $\theta_p$ , for which  $\tan \theta_p = n_t / n_i$ .

At the Brewster angle of incidence the beam is completely transmitted ( $T_{\parallel} = 1$ ) except for the small absorption losses in the material.

Equation (2.A.2) gives the fraction  $T_{\perp}$  of the light transmitted through a single interface: from air to the dielectric material. The total transmission of both interfaces of a plate is the square of  $T_{\perp}$ . If  $n$  plates are used at the Brewster angle, the transmittance of the perpendicular component is given by

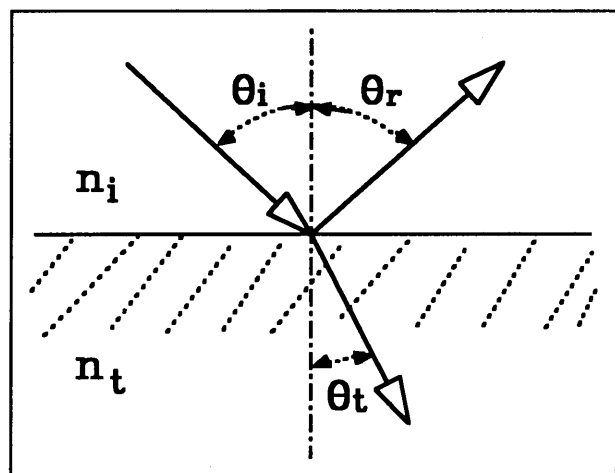


Figure 2.A.2

[3] OPTICS, E. Hecht, A. Zajac, Addison-Wesley Publishing Company, London, (1974)

$$T_{\perp}' = T_{\perp}^{2n} = (1 - R_{\perp})^{2n} = [1 - \sin^2(2\theta_p - 90^\circ)]^{2n} . \quad (2.A.3)$$

Table 2.A.1 shows the number of plates needed for a polarizer with a polarization ratio of 250:1 on transmittance for a number of dielectric materials. From this table it is clear why only two germanium-Brewster plates were used as the polarization element.

<i>Material</i>	<i>Refractive index <math>n_i</math></i>	$\theta_p$	<i>n</i>	$T_{\perp}'$
Ge	4	75.96	2	0.0024
ZnSe	2.4	67.38	4	0.004
KCl	1.46	55.6	20	0.0037

**Table 2.A.1** *Brewster stack polarizer calculations for various dielectric materials and number n of Brewster plates used in the stack for 10.6  $\mu\text{m}$  CO<sub>2</sub> radiation*

## ***LIST OF SYMBOLS: CHAPTER 2***

$a$	: radius of the waveguide core
$F$	: material (metal and dielectric layer) contributions to $\alpha_m$
$J_n(x)$	: Bessel function of order $n$
$k$	: free space propagation constant
$M^2$	: beam quality parameter
$n$	: real part of the refractive index
$n_0$	: refractive index of the hollow waveguide core (the air)
$n_d$	: refractive index of the dielectric layer
$n_t$	: refractive index of the Brewster plate
$n_i$	: refractive index of the medium surrounding the Brewster plate
$P$	: power transmittance through a waveguide
$T_{\parallel}$	: parallel polarized component of the transmitted beam
$T_{\perp}$	: perpendicular polarized component of the transmitted beam
$T_{\perp}^t = T_{\perp}^{2n}$	: the transmittance of the perpendicular polarized component through a Brewster stack polarizer
$R_{\parallel}$	: parallel polarized component of the reflected beam
$R_{\perp}$	: perpendicular polarized component of the reflected beam
$u_{nm}$	: the $m$ -th root of the equation $J_{n-1}(u)=0$
$u_m$	: the $m$ -th root of the equation $J_0(u)=0$
$W_0$	: the actual minimum beam waist of the $HE_{11}$ waveguide mode at the exit aperture of the waveguide
$\alpha_m$	: attenuation constants for the $HE_{1m}$ waveguide modes
$\alpha_{diel}$	: dielectric layer contribution to $\alpha_m$
$\alpha_{metal}$	: cladding material contribution to $\alpha_m$
$\gamma$	: axial propagation constant
$\delta a$	: dielectric layer thickness
$\theta_p$	: Brewster angle
$\eta_{1m}$	: the coupling coefficients for the $HE_{1m}$ waveguide modes by the $TEM_{00}$ free space laser mode also used as $\eta_m$
$\kappa$	: imaginary part of the refractive index
$\omega$	: angular frequency
$\lambda$	: free space wavelength
$v = n + i\kappa$	: complex refractive index

- $\omega_0$  : minimum radius (waist) of the Gaussian beam at the entrance aperture of the waveguide or the angular frequency (see context)
- 10P20 : this is the strongest CO<sub>2</sub> laser line on the 10  $\mu$ m vibrational band for  $\Delta J = +1$  (P rotational transition) and  $J_b = 20$
- 10R18 : this is one of the stronger CO<sub>2</sub> laser line on the 10  $\mu$ m vibrational band for  $\Delta J = -1$  (R rotational transition) and  $J_b = 18$



### 3. *ROTATIONAL RAMAN GAIN CALCULATIONS*

#### 3.1 *INTRODUCTION*

The Raman gain per unit length can be expressed in the following form [1,2,3]:

$$G = gI_P, \quad (3.1a)$$

$$\text{where } g = \frac{2 \lambda_S^2 \lambda_P \Delta N}{\pi n_S^2 h c \Delta \nu_R} \left( \frac{d\sigma}{d\Omega} \right). \quad (3.1b)$$

The parameter  $g$  is called the steady state plane wave gain coefficient with units  $\text{m/W}$ . The number density difference of molecules  $\Delta N(J,T)$  with the rotational state  $J$ , Raman line width  $\Delta \nu_R$  (the FWHM of the Raman transition) and the differential cross section  $d\sigma/d\Omega$  for the Stokes transition from rotational level  $J$  to rotational level  $J+2$  (both within the same vibrational state) must be determined.

We also need to consider the influence of the polarization of the laser beam. Existing models for stimulated Raman scattering consider only linearly polarized plane waves. In this chapter a constant factor ( $\beta_p$ ) describes the increase in gain due to circularly polarized pump and output beams. An expression for the plane wave gain coefficient will also be found which will be used in later calculations.

#### 3.2 *ENERGY LEVELS AND POPULATION DIFFERENCE $\Delta N$ FOR PARAHYDROGEN*

Figure 3.1 is the energy level diagram of the rotational energy levels for hydrogen with some of the allowed Raman transitions. These are determined by the selection rule  $\Delta J = \pm 2$ , with  $\Delta J = +2$  corresponding to a Stokes shift. An incident (pump) laser photon  $\omega_P$  which induces a rotational transition in the molecule, results in a Stokes photon at  $\omega_S = \omega_P - \omega_R$ , where  $\omega_R$  is the transition frequency. The  $\Delta J = -2$  transition corresponds to an anti-Stokes photon at  $\omega_{AS} = \omega_P + \omega_R$ . Both are referred to as S branch transitions, and labelled  $S_\nu(J)$ , where  $\nu$

is the vibrational quantum number and  $J$  denotes the lower of the two energy levels. The  $S_0(0) \approx 354 \text{ cm}^{-1}$  transition for parahydrogen is of primary interest for this work.

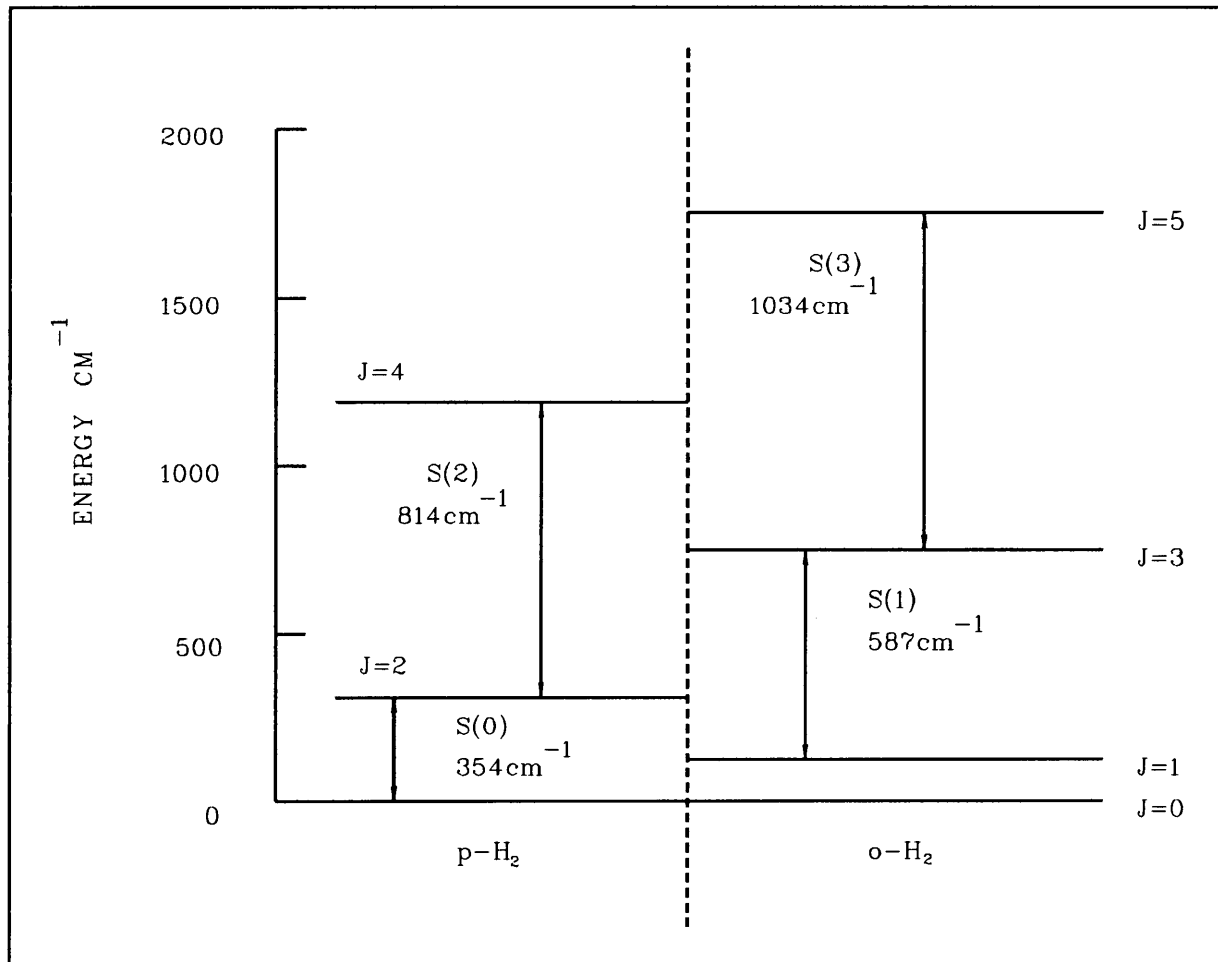


**Figure 3.1** Rotational energy level diagram of hydrogen showing the allowed transitions

The population difference is defined by

$$\Delta N = N_g - \left( \frac{k_g}{k_f} \right) N_f, \quad (3.2)$$

where  $N_g$  is the population of the lower state,  $N_f$  the population of the upper final state and  $k_g, k_f$  are the degeneracies of the lower and final states respectively.

In addition to the rotational degeneracy factor  $(2J+1)$ , there is also a nuclear degeneracy factor. This degeneracy is the result of the nuclear spin. For the hydrogen molecule there are two possibilities for the spins of the two nuclei. They can be parallel (orthohydrogen) or anti-parallel (parahydrogen). The nuclear spin for a hydrogen nucleus is  $\frac{1}{2}$ . Thus it is a fermion described by an anti-symmetric wave function. As an approximation one can write the molecular wave function as the product of the electronic, vibrational, rotational and spin wave functions. The total symmetry is determined by all the components. The relevant

(ground state) vibrational wave function is always symmetric, as is the ground state electronic wave function. Even rotational wave functions are symmetric, and odd ones are anti-symmetric. There are in nature three symmetric (spins parallel) and one anti-symmetric (spins anti-parallel) nuclear spin functions. Therefore to obtain an anti-symmetric total wave function the odd rotational levels must be paired with orthohydrogen and the even rotational levels with parahydrogen. The odd and even rotational transitions have a statistical weight factor of 3:1. The interest is in the S(0) (parahydrogen) level (an even rotational level) for the 16  $\mu\text{m}$  generation for a CO<sub>2</sub> pump laser.

It is possible to obtain pure parahydrogen by cooling the gas to very low temperatures. At low temperatures hydrogen returns to the two lowest rotational levels: J=0 for parahydrogen and J=1 for orthohydrogen. The J=1 state is not a thermal equilibrium state and after a few days at low temperature hydrogen will return to the J=0 state which results in pure parahydrogen. This conversion may be accelerated by the use of a catalyst. For efficient 16  $\mu\text{m}$  generation (maximum gain) virtually all the gas molecules should be initially in the J=0 rotational state. This can be achieved if the parahydrogen is cooled to between 77 K and 100 K (i.e. temperature for liquid N<sub>2</sub>).

The fractional population distribution at thermal equilibrium is given by the Maxwell-Boltzmann distribution

$$\frac{N_J}{N} = \frac{\sigma (2J+1)}{Q_{rot}} e^{\left(-J(J+1) \frac{\theta_r}{T}\right)}, \quad (3.3)$$

where  $Q_{rot} = \sum_{J=0}^{\infty} \sigma(2J+1) e^{\left(-J(J+1) \frac{\theta_r}{T}\right)}$  is the rotational partition function with  $\sigma = \begin{cases} 1 & \text{for even } J \\ 3 & \text{for odd } J \end{cases}$

the nuclear spin degeneracy,  $\theta_r = 87.6 \text{ K}$  and N the molecular number density.

The population difference for the S(0) transition in 100% parahydrogen changes equation (3.3) to

$$\Delta \equiv \frac{\Delta N}{N} = \frac{1}{N} \left( N_{J=0} - \frac{k_{J=0}}{k_{J=2}} N_{J=2} \right) = \frac{\left( 1 - e^{\frac{-6\theta_r}{T}} \right)}{Q_{rot}^{para}}, \quad (3.4)$$

where  $Q_{rot}^{para} = \sum_{\text{even } J} (2J+1) e^{\left(\frac{-J(J+1)\theta_r}{T}\right)}$ .

smaller. At not too high densities ( $<0.2$  atm) the pressure broadened Raman lines are well separated from each other and the line shape is Lorentzian. Rabinowitz *et al.* [5] show that the spontaneous Stokes line width for  $S_0(0)$  narrows considerably before gain saturation. To a first approximation the line width is given by [5]

$$\Delta v_R = \Delta v_0 \sqrt{\left(\frac{\ln 2}{G_T}\right)} = \beta \Delta v_0 . \quad (3.6)$$

Here  $\Delta v_0$  is the spontaneous line width and  $G_T$  follows from  $e^{G_T}$  which is the total  $S(0)$  power gain factor, and  $\beta$  the narrowing coefficient. Assuming a total  $S(0)$  output power  $P_s \approx 250$  kW (10 mJ, 40 ns) and that the Stokes signal grows from noise ( $P_{s0} \approx 3.3 \times 10^{-10}$  W), then  $P_s = P_{s0} e^{G_T}$  implies that  $G_T \sim 35$ , and  $\beta \approx 0.14$ . However, for the purpose of the gain calculations  $\beta = 1$  will be used, in order to compare the calculations with published results.

The hydrogen Raman line shape contains contributions from both the Doppler effect and collisional broadening (pressure broadening). At very low pressures the Doppler effect dominates and the line shape is Gaussian [4] and essentially independent of the gas density. At increasing pressures the line is dramatically narrowed by phase preserving velocity changing collisions until collisional broadening causes the line to broaden again at high pressures. This narrowing of the line was first described by Dicke [6]. At pressures above  $10^{-3}$  atm the line width is given [4,7]

$$\Delta v_0 = \frac{2 \pi D_0 v_R^2}{c^2 \rho} + c \rho \gamma , \quad (3.7)$$

where  $D_0$  is the self diffusion coefficient,  $v_R$  the Raman frequency,  $c$  the speed of light,  $\rho$  the density in amagat and  $\gamma$  the collisional broadening coefficient with the units<sup>[1]</sup> of  $\Delta v_0$  in  $s^{-1}$ . This expression assumes a collinear propagating geometry, which is consistent with the Raman generation scheme.

$D_0$ ( $m^2$ amagat $s^{-1}$ )	$\gamma$ ( $m^{-1}$ amagat $^{-1}$ )
$1.176 \times 10^{-6} T^{0.8314}$	0.31

**Table 3.1** Input values for the line width calculation [4,7,8]

<sup>[1]</sup> Dimension check:  $[D_0] = m^2 \text{ amagat } s^{-1}$ ,  $[\gamma] = m^{-1} \text{ amagat}^{-1}$ ,  $[\text{amagat}] = Pa \text{ K}^{-1}$ ,  $[P] = Pa = kg \text{ s}^{-2} m^{-1}$ ,  $[T] = K$ . Using these the dimensions for  $[\Delta v_0] = s^{-1}$ .

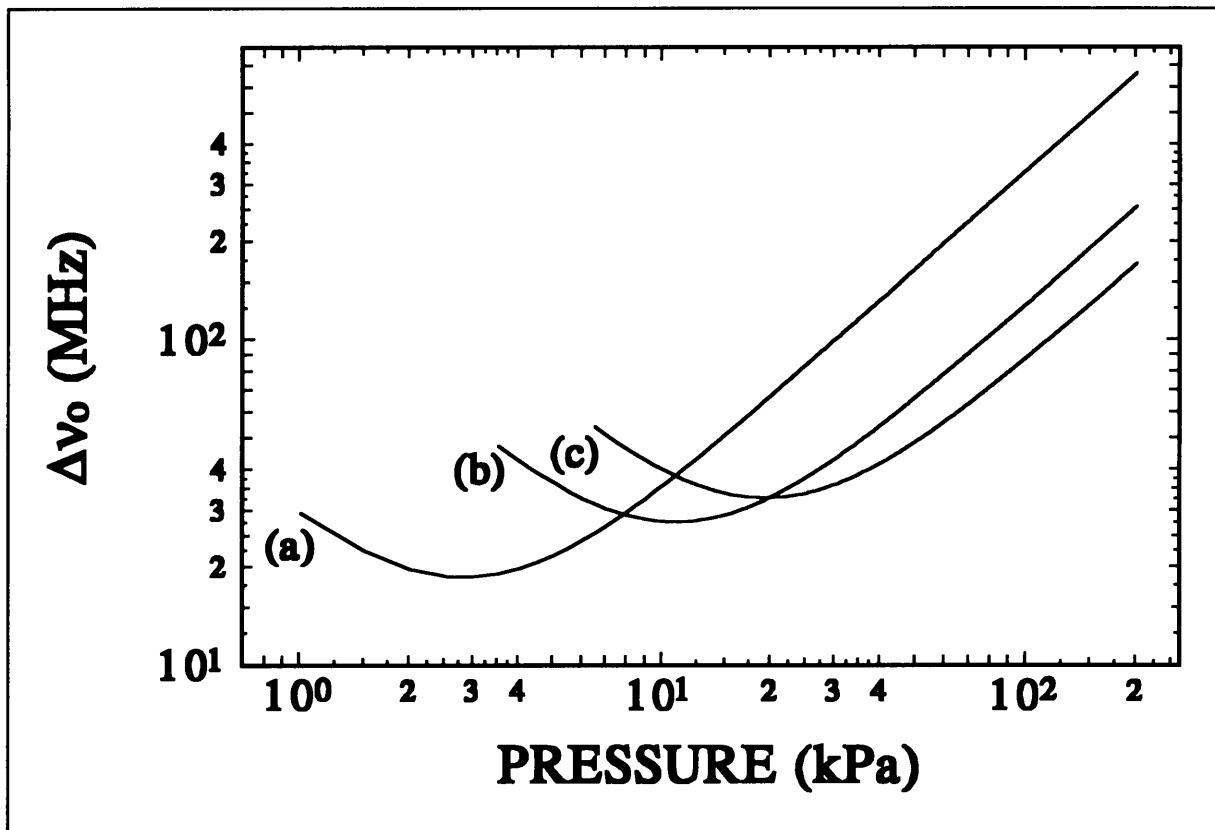


**Figure 3.3** Raman line width ( $\Delta v_0$ ) as a function of pressure for (a)  $T=77$  K, (b)  $T=200$  K and (c)  $T=300$  K

The Raman line width was calculated for the input values shown in Table 3.1. In equation (3.7)  $\Delta v_0$  is a function of pressure and temperature which is incorporated by the unit amagat. Using the following relationship [9]

$$\rho(\text{amagat}) = \frac{P}{3.622 \times 10^{-8} T} \quad (3.8)$$

the line width as a function of pressure  $P$  can be calculated at different temperatures as shown in Figure 3.3. Of interest for the  $\text{CO}_2$  Raman work are the low pressures ( $P \leq 200$  kPa) because of the fact that scattering of  $\text{CO}_2$  radiation in hydrogen can be important at pressures higher than 200 kPa.

From equations (3.7) and (3.8)

$$\Delta v_0 = A \frac{T}{P} + B \frac{P}{T}, \quad (3.9)$$

where  $A = \frac{2.23 \times 10^{-7} D_0 v_R^2}{c^2}$  and  $B = \frac{c \gamma}{3.622 \times 10^{-8}}$ .

From equations (3.4), (3.5) and (3.9) the ratio  $\Delta N / \Delta v_R$  as a function of temperature and pressure is given by

$$\frac{\Delta N}{\Delta \nu_R} = \frac{P}{\beta k T} \left( A \frac{T}{P} + B \frac{P}{T} \right)^{-1} \Delta \quad (3.10)$$

At low pressures the line width  $\Delta \nu_R$  is roughly a constant (Figure 3.3). From equation (3.5) the densities  $N$  and  $\Delta N$  increase as the pressure increases and thus the gain increases (Figure 3.4). At higher pressures ( $> 50$  kPa) both the Raman line width and the number density increase linearly with pressure and the gain remains essentially constant.

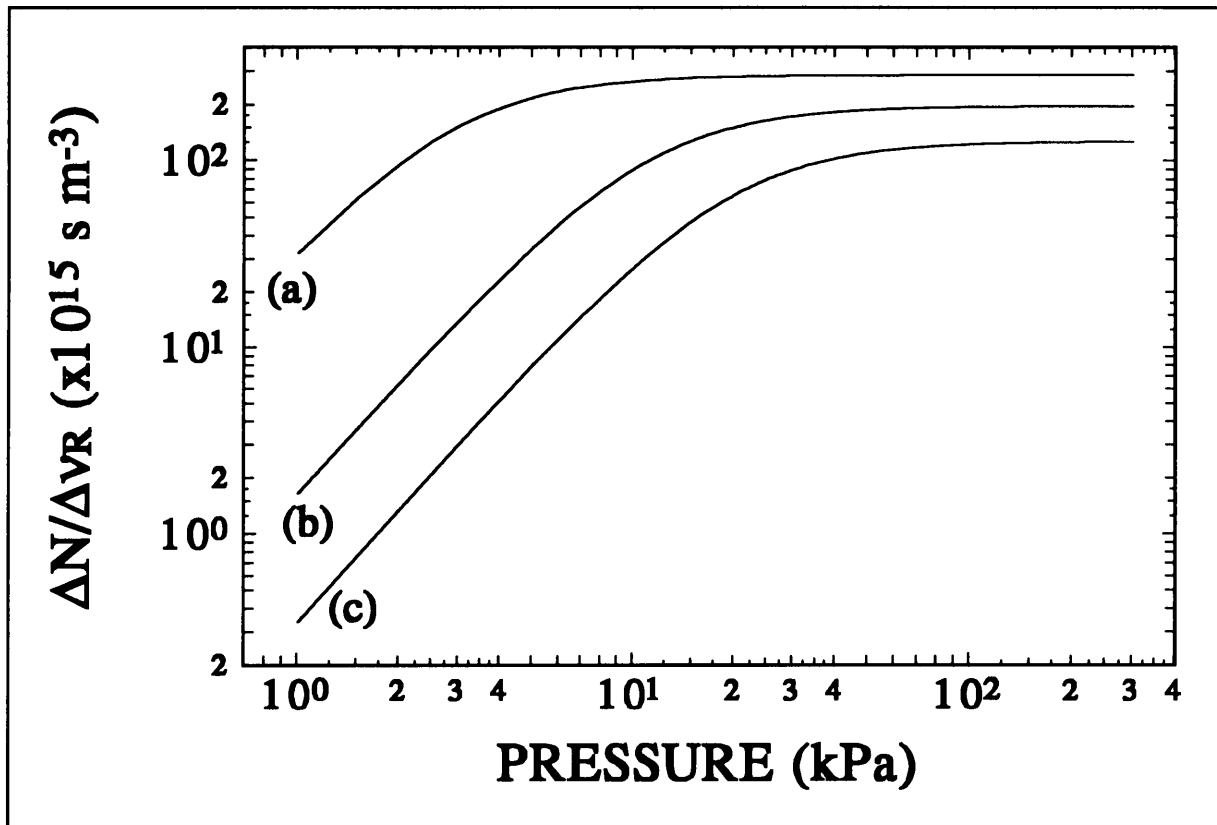


Figure 3.4 Ratio  $\Delta N/\Delta \nu_R$  as a function of pressure for (a)  $T=77$  K, (b)  $T=200$  K and (c)  $T=300$  K

### 3.4 DIFFERENTIAL SCATTERING CROSS SECTION $d\sigma/d\Omega$ AND POLARIZATION EFFECTS

We now discuss the spontaneous Raman cross section of the  $S(0)$  transition for linearly polarized radiation. In a diatomic gas, the stimulated Raman scattering has an intensity proportional to  $\gamma_{00}^2$  - the square of the anisotropic part of the molecular polarizability [10,11,12]. The cross section is also a function of the rotational Raman transition [11].

The angular dependence of the differential scattering cross section for the rotational lines and polarized incident light is given by [11]

$$\frac{d\sigma}{d\Omega} = \frac{3}{8\pi} \sigma_0 \left[ \frac{6 + \sin^2 \theta}{10} \right], \quad (3.11)$$

where  $\theta$  is the angle between the observation direction (propagation direction of the Raman shifted radiation) and the incident pump laser polarization vector. The total cross section  $\sigma_0$  is given by [11]

$$\sigma_0(J) = \frac{128 \pi^5}{9 \lambda_p \lambda_s^3} C(J) \gamma_{00}^2, \quad (3.12)$$

where  $\lambda_p$  is the wavelength of the incident radiation,  $\lambda_s$  the wavelength of the Raman line,  $\gamma_{00}$  the anisotropic polarizability of the initial and final states in the ground vibrational state. The

coefficient  $C(J)$  is given by  $C(J) = \frac{(J+1)(J+2)}{(2J+3)(2J+1)}$  for the Stokes lines (the lines of interest for

this work) with  $J$  the initial rotational state.

There seems to be a  $J$  dependence of  $\gamma_{00}$  for values presented in the literature [11]. This is not a problem as  $J=0$  for the parahydrogen transition of interest for this calculation. The numerical value  $\gamma_{00}=0.3013 \times 10^{-30} \text{ m}^3$  can be used [2,11]. For scattering collinear with the pump,  $\theta=90^\circ$ , equation (3.11) becomes  $\frac{d\sigma}{d\Omega} = \frac{21}{80\pi} \sigma_0$ .

For spontaneous rotational Raman scattering, the scattered Stokes light is strongly depolarized. The ratio of Stokes light with polarization components parallel and perpendicular to pump polarization is 4/3. Two separate cross sections can then be defined with

$$\frac{d\sigma}{d\Omega} = \frac{d\sigma^{\parallel}}{d\Omega} + \frac{d\sigma^{\perp}}{d\Omega}, \quad (3.13)$$

$$\text{where } \frac{d\sigma^{\parallel}}{d\Omega} = \frac{3}{20\pi} \sigma_0 \text{ and } \frac{d\sigma^{\perp}}{d\Omega} = \frac{9}{80\pi} \sigma_0.$$

From equation (3.1) it is clear that  $G \propto d\sigma/d\Omega$  and therefore the gain for light with parallel polarization is 4/3 times higher. These calculations were done for linear polarized light. It was shown by Minck *et al.* [10] that for pure rotational transitions the largest nonlinear polarization of the hydrogen molecules, and hence the largest gain, results from counter rotating circularly polarized pump and Raman beams. This gives a gain 3/2 times larger than linearly polarized beams. Thus if the pump beam is right hand circularly polarized the resultant Stokes beam will be left hand circularly polarized. Another advantage of using

circularly polarized pump beams is that no anti-Stokes is expected since the nonlinear polarization for anti-Stokes is zero for circularly polarized beams [10].

The rotational Raman cross section for the  $S_0(0)$  transition is then

$$\frac{d\sigma}{d\Omega} = 138.5 \beta_P \frac{\gamma_{\infty}^2}{\lambda_P \lambda_S^3}. \quad (3.14)$$

Here  $\beta_P$  is the scattering enhancement due to the polarization. Thus  $\beta_P=1$  for linearly polarized light and  $\beta_P=3/2$  for circularly polarized light.

### 3.5 GAIN CALCULATIONS

An expression in terms of the experimental conditions must be found for the gain coefficient  $G$  shown in equation (3.1). The pump intensity  $I_P$  will generally be depleted. We now discuss [in equation (3.1)] the plane wave gain coefficient  $g$ . The population density difference  $\Delta N$  is treated as a variable in Chapter 4. For the sake of comparison with published data, we here treat  $\Delta N$  as a constant, thus assuming no medium depletion. Equations (3.1b), (3.10) and (3.14) give the small signal gain coefficient as

$$g = K \frac{\beta_P P \Delta(T)}{T \lambda_S} \left( A \frac{T}{P} + B \frac{P}{T} \right)^{-1}, \quad (3.15)$$

$$\text{where } K = \frac{88.2 \gamma_{\infty}^2}{\beta c n_S^2 h k}.$$

This formula gives results (see Table 3.2) in general agreement with those of Carlsten *et al.* [2]. The plane wave gain coefficient is shown in Figure 3.5 as a function of pressure for the three temperatures which are of interest to this work. In conclusion, it is clear that the experimental conditions in terms of temperature and pressure will be prescribed by the conditions for optimum gain.



P(kPa) → T(K) ↓	50	75	100	150
77	$1.1 \times 10^{-12}$	$1.1 \times 10^{-12}$	$1.1 \times 10^{-12}$	$1.1 \times 10^{-12}$
200	$7.06 \times 10^{-13}$	$7.2 \times 10^{-13}$	$7.3 \times 10^{-13}$	$7.35 \times 10^{-13}$
300	$4.16 \times 10^{-13}$	$4.45 \times 10^{-13}$	$4.61 \times 10^{-13}$	$4.7 \times 10^{-13}$

**Table 3.2** *Plane wave gain coefficient (m/W) for a circularly polarized pump beam for specific temperature and pressure conditions*

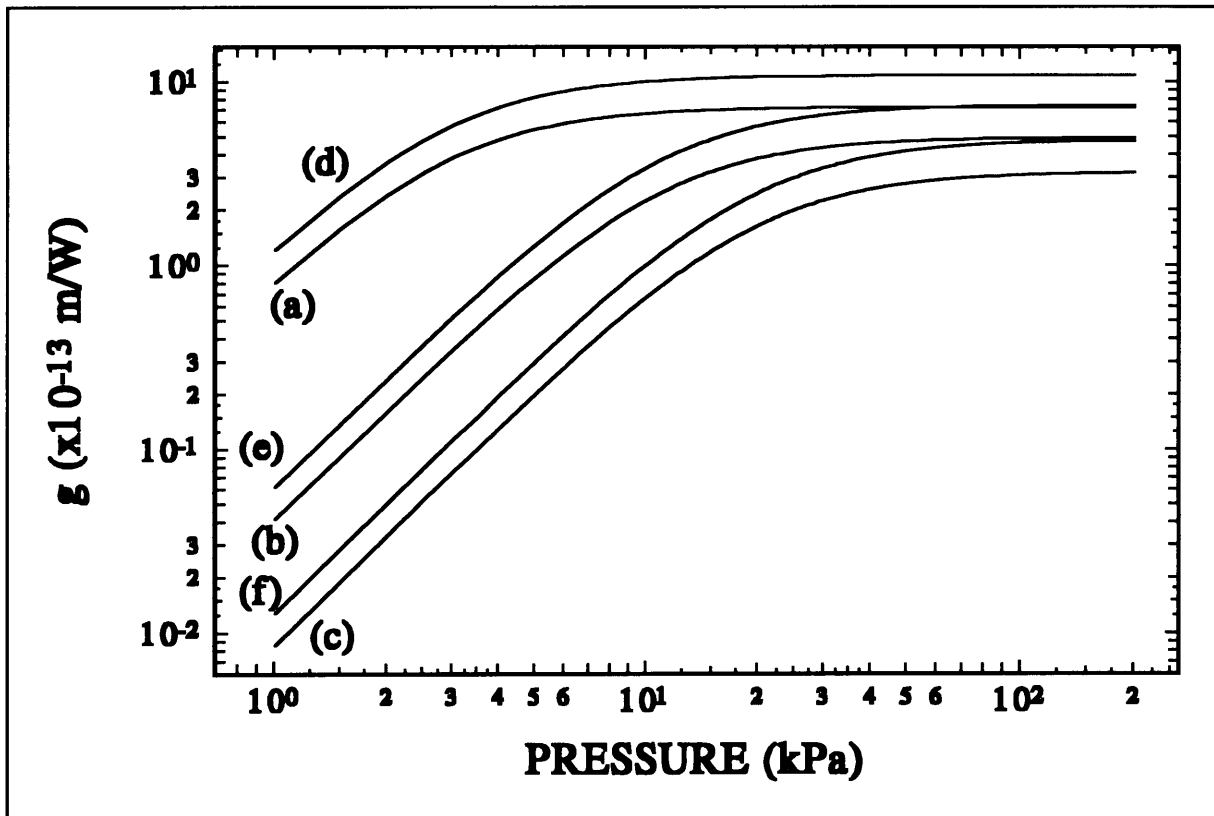


**Figure 3.5** *g as a function of pressure for  $\beta_p=1$  (a)77 K, (b)200 K, (c)300 K and  $\beta_p=1.5$  (d)77 K, (e) 200 K, (f)300 K*

### 3.6 REFERENCES: CHAPTER 3

1. Multiple pass Raman gain cell  
W.R. Trutna, R.L. Byer  
Appl Opt **19**(2),301,(Jan 1980)
2. Stimulated rotational Raman scattering in CO<sub>2</sub>-pumped para-H<sub>2</sub>  
J.L. Carlsten, R.G. Wentzel  
IEEE J of Quantum Elect **QE-19**(9), 1407,(Sept 1983)
3. Liquid nitrogen and room-temperature SRS gain coefficient in isotropic hydrogen molecules  
K. Sentrayan, L. Major, A. Michael, V. Kashawaha  
J Phys D: Appl Phys **25**,1697,(1992)
4. Measurement of the self-broadening of the H<sub>2</sub> Q(0-5) Raman transitions from 295 K to 1000 K  
L.A. Rahn, R.L. Farrow, G.J. Rosasco  
Phys Rev A **43**(11), 6075, (June 1991)
5. Efficient tunable H<sub>2</sub> Raman lasers  
P. Rabinowitz, A Stein, R. Brickman and A Kaldor  
Appl Phys Lett **35**(10), 739,(Nov 1979)
6. The effect of collisions upon the Doppler width of spectral lines  
R.H. Dicke  
Phys Rev **89**(2), 472,(Jan 1953)
7. Dicke narrowing and collisional broadening of the S<sub>0</sub>(0) and S<sub>0</sub>(1) Raman lines of H<sub>2</sub>  
V. Cooper, A. May, E. Hara, H. Knapp  
Canadian J of Phys **46**, 2019, (1968)
8. Laser wavelength, pressure and temperature dependence on the stimulated Raman scattering gain in H<sub>2</sub>  
K. Sentrayan, L. Major, H. Bryant, A. Micheal, V. Kashawaka  
Spec Lett **25**(5), 627,(1992)
9. Using "Amagat"  
T.I. Salamon  
Informal AEC report (1992)
10. Stimulated pure rotational Raman scattering in deuterium  
R.W. Minck, E.E. Hagenlocker, W.G. Rado  
Phys Rev Lett **17**(5), 229, (Aug 1966)

11. Absolute Raman scattering cross section of molecular hydrogen  
R.W. Carlson, W.R. Fenner  
The Astrophysical Journal **178**,551,(Dec 1972)
12. Relative Raman cross sections for the S(0) through S(4) rotational transitions in hydrogen  
R.C. Harney, J.E. Randolph, F.P. Milanovich  
The Astrophysical Journal **200**, L197,(Sept 1975)

## ***LIST OF SYMBOLS: CHAPTER 3***

$c$	: speed of light
$D_0$	: optical diffusion coefficient
$g$	: steady state plane wave gain coefficient
$G$	: Raman gain per unit length
$h$	: Planck's constant
$I_p$	: pump beam power density ( $W/m^2$ )
$J$	: the initial rotation level
$k$	: Boltzman's constant
$k_g$	: degeneracy of the lower rotational level
$k_f$	: degeneracy of the final rotational level
$n_s$	: refractive index of the Raman medium at the Stokes wavelength
$N_g$	: population density of the lower rotational level
$N$	: total number density of the molecules in a unit volume
$N_J$	: number density of molecules in the $J$ rotational level
$N_f$	: population density of the final rotational level
$P_s$	: Stokes output power
$P_{so}$	: Stokes input power (background noise signal)
$P$	: pressure
$Q_{rot}$	: rotational partition function for hydrogen
$Q_{rot}^{para}$	: rotational partition function for parahydrogen
$S_0(0)=S(0)$	: the Stokes transition from $J=0$ to $J=2$ for the ground vibrational state in parahydrogen
$S_0(1)=S(1)$	: the Stokes transition from $J=1$ to $J=3$ for the ground vibrational state in orthohydrogen
$v$	: vibrational quantum number
$\beta$	: line width narrowing coefficient
$\beta_p$	: polarization gain enhancement factor
$\gamma$	: collisional broaden coefficient
$\gamma_{00}$	: anisotropic part of the molecular polarizability of the initial and final Stokes in the ground vibrational state
$\frac{d\sigma}{d\Omega}$	: differential cross section for the Stokes transition

$\frac{d\sigma^{\parallel}}{d\Omega}$	: parallel component of the scattering cross section
$\frac{d\sigma^{\perp}}{d\Omega}$	: perpendicular component of the scattering cross section
$\Delta N$	: molecular number density difference between the J and J+2 rotational levels in the ground vibrational state
$\Delta \equiv \Delta N/N$	: normalised population difference density
$\Delta \nu_R$	: Raman transition line width (Hz)
$\Delta \nu_0$	: spontaneous Raman line width (Hz)
$\theta$	: angle of observation (or pump beam propagation direction) relative to the incident beam polarization
$\lambda_s$	: Stokes beam wavelength
$\lambda_p$	: pump beam wavelength
$\rho$	: density of the Raman medium measured in amagat ( $\propto P/T$ )
$\sigma_0$	: total cross section
$\omega_p$	: pump laser frequency
$\omega_R$	: Raman transition frequency
$\omega_s$	: Stokes frequency
$\omega_{AS}$	: anti-Stokes frequency
$e^{G_T}$	: total $S_0(0)$ power gain factor

# 4. THEORETICAL ANALYSIS OF STIMULATED ROTATIONAL RAMAN CONVERSION

## 4.1 INTRODUCTION

Stimulated Raman scattering for wavelength conversion of high-power laser radiation to longer wavelengths is drawing increasing attention for obtaining wavelengths that are not readily available. In December 1964 [1] and later in 1970 [2] Bloembergen *et al.* published papers on Raman conversion that started this new field of nonlinear optics. Numerous papers have been published on this subject since 1964. For these wavelengths there are many applications, of which isotope separation is but one. Other applications are in resonance laser photochemistry where the use of multifrequency radiation can ensure efficient excitation of atoms and molecules with a high selectivity. Various schemes using combinations of pulses of different frequencies are used increasingly in nonlinear spectroscopy [3,4,5,6,7,8].

This chapter will deal with Raman conversion in parahydrogen with a CO<sub>2</sub> laser as the pump. Extensive work was done on 10.6 μm conversion in parahydrogen by Byer and Trutna [9,10] and other researchers working in the same field [11,12,13,14,15,16,17] in the late 1970's and 1980's. A few papers [18,19,20] deal with Raman conversion in fibres and waveguides, with the waveguides filled with hydrogen as the Raman medium [21,22].

The parameters that affect this wavelength conversion can be grouped under three categories:

- the stimulated Raman gain which includes the molecular density in the ground state,
- pump and Stokes beam intensities and the losses for the pump and Stokes wavelengths, and
- Raman cell design.

All three the groups must be considered to optimize the process. We present here a rate equation model based on the work by E. Margalith and G.W. Sutton [23]. Their model is based on the conservation of photons. An analytical solution for the Raman conversion was also found by Cotter and Hanna [24] using a number of simplifications.

Rabinowitz *et al.* [21] used a 1.064  $\mu\text{m}$  Nd:YAG laser with a hydrogen-filled waveguide Raman cell. For isotope separation, Kurnit *et al.* [22] used a 10.6  $\mu\text{m}$  CO<sub>2</sub> laser for the conversion of the wavelengths in a hollow dielectric waveguide filled with parahydrogen .

## 4.2 THEORETICAL MODEL

The model was developed to establish the waveguide Raman cell parameters for useful 16  $\mu\text{m}$  output. This application of the model will be verified using results obtained from a multipass Raman cell. We include the effect of temperature and pressure on the Raman gain (which was dealt with in Chapter 3) and most of the losses.[15,25,26].

The following assumptions are made:

- All the molecules are initially in the ground state (for the cold cell).
- The spontaneous lifetime of the final state is much longer than the pulse duration. This means that each molecule can contribute only once to the conversion process.
- All the loss processes - absorption, scattering, waveguide and reflection losses - are linear.
- The power gain for stimulated Raman conversion is given by [23]:

$$G = \alpha \left[ N_g - \left( \frac{k_g}{k_f} \right) N_f \right] I_P . \quad (4.1)$$

Here  $\alpha$  is the small signal gain coefficient per molecule,  $N_g$  and  $N_f$  are the molecular population densities, where  $g$  and  $f$  denote the ground and final states respectively, and  $k_i$  is the degeneracy of the  $i$ -th state.  $I_p$  and  $I_s$  are the power densities of the pump and first Stokes respectively.

The equations describing the change in the pump and Stokes photon number density are [23], [24]:

$$\left( \frac{\partial}{\partial z} + \frac{1}{c} \frac{\partial}{\partial t} \right) N_s = G N_s - \delta_s N_s , \quad (4.2)$$

$$\left( \frac{\partial}{\partial z} + \frac{1}{c} \frac{\partial}{\partial t} \right) N_p = -G N_s - \delta_p N_p . \quad (4.3)$$

$N_p$  and  $N_s$  are the number densities of pump and first Stokes photons respectively, with  $c$  the speed of light, and  $\delta_i$  ( $i=P,S$ ) the linear loss coefficients. The depletion of the ground state molecules equals the conversion rate, thus

$$\frac{\partial N_g}{\partial t} = -c G N_s . \quad (4.4)$$

Neglecting terms of order  $1/c$  and using the relations

$$\Delta N = N_g - \left(\frac{k_g}{k_f}\right) N_f , \quad N_g = N_o - N_f = \left(\frac{k_g}{k_g + k_f}\right) N_o + \left(\frac{k_f}{k_g + k_f}\right) \Delta N , \quad (4.5)$$

equations (4.2) to (4.4) can be rewritten as

$$\frac{\partial N_s}{\partial z} = G N_s - \delta_s N_s , \quad (4.6)$$

$$\frac{\partial N_p}{\partial z} = -G N_s - \delta_p N_p , \quad (4.7)$$

$$\frac{\partial(\Delta N)}{\partial t} = - \left(\frac{k_g + k_f}{k_f}\right) c G N_s . \quad (4.8)$$

Boundary and initial conditions for  $N_p(z,t)$ ,  $N_s(z,t)$  and  $N_g(z,t)$ :

- $N_p(0,t)=N_{p0}(t)$ : input pump photon density (the actual pulse shape).
- $N_s(0,t)=N_{s0}(t)$ : input Stokes seed. In the model the input Stokes is taken as thermal background radiation. The Stokes initial condition will be discussed further in Section 4.3.2.
- $N_g(z,0)=N_0$  : initial molecular density.

A better way of constructing a useful and flexible model is to introduce normalised variables [3,15,23]. Introducing degeneracy ( $k_i = 2J+1$ ) of the ground and final states for the hydrogen molecule (i.e.  $v=0$ :  $J=0$  and  $J=2$ ,  $k_g=1$  and  $k_f=5$ ) equation (4.8) becomes

$$\frac{\partial(\Delta N)}{\partial t} = -\frac{6}{5} c G N_s , \quad (4.9)$$

Using the relations  $I_i = c h \nu_i N_i$  ;  $i = P, S$  and  $I_{P0} = c h \nu_P N_{P0} \approx E / (A_i T_{PL})$  where  $E$  is the energy of the pulse,  $T_{PL}$  is the pulse length and  $A_i$  is the input beam area (the area on entering the optical system). The area  $A_i$  is calculated with the beam radius at  $z=0$  defined as the radius at  $1/e^2$  of the peak intensity radius. By using normalised variables  $\Delta = \Delta N / N_o$ ,  $K_i = I_i / I_{P0}$  ( $i = P, S$ ) and rewriting the gain [equation (4.1)] as

$$G = \gamma \alpha \Delta N I_p , \quad (4.10)$$

where  $\gamma$  is the excitation lag factor for the polarization of the molecule, equations (4.6), (4.7) and (4.9) can be written as:



$$\frac{dK_S}{dz} = \gamma \kappa_1 K_P K_S \Delta - \delta_S K_S, \quad (4.11)$$

$$\frac{dK_P}{dz} = -\gamma \left( \frac{v_P}{v_S} \right) \kappa_1 K_P K_S \Delta - \delta_P K_P, \quad (4.12)$$

$$\frac{d\Delta}{dt} = -\gamma \kappa_2 K_P K_S \Delta, \quad (4.13)$$

where  $\kappa_1 = \alpha N_o I_{P_o} = \alpha N_o E / (A_i T_{PL})$  and  $\kappa_2 = 6 \alpha E^2 / (5 A_i^2 T_{PL}^2 h v_S)$ . As a first order approximation  $\gamma$  can be written as  $\gamma = 1 - \exp(-t^2/\Gamma^2)$  where  $t$  is time and  $\Gamma$  the excitation lag time, which is related to the Raman line width as  $\Gamma = 1/\Delta v_R$ .

The set of coupled differential equations (4.11) - (4.13) must be solved under the following conditions:

- The input and output power are normalised with respect to the input pulse  $I_{P_o}$ .
- The undepleted normalised population difference at  $t=0$  as a function of pressure and temperature (see Section 3.2) between the levels  $J=0$  and  $J=2$  will be used, i.e.  $\Delta_o = \Delta N_o / N_o$ .

### 4.3 MODEL FOR RAMAN CONVERSION IN A MULTIPASS RAMAN CELL

The model will be verified using results obtained for the Raman conversion of the 10R18 CO<sub>2</sub> laser line in parahydrogen in a 25 passes multipass Raman amplifier. With the knowledge that the output from the model corresponds to the experiment, the design criteria for the waveguide Raman cell in terms of waveguide length and initial laser input power can then be specified.

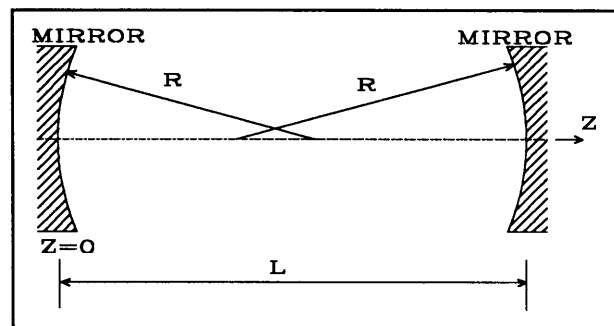


Figure 4.1 Symmetric resonator with applicable resonator parameters shown

The multipass Raman cell can be seen as a symmetric confocal resonator with the beam waist  $W_0$  is at the centre (see Figure 4.1). The waist  $W_0$  for this resonator is given by (see

Chapter 5):

$$W_o^2 = \frac{M^2 \lambda_P}{\pi} \sqrt{\frac{L}{2} (R-L/2)}, \quad (4.14)$$

with

$$W_{1,2}^2 = \frac{M^2 \lambda_P L}{2\pi} \sqrt{\frac{2 R^2}{L (R - L/2)}}$$

the spot size on the concave mirrors and  $M^2$  the beam quality parameter (see Chapter 5).

The spot size in the cavity, at any given propagation position  $z$ , is given by

$$W^2(z) = W_o^2 + \left[ \frac{M^2 \lambda_P (z - L/2)}{\pi W_o} \right]^2.$$

Thus, the cross sectional area  $A(z)$  at a given distance is then  $A(z) = \pi W^2(z)$ . The initial beam cross section  $A_i$  is larger than the minimum spot size at the centre of the Raman cell. As the pump beam propagates towards the waist, it becomes more intense. This enhances the gain by a factor  $\eta(z) = A_i/A(z)$ .

For the Raman cell,  $A_i$  is given by

$$A_i = \pi W_{1,2}^2 = \frac{M^2 \lambda_P L}{2} \sqrt{\frac{2 R^2}{L (R - L/2)}}.$$

Thus

$$\eta(z) = \frac{W_{1,2}^2}{W^2(z)} = \frac{\frac{M^2 \lambda_P L}{2\pi} \sqrt{\frac{2 R^2}{L (R - L/2)}}}{W_o^2 + \left( \frac{M^2 \lambda_P (z - L/2)}{\pi W_o} \right)^2}. \quad (4.15)$$

Using equation (4.15) as a modification of the normalised gain [ $\kappa_i' = \eta(z) \kappa_i$  where  $i=1,2$ ], equations (4.11)-(4.13) can be solved for a multipass Raman cell. It is clear from Figure 4.2 that the maximum gain is achieved at the focus of the beam. Furthermore, the enhancement  $\eta(z)$  is independent of  $M^2$  (see equations (4.14) and (4.15)). The Raman process is an intensity driven process. Clearly the largest intensities are in the central portion of the Raman cell - within the Rayleigh range  $z_R$  (see Figure 4.2) from the centre. Thus most of the Raman conversion takes place in this region.

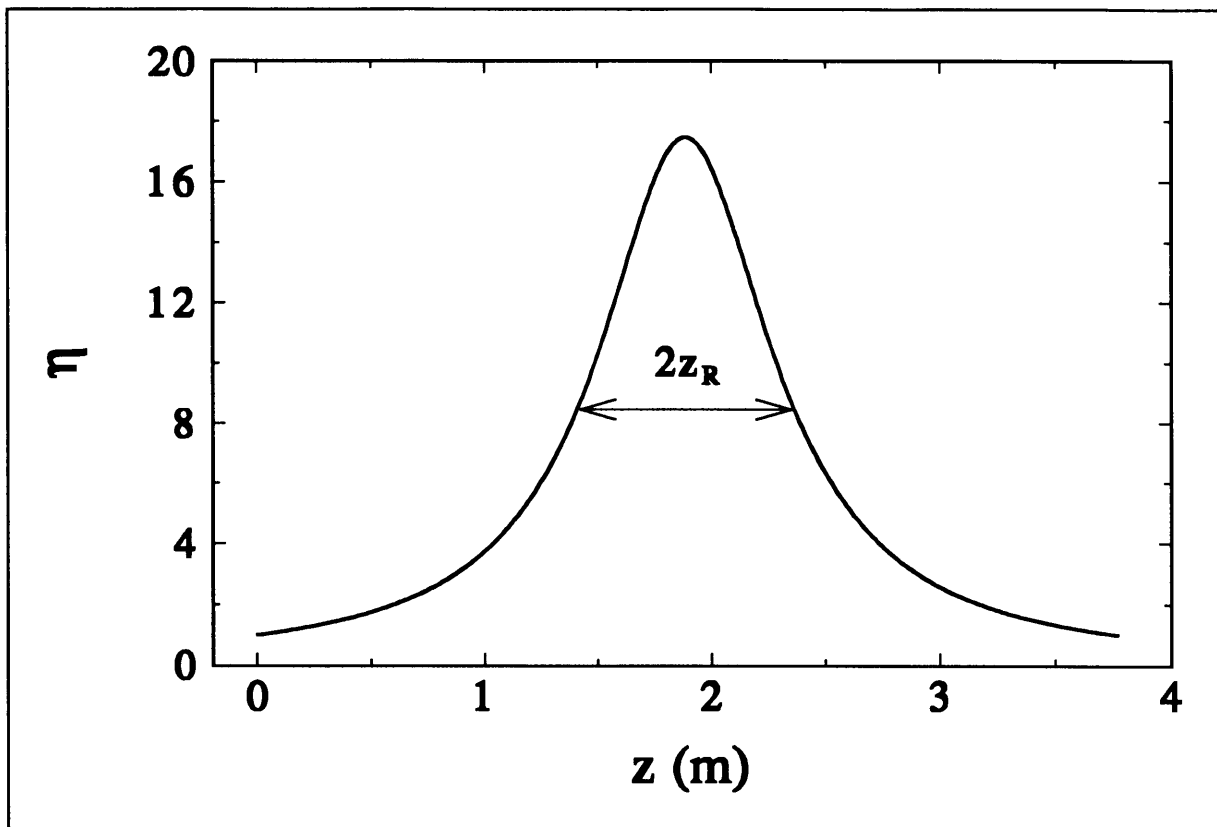


**Figure 4.2** Gain enhancement in the Raman cell due to focusing of the pump beam (multipass cell parameters:  $L=3.771\text{m}$ ,  $R=2\text{m}$  and  $\lambda=10.2\mu\text{m}$ )

### **4.3.1 GAIN ENHANCEMENT DUE TO RAY CROSSINGS IN THE MULTIPASS CELL**

A multipass cell has an important property, which it owes to its uniqueness of design: the crossing of the beams in the active volume. A result of these crossings is the compression of the Stokes output pulses. It is therefore possible to get a Stokes pulse with higher peak power than the input pulse [27].

In regions of beam intersection, the Stokes wave can experience increased gain and extract energy from both intersecting parts of a pump pulse. Only the *resultant* intensity of the intersecting pump waves contribute to the Stokes gain[27]. The intersecting regions are short compared to  $L$ . The additional gain produced at an intersection is a small fraction of the forward gain per pass.

Equation (4.10) can be rewritten as  $G = G_o + \Delta G = \gamma \alpha \Delta N I_p (1 + \Delta I_p / I_p)$  where  $\Delta I_p$  is the increase in the pump power due to crossings. In this section a first-order expression will be derived for  $\Delta I_p / I_p$ , which is an enhancement of the gain coefficient. No interference

contributions are expected as the coherence length  $l_c = c/\Delta\nu \approx 3\text{ m}$  which is close to the length of the multipass Raman cell. An empirical lower estimate for the average number of crossings in a pulse of length  $cT_{PL}$  is given by

$$m = \left( \frac{Ln}{cT_{PL}} - 1 \right) \frac{c^2 T_{PL}^2}{2L^2 n}$$

for  $2cT_{PL} < Ln$  where  $L$  is the length of the cell,  $n$  the number of passes and  $T_{PL}$  the pulse length. Assume a pump pulse of rectangular shape with a power density  $I_p$  and width  $T_{PL}$ . Then the average intensity enhancement within the time of the pulse can be expressed as  $\Delta I_p/I_p = mA_{int}/A_{tot}$  where  $A_{int}$  and  $A_{tot}$  are the intersected and total areas respectively.

Assume two parallel beams crossing, as shown in Figure 4.3, the ratio of the intersected area to the total area is given by

$$A_{int}/A_{tot} = D/(L \sin \theta)$$

Let  $D = 2\sqrt{2}W_0$  be the diameter of the beam (beam diameter at the Rayleigh range). For most of the multipass cells  $\theta \approx 1.6^\circ$  is used. The gain enhancement is then given by

$$(\sigma - 1) = \frac{\Delta I_p}{I_p} = \frac{2\sqrt{2}W_0 m}{L \sin \theta} \tag{4.16}$$

and is shown in Table 4.1.

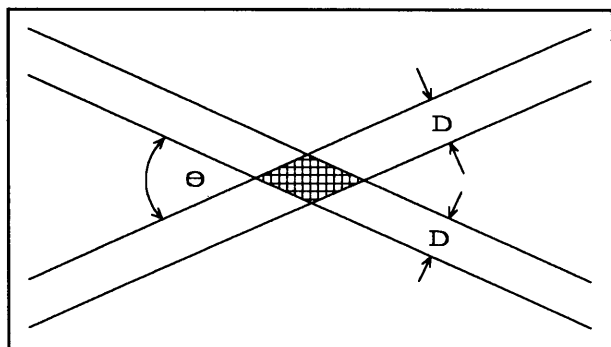


Figure 4.3 Two parallel beams crossing in the centre of a multipass cell

<i>Passes</i>	20	25	36
<i>m</i>	2.39	2.7	3.1
$\Delta I_p/I_p$	0.1*	0.11	0.12

(\*This compares with an estimate of 10%, published by Perry et al. [27])

Table 4.1 Gain enhancement ( $\sigma-1$ ) estimates for an multipass cell of  $L=3.77\text{ m}$  and  $W_0 \approx 1.5\text{ mm}$  ( $W_0 = M \omega_0$ ) as a function of number of passes ( $n$ ) and  $T_{PL} \approx 100\text{ ns}$

### 4.3.2 CALCULATION OF THE STOKES SEED

The input Stokes is taken as the background<sup>[1]</sup> radiation in a specific solid angle and direction. From Planck's law the total black-body radiation is given by[28]

$$M_{\lambda_s} = 2 \pi h c^2 \lambda_s^{-5} \left[ \exp\left(\frac{hc}{\lambda_s kT}\right) - 1 \right]^{-1}$$

into  $4\pi$  steradian, with the units of  $M_{\lambda_s} = \text{W/m}^3$ . The radiation in a specific direction and solid angle  $d\Omega$  is given by

$$M_{\lambda_s, d\Omega} = \frac{1}{2} h c^2 \lambda_s^{-5} \left[ \exp\left(\frac{hc}{\lambda_s kT}\right) - 1 \right]^{-1} d\Omega . \quad (4.17)$$

Let  $dA$  be the area on a sphere of radius  $r$  (Figure 4.4), with the centre in the middle of the Raman cell, then the solid angle is defined as  $d\Omega = dA/r^2$ . For these calculations an input beam diameter of 10 mm ( $dA \approx 8 \times 10^{-5} \text{ m}^2$ ) and  $r = L/2 \approx 1.9 \text{ m}$  is assumed. These values result in a solid angle  $d\Omega \approx 2.2 \times 10^{-5}$ .

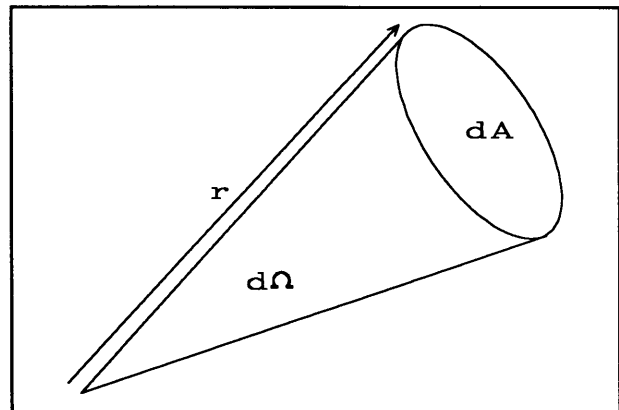


Figure 4.4 Solid-angle definition

Assuming a narrow  $\text{CO}_2$  line width of  $\Delta\nu$ , the power radiated into a line width of  $\Delta\nu$  at  $\lambda_s = 16 \mu\text{m}$  can then be calculated. Also assume that only 50% of the photons have the correct polarization. Consequently equation (4.17) can be rewritten as

$$P_{so} = 1.1 \times 10^{-30} \Delta\nu \lambda_s^{-3} \left[ \exp\left(\frac{1.44 \times 10^{-2}}{\lambda_s T}\right) - 1 \right]^{-1} . \quad (4.18)$$

The Stokes seed as a function of temperature  $T$  is shown in Figure 4.5 and Table 4.2.

The Stokes seed reported in Table 4.2 at 77 K does not take into account the seeding from the room temperature laboratory. Stokes seed photons of the correct polarization and solid angle can enter the Raman cell via the input and output windows. ZnSe is used as the input and

[1] The spontaneous Raman noise in a single polarization and single spatial mode within the Raman linewidth is given by  $P_{so} = h \nu_s \Delta\nu_s \approx 10^{-12} \text{ W/m}^2$  [29]. This seeding is considerably smaller than the black-body radiation seeding through the Raman cell windows.

output windows (3 input or output windows with a window thickness of 5 mm). These windows introduce reflection ( $\sim 17\%$  /surface) and absorption ( $\sim 20\%$  /cm)  $16\ \mu\text{m}$  seed losses. With these losses included the  $16\ \mu\text{m}$  seeding through the Raman cell windows for a 77 K Raman cell is<sup>[2]</sup>  $P_{\text{so}} = 1.4 \times 10^{-9} \times (0.83)^6 \times (0.9)^3 \approx 3.3 \times 10^{-10}\ \text{W/m}^2$ .

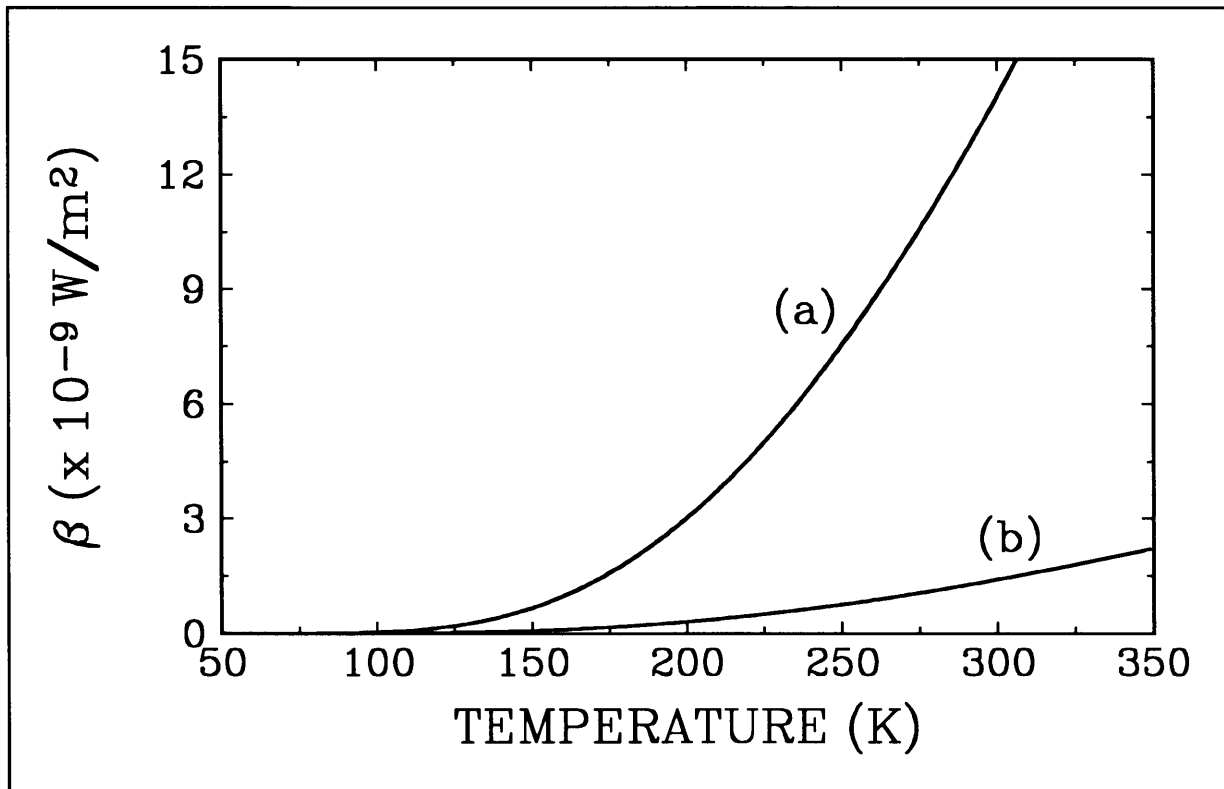


**Figure 4.5** Stokes seed: (a) broad-band ( $\Delta\nu \approx 1\ \text{GHz}$ ) and (b) narrow-band ( $\Delta\nu \approx 100\ \text{MHz}$ ) laser emission at  $16\ \mu\text{m}$  ( $d\Omega \approx 2.2 \times 10^{-5}$  steradian)

Temp (K) $\rightarrow$ $\Delta\nu \downarrow$	77	200	300
1 GHz	$2.3 \times 10^{-12}$	$3.1 \times 10^{-9}$	$1.4 \times 10^{-8}$
100 MHz	$2.3 \times 10^{-13}$	$3.1 \times 10^{-10}$	$1.4 \times 10^{-9}$

**Table 4.2** Stokes seed ( $\lambda_s = 16\ \mu\text{m}$ ) for broad band ( $\Delta\nu = 1\ \text{GHz}$ ) and narrow band ( $\Delta\nu = 100\ \text{MHz}$ )  $\text{CO}_2$  laser emission

<sup>[2]</sup> Due to multiple (to and fro) reflections the actual transmission will be a few percent higher than this value. This has a minimal effect of  $G_T$  and  $\beta$  in equation (3.6).

### 4.3.3 CALCULATIONS OF RAMAN CONVERSION IN A MULTIPASS CELL

With the focusing and crossing enhancements  $\eta(z)$  and  $\sigma$ , equations (4.11)-(4.13) become:

$$\left. \begin{aligned} \frac{dK_S}{dz} &= \eta \gamma \sigma \kappa_1 \Delta K_P K_S - \delta_S K_S \\ \frac{dK_P}{dz} &= -\eta \gamma \sigma \kappa_1 \left( \frac{\lambda_S}{\lambda_P} \right) \Delta K_P K_S - \delta_P K_P \\ \frac{d\Delta}{dt} &= -\eta \gamma \sigma \kappa_2 \Delta K_P K_S \end{aligned} \right\} \quad (4.19)$$

where  $\eta$ ,  $\gamma$ ,  $\sigma$ ,  $\kappa_1$  and  $\kappa_2$  are defined in previous sections of this chapter. We now solve these differential equations for the input values in Table 4.3.

The input pump pulse is an actual CO<sub>2</sub> pulse measured with a photon drag detector on input to the multipass cell. The pulse was digitized using a 1 GHz sampling oscilloscope and transferred to an input data file via GPIB interface for an IBM compatible computer (see Figure 4.6).

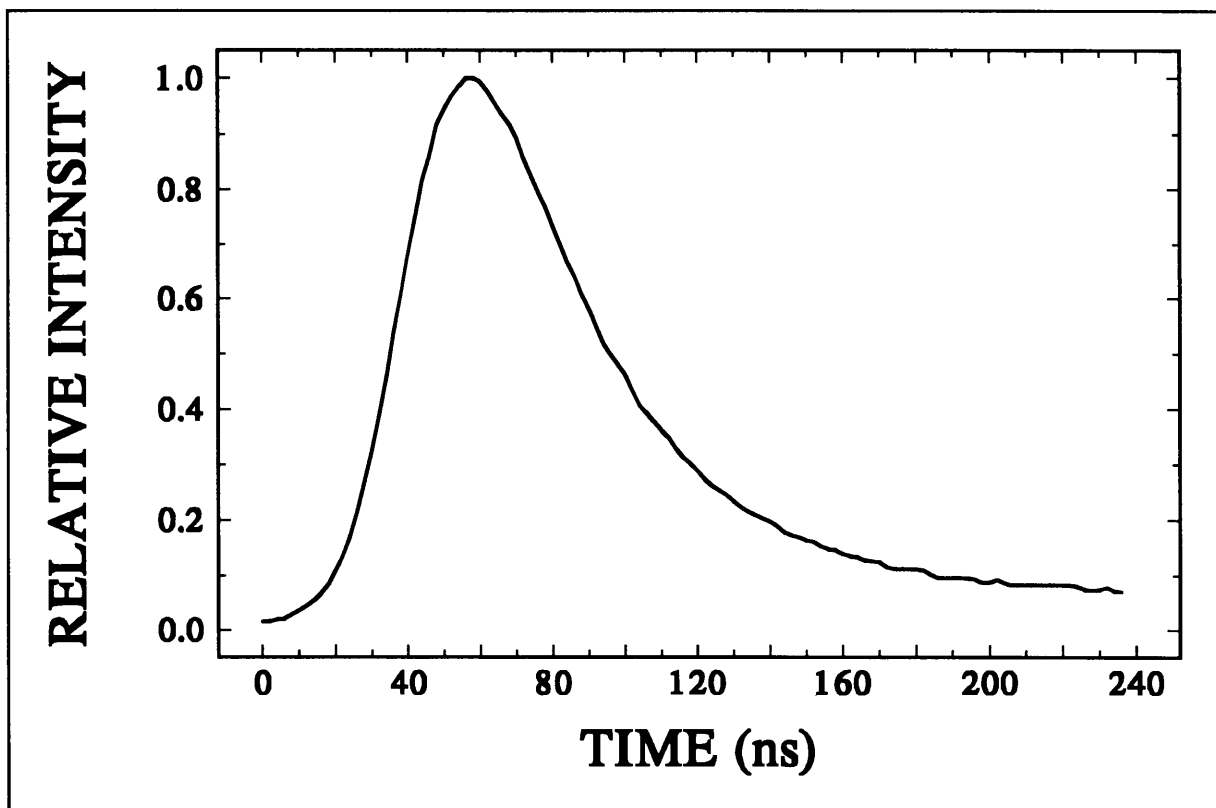


Figure 4.6 Normalised input pump pulse (actual photon drag signal)

<i>Cell temp → Constants and Input values ↓</i>	<i>Warm cell (300 K)</i>	<i>Cold cell (77 K)</i>
$\lambda_p, \lambda_s$ ( $\mu m$ )	10.2, 16	10.2, 16
<i>Plane gain coefficient - g (Chapter 3)</i>	$4.7 \times 10^{-13}$	$1.1 \times 10^{-12}$
$P_{s_0}$ ( $W/m^2$ ) at $\Delta\nu = 100$ MHz	$1.4 \times 10^{-9}$	$3.3 \times 10^{-10}$
$\delta_s$ (/m)	0.002	0.002
$\delta_p$ (/m)	0.002	0.002
$\Delta_0$ (/m <sup>3</sup> )	0.43	0.99
$\Gamma$ (s)	$5 \times 10^{-9}$	$30 \times 10^{-9}$
$\sigma$	1.11	1.11
$T_{PL}$ (ns)	60	60
$L$ (m)	3.77	3.77
$R_m$ (mirror reflectivity)	0.985	0.985
<i>Input energy (J)</i>	A number of input energy values were used.	
<i>Hydrogen pressure (kPa)</i>	150	50

**Table 4.3** *Input/Initial values for Raman conversion in an multipass cell*

The scheme used for solving the equations is as follows (see Figure 4.7):

- First pass (through the multipass Raman cell):
  - Segment both pump pulse and Stokes seed ( $\leq 500$ ).
  - Segment medium ( $\leq 1000$ ) (for a single pass through the multipass cell).
  - Initialize the pump, Stokes and medium arrays with the appropriate initial conditions.
  - Solve equations using the fourth order Runge-Kutta for a single pass by allowing each element of the pump and Stokes pulse to propagate through the medium (see Figure 4.7).
- Subsequent passes:
  - Multiply pump and Stokes pulses with the reflectivity ( $R_m$ ) of mirrors.
  - Initialize medium array with initial conditions  $\Delta_0$ .
  - Initialize pump and Stokes array with the result from the previous pass.
  - Solve equations again for a single pass.

By following this scheme the buildup of the Stokes pulse and depletion of the pump pulse can



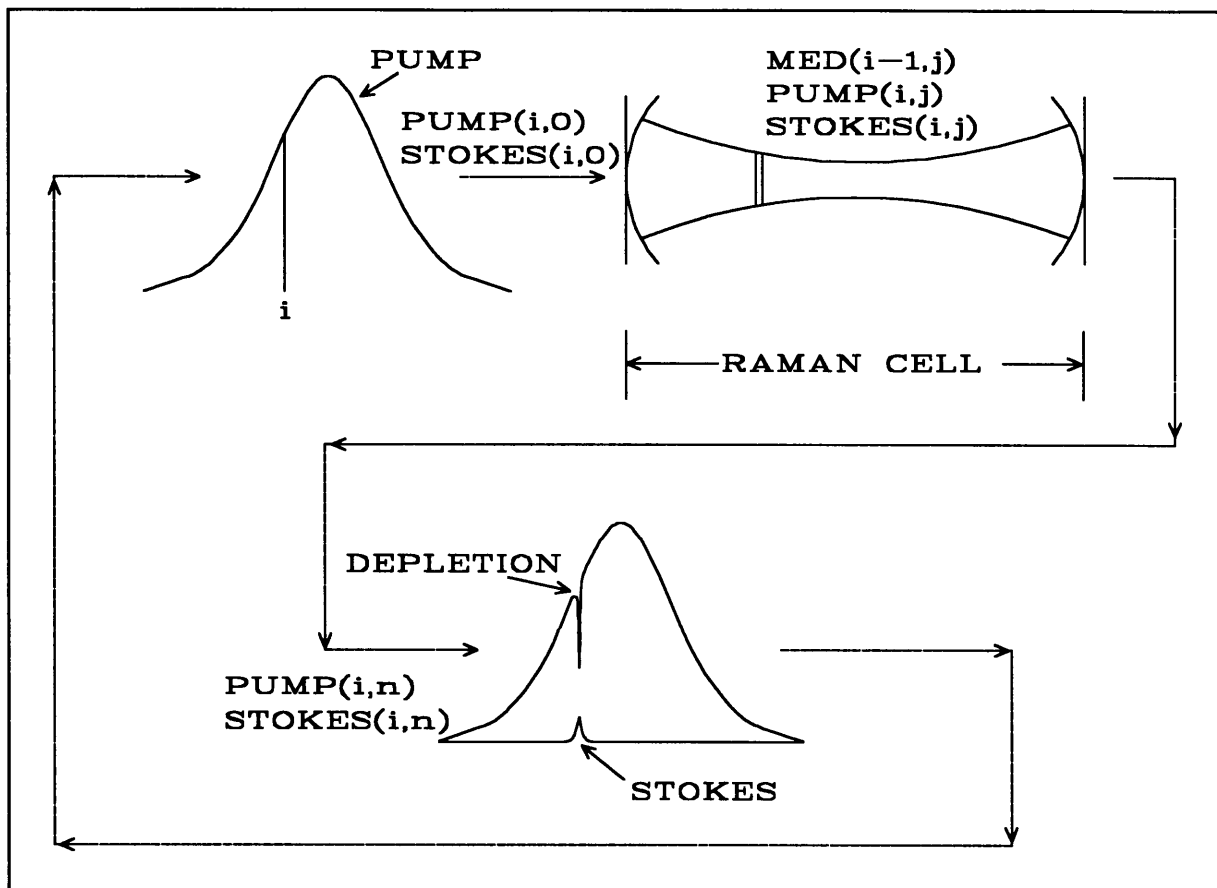


**Figure 4.7** Computing scheme

By following this scheme the buildup of the Stokes pulse and depletion of the pump pulse can be calculated and followed for each pass through the multipass cell. The code for solving the equations was written in TURBO PASCAL on a 486 IBM compatible computer (see Appendix 4.A). A single run on the computer takes about 18 minutes. A typical output is shown in Figure 4.8.

#### **4.3.4 DISCUSSION OF MULTIPASS CELL CALCULATION RESULTS**

Comparing the results obtained from the model with the experimental results is always the final check needed to verify the assumptions made while deriving the equations. In Figure 4.9 the measured output for a 1.2 J CO<sub>2</sub> pulse in a cold (77 K) multipass Raman cell of 25 passes is compared with a modeled output.

The results reported in Figure 4.9a have no sharp edges comparing to Figure 4.9b. This is due to the finite time resolution of the detector (photon drag) and the oscilloscope. The combined measuring time resolution is less than 4.5 ns comparing to a step size of less than 1 ns for the model calculations. Furthermore, it is difficult to compare absolute energy values

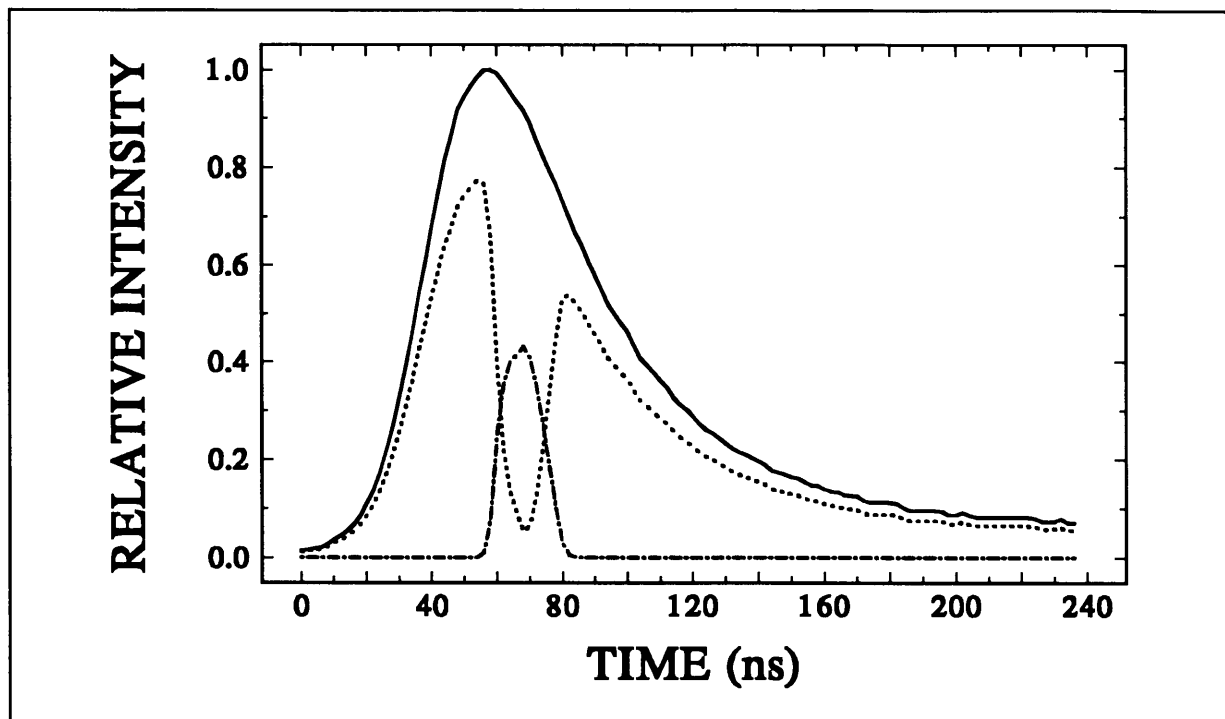


*Figure 4.8* A typical result with the input pump pulse (solid), the depleted pump pulse (dashed) and the output Stokes pulse (dot-dashed) after several passes

as detector calibrations are seldom better than 10%. In most cases the detectors are used above the specified surface energy densities. This has an influence on the energy measuring accuracy.

With these limitations in mind, one can say that the model predictions are in agreement with the measured Raman output. The larger Stokes onset time (asymmetric Stokes output with respect to the peak pump intensity position) in Figure 4.9a comparing to Figure 4.9b indicates that the definition of  $\gamma$  is probably not 100% correct. The difference in energy output predictions is probably due to the exit window losses (reflection and absorption) and larger linear Raman cell losses. From Figure 4.9a a lagtime (difference between the pump peak intensity and the centre of the Stokes pulse) of  $\Gamma \approx 30$  ns is measured. This means that the Raman line width  $\Delta\nu_R = 1/\Gamma$  for the S(0) transition is about 35 MHz. This value is of the correct order (see Figure 3.3) and is a useful indirect measurement of the S(0) line width in cold parahydrogen.

The second important verification of the model is to compare the experimental Raman threshold with that predicted by the model. Figure 4.10 shows the calculated threshold for a multipass cell filled with 50 kPa parahydrogen at 77 K. Evidently, the model predicts a value of 10 MW that is much smaller than the experimental value of 14 MW. This is due to an imperfect pump beam (see Section 5.10).

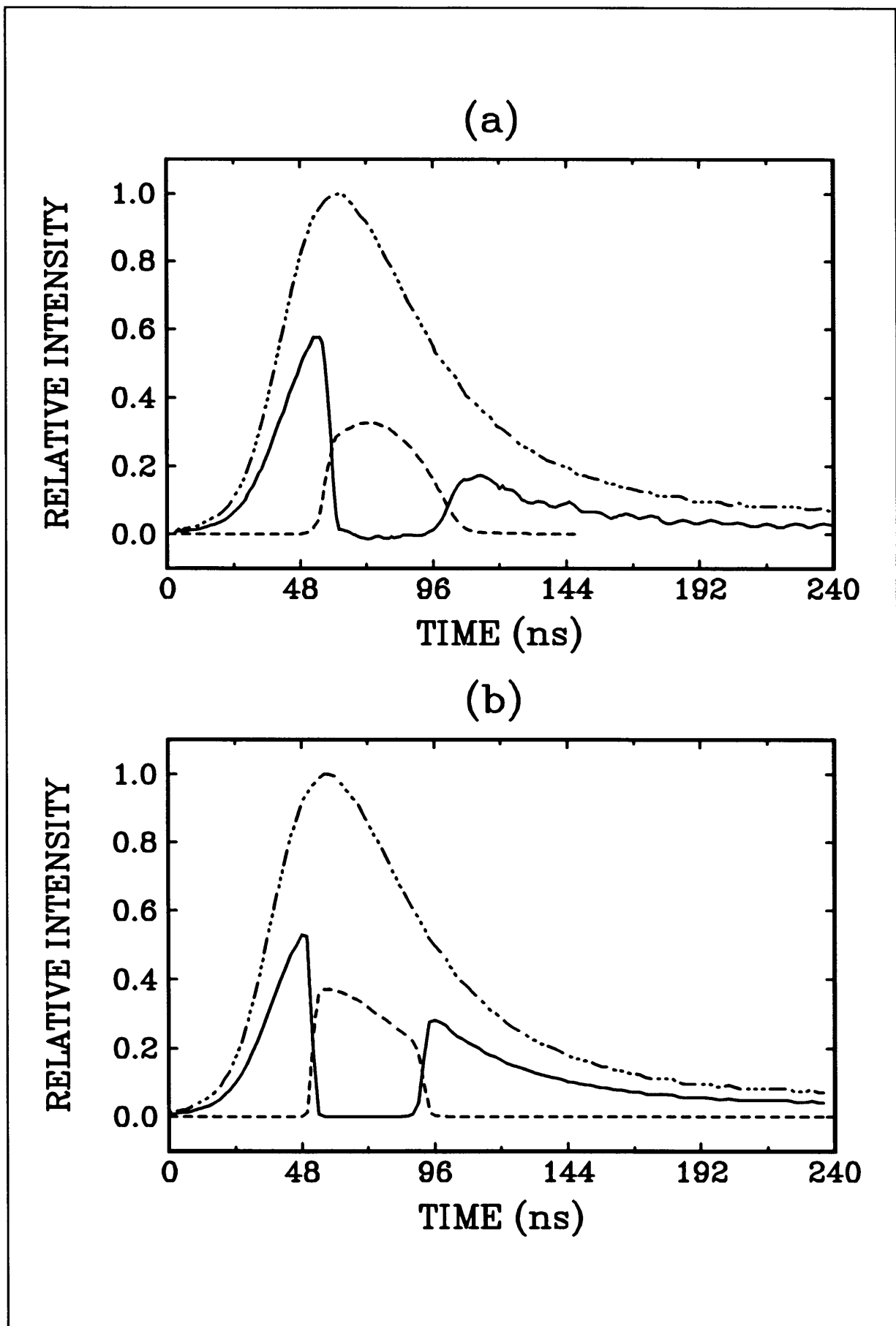
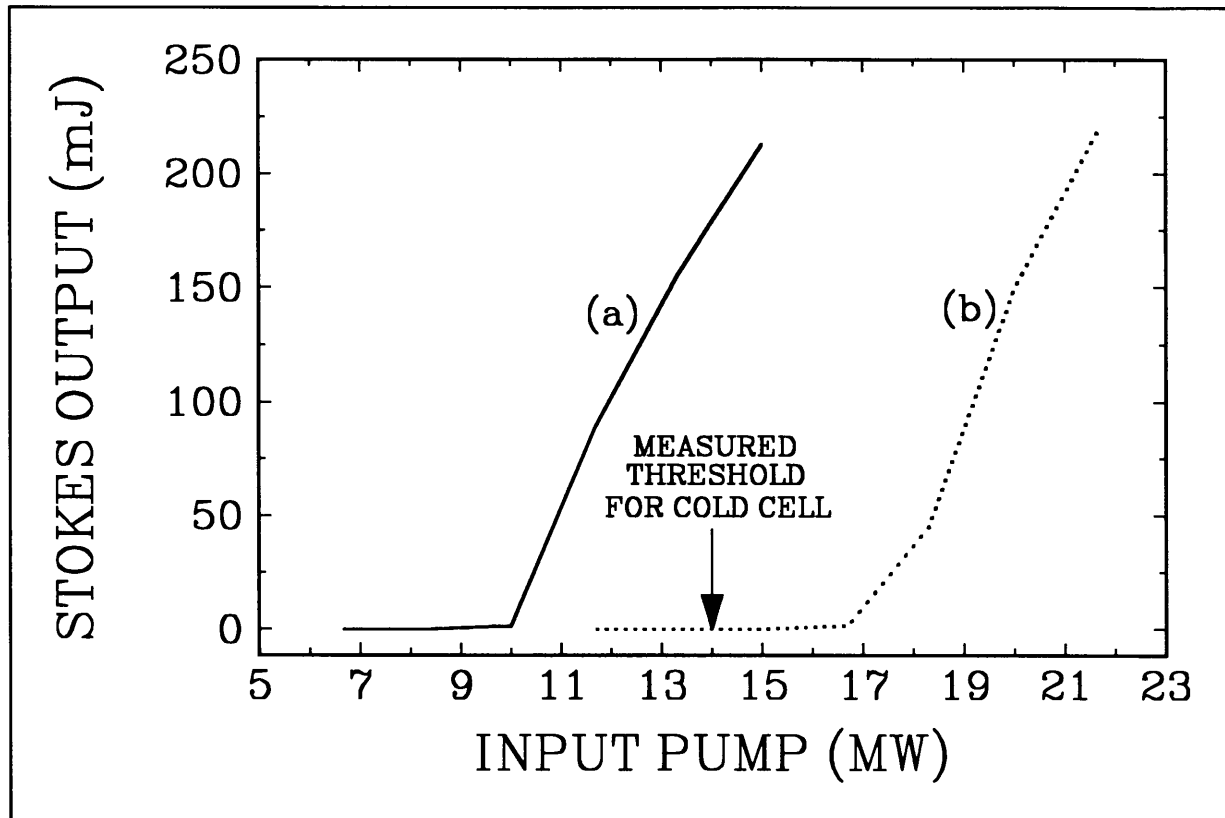


Figure 4.9 (a) Experimental and (b) model results for an input pulse of 1.2 J in 60 ns for a 25 passes multipass Raman cell and  $M^2=1.3$



**Figure 4.10** Stokes output for the 10R18 CO<sub>2</sub> line for a 25 passes parahydrogen Raman cell at (a)  $P=50$  kPa,  $T=77$ K and (b)  $P=150$  kPa,  $T=300$  K

Finally, to conclude the results from the model, it is useful to know the Stokes growth as a function of the number of passes in the multipass cell. From Figure 4.11 it is evident that only the last third of the passes are used for the conversion of the 10  $\mu$ m beam to a red-shifted 16  $\mu$ m beam. It is therefore apparent that if this relationship between the 16  $\mu$ m output and number of passes is known, a multipass cell can be designed for maximum output and minimum passes.

However, an advantage of an oversupply of passes is that a larger tolerance on the parahydrogen : orthohydrogen ratio in the multipass cell can be allowed before a significant drop in 16  $\mu$ m output is experienced.

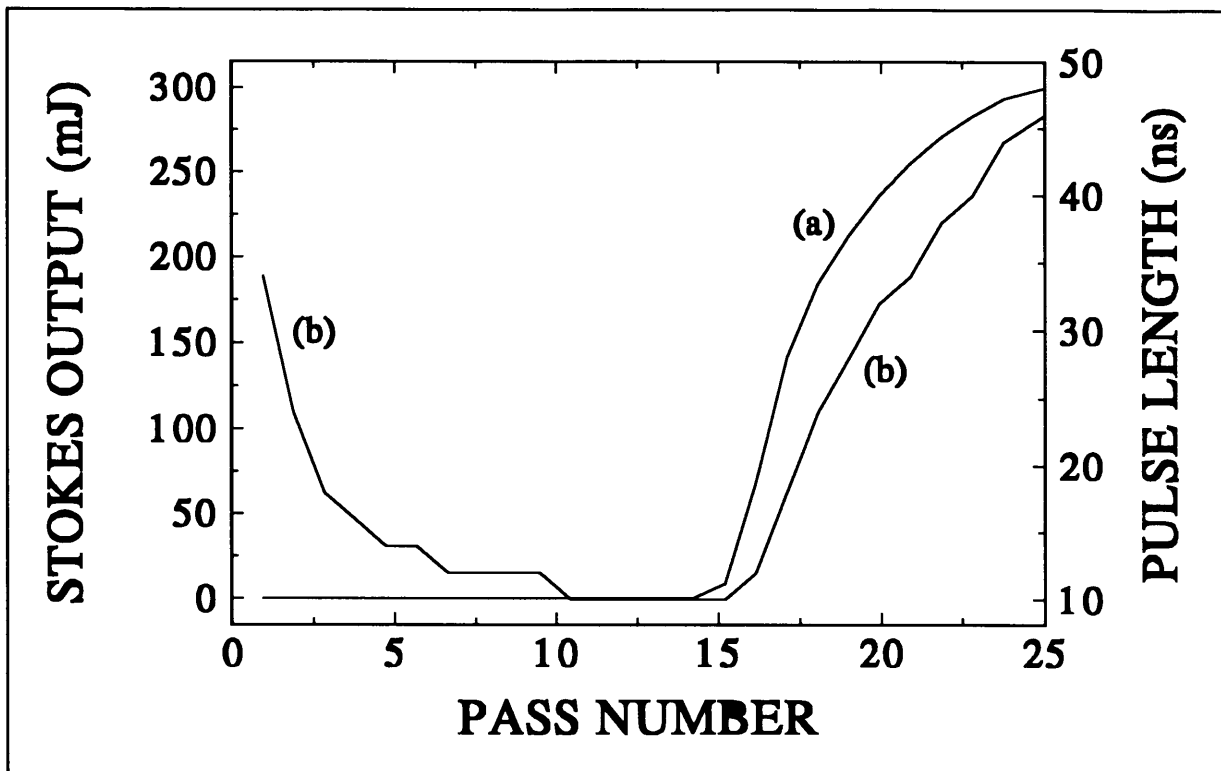


Figure 4.11 Stokes output (a) and Stokes pulse length (b) as a function of the number of passes ( $T=77\text{ K}$ ,  $E=50\text{ kPa}$ ,  $E=1.2\text{ J}$ ,  $M^2=1.3$ )

#### 4.4 MODEL FOR WAVEGUIDE RAMAN CELL

The waveguide Raman cell consists of a hollow nickel pipe with a germanium layer on the inner surface of the guide. The guide ( $2a=2.3\text{ mm}$ ) contains the parahydrogen for the conversion of the wavelength. Using a waveguide simplifies the equations derived in Section 4.2 considerably due to the constant area  $A_i$ . This area corresponds to the area of the  $HE_{11}$  mode in the waveguide. Furthermore, it is a single-pass system which means that there is no gain enhancement due to beam crossings. Keeping this in mind equations (4.11)-(4.13) can be rewritten as follows:

$$\left. \begin{aligned}
 \frac{dK_S}{dz} &= \gamma \kappa_1 \Delta K_P K_S - \delta_S K_S \\
 \frac{dK_P}{dz} &= -\gamma \kappa_1 \left( \frac{\lambda_S}{\lambda_P} \right) \Delta K_P K_S - \delta_P K_P \\
 \frac{d\Delta}{dt} &= -\gamma \kappa_2 \Delta K_P K_S
 \end{aligned} \right\} \quad (4.20)$$

with  $\kappa_1$  and  $\kappa_2$  defined in Section 4.2. The constants  $\delta_P$  and  $\delta_S$  now consist mainly of losses due to waveguide transmission. Input values are shown in Table 4.3 except for  $R_m$ , which is now a waveguide loss. A number of different values for  $\delta_P$  and  $\delta_S$  are used.

Designing an optimum waveguide Raman cell the length of the cell must be optimized with respect to the available CO<sub>2</sub> laser power. As a first-order approximation for the model calculations, assume a system with no pump and medium depletion that is with  $K_p$  and  $\Delta$  constant. The Stokes equation in equation (4.20) can then be written as

$$\frac{dK_S}{dz} = \kappa_1 K_P K_S \Delta \quad (4.21)$$

for no losses in the waveguide and no excitation lag time, thus  $\gamma = 1$ . Then

$$\int_{K_{S0}}^{K_S(L)} \frac{dK_S}{K_S} = \int_0^L \kappa_1 K_P \Delta dz \quad \text{and} \quad K_S(L) = K_{S0} e^{\kappa_1 K_P \Delta L},$$

where  $L$  is the length of the waveguide Raman cell. For a single-pass output of  $I_S(L) = \delta I_{P0}$  and no depletion of the pump power it follows that

$$\delta = \frac{I_{S0}}{I_{P0}} e^{\kappa_1 K_P \Delta L}. \quad (4.22)$$

<i>VARIABLE</i>	<i>NUMERICAL VALUE</i>
E(J)	1.5
Waveguide diameter - D (m)	$2.3 \times 10^{-3}$
$A_0 = \pi D^2/4$ (m <sup>2</sup> )	$4.16 \times 10^{-6}$
$g = \alpha N_0$ (m/W)	$1.1 \times 10^{-12}$
$T_{PL}$ (s)	$60 \times 10^{-9}$
$I_{P0} = E/(T_{PL} A_0)$ (W/m <sup>2</sup> )	$6.01 \times 10^{12}$
$I_{S0}$ (W/m <sup>2</sup> )	$5 \times 10^{-12}$

**Table 4.4** *Input values for  $L_{min}$  calculations*

From this equation a minimum waveguide length  $L_{min}$  can be calculated for an expected Stokes output. Using the definition for  $\kappa_1$  and remember that  $K_p \approx 1$  and  $\Delta \approx 1$ , equation (4.22) can be rewritten as

$$L_{min} = \frac{\ln\left(\frac{\delta I_{P0}}{I_{S0}}\right)}{g I_{P0}}. \quad (4.24)$$

For the variable values given in Table 4.4, the minimum waveguide length is calculated as a

function of  $\delta$ . Table 4.5 shows the approximate waveguide lengths for values of  $\delta$ .

$\delta$	$L_{min}$ (m)
0.001	7.3
0.01	7.7
0.05	7.9
0.1	8.0

**Table 4.5**  $L_{min}$  calculations as a function of expected Stokes output

The lengths predicted in Table 4.5 are much longer than the waveguides that were manufactured (see Chapter 2). However, before the waveguide length can be specified equations (4.19) must be solved numerically with all possible losses included.

#### **4.4.1 DISCUSSION OF CALCULATION RESULTS**

The pump laser specification was fixed at 1.5 J in 60 ns with circular polarization input into the waveguide Raman cell. This specification was used as this is the system available for plant operation at high repetition rates ( $> 1$  kHz).

Furthermore, a cold parahydrogen waveguide Raman cell at 50 kPa was used for the calculations. These conditions, with the polarization, meant that maximum Raman gain may be achieved in the waveguide Raman cell. Figure 4.12 shows the calculated Raman output for the S(0) transition in parahydrogen as a function of waveguide length for a number of waveguide transmission loss values. Clearly the losses introduced have a serious effect on the Raman threshold. This means that waveguides of extended lengths are needed for sufficient Raman output.

It is clear from Chapter 2 that it is technically very difficult to manufacture a waveguide of these lengths. However, it is possible to use the available waveguides as Raman amplifiers. Figure 4.13 shows the Raman output that can be expected for several different Stokes seed contributions for a 2.2 m nickel-germanium waveguide with a 2.3 mm bore.

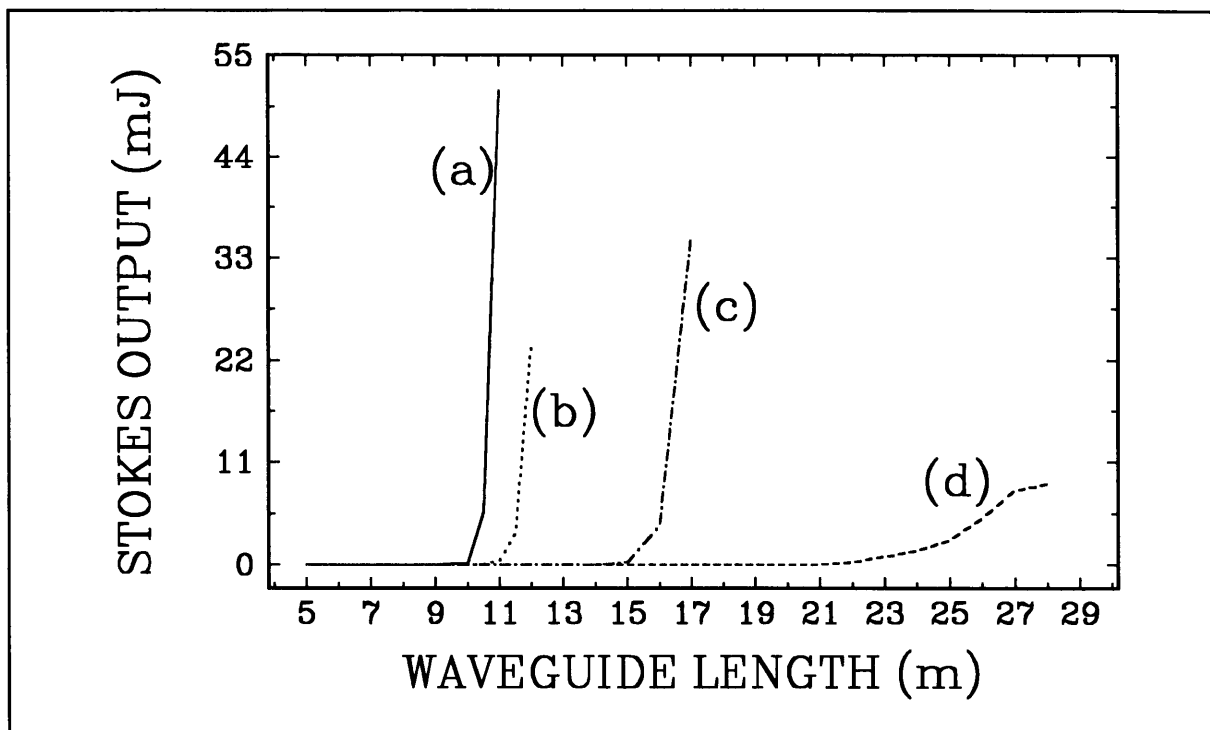


**Figure 4.12** Raman output for a parahydrogen waveguide Raman cell at 77 K for (a) 0%, (b) 2%, (c) 5% and (d) 10% waveguide losses ( $CO_2$  input = 1.5 J in 60 ns)

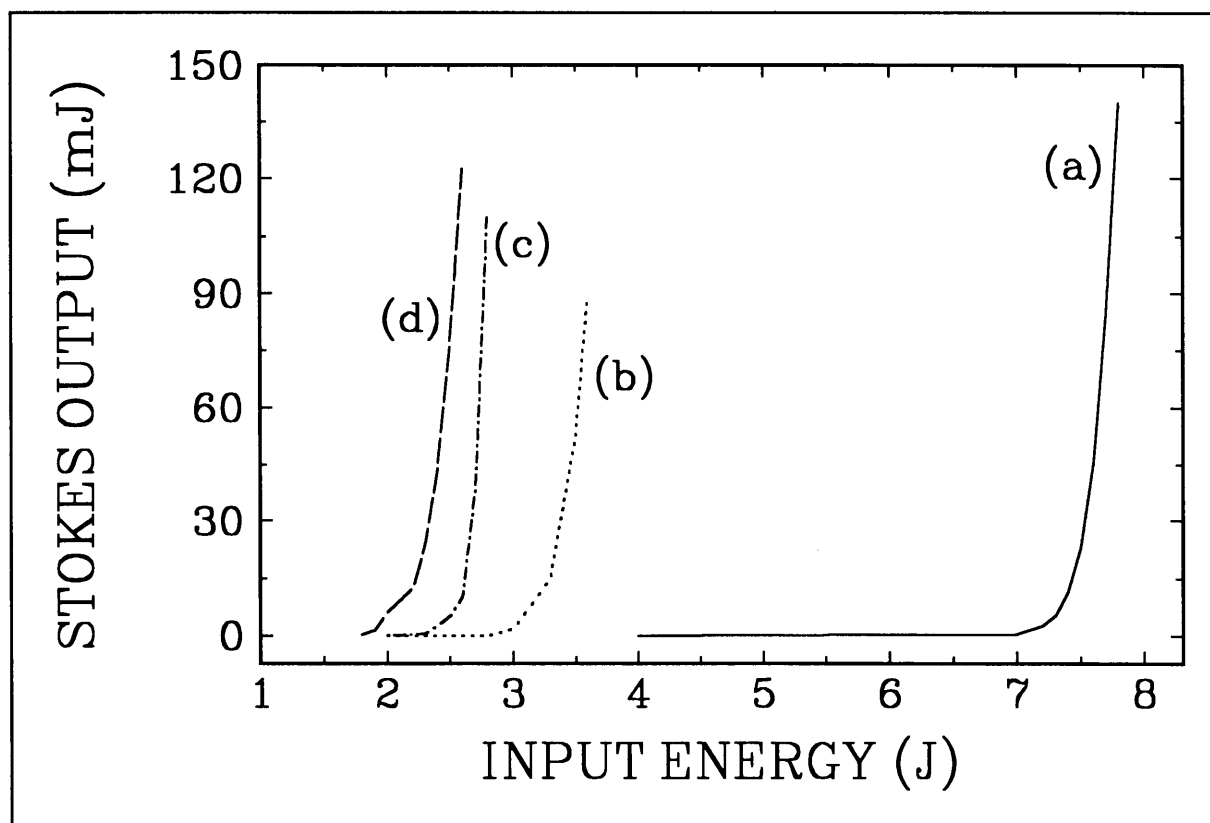


**Figure 4.13** Waveguide Raman amplifier output: (a) thermal noise, (b) 1  $\mu J$ , (c) 100  $\mu J$  and (d) 1 mJ Stokes seed ( $L = 2.2$  m,  $T = 77$  K,  $CO_2$  pulse of 60 ns)



### 4.4.2 EXPERIMENTAL RESULTS

An experiment was designed, using a 2.2 m waveguide and a 2.2 J in 60 ns input at 10  $\mu\text{m}$  (see Figure 4.14). The aim was to measure a small amount of Raman conversion in cold parahydrogen. No output was measured at 16  $\mu\text{m}$  even with the use of a cryogenic cooled MCT (Hg-CdTe) detector optimized for the 10  $\mu\text{m}$  to 16  $\mu\text{m}$  range. A 1 m monochromator employing a 60 lines/mm grating was used for the 16  $\mu\text{m}$  wavelength detection. This result confirmed the predicted Stokes output from the model. As no seed was available, the Raman amplifier scheme was never tested.

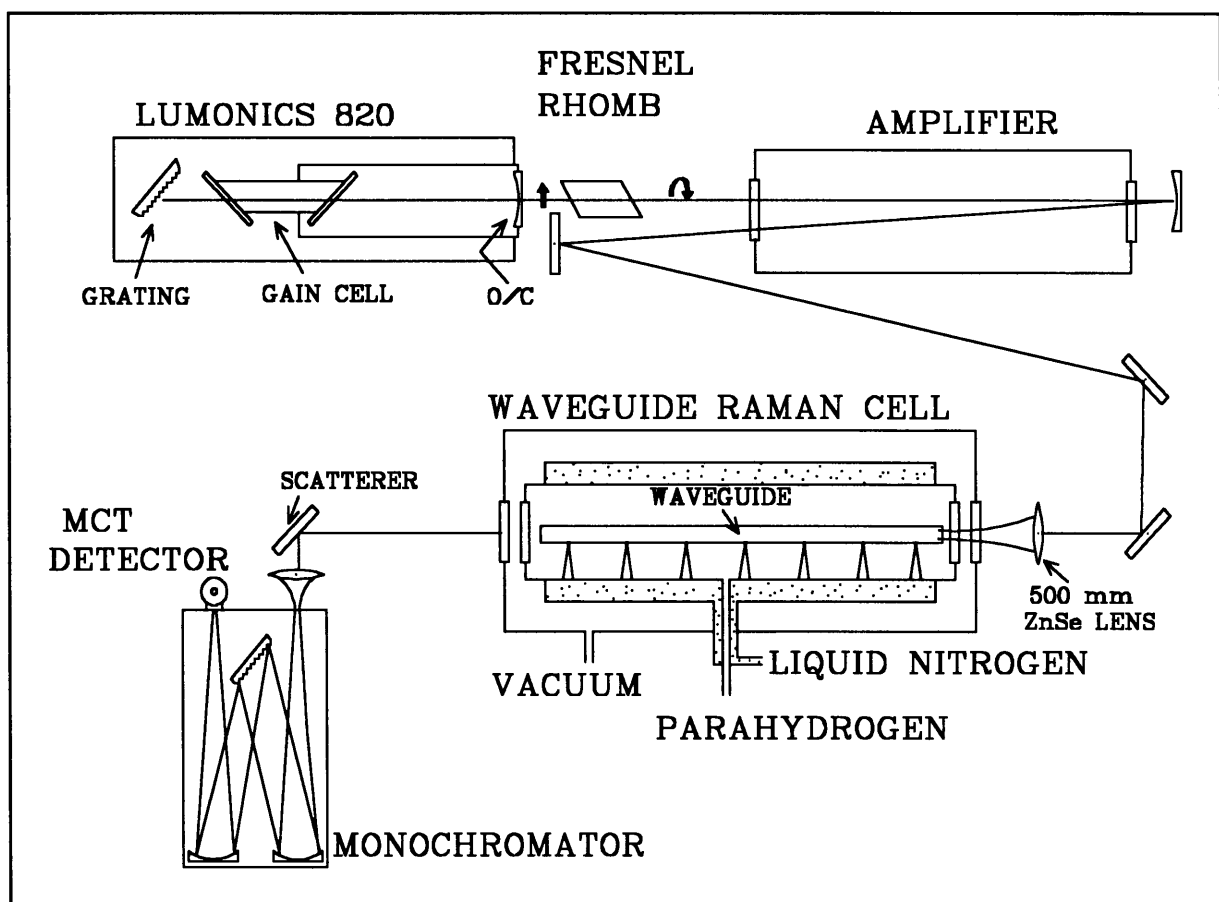


**Figure 4.14** Experimental layout for waveguide Raman cell measurements

## 4.5 REFERENCES: CHAPTER 4

1. Multimode effects in stimulated Raman emission  
N. Bloembergen, Y.R. Shen  
Phys Rev Lett **13**(24),720,(Dec 1964)
2. Theory of Stokes pulse shapes in transient stimulated Raman scattering  
R.L. Carman, F. Shimizu, C.S. Wang, N. Bloembergen  
Phys Rev A **2**(1),60,(July 1970)
3. Quantitative investigations of the stimulated Raman effect using sub-nanosecond light pulses  
D. von der Linde, M. Maier, W. Kaiser  
Phys Rev **178**(1),178,(Febr 1969)
4. High-Efficiency joule level Raman generation in Pb vapour  
S.J. Brosnan, H. Kormine, E.A. Stappaets, M.J. Plummer, J.B. West  
Opt Lett **7**(4),154,(April 1982)
5. Powerful tunable infrared generation by stimulated Raman scattering  
R. Frey, F. Pradere  
Opt Comm **12**(1),98,(Sept 1974)
6. Observation of stimulated anti-Stokes Raman scattering in inverted atomic iodine  
R.L. Carman, W.H. Lowdermilk  
Phys Rev Lett **33**(4),190,(July 1974)
7. Coherent propagation of high-power light pulses through a medium under conditions of two-quantum interaction  
I.A. Poluéktov, Yu. M. Popov, V.S. Roitberg  
JEPT Lett **20**(8),243,(Oct 1974)
8. Stimulated Raman scattering of radiation from an electric-discharge pulse periodic XeCl laser in compressed H<sub>2</sub>  
V.Yu. Baranov, V.M. Borisov, A.Yu. Vinokhodov, Yu.B. Kiryukhin,  
Yu.Yu. Stepanov  
SOV J Quantum Electron **15**(5),727,(May 1985)
9. Multiple-pass Raman gain cell.  
W.R. Trutna, R.L. Byer  
Appl Opt **19**(2),301,(Jan 1980)

10. A 16  $\mu\text{m}$  source for laser isotope enrichment  
R.L. Byer  
IEEE J Quantum Electron Correspondence ,732,(Nov 1976)
11. Parametric study of a Raman p-H<sub>2</sub> laser with over 30 MW emission at 16  $\mu\text{m}$   
M Bernardini, A Ferrario, M. Giorgi, S. Marchetti, A. Palucci  
IL NUOVO CIMENTO **4D**(6),520,(Dec 1984)
12. Multiple pass stimulated Raman conversion with pump depletion  
R.T.V. Kung  
IEEE J Quantum electron **QE-17**(4),509,(April 1981)
13. Single mode 30 MW CO<sub>2</sub> laser system for 16  $\mu\text{m}$  Raman scattering in p-H<sub>2</sub>  
M. Bernardini, A DI Giulio, M. Giorgi, S. Marchetti  
IL NUOVO CIMENTO **73B**(1),112,(1983)
14. Output performance of a liquid-N<sub>2</sub> cooled para-H<sub>2</sub> Raman laser.  
K. Midorikawa, H. Tashiro, Y. Aoki, K. Oshasdi, K. Nagasaka,  
K. Toyoda, S Namba  
J Appl Phys **57**(5),1504,(March 1985)
15. Transient effects and pump depletion in stimulated Raman scattering  
J.L. Carlsten, R.G. Wenzel  
Reference: Unknown
16. Stimulated pure rotational Raman scattering in deuterium  
R.W. Minck, E.E. Hagenlocker, W.G. Rado  
Phys Rev Lett **17**(5),229,(August 1966)
17. Efficient tunable H<sub>2</sub> Raman laser  
P. Rabinowitz, A. Stein, R. Brickman, A. Kaldor  
Appl Phys Lett **35**(10),739,(Nov 1979)
18. Short-pulse ultraviolet fiber Raman laser pumped by a XeCl excimer laser  
T. Mizunami, T. Miyazaki, K. Takagi  
J Opt Soc of AM B **4**(4),498,(April 1987)
19. Theory of the synchronously pumped fiber Raman laser.  
M. Nakazawa, M. Kuznetsov, E.P. Ippen  
IEEE J Quantum Electron **QE-22**(10),1953,(Oct 1986)
20. Waveguide effects in superfluorescence and stimulated Raman scattering  
J. Mostowski, B. Sobolewska  
Phys Rev A **34**(4),3109,(Oct 1986)

21. Waveguide Raman laser  
P. Rabinowitz, A. Kaldor, R. Brickman, W. Schmidt  
Appl Opt **15**(9),2005,(Sept 1976)
22. CO<sub>2</sub>-pumped p-H<sub>2</sub> rotational Raman amplification in a hollow dielectric waveguide  
N.A. Kurnit, G.P. Arnold, L.W. Sherman, W.H. Watson, R.G. Wenzel  
CLEOS 1980.
23. A theoretical analysis of stimulated Raman conversion  
E. Margalith, G.W. Sutton  
J Appl Phys **59**(2),327,(January 1986)
24. Saturation and tuning behaviour of stimulated electronic Raman scattering  
D. Cotter, D. C. Hanna  
IEEE J Quantum Electron **QE-14**(3),184,(March 1978)
25. Stimulated rotational Raman scattering in CO<sub>2</sub> pumped para-H<sub>2</sub>.  
J.L. Carlsten, R.G. Wenzel  
IEEE J Quantum Electron **QE-19**(9),1407,(Sept 1983)
26. Room-temperature operation of a para-H<sub>2</sub> rotational Raman laser  
K. Midorikawa, H. Tashiro, Y. Aoki, K. Nagasaka, K. Toyoda,  
S. Namba  
Appl Phys Lett **47**(10),1033,(November 1985)
27. High conversion efficiency ultraviolet fiber Raman oscillator - amplifier system  
R. Pini, R. Salinabeni, M. Vannini, A.F.M.Y. Haider, C. Lin  
Appl Opt **25**(7),1048,(April 1986)
28. OPTICS  
E. Hecht, A. Zajac  
Addison-Wesley Publishing Company, London, (1974)
29. Generation of 16  $\mu$ m radiation using stimulated Raman scattering in H<sub>2</sub>.  
W.R. Trutna  
PhD Dissertation, Stanford University (1979)

# APPENDIX 4.A: MULTIPASS RAMAN CELL AND WAVEGUIDE RAMAN CELL TURBO PASCAL CODE

## 4.A.1 MULTIPASS RAMAN CELL CODE

```
{This program is the modelling of the Raman process. The model is }
{ based on the theory developed by E Margalith & GW Sutton }
{ ProgramName: MPCNOISE.PAS }
{ DataFile : co2.dta }
{ FileWrite : co2dep.dta }
{ : co216.dta }
{ : thres.dta }
```

```
program raman_MPC;
{$N+}

{$M 65500,0, 655360}
uses crt, stdhdr, segraph, worlddr;
```

```
const
  name1 = 'c:co2.dta';
  name2 = 'c:co2dep13.dta';
  name3 = 'c:co21613.dta';
  name4 = 'c:thres13.dta';
  lag = 30e-9;
  N = 250;
  aantal = 500;
  SPL = 2.998E+0008;
  PLANCK = 6.626E-0034;
  boltz = 1.38e-23;
  PI = 3.1415927;
  SIR_LIN = 1.5;
```

```
type
  matr_m = array[0..AANTAL] of real;
  matr_n = array[0..N, 1..2] of real;
  vekt = array[0..AANTAL] of real;
  kvek = array[1..4] of real;
  vekx = array[0..N] of real;
```

```
var
  x, y : VeryLongVector;
  i, j, M, maxX, maxY, passes, NUMpasses : integer;
  leng, plen, tlen, seed, k1, k2, neta,
  beta, lamst, lamp, energie, w0, ref,
  pressure, temperatuur, ht, medium,
  RamTrans, area, hstreep, Na, gamma,
  alfa, alfa_pw, I_po, hx, deltaP,
  deltaS, RM, M2, ZZR, w12, wz : real;
```

```

npomp, stok           : ^matr_m;
med                   : ^matr_n;
tyd, treal, pp, ss1, ss0, pp0, mm : vekt;
pos, preal            : vekx;
files, f1             : text;
int_pp0, int_ss1, tot_pp0, tot_ss1,
FWHM_ss1, factor      : real;
fileExt, Enstr, tStr   : string;

{
{ Function to calculate pump D.E.
{
}
}

function pump(p,s1,m :real) :real;
begin
  pump:=-beta*neta*gamma*k1*(lamst/lamp)*p*s1*m-deltaP*p;
end;

{
{ Function to calculate stokes 1 D.E.
{
}
}

function stol(p,s1,m :real) :real;
begin
  stol:=beta*neta*gamma*k1*p*s1*m-deltaS*s1;
end;

{
{ Function to calculate medium D.E.
{
}
}

function medu(p,s1,m :real) :real;
begin
  medu:=-k2*beta*neta*gamma*p*s1*m;
end;

{
{ Solve of the pump equation
{
}
}

function pump_oplos(p,s1,m :real):real;
var kp,ap :kvek;
begin
  ap[1]:=p;
  ap[2]:=s1;
  ap[4]:=m;
  kp[1]:=hx*pump(ap[1],ap[2],ap[4]);
  ap[1]:=p+kp[1]/2;
  ap[2]:=s1+kp[1]/2;
  ap[4]:=m+kp[1]/2;
  kp[2]:=hx*pump(ap[1],ap[2],ap[4]);
  ap[1]:=p+kp[2]/2;

```

```

ap[2]:=s1+kp[2]/2;
ap[4]:=m+kp[2]/2;
kp[3]:=hx*pump(ap[1],ap[2],ap[4]);
ap[1]:=p+kp[3];
ap[2]:=s1+kp[3];
ap[4]:=m+kp[3];
kp[4]:=hx*pump(ap[1],ap[2],ap[4]);
pump_oplos:=p+(kp[1]+2*kp[2]+2*kp[3]+kp[4])/6;
end;

```

```

{
{ Solve of the STOKES1 equation
{

```

```

function stok1_oplos(p,s1,m :real):real;
var kp,ap :kvek;
begin
  ap[1]:=p;
  ap[2]:=s1;
  ap[4]:=m;
  kp[1]:=hx*sto1(ap[1],ap[2],ap[4]);
  ap[1]:=p+kp[1]/2;
  ap[2]:=s1+kp[1]/2;
  ap[4]:=m+kp[1]/2;
  kp[2]:=hx*sto1(ap[1],ap[2],ap[4]);
  ap[1]:=p+kp[2]/2;
  ap[2]:=s1+kp[2]/2;
  ap[4]:=m+kp[2]/2;
  kp[3]:=hx*sto1(ap[1],ap[2],ap[4]);
  ap[1]:=p+kp[3];
  ap[2]:=s1+kp[3];
  ap[4]:=m+kp[3];
  kp[4]:=hx*sto1(ap[1],ap[2],ap[4]);
  stok1_oplos:=s1+(kp[1]+2*kp[2]+2*kp[3]+kp[4])/6;
end;

```

```

{
{ Solve of the MEDIUM equation
{

```

```

function med_oplos(p,s1,m :real):real;
var kp,ap :kvek;
begin
  ap[1]:=p;
  ap[2]:=s1;
  ap[4]:=m;
  kp[1]:=ht*medu(ap[1],ap[2],ap[4]);
  ap[1]:=p+kp[1]/2;
  ap[2]:=s1+kp[1]/2;
  ap[4]:=m+kp[1]/2;
  kp[2]:=ht*medu(ap[1],ap[2],ap[4]);
  ap[1]:=p+kp[2]/2;
  ap[2]:=s1+kp[2]/2;

```

```

ap[4]: =m + kp[2]/2;
kp[3]: =ht*medu(ap[1],ap[2],ap[4]);
ap[1]: =p + kp[3];
ap[2]: =s1 + kp[3];
ap[4]: =m + kp[3];
kp[4]: =ht*medu(ap[1],ap[2],ap[4]);
med_oplos: =m + (kp[1] + 2*kp[2] + 2*kp[3] + kp[4])/6;
end;

```

```

{ Read Input pulse }

```

```

procedure input_pulse(var treal :vekt;
                      var pp0: vekt;
                      var ht :real;
                      var M :integer);

```

```

var i :integer;
    files :text;
begin
  i:= 1;
  assign(files,name1);
  reset(files);
  repeat
    readln(files,treal[i],pp0[i]);
    treal[i]:=treal[i]*1e-9;
    i:=i+1;
  until eof(files);
  M:=i-1;
  ht:=(treal[M]-treal[1])/M;
  close(files);
end;

```

```

{
{ FWHM FOR STOKES & PUMP
{
}
}
}

```

```

procedure halfwydte(ss,tt :vekt;
                   var FWHM :real);
var i,kk :integer;
    lk,rk,beg,half :real;
begin
  beg:=ss[1];
  for i:=2 to M do
    begin
      if ss[i] >=beg then
        begin
          beg:=ss[i];
          kk:=i;
        end;
    end;
  half:=beg/2.0;
  for i:=1 to kk do

```



```

begin
  if ss[i] <= half then lk:=tt[i];
end;
for i:=kk to M do
  begin
    if ss[i] >= half then rk:=tt[i];
  end;
FWHM:=rk-lk;
end;

{
{ Procedure calculating the gain enhancement
{
}
}

procedure enhanceNums(R,L,lamda,MM:real;
                    var wo,wm,zr:real);
var z,a :real;
    i :integer;
begin
  wo:=(MM*lamda/pi)*sqrt((L/2)*(R-L/2));
  wm:=(MM*lamda*L)/(2*pi)*sqrt((2*R*R)/(L*(R-L/2)));
  zr:=pi*wo/(MM*lamda);
  wo:=sqrt(wo);
  wm:=sqrt(wm);
end;

{
{ Main programs
{
}
}

begin
clrscr;
write('Enter Number of Passes: ');readln(NUMpasses);
write('Enter Input enegy: ');readln(energie);
assign(f1,name4);
rewrite(f1);
new(npomp);
new(stok);
new(med);
input_pulse(treal,pp0,ht,M);
halfwydte(pp0,treal,plen);
writeln('plen = ',plen);
tlen:=treal[M];
leng:=3.771;           {Lengte van Raman Cell (m)}
Ref:=0.985;           {Reflection losses for both pump & stokes/reflection}
lamp:=10.2E-6;        {Golflengte van Inset laserpulse (m)}
RamTrans:=354;        {Raman Oorgang (/cm)}
pressure:=0.5;         {Druk van p-H2 (atm)}
temperatuur:=77.0;    {Temperatuur van p-H2 (K)}
beta:=1.11;           {Gain enhancement due to crossings}
RM:=2;                {Radius of curvature of Raman cell mirrors}
M2:=1.45;              {Beam characterization factor M-square}

```

```

deltaP:=0.002;           {Pump beam linear losses /m}
deltaS:=0.002;           {Stokes beam linear losses /m}
pos[0]:=0.0;
if temperatuur=77 then
  begin
    medium:=0.99;
    alfa_pw:=7.3e-13;
    seed:=3.3e-10;
  end
else
  begin
    medium:=0.43;
    alfa_pw:=2.77e-13;
    seed:=1.4e-9;
  end;
for j:=0 to N do
  begin
    med^[j,1]:=medium;
  end;
enhanceNums(RM,leng,lamp,M2,w0,w12,ZZR);
area:=PI*SQR(w12);
writeln('area=',area);
lamst:=1/(100*(1/(lamp*100)-ramtrans));
hstreep:=planck/(2*PI);
na:=101e3*pressure/(boltz*temperatuur);
writeln('na=',na);
alfa_pw:=SIR_LIN*alfa_pw;
k1:=alfa_pw*energie/(plen*area*medium);
writeln('k1=',k1);
writeln('alfa_pw=',alfa_pw);
I_po:=energie/(plen*area);
writeln('I_po=',I_po);
alfa:=alfa_pw/(na*medium);
k2:=6*alfa*SQR(energie)*lamst/(5*SQR(area)*SQR(plen)*planck*spl);
writeln('k2=',k2);
hx:=leng/n;
for j:=0 to n do
  begin
    pos[j]:=hx*j;
  end;
writeln('Enter to continue....');
readln;

{ Integrate Pump }

int_pp0:=0.0;
for i:= 1 to M-1 do
  begin
    int_pp0:=int_pp0+(treal[i+1]-treal[i])*pp0[i];
  end;
factor:=energie/int_pp0;
tot_pp0:=energie/plen;

```

```

writeln(f1,0,' ',energie,' ',tot_pp0,' ',plen*1e9);

{ Solve the four D.E. }

for i:=1 to M do
  begin
    ss0[i]:=seed/I_po;
  end;
for passes:=1 to NumPasses do
begin
clrscr;
gotoxy(1,1);writeln('Energie: ',energie);
pos[0]:=0.0;

for i:=1 to M do
  begin
    npomp^[i]:=pp0[i];
    stok^[i]:=ss0[i];
  end;
for i:=1 to M do
  begin
    gamma:=1-exp(-treal[i]*treal[i]/SQR(lag));
    for j:=1 to N do
      begin
        wz:=SQR(w0)*(1+SQR((pos[j]-leng/2)/ZZR));
        neta:=SQR(w12)/wz;
        npomp^[i]:=pump_oplos(npomp^[i],stok^[i],med^[j,1]);
        stok^[i]:=stok1_oplos(npomp^[i],stok^[i],med^[j,1]);
        med^[j,2]:=med_oplos(npomp^[i],stok^[i],med^[j,1]);
      end;
    for j:=1 to N do
      begin
        med^[j,1]:=med^[j,2];
      end;
    gotoxy(16,3);writeln(i,' ',passes);
    gotoxy(15,4);writeln(npomp^[i]);
    gotoxy(15,5);writeln(stok^[i]);
    gotoxy(15,7);writeln(med^[N,2]);
    pp[i]:=npomp^[i];
    ss1[i]:=stok^[i];
    mm[i]:=med^[N,2];
  end;

{ Integrate Stokes1 }

int_ss1:=0.0;
for i:=1 to M do
  begin
    int_ss1:=int_ss1+(treal[i+1]-treal[i])*ss1[i];
  end;
int_ss1:=factor*int_ss1;

```

```

halfwydte(ss1,treal,FWHM_ss1);
tot_ss1:=int_ss1/(FWHM_ss1);
writeln(f1,passes,' ',int_ss1,' ',tot_ss1,' ',FWHM_ss1);
for i:=1 to M do
  begin
    pp0[i]:=ref*pp[i];
    ss0[i]:=ref*ss1[i];
  end;
for j:=0 to N do
  begin
    med^[j,1]:=medium;
  end;
end;
dispose(npomp);
dispose(stok);
dispose(med);

assign(files,name2);
rewrite(files);
for i:=1 to m do
  begin
    writeln(files,treal[i],pp[i]);
  end;
close(files);
assign(files,name3);
rewrite(files);
for i:=1 to m do
  begin
    writeln(files,treal[i],ss1[i]);
  end;
close(files);
input_pulse(treal,pp0,ht,M);
{-----Plot Graphs-----}
InitSEGraphics('c:\tp7\bgi');
GetMaxCoords(maxX,maxY);
DefGraphWindow(0,0,maxX,maxy,1);
SetWin2PlotRatio(1, 0.2,0.14,0.05,0.14 );
SetCurrentWindow(1);
clearWindow;
SetLineStyleXX(0,0,3);
BorderCurrentWindow(15);
for i:=1 to m do
  begin
    x[i-1]:=treal[i];
    y[i-1]:=pp0[i];
  end;
AutoAxes(x,y,M,1);
LinePlotData(x, y, M,12,0);
SelectColor(3);
TitleWindow('RAMAN CONVERSION');
TitleXAxis('Time (ns)');
TitleYAxis('Normalised Output');

```

```
for i:=1 to m do y[i-1]:=pp[i];
LinePlotData(x, y, M, 14,0);
for i:=1 to m do y[i-1]:=ss1[i];
LinePlotData(x, y, M, 15,0);
str((int_ss1*1000):5:2,Enstr);
str((FWHM_ss1*1e9):5:2,tStr);
labelGraphWindow(250,850,'S0 Output: '+Enstr+' mJ in
'+tStr+'ns',0,0);
readln;
closeSegraphics;
close(f1);
end.
```

#### **4.A.2 WAVEGUIDE RAMAN CELL CODE**

This code is similar to the multipass Raman cell code in 4.A.1. The following changes are in the waveguide Raman conversion code:

- enhancements due to beam crossings and beam focusing are not included,
- it is a single pass system,
- the length  $L$  is now the waveguide length, and
- the area of the pump beam is the  $HE_{11}$  area and is a constant through the waveguide.

## ***LIST OF SYMBOLS: CHAPTER 4***

$a$	: waveguide radius
$A_i$	: transverse area of the pump beam on entering the Raman amplifier system
$A_{int}$	: area of a beam crossing (Figure 4.3)
$A_{tot}$	: total beam area (Figure 4.3)
$A(z)$	: beam area at any $z$ position along the propagation axis
$c$	: speed of light ( $c=3 \times 10^8$ m/s)
$E$	: energy of the pump pulse in joule (J)
$G$	: Raman gain coefficient
$h$	: Planck's constant ( $h=6.64 \times 10^{-34}$ J s)
$I_{Po}$	: initial or input pump power density ( $W/m^2$ )
$I_p$	: pump power density ( $W/m^2$ )
$I_s$	: Stokes power density ( $W/m^2$ )
$J$	: rotational level
$k$	: Boltzman's constant
$k_g$	: degeneracy of the ground state
$k_f$	: degeneracy of the final state
$K_p$	: normalised pump power density
$K_s$	: normalised Stokes power density
$l_c$	: coherence length (m)
$L$	: length of the multipass Raman cell or waveguide Raman cell
$L_{min}$	: minimum length of a waveguide Raman cell
$m$	: average number of crossings per pass
$M^2$	: laser beam quality parameter
$M_{\lambda_s}$	: Black-body radiation at the Stokes wavelength
$n$	: number of passes through the multipass Raman cell
$N_g$	: ground state molecular number density
$N_f$	: final state molecular number density
$N_p$	: pump photon number density
$N_s$	: Stokes photon number density
$N_0$	: total molecular number density ( $N_0 \approx N_g + N_f$ )
$N_{Po}$	: initial or input pump photon number density
$N_{So}$	: initial Stokes photon number density as a seed for the stimulated Raman conversion process

- $P_{so}$  : thermal noise Stokes seed (initial Stokes)
- $R$  : radius of curvature of the multipass Raman cell mirrors
- $R_m$  : reflection of Raman cell mirrors
- $t$  : time
- $T$  : temperature (K)
- $T_{PL}$  : pulse length of the input pump pulse
- $W(z)$  : actual beam radius at any  $z$  position along the propagation axis
- $W_0$  : actual waist of the injected laser beam in the Raman cell
- $W_{1,2}$  : actual beam radius on the concave Raman cell mirrors
- $z$  : position along the propagation axis
- $\alpha$  : small signal gain per molecule
- $\gamma$  : excitation lag term for the molecule polarization
- $\Gamma$  : excitation lag time ( $\Gamma = 1/\Delta\nu_R$ )
- $\delta$  : the ratio of the pump power to the Stokes output power
- $\delta_p$  : linear losses for the pump wavelength
- $\delta_s$  : linear losses for the Stokes wavelength
- $\Delta$  : normalised population difference
- $\Delta_0$  : initial normalised population difference
- $\Delta I_p$  : fractional increase in the pump intensity at beam crossings
- $\Delta N$  : population difference number density
- $\Delta N_0$  : initial population difference
- $\Delta\nu_R$  : Raman transition [S(0)] line width
- $\Delta\nu$  : pump ( $CO_2$ ) laser bandwidth (FWHM)
- $\eta(z)$  : gain enhancement owing to focusing characteristic of the Raman cell
- $\theta$  : the intersecting angle between two crossing beams in a multipass Raman cell
- $\kappa_1, \kappa_2$  : normalised Raman gain coefficients
- $\lambda_p$  : pump laser wavelength
- $\nu_p$  : pump photon frequency
- $\nu_s$  : Stokes photon frequency
- $\sigma$  : gain enhancement owing to the beam crossings in the Raman cell
- 10R18 : one of the stronger  $CO_2$  laser lines in the  $10 \mu m$  band for the R18 rotational transition:  $\Delta J = -1$  for R transitions, and  $\Delta J = +1$  for P transitions.  $J = 18$  is the initial rotational level

## ***5. LASER BEAM PROPAGATION***

### ***5.1 INTRODUCTION***

In Section 4.3.4 (Figure 4.10) it was shown that the theoretical model does not agree with the measured Raman threshold values for the cold 25 passes Raman cell. An investigation into these discrepancies showed that the beam quality has a key influence on the Raman cell performance. A detailed investigation of laser beam propagation is thus needed.

The popular view that a laser beam is a bundle of parallel rays that obey geometrical optics is an over simplification. In the case of Gaussian beams they obey a hyperbolic propagation law for a fundamental smallest beam radius  $\omega_0$  at a position  $z_0$ . For a simple Gaussian-like beam a further beam parameter is introduced - the  $M^2$  parameter [1,2]. In general at least ten beam parameters are needed to fully describe a general astigmatic beam [3]. The  $M^2$  parameter is a measure of the influence that the higher order modes, imbedded in the lowest order  $TEM_{00}$  laser mode, have on the propagation of a laser beam.

In this chapter the propagation of ideal Gaussian beams, simple stigmatic beams and simple astigmatic beams will be discussed. The propagation equations for free space and thin lenses will also be derived. These expressions are important for maximum amplifier extraction and Raman cell transmission.

### ***5.2 RESONATORS AND MODES***

To sustain laser oscillation an optical feedback must be provided. This is normally accomplished with an optical resonator consisting of a pair of spherical mirrors facing each other (see Figure 5.1)

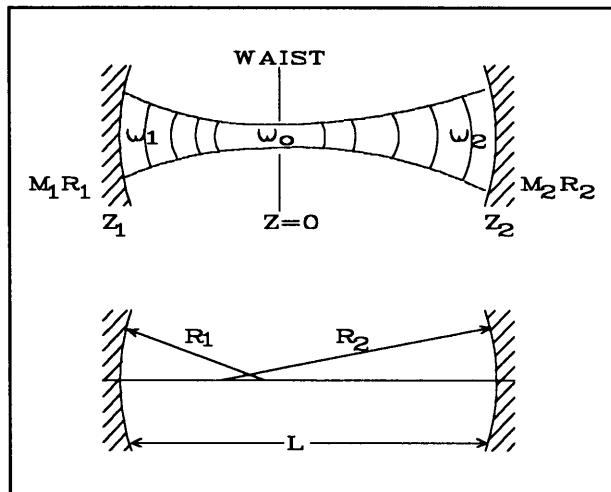
These structures can sustain oscillation of electromagnetic waves as well-defined axial resonance frequencies, which are referred to as axial modes. The amplitude or intensity variations, in the plane perpendicular to the propagation direction, are referred to as the transverse modes.



### 5.2.1 STABLE RESONATOR GEOMETRY

Figure 5.1 shows a cross-sectional view of an optical resonator. The mirror spacing is  $L$  and the radii of curvature of the mirrors is  $R_1$  and  $R_2$ . For stable resonators the energy is extracted by using a partially transmitting mirror. The resonator parameters for a resonator are defined as

$$g_1 = 1 - \frac{L}{R_1}, \quad g_2 = 1 - \frac{L}{R_2}, \quad (5.1)$$



with the radius of curvature  $R_i$  ( $i = 1, 2$ ) defined as positive if the mirror is concave with respect to the resonator interior and negative if the mirror is convex. In Figure 5.1 both  $R_1$  and  $R_2$  are positive. A resonator is defined as stable if  $0 < g_1 g_2 < 1$  is satisfied. A stability diagram using this inequality can be drawn and is shown in Figure 5.2 [4]. A resonator is stable if the  $g_1 g_2$  point falls within the shaded region.

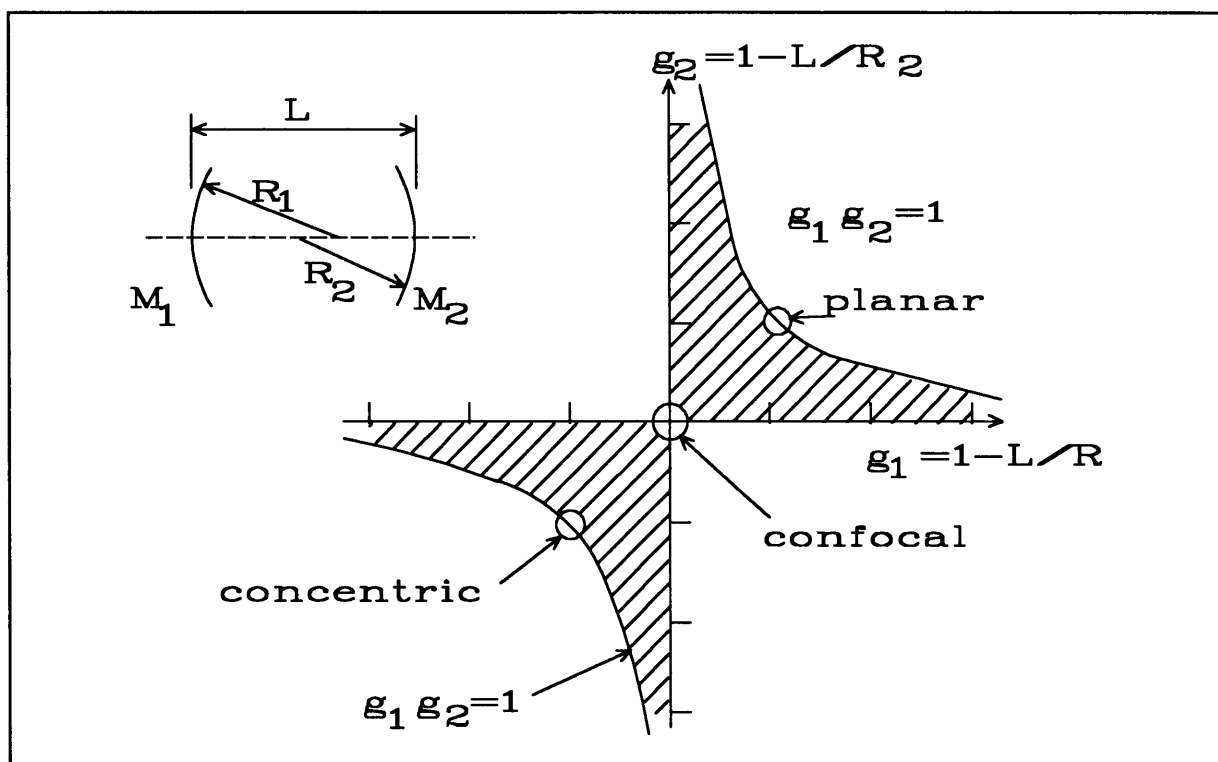
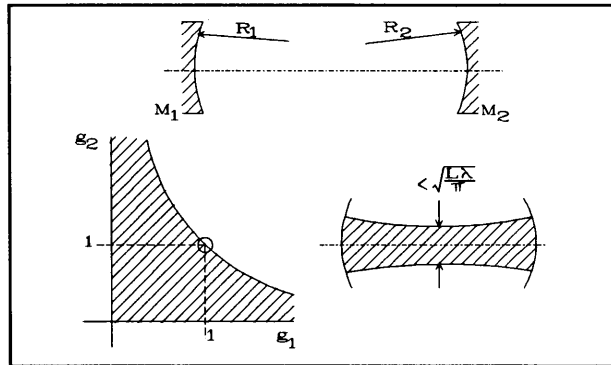


Figure 5.2 Stability diagram with the shaded areas defining the stable resonator regions [4,5]

From this diagram four resonator types can be distinguished.

**a. NEAR-PLANE PARALLEL RESONATORS ( $g_1g_2 \approx 1$ )**

This resonator has the largest mode volume but is relatively difficult to keep in alignment due to the fact that  $g_1g_2 \approx 1$  which implies a near unstable configuration. A further problem experienced with this resonator is its diffraction losses. Due to fairly high cavity losses and marginal stability, this resonator is difficult to use with a low-gain laser (see Figure 5.3).



**Figure 5.3** Near-plane parallel resonator ( $g_1g_2 \approx 1$ )

**b. SYMMETRIC CONFOCAL RESONATOR ( $g_1g_2 = 0$ )**

The spot sizes at the mirrors have the smallest value of any stable symmetric resonator. Since the diffraction losses depend on the ratio of the  $(1/e^2)$  beam radius  $\omega_{1,2}$  on the mirror to the mirror radius  $a$  ( $2a = \text{mirror diameter}$ ), these losses will be smaller than for any other stable resonator.

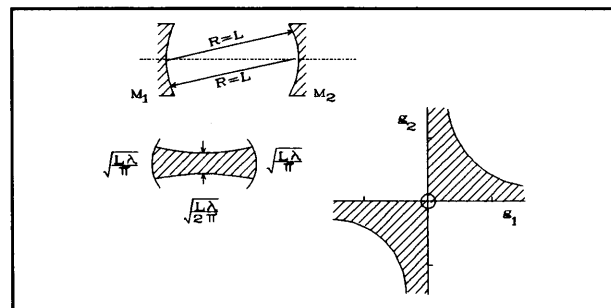


**Figure 5.4** Symmetric confocal resonator ( $g_1g_2 = 1$ )

**c. NEAR-CONCENTRIC RESONATOR ( $g_1g_2 \approx 1$ )**

This resonator type is on the symmetric laser diagonal and is basically an unstable resonator in the ideal concentric configuration. The minimum spot size possible with this resonator is much smaller than achieved with any other resonator type. For this resonator  $R_1 = R_2 \approx L/2$ . This resonator is exceptionally stable for  $R_1 = R_2 < L/2$  (see Figure 5.5).

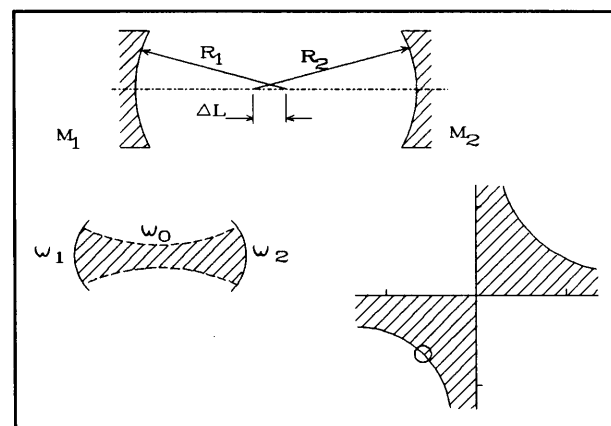


**Figure 5.5** Concentric resonator ( $g_1g_2 = 1$ ,  $g_1 = g_2 = -1$ )

**d. NEAR-HEMISPHERICAL RESONATOR ( $g_1g_2 \approx 1$ )**

This is the most widely used resonator for gas lasers and is relatively simple to align and to keep in alignment, if  $L$  is selected as slightly smaller than the radius of curvature of the mirror. This resonator can be a problem for a high-power laser as the smallest spot is situated on the flat ( $R \rightarrow \infty$ ) mirror (see Figure 5.6).

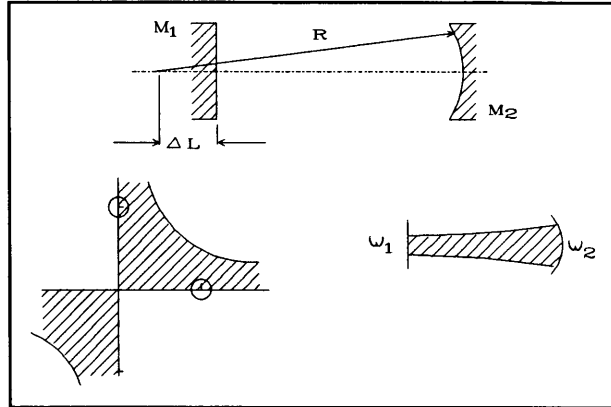


**Figure 5.6 Hemispherical resonator ( $g_1g_2 = 1$ )**

**5.2.2 TRANSVERSE MODES**

Solving Maxwell's equation in cartesian coordinates (rectangular geometry) the transverse field distribution of a  $TEM_{mn}$  mode is given by [6]

$$E_{n,m}(x,y) = E_0 H_m\left(\frac{\sqrt{2}x}{\omega(z)}\right) H_n\left(\frac{\sqrt{2}y}{\omega(z)}\right) e^{\left[-\frac{(x^2+y^2)}{\omega^2(z)}\right]}, \text{ where } H_n(x) = (-1)^n e^{x^2} \frac{d^n}{dx^n} e^{-x^2}$$

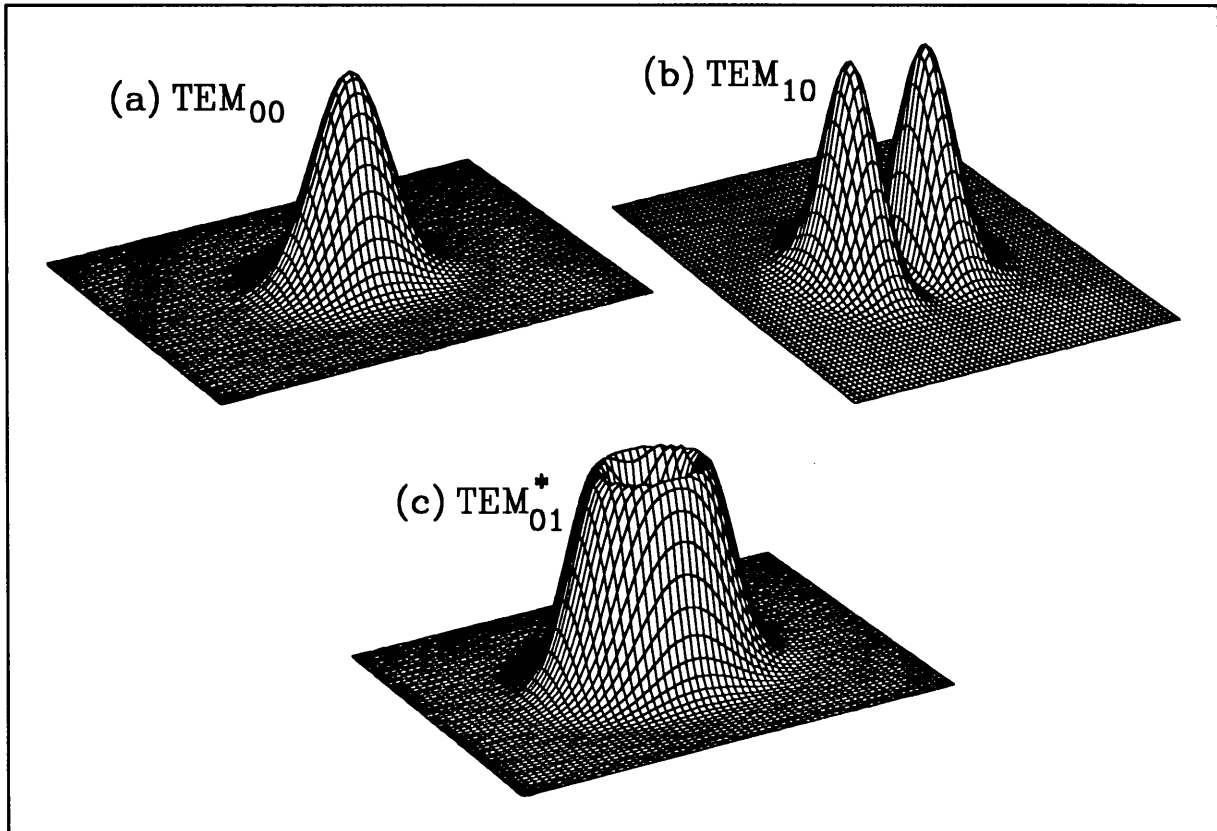


**Figure 5.7 Hermite-Gaussian modes: (a) and (b) are pure modes and (c) the doughnut mixed mode,  $TEM^*_{01}$**

which is the Hermite polynomial of order  $n$ . These modes are normally referred to as the Hermite-Gaussian modes. In practice these modes can be mixed which will, for example, result in the  $TEM_{01}^*$  mode that is a linear sum of the  $TEM_{10}$  and  $TEM_{01}$  modes and has a doughnut-like intensity distribution (see Figure 5.7). In cylindrical coordinates, the following solutions of Maxwell's equations (called Laguerre-Gaussian modes  $TEM_{p,l}^*$ ) exist:

$$E_{p,l}(r,\theta) = E_0 \left( \frac{\sqrt{2} r}{\omega(z)} \right)^l L_p^l \left( \frac{2r^2}{\omega^2(z)} \right) e^{\left[ -\frac{r^2}{\omega^2(z)} \right]} \begin{bmatrix} \sin l\theta \\ \cos l\theta \end{bmatrix}, \text{ where } L_p^l(x) = e^x \frac{x^{-l}}{p!} \frac{d^p}{dx^p} (e^{-x} x^{p+l}).$$

### 5.3 THE PARAXIAL WAVE EQUATION AND THE COMPLEX BEAM PARAMETER

For the purpose of beam propagation only stable laser modes will be considered. Laser beams produced by unstable resonators or light diffracted by hard and soft apertures will not be considered. The radiation generated by lasers normally appears as a beam whose transverse dimensions extent is large compared to the wavelength.

The propagation of beams in free space is given by the wave equation [7],

$$\nabla^2 E - \frac{1}{c^2} \frac{\partial^2 E}{\partial t^2} = 0, \quad (5.2)$$

where  $E$  is the scalar electric field and  $k=2\pi/\lambda$  the wave vector. There is an infinite number of possible solutions to this equation, depending on the boundary conditions that are imposed. Stable resonators require light to oscillate with minimal divergence along the axis connecting two (in general) spherical mirrors. Such a light beam can be described by a complex amplitude  $E$  that varies across the  $x$ - $y$  plane to account for the spatial variation of the irradiance and the deviations in phase corresponding to the non-planar wave fronts. Using the paraxial approximation<sup>[1]</sup> the spatial dependence of the electric field can be written as

$$E(x,y,z,t) = \epsilon(x,y) e^{-i\omega t + ikz}, \quad (5.3)$$

where  $\omega = kc$ .

---

<sup>[1]</sup> This approximation holds if the angular deviation from the propagation axis ( $z$ ) is small enough that the sine and tangent of the angle can be approximated by the angle itself or  $z \gg (x^2 + y^2)^{1/2}$  [5].

Substituting this relation in equation (5.2) and using the slowly varying envelope approximation  $\left| \frac{\partial^2 \epsilon}{\partial z^2} \right| \ll \left| 2k \frac{\partial \epsilon}{\partial z} \right|$  it gives

$$\frac{\partial^2 \epsilon}{\partial x^2} + \frac{\partial^2 \epsilon}{\partial z^2} - 2ik \frac{\partial \epsilon}{\partial z} = 0 . \quad (5.4)$$

Equation (5.4) is known as the paraxial wave equation and is still valid for light beams with half cone-angles up to 30° [4] from the propagation axis.

Using the boundary conditions:

- a. the waves resonating within the laser cavity must be spherical (to match the mirror curvature of reflection), and
- b. the lowest-order low-divergence mode is favoured,

The solution of equation (5.4) for the complex amplitude,  $\epsilon(x,y,z)$ , corresponds to a Gaussian beam of the form

$$\epsilon = e^{-i\left(\phi(z) + \frac{kr^2}{2q(z)}\right)} , \quad (5.5)$$

where  $r^2 = x^2 + y^2$ .  $\phi(z)$  and  $q(z)$  are determined by substituting equation (5.5) in equation (5.4). Thus

$$\frac{k(x^2+y^2)}{q^2(z)} + \frac{2i}{q(z)} + z \frac{\partial \phi(z)}{\partial z} - \frac{k(x^2+y^2)}{q^2(z)} \frac{\partial q(z)}{\partial z} = 0 , \quad (5.6)$$

which must be valid for any value of  $x$ . This requirement leads to two first-order differential equations,

$$\frac{\partial q(z)}{\partial z} = 1 , \quad \frac{\partial \phi(z)}{\partial z} = - \frac{i}{q(z)} \quad (5.7)$$

The  $z$ -dependence of the parameter  $q$  known as the complex beam parameter, is given by

$$q(z) = q_0 + (z-z_0) \quad (5.8)$$

In equation (5.5) the complex beam parameter was introduced as  $1/q(z)$ . Expand  $1/q(z)$  in real and imaginary parts as follows [8]:

$$\frac{1}{q(z)} = \frac{1}{R(z)} - \frac{i \lambda}{\pi \omega^2(z)} \quad (5.9)$$

where  $R(z)$  and  $\omega(z)$  are real parameters. Substituting equation (5.9) in equation (5.5),

$$\varepsilon = e^{-i\left(\phi(z) + \frac{kr^2}{2R(z)}\right)} e^{-\frac{r^2}{\omega^2(z)}} \quad (5.10)$$

Here the real exponential describes the Gaussian amplitude distribution, with  $\omega(z)$  the spot radius at  $1/e$  of the maximum field [ $1/e^2$  of the intensity] (see Figure 5.8). The (oscillatory) imaginary exponential (equation 5.10) has two terms in the exponent. These describe deviations in the phase from the ideal plane wave solution.

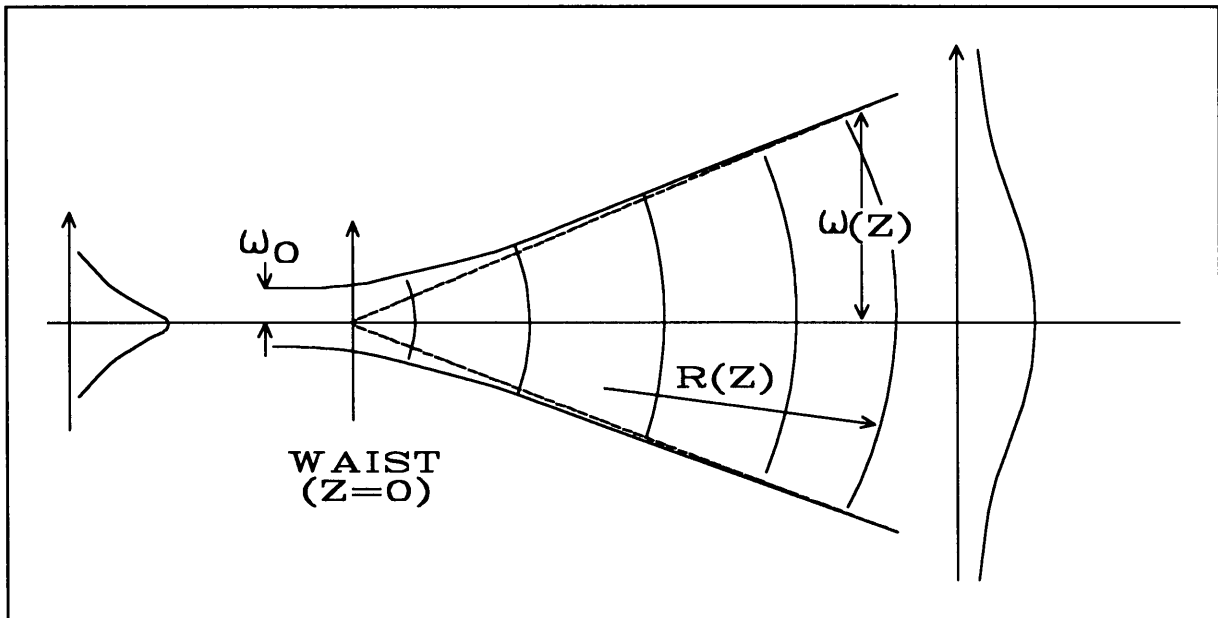


**Figure 5.8** Gaussian beam radius propagation

The second describes the transverse deviation which corresponds to a spherical wave front of radius  $R(z)$ , that shows the spherical wave nature of this solution. The other (longitudinal) phase term  $\phi(z)$  corresponds to a small on-axis phase-shift between this Gaussian beam solution and the infinite plane wave. At  $z = z_0$ , where the wave fronts are plane ( $R(z_0) = \infty$ ), equation (5.9) gives

$$q(0) = q_0 = \frac{i\pi\omega_0^2}{\lambda} \quad (5.11)$$

where  $\omega_0 = \omega(z_0)$  is the waist radius.

## 5.4 GAUSSIAN BEAM PROPAGATION

The lowest-order mode  $TEM_{00}$  has a Gaussian amplitude distribution, which means that the field amplitude varies in the  $xy$  plane as

$$E(z) = E_0 e^{-\frac{r^2}{\omega^2(z)}},$$

where  $r^2 = x^2 + y^2$ . Therefore the irradiance distribution will vary as

$$I(x,z) = |E(x,z)|^2 = I_0 e^{-\frac{2r^2}{\omega^2(z)}},$$

where the peak irradiance is related to the total power  $P$  in the beam by  $I_0 = 2P/(\pi\omega^2(z))$ .

As discussed in the previous section, there is always a position along the propagation path where the wave fronts become plane waves. This position is defined as the waist  $\omega_0$  of a beam at position  $z = z_0$ , with  $z$  measured from some arbitrary reference plane (see Figure 5.9). The propagation is given by a hyperbolic equation and can be written as [4,5,6,7]

$$\omega^2(z) = \omega_0^2 \left( 1 + \left( \frac{z - z_0}{z_R} \right)^2 \right), \quad (5.12)$$

where  $z_R = \pi\omega_0^2/\lambda$  is known as the Rayleigh range of the beam. At the Rayleigh range  $\omega^2(z_R) = 2\omega_0^2$ . At this propagation position the area of the laser beam doubles. The region  $-z_R$  to  $z_R$  shown in Figure 5.9 is known as the confocal parameter,  $b = 2z_R$ . In this region the beam is assumed to be collimated.

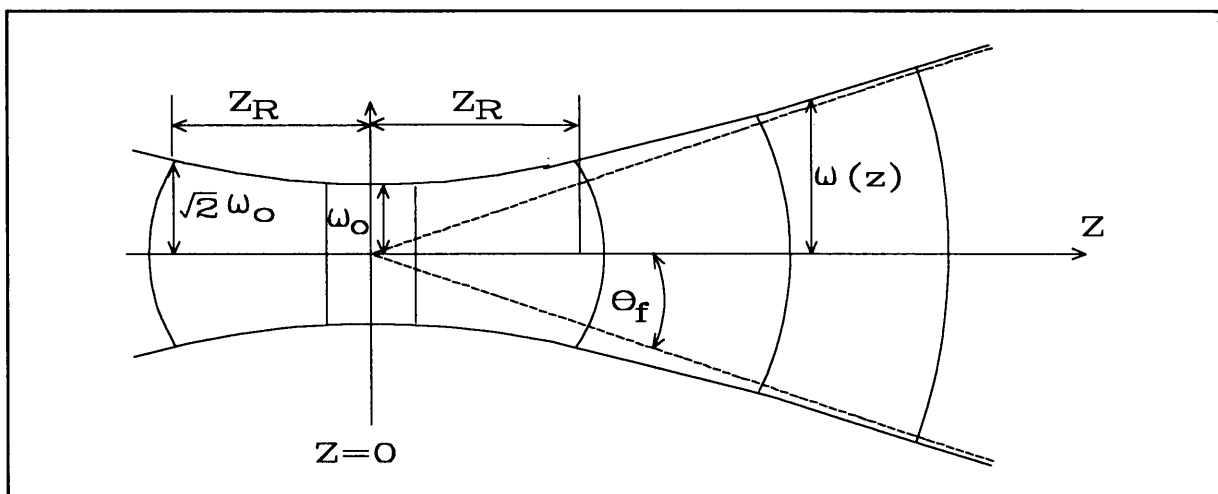


Figure 5.9 Gaussian propagation through free space

The change of the wave front radius along the propagation path can be written in terms of the Rayleigh range

$$R(z) = (z-z_0) \left( 1 + \left( \frac{z_R}{z-z_0} \right)^2 \right). \quad (5.13)$$

Three deductions can be made from this equation:

$$R(z) = \begin{cases} \infty & \text{for } |z-z_0| \ll z_R \\ 2z_R & \text{for } |z-z_0| = z_R \\ z-z_0 & \text{for } |z-z_0| \gg z_R \end{cases}.$$

For  $z \rightarrow z_0$  the radius of curvature  $R \rightarrow \infty$  which is consistent with the plane wave front at the waist position. For  $z-z_0 \gg z_R$  the radius of curvature  $R(z) \sim z-z_0$  corresponds to a spherical wave diverging from a point source at  $z = z_0$ . From this the far-field half angle can then be defined in the paraxial approximation as

$$\theta_f = \frac{\omega(z)}{z-z_0} = \frac{\lambda}{\pi \omega_0} \quad (z-z_0 \gg z_R). \quad (5.14)$$

## 5.5 GAUSSIAN BEAM PROPAGATION THROUGH A THIN-LENS SYSTEM

Consider a Gaussian beam propagating through an optical system consisting of a single thin lens (see Figure 5.10). The effect of a lens on the radius of curvature is to transform the complex curvature from  $R_1$  to  $R_2$  according to [4,7] (see Figure 5.11)

$$\frac{1}{R_2} = \frac{1}{R_1} - \frac{1}{f}, \quad (5.15)$$

where  $f$  is the focal length of the lens.

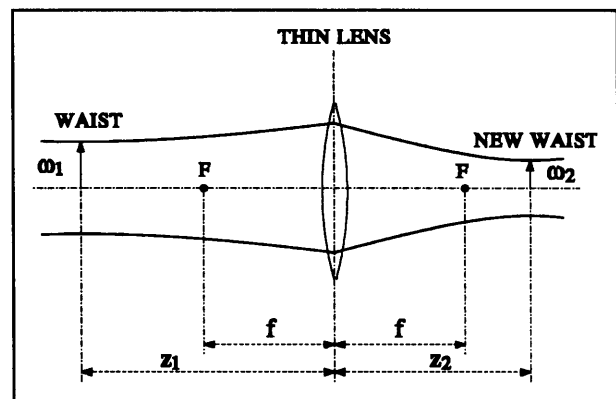


Figure 5.10 Gaussian beam propagation through a thin-lens system

An incoming beam with a specific transverse mode remains in this mode after passing through the lens system. The lens will change the beam parameters  $\omega(z)$  and  $R(z)$ . As shown in equation (5.15) and Figure 5.11 the incoming beam parameters are labelled as 1 and the corresponding outgoing parameters 2. The radius of curvature is taken to be positive if the



wave front is convex as viewed from  $z = \infty$ .

The transformation of the complex phase front  $q$  is exactly the same as described by equation (5.15). As  $\omega_1 = \omega_2$  immediately before and after the lens, the transformed  $q$ -parameter is given by

$$\frac{1}{q_2} = \frac{1}{q_1} - \frac{1}{f},$$

where the  $q$ 's are the phase fronts before and after the lens. Using the ABCD-law [4,5,9,10]

$$q_2 = \frac{Aq_1 + B}{Cq_1 + D},$$

where A,B,C and D are the matrix elements of the transfer matrix for the optical system.

Using the variables as defined in Figure 5.12,  $q_2$  can be written as (see Appendix 5.A)

$$q_2 = \frac{\left(1 - \frac{z_2}{f}\right)q_1 + z_1 + z_2 - \frac{z_1 z_2}{f}}{-\frac{q_1}{f} + \left(1 + \frac{z_1}{f}\right)}. \quad (5.16)$$

The radius of curvature of a spherical wave  $R$  follows this law and the transformed radius can also be given by equation (5.16) replacing the complex curvature  $q$  by the curvature  $R$ . The procedure described in Appendix 5.A can be used for more complicated optical structures.

Using the parameters shown in Figure 5.12 the size and location of the transformed beam waist can be written as [6]

$$\frac{1}{\omega_2^2} = \frac{1}{\omega_1^2} \left(1 - \frac{z_1}{f}\right)^2 + \frac{1}{f^2} \left(\frac{\pi \omega_1}{\lambda}\right)^2 \quad (5.17)$$

and

$$z_2 = f + \frac{(z_1 - f)f^2}{(z_1 - f)^2 + \left(\frac{\pi \omega_1^2}{\lambda}\right)^2}. \quad (5.18)$$

A useful approximation arises from equation (5.17) if  $z_1 \gg f$ . In this case

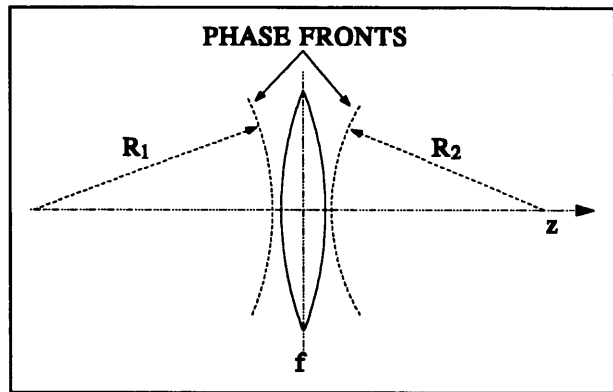


Figure 5.11 Thin-lens transformation for a spherical beam [4]

$$\omega_2 = f \left( \frac{\lambda}{\pi \omega_1} \right) = f \theta_f, \quad (5.19)$$

where  $\theta_f = \lambda / \pi \omega_1$  is the far-field half angle divergence of the incident laser beam.

## 5.6 MODE MATCHING OF GAUSSIAN BEAMS

In many practical cases a laser beam travels over extensive distances, and usually the beam has to travel through finite apertures. This is the case for a CO<sub>2</sub> laser chain with the oscillator generating a near Gaussian beam that is subsequently amplified by a number of amplifiers. To optimise the propagation through the chain the Gaussian beam must be matched to the prescribed geometrical limitations in terms of apertures, the length of the apertures (for example the electrode structure) and the distances between amplifier systems. Furthermore, these beams are often injected into another optical system with its own set of beam parameters. These systems are multireflection cells (Raman amplifiers) or waveguides.

The transformation of a beam with one set of beam parameters  $\omega_1$  and  $z_1$  to a prescribed set of parameters  $\omega_2$  and  $z_2$  is normally accomplished using a thin lens. More elaborate optical systems can also be used. For this discussion only thin-lens mode matching will be considered (see

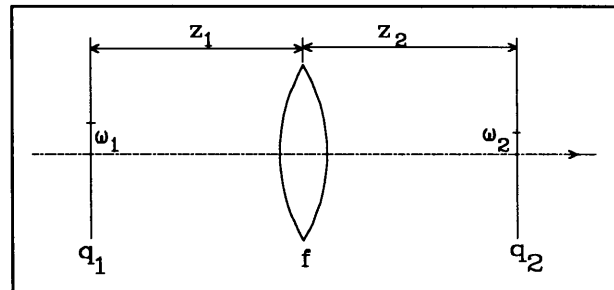


**Figure 5.12** Gaussian beam mode matching

Figure 5.12). This mode-matching analysis is adopted from Kogelnik and Li [9]. The size and location of the waists of both the incident and transformed beams are known or can be computed by using equations (5.17) and (5.18). In order to match a beam to a set of prescribed parameters a suitable lens of focal length  $f > f_0$  is used. The variable  $f_0$  is the minimum focal length needed for the transformation and is defined by the parameters of the two beams. With known lens focal length and beam waists, the distances between the two waists have to be calculated according to the procedure and equations described below.

The two beam waists are assumed to be located at positions  $z_1$  and  $z_2$  from the lens respectively. The complex beam parameters at the waists are then given by equation (5.11) as

where  $\omega_1$  and  $\omega_2$  are the beam radii of the beams at the waist positions  $z_1$  and  $z_2$ . By

$$q_1 = \frac{i\pi\omega_1^2}{\lambda}, \quad q_2 = \frac{i\pi\omega_2^2}{\lambda} \quad (5.20)$$

substituting equation (5.20) in equation (5.16) the real and imaginary parts of this equation give[9],

$$(z_1 - f)(z_2 - f) = f^2 - f_0^2, \quad \frac{z_1 - f}{z_2 - f} = \frac{\omega_1^2}{\omega_2^2} \quad (5.21)$$

$$\text{with } f_0 = \frac{\pi\omega_1\omega_2}{\lambda}.$$

It is then obvious that the minimum focal length  $f_0$  is defined by the waist sizes of the matching beams. Any lens with a focal length  $f > f_0$  can therefore be used for the mode-matching transformation. Once a focal length  $f$  is chosen the distances  $z_1$  and  $z_2$  have to be adjusted to satisfy the matching conditions in equation (5.21) rewritten as [4]

$$z_1 = f \pm \frac{\omega_1}{\omega_2} \sqrt{f^2 - f_0^2}, \quad z_2 = f \pm \frac{\omega_2}{\omega_1} \sqrt{f^2 - f_0^2}. \quad (5.22)$$

Either the plus or the minus signs can be used (never combine the signs). These two equations are of extreme importance for the transportation of a beam through a master oscillator power amplifier chain and injecting the beam into a Raman cell or a waveguide for maximum transmission.

## ***5.7 BEAM PARAMETERS OF NON-IDEAL LASER BEAMS***

In practice all laser beams are non-ideal as no Gaussian beams exist. In this section the relationship between pure Gaussian beams and actual beams will be discussed. The aim is to use all the Gaussian beam propagation equations (that were discussed in the previous sections) to describe the propagation of actual beams as this theory is well understood. In this section a quality factor is introduced that is the measure of the beam as a function of pure Gaussian properties.

Consider a monochromatic beam propagating within the paraxial approximation. In general this beam is non-Gaussian, non-spherical, non-collimated, nor is it diffraction-limited. This means that the wave front can be curved or wrinkled and the amplitude profile of the beam of light can be complicated and irregular. The aim is then to extract an average radius of

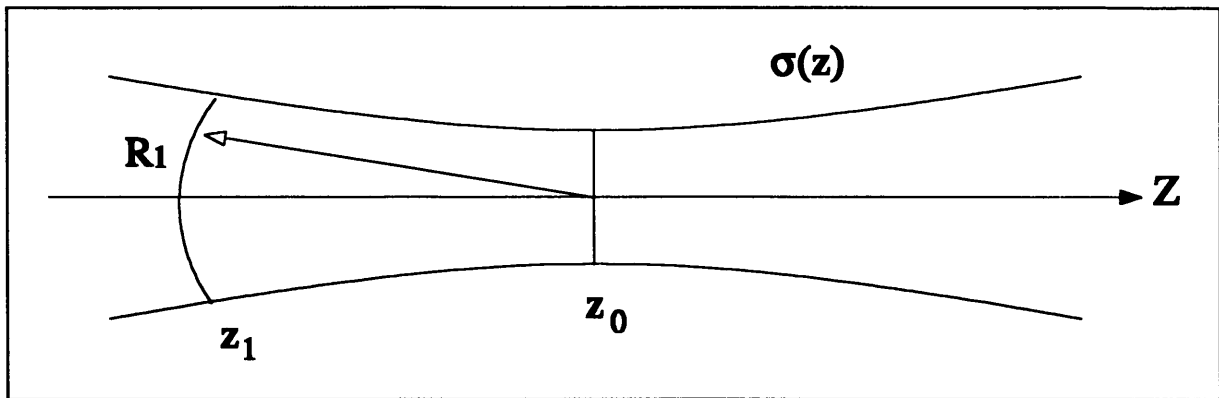


**Figure 5.13** The propagation of an arbitrary wave front from  $z = z_1$  towards a waist at  $z = z_0$  [11]

curvature  $R(z)$  for such a beam at a position  $z$  along the propagation axis (see Figure 5.13).

Let  $E(x, z)$  be the complex amplitude profile and  $P(s, z)$  the related complex amplitude in the spatial frequency domain. The expressions for  $E(x, z)$  and  $P(s, z)$  can be written as a Fourier transform pair given by [11, 12]

$$E(x, z) = \int_{-\infty}^{\infty} P(s, z) e^{-i2\pi s x} ds \quad \text{and} \quad P(s, z) = \int_{-\infty}^{\infty} E(x, z) e^{i2\pi s x} dx.$$

The spatial frequency variable  $s$  is related to the angular direction  $\theta$  of a corresponding plane wave component of the beam by  $s = \frac{\sin\theta}{\lambda} \approx \frac{\theta}{\lambda}$  in the paraxial approximation.

Defining the beam variances in  $x, s$  as [12, 13, 14]

$$\sigma_x^2(z) = \frac{1}{P_x} \int_{-\infty}^{\infty} (x - x_c)^2 |E(x, z)|^2 dx \quad (5.23)$$

and

$$\sigma_s^2(z) = \frac{1}{P_s} \int_{-\infty}^{\infty} (s - s_c)^2 |P(s, z)|^2 ds \quad (5.24)$$

with  $P_x = \int_{-\infty}^{\infty} |E(x, z)|^2 dx$ ,  $P_s = \int_{-\infty}^{\infty} |P(s, z)|^2 ds$ , and the means of  $E(x, z)$  and  $P(s, z)$  are

$$x_c = \frac{1}{P_x} \int_{-\infty}^{\infty} x |E(x, z)|^2 dx \quad \text{and} \quad s_c = \frac{1}{P_s} \int_{-\infty}^{\infty} s |P(s, z)|^2 ds \quad \text{respectively.}$$

It can be shown that [11, 12, 16]

$$\sigma_{x0} \sigma_s \geq \frac{1}{4\pi} \quad (5.25)$$

where  $\sigma_{x0}$  is the minimum beam variance and is related to the real beam waist  $W_0$  by [15]

$$W_0 = 2 \sigma_{x0}.$$

For an ideal Gaussian (TEM<sub>00</sub>) beam, the inequality changes to

$$\sigma_{x0}^g \sigma_s^g = \frac{1}{4\pi}. \quad (5.26)$$

Using equations (5.25) and (5.26) a beam propagation factor can now be defined as [11,16]

$$M^2 = \frac{\sigma_{x0} \sigma_s}{\sigma_{x0}^g \sigma_s^g} = 4\pi \sigma_{x0} \sigma_s \geq 1. \quad (5.27)$$

Using equation (5.27) the generalised Rayleigh range of a non-ideal laser beam can be written as [11,17]

$$Z_R = \frac{\sigma_{x0}}{\lambda \sigma_s} = \frac{\pi}{2} \left( \frac{2 \sigma_{x0}}{M} \right)^2 = \frac{\pi W_0^2}{\lambda M^2} \quad (5.28)$$

where  $W_0$  is the actual beam waist.

The propagation of the spatial variance along the optical axis is given by [11,12,16,17,18],

$$\sigma_x^2(z) = \sigma_{x0}^2 \left( 1 + \frac{\lambda^2 \sigma_s^2}{\sigma_{x0}^2} (z - z_0)^2 \right). \quad (5.29)$$

Using the relationship for the Rayleigh range in equation (5.28) and  $W(z) = 2\sigma_x(z)$ , the propagation equation can be rewritten as

$$W^2(z) = W_0^2 \left( 1 + \left( \frac{z - z_0}{Z_R} \right)^2 \right). \quad (5.30)$$

Comparing equation (5.30) and equation (5.12) it is clear that a non-ideal beam propagates exactly as an ideal Gaussian beam, with the exception that the beam radius  $W(z)$  is the real beam radius is now the actual beam radius defined as  $W(z) = 2\sigma_x(z)$  and the new Rayleigh range is given by equation (5.28). Using the non-ideal beam Rayleigh range an effective radius of curvature can be defined as

$$R(z) = (z - z_0) \left( 1 + \left( \frac{Z_R}{z - z_0} \right)^2 \right). \quad (5.31)$$

The  $M^2$  factor can thus be seen as a modification of the wavelength  $\lambda$  to a wavelength

$\lambda' = M^2\lambda$ . All the equations derived for Gaussian beams are applicable if this modified wavelength and actual beam sizes are used.

## 5.8 BEAM PARAMETER MEASUREMENTS

The usefulness of the propagation law [equations (5.29) or (5.30)] as a way of extracting the beam parameters is quite obvious [19]. From the measured beam radii  $W^{(i)}$ , at positions  $z^{(i)}$  along the propagation axis, estimations for  $z_0$ ,  $W_0$  and  $M^2$  can be extracted (see Figure 5.14).

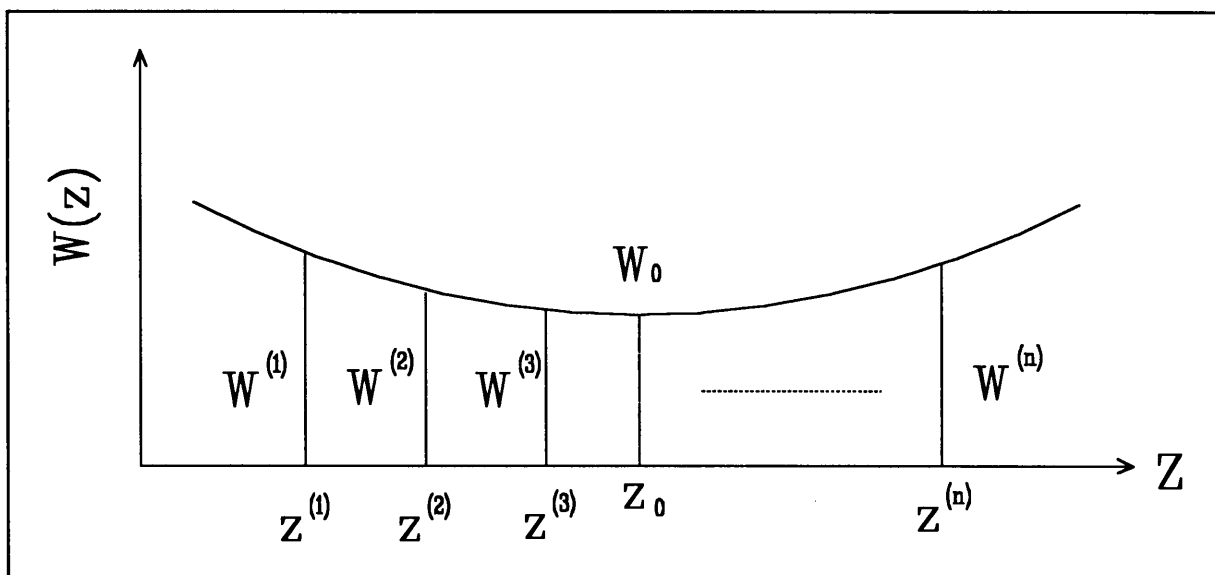


Figure 5.14 Measured radii  $W^{(i)}$  at different positions  $z^{(i)}$  along the propagation path

A minimum of three measurements is needed, with one in the far field and the remaining measurements around the beam focus. In practice it was found that at least 12 to 16 beam measurements along the propagation path are needed to obtain accurate estimations for  $z_0$ ,  $W_0$  and  $M^2$ . A second-order least-squares fit was used to estimate the parameters in the propagation equations (5.29) and (5.30) (see Appendix 5.B).

A second method described by the International Standardization Organization (ISO) [20] requires a laser beam being passed through an on-axis focusing lens. By taking 5 beam-width measurements along the beam path (Figure 5.15) the beam parameters can be calculated.

The measurement procedure is as follows:

- one beam width measurement at the lens focal plane (to determine the laser divergence

directly - equation (5.32)),

- three other beam width measurements in the vicinity of the minimum beam diameter,
- the fifth beam width measurement is used to verify the calculations,
- distances from the lens for each width measurement are also needed and lastly
- the positions 1 and 2 (Figure 5.15) should be selected where  $D(1)=D(2)$ .

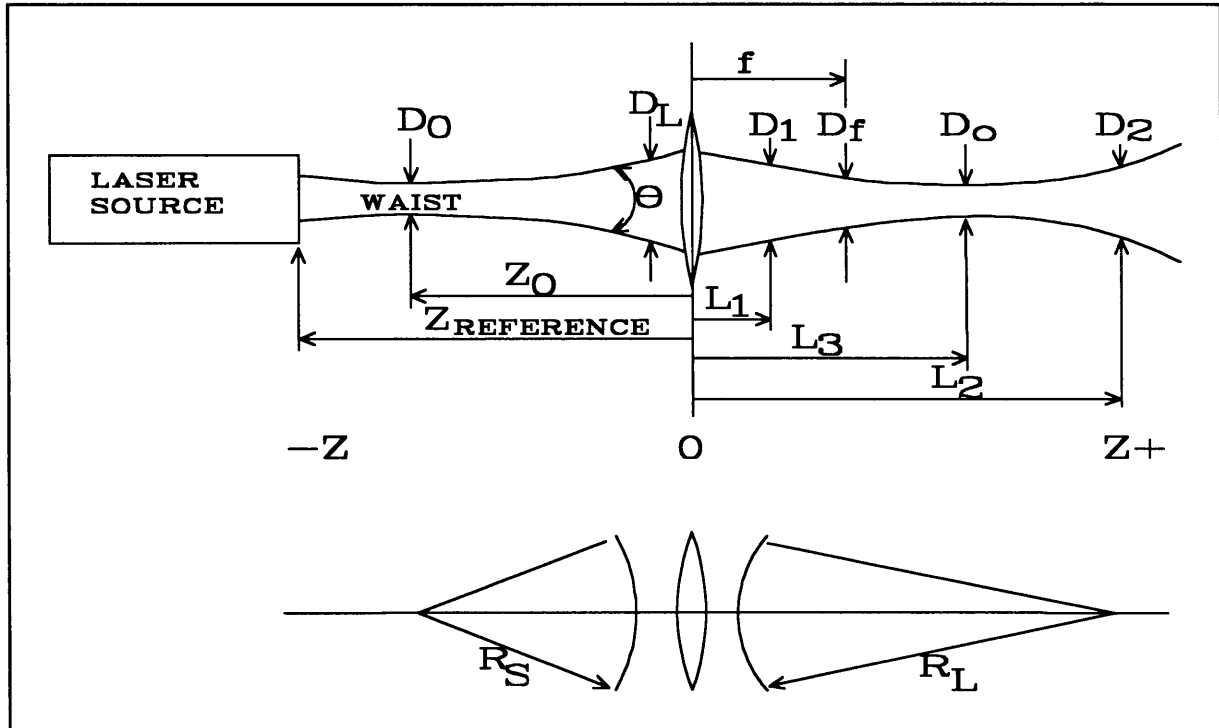


**Figure 5.15** Experimental setup used for the ISO standard [20]

The last requirement can have an effect on the measuring time. Searching for the positions 1 and 2 for which  $D(1)=D(2)$  will probably be an iterative process as they are on either side of the focus position. For CW laser characterization it is possible to identify this position using real-time CCD cameras which allow easy and quick measurements. For most high-power  $\text{CO}_2$  systems, pulsed or CW, useful two-dimensional devices are extremely expensive and difficult to obtain. This forces the user to use scanning methods (see Section 5.9) for the measurement of beam widths. The latter is an useful technique for a quick and accurate estimation of the beam parameters.

Once the data have been gathered the divergence (half angle) can be calculated from

$$\theta = \frac{D_f}{2f} \tag{5.32}$$

The divergence is thus found by measuring the beam width at the geometrical focal distance from the lens and dividing it by the geometrical focal length of the lens. This is true for all laser modes and an useful way of checking the propagation law method. The beam quality propagation parameter is given by

$$M^2 = \frac{\pi D_{0L}^2}{2\lambda(L_2-L_1)} \left( \frac{D_1^2}{D_{0L}^2} - 1 \right)^{1/2}.$$

Eleven algebraic steps are needed for the calculation of  $W_0$  ( $D_0 = 2W_0$ ),  $z_0$  and  $M^2$ . If the beam is non-circular the major and minor symmetric axis must be located and two sets of measurements have to be made with the same calculations for the two axes. The procedure and equations are copies from the ISO publication [20]. The calculations are:

- Distance from  $D_{0L}$  to lens

$$L_3 = \frac{(L_2-L_1)}{2} + 1$$

- Beam width at the lens

$$D_L = D_{0L} \sqrt{1 + \left( \frac{4\lambda M^2 L_3}{\pi D_{0L}^2} \right)^2} \quad (5.33)$$

- Radius of curvature on the measurement side of the lens

$$R_L = L_3 \left( 1 + \left( \frac{\pi D_{0L}^2}{4\lambda M^2 L_3} \right)^2 \right)$$

- Radius of curvature on the source side of the lens

$$\frac{1}{R_s} = \frac{1}{f} - \frac{1}{R_L}$$

- Calculation of laser beam width minimum

$$D_0 = 2W_0 = D_L \left( 1 + \left( \frac{\pi D_L^2}{4\lambda M^2 R_s} \right)^2 \right)^{-1/2}$$

- Calculation of minimum beam width (waist) location

$$z_0 = R_s \left( 1 + \left( \frac{4\lambda M^2 R_s}{\pi D_L^2} \right)^2 \right)^{-1/2}$$



- Confirming the calculation: calculate  $D_L$  at lens using the numbers for  $D_0$ ,  $z_0$

$$D_L(\text{check}) = D_0 \sqrt{1 + \left( \frac{4 \lambda M^2 z_0}{\pi D_0^2} \right)^2} \quad (5.34)$$

- Compare  $D_L$ , calculated in equation (5.33), with the value above in equation (5.34).  
These values should agree exactly!

## 5.9 BEAM-WIDTH MEASUREMENT METHODS

In this section procedures will be described for the measurement of beam widths using four different techniques: scanning slit, scanning knife edge, variable aperture and two dimensional scanning pinhole or two dimensional detectors. Here we assume that the irradiance profile has a best-fit Gaussian profile given by

$$I(x,y) = I_0 e^{\left( -2 \frac{(x^2+y^2)}{W^2} \right)}$$

where  $I_0 = P/\pi W^2$ , and P the total power of the beam. The radius W is the  $1/e^2$  radius at which  $I(x,y)$  falls to  $1/e^2$  of  $I_0$ .

A fifth technique is a one dimensional scanning pinhole, but it is not an approved ISO method and will not be discussed. An accurate location of the centre of the profile is required, which makes this technique prone to large location errors resulting in diameter errors.

### 5.9.1 SCANNING SLIT METHOD

It can be shown (see Appendix 5.C) that for sufficiently small slit widths,  $d$ , a scanned profile (Figure 5.16) will reproduce the original irradiance profile within acceptable errors of less than 1%. The ISO standard [20] for the maximum slit width is  $d/D < 1/20$  - measuring error less than 0.17 %.

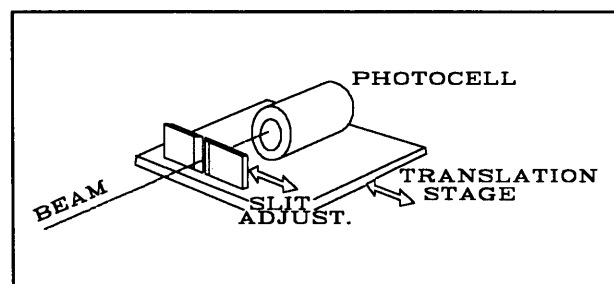
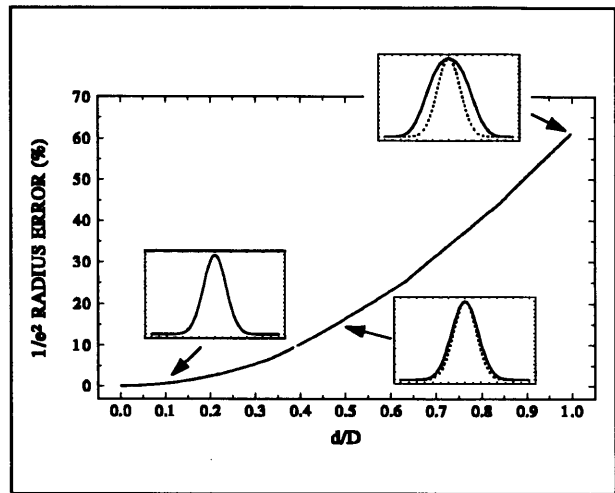


Figure 5.16 Scanning slit method [20]

The  $1/e^2$  radius error as a function of slit width and beam size is given by (Appendix 5.C and [22]):

$$\Delta W = \frac{2}{3} \left( \frac{d}{D} \right)^2$$

where  $d$  is the slit width and  $D=2W$ , the beam diameter. Figure 5.17 shows the measurement error as a function of slit width  $d$  normalised with the beam diameter  $D = 2W$ . Evidently, significant errors can occur at slit widths of the order of the beam radius.



**Figure 5.17** The  $1/e^2$  radius error as a function of slit width ( $d/D$ )

### 5.9.2 SCANNING KNIFE EDGE

A simple and widely used measurement technique is the knife-edge method. This method consists of an opaque knife-edge scanning transversely across a beam profile (see Figure 5.18). The signal obtained by this method is in fact the integrated intensity profile in the  $x$  and  $y$  axis given in equation (5.35). Using the integrated information the beam diameter can be calculated for conveniently specified clip levels (see Appendix 5.D). The clip level width  $D_c$  for the beam in either direction is defined as the width between points in the beam where the transmitted intensity passing the knife-edge rises from a low clip level  $\epsilon P_0$  to an upper clip level  $(1-\epsilon)P_0$  where  $P_0$  is the total power/energy in the beam. It can be shown for a Gaussian-like intensity profile that (Appendix 5.D)

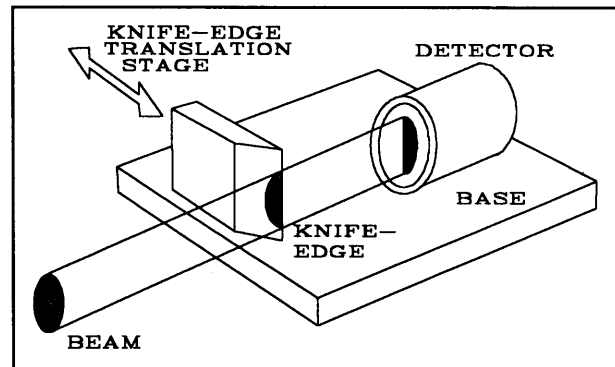


**Figure 5.18** Scanning knife-edge method

$$(1-2\epsilon) = \operatorname{erf} \left( \frac{D_c}{\sqrt{2}W} \right) \tag{5.35}$$

where  $W$  is the real beam radius. The clip levels 10% and 90% are convenient and thus most commonly used -  $2W = 1.561D_c$ . Using clip levels 2.3% and 97.7% the beam radius is measured directly. It is clear that for these clip levels no scale factor is needed. The 10%-

90% levels produce better results as the intensity variations are more manageable. This implies smaller measuring errors. Siegman *et al.* [23] describe a number of other types of beams that can be measured using this method with all the related clip level relationships given. For the purpose of this work, only Gaussian-like beams are of interest and the other clip level relationships will not be discussed.

It is then clear that the user should know something of the beam shape in order to use this method. Furthermore, care should be taken that the total power of the beam is measured. Using this method with a pulsed CO<sub>2</sub> laser can be problematic, as the pulse-to-pulse variations of 10% are well within laser output specifications. In order to obtain reasonable results averages should be taken, which may be time consuming.

### 5.9.3 VARIABLE-APERTURE METHOD

This method uses the ratio of power enclosed in a radius  $r_c$  to the total beam power for calculating the  $1/e^2$  beam radius (see Figure 5.19). Using a scaling factor, the real beam radius can be calculated. The power content for an aperture of radius  $r_c$  is given by (see Appendix 5.E):

$$\epsilon = 1 - e^{-\frac{2r_c^2}{w^2}}$$

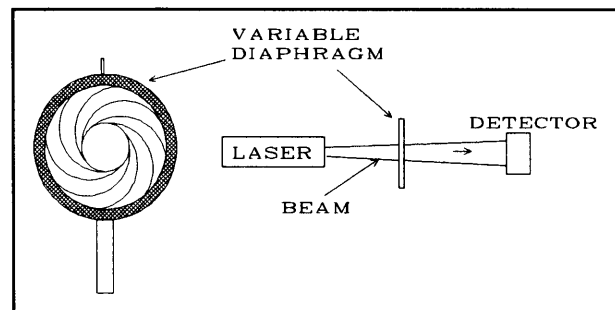


Figure 5.19 Variable-aperture method

From a power content value  $\epsilon = 0.865$  the beam radius is measured directly. The following criteria have to be satisfied:

- The beam must be circular within 1.15:1 [20].
- The variable aperture must be aligned relative to the beam centre to within 10 % of the beam diameter.

These criteria limit the usefulness of the method to such an extent that it is not supported by the ISO as a way of measuring general laser beams. This, however, does not imply that this method is useless. It is accurate for symmetric Gaussian-like beams, which are exactly the type of beams needed for maximum transmission through a Raman amplifier.

### 5.9.4 BEAM-WIDTH MEASUREMENT USING THE BEAM VARIANCES THEORY ( $W=2\sigma_x$ )

This is by far the most accurate method and in many cases free from large errors. There is one exception. The second moment [18]

$$\sigma_x^2 = \frac{\int_{-\infty}^{\infty} (x-x_c)^2 I(x) dx}{\int_{-\infty}^{\infty} I(x) dx} \quad (5.36)$$

for hard diffracted beams has an infinite moment but this lacks physical meaning. The definition (equation (5.36)) of the second moment clearly shows a large weighted contribution due to the energy in the side lobes away for the centroid  $x_c$  of the beam. These parts of the beam are not useful and have no real use in practice. It was shown by Loosen *et al.* [21] that a (software) Gaussian window function (see Figure 5.20) can be used to suppress the effect of the power in the side lobes of the diffracted beam. From this figure it is clear that the error introduced by this window function is less than 1% for a window function with a  $1/e^2$  radius of about four times that of the 86% power content radius of the measured beam. Using a window function Loosen *et al.* [21] showed that the output of an unstable resonator follows the propagation law (equation (5.29)).

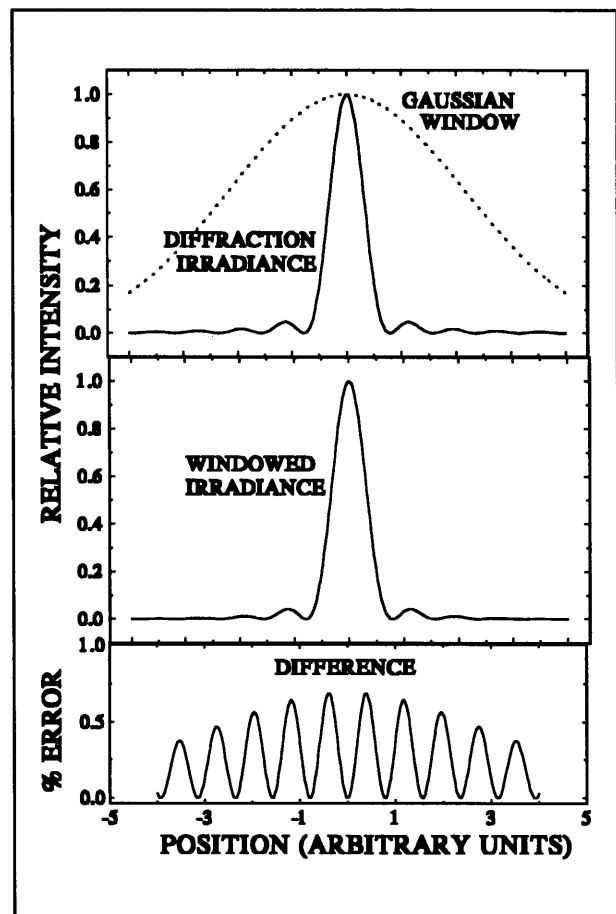


Figure 5.20 Simulated diffraction intensity distribution vs the Gaussian-windowed diffraction intensity

From equation (5.36) it is evident that one needs the actual intensity distribution of the beam. For a symmetrical beam a slit scan, following the real profile in one dimension, can be used. However, for a more general beam the full two-dimensional intensity distribution has to be obtained. The following two techniques are usually followed:

### 5.9.4.1 SCANNING PINHOLE DEVICES

The principle of this method is shown in Figure 5.21. Two ways of scanning the beam are: (a) scan the detector across the stationary intensity distribution and (b) scan the beam across the stationary detector system. In most cases option (a) is preferred as it limits the aberration introduced due to possible non-perfect optical elements. This scanning method is most often used in the industry for high-power CW laser beams.

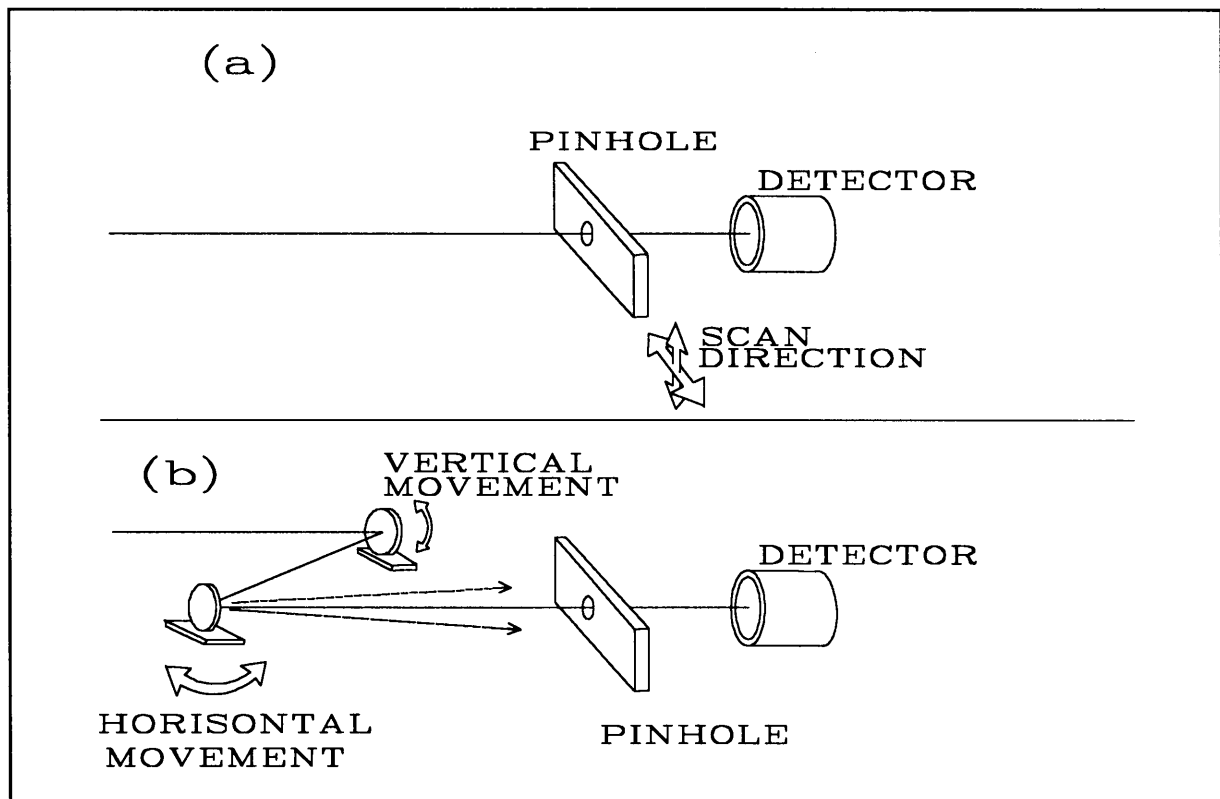


Figure 5.21 Layout of pinhole devices (a) scanning pinhole or (b) the scanning beam

### 5.9.4.2 SINGLE-SHOT DEVICES

Here Si-CCD's and pyro-electric vidicon detectors are used. These detectors are widely used in the visible and the near-infrared. There are discrete-element pyro-electric detectors available on the market but they are expensive. With the aid of these devices intensity variations of a pulsed laser beam can be analyzed in a single shot. From this data a number of methods can be employed to obtain the beam radius. They are:

- a software knife edge
- a software variable aperture, and
- the ISO-approved moment calculation (equation (5.36)).

## 5.10 RAMAN THRESHOLD IN COLD PARA-HYDROGEN FOR NON-IDEAL GAUSSIAN BEAMS

In Chapter 4 (Section 4.3.4) the Raman threshold for a 25 passes multipass Raman cell was calculated. It was shown (Figure 4.10) that the measured threshold pump intensity is considerably larger than the calculated threshold for an ideal Gaussian pump beam. The assumption that the input beam is an ideal Gaussian beam is thus an over-simplification. In this section the threshold power as a function of  $M^2$  is calculated for a cold 25 passes Raman amplifier.

The non-dimensional gain  $\kappa_1$  (Section 4.2) is inversely proportional to  $A_i$ , the initial beam area and  $A_i$  is directly proportional to  $M^2$  (Section 4.2). Clearly a much smaller power density is achieved with a  $M^2 > 1$ . It was also shown that the gain enhancement  $\eta(z)$  is independent of the beam quality factor (equation (4.15)). Thus for  $M^2 > 1$  the initial area  $A_i$  implies a smaller power density. The required power for achieving Raman threshold is then proportional to  $M^2$  for the same Raman cell parameters.

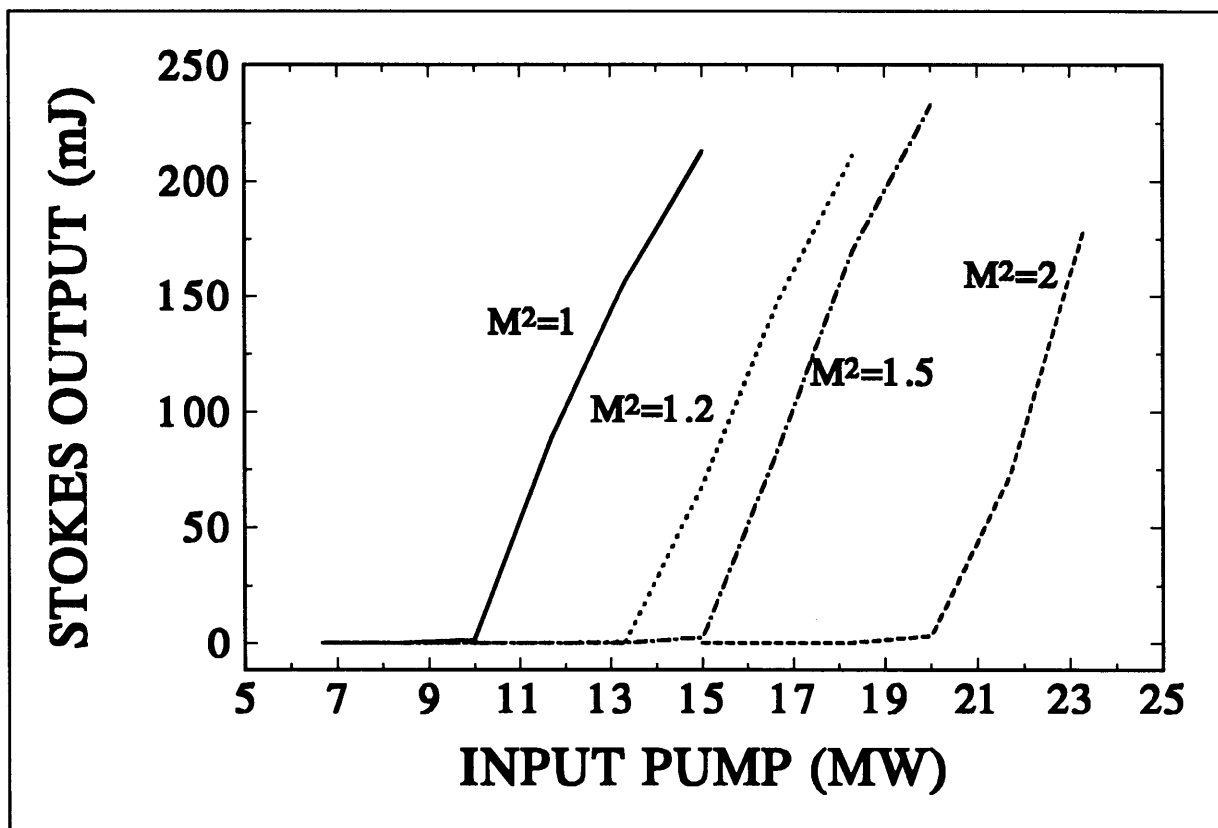


Figure 5.22 Stokes output calculations as a function of  $M^2$  for a 25 passes cold multipass Raman cell

Figure 5.22 shows the Stokes output calculations for a few  $M^2$  input values. From beam quality measurements (Section 5.11) it is shown that  $1.1 < M^2 < 1.5$  owing to aberrations introduced to the beam by propagation through finite apertures, imperfect transmission and reflection optics.

Figure 5.22 shows that  $M^2$  should be minimised for optimum output from the Raman amplifier. The threshold measurement for a (35 passes) Raman amplifier (Section 6.2.3) is in agreement with the non-ideal laser beam calculation. Similar agreement with theory was reported by Van den Heuvel *et al.* [24] for the Raman conversion of a Nd:YAG laser pump beam. Most of the threshold measurements were performed for a 35 passes multipass Raman cell designed for high repetition rate operation (see Chapter 6).

## **5.11 CHARACTERIZATION OF THE CO<sub>2</sub> BEAM FOR OPTIMUM RAMAN OUTPUT**

As the input laser beam quality (small  $M^2$ ) is so important for the optimization of the Raman conversion, it was necessary to characterize the output beam from the master oscillator power amplifier chain.

The high repetition rate laser chain, pumping a 35 passes cold Raman cell, was used for this investigation. The output quality of the beam depends on a number of laser parameters. They are:

- oscillator alignment, intracavity aperture size and the position for the selection of the TEM<sub>00</sub> mode,
- chain alignment to minimise beam aberrations due to gain saturation and diffraction effects, and
- laser discharge dynamics at high repetition rates and the effect of discharge instabilities on output beam quality.

The beam quality of a locally developed high repetition rate TEA-CO<sub>2</sub> laser chain was investigated. The chain consists of an oscillator and three amplifiers with a total optical path of approximately 45 m. The output from the chain varies from 1.6 J in 60 ns to 2.1 J in 80 ns on the stronger lines in the 10  $\mu$ m R-branch.

This master oscillator power amplifier chain (Figure 5.23) was developed to pump a high repetition rate multipass Raman cell. The path is long and the output beam must be mode-matched into the Raman cell. It is therefore necessary to know the  $M^2$  value, the beam waist and the position of the beam waist of the amplified output beam. These values are mainly determined by the oscillator and were thus measured as a function of different oscillator variables.

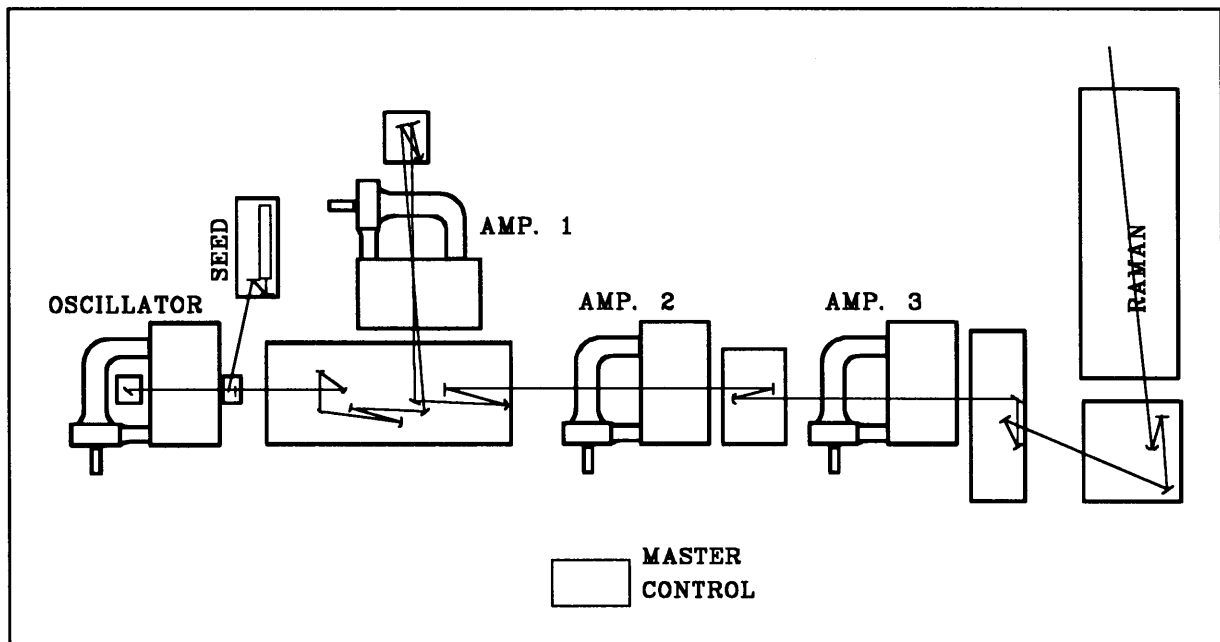


**Figure 5.23** *Experimental layout of MOPA chain with optical path shown*

Measurements of the beam quality after each amplifier are shown in Table 5.1. It is very difficult to quantify these values as a slight misalignment through the amplifiers has a detrimental effect on  $M^2$  due to diffraction effects. Efficient amplification is needed as high repetition operation of the lasers ( $> 1.5$  kHz) is less problematic at a minimal electrical input to the discharge. Obviously, the area of the beam has to be as large as possible on propagation through the amplifiers for optimum amplification. This condition requires small tolerances on the alignment through the amplifiers.

The TEA- $\text{CO}_2$  oscillator has an active volume of  $15 \times 15 \times 600$  mm<sup>3</sup> (Figure 5.24) and can be operated up to repetition rates of 2 kHz. Single longitudinal-mode operation, on the required rotational line, was obtained using injection seeding through transverse polarization coupling [25,26]. Line selection was ensured by using a 150 lines/mm flat grating in a Littrow configuration. The output coupler is a curved mirror, 10 m radius, with a 60 % reflectivity at  $10.2 \mu\text{m}$ . The total resonator length is 1432 mm, which implies that the intracavity aperture should be approximately 7.5 mm in diameter for the Fresnel number,  $N \approx 1$  (see page 12



in [8]).

Path Position: After	$M^2$
Oscillator	1.173
Amplifier 1 - second pass	1.193
Amplifier 2	1.416
Amplifier 3	1.449

**Table 5.1**  $M^2$  measurements after propagation of the amplifiers in the MOPA chain

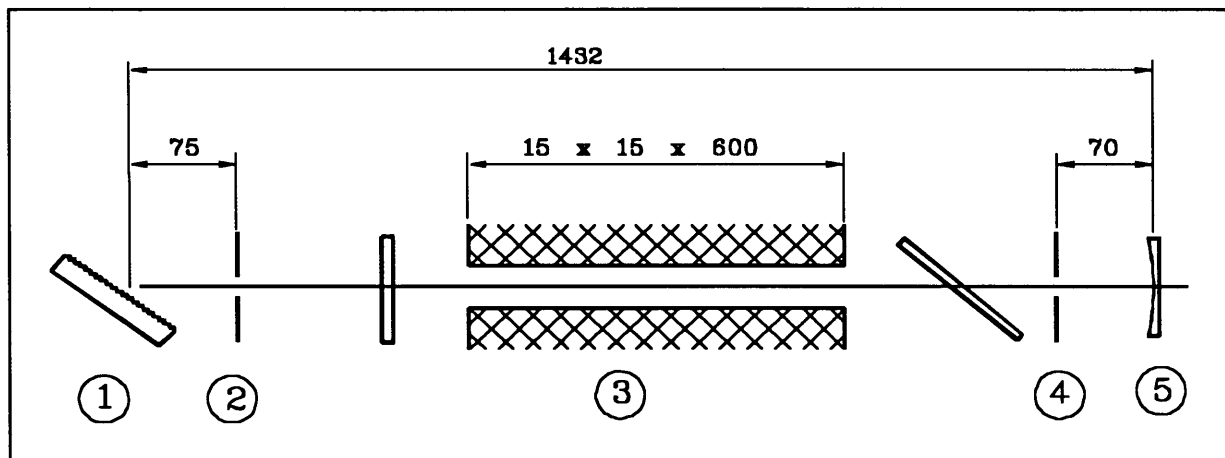


**Figure 5.24** Resonator layout with (1) the grating, (2) aperture position A, (3) discharge volume, (4) aperture position B and (5) output coupler

The beam-quality factor was measured using the propagation equation (5.30) as described in the second paragraph of Section 5.8 and a scanning slit for measuring the beam profiles. A software knife-edge was employed to calculate the beam radii at the scan positions as shown in Figure 5.14. The beam parameters were calculated using the procedure described in Appendix 5.B.

The measurement setup for the beam radius consisted of a  $f = 2.5$  m focusing optic and a scanning slit with a pulsed energy meter or a CW power meter (Figure 5.25). The pulsed energy meter was used at repetition rates up to 300 Hz, which is the repetition rate limit for the detector. A CW power meter was used for measurements at repetition rates higher than 300 Hz. In all the beam width measurements the average beam profiles were measured. The slit size could be varied between 0.3 mm and 0.6 mm, which allowed the measurement to stay within the limit of 1/10 of the 1/e-beam radius for the slit size (see Appendix 5.C and [20]).

PAGES 27 AND 28 NOT RECEIVED

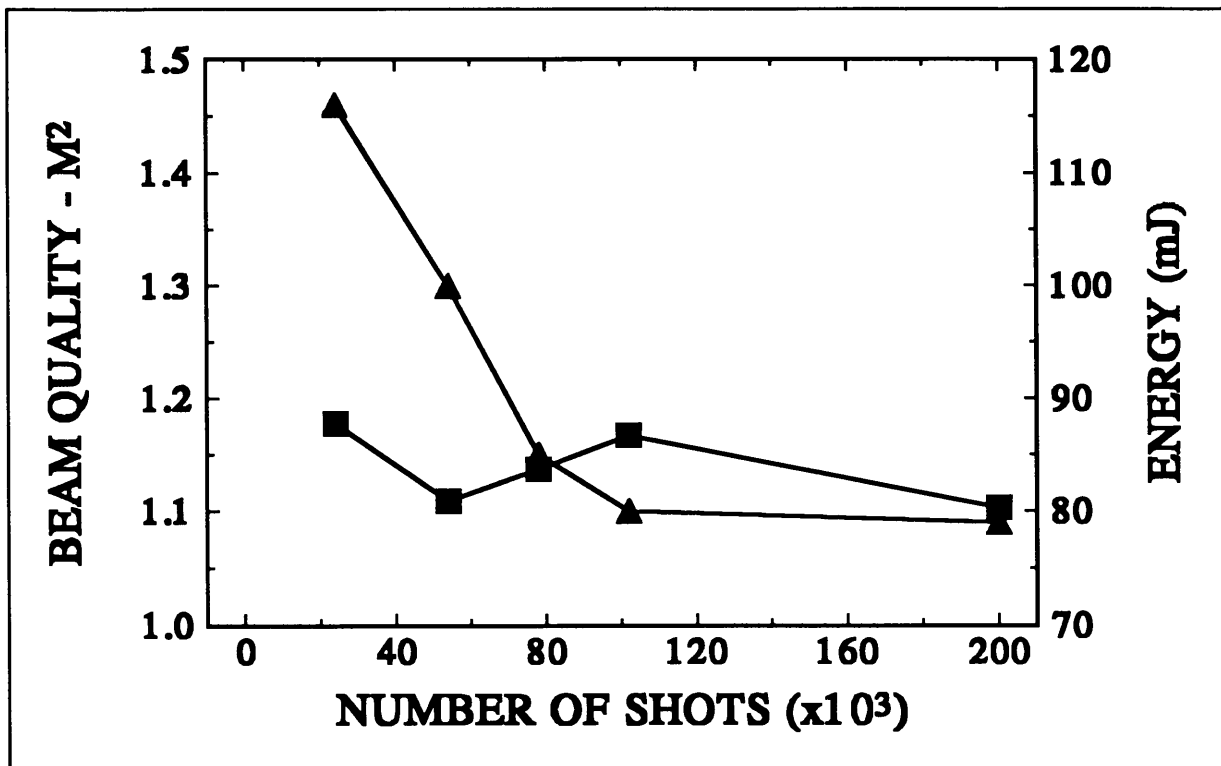


Figure 5.27 Measured  $M^2$  (■) and output energy (▲) as a function of gas deterioration

rate dependence of  $M^2$  (Figure 5.28). Laser beam degradation at repetition rates exceeding 300 Hz caused a drastic drop in output performance from the Raman cell. Similar results were reported, for Nd:YAG as the pump laser, by Van den Heuvel *et al.* [24]. A visual inspection showed discharge instabilities and arcing between 350 Hz and 500 Hz. A remedy for this problem is an increase in the gas flow velocity. However, this generates its own problems because of the high input power needed to circulate the heavy gas at a total pressure of 750 mBar. The output from the lean mix was about 25% lower than that of the rich mix, but is still useful as oscillator output as the amplifiers can still be saturated. From this figure it is clear that a gas mix can be selected which will be slightly off the optimum with respect to output performance but will allow 2 kHz repetition rates with a high-quality output beam. A useful output beam, at 1.8 kHz, was obtained even though no shock-wave prevention techniques were used. With the aid of shock-wave suppressors, 1.2 kHz operation in similar lasers was achieved for the rich mix. At higher repetition rates discharge wandering, streamers and arcing were detected. The lean mix does not show any visible discharge degradation at repetition rates of up to 2 kHz in these lasers.

In conclusion, the resonator design and laser condition have an influence on the output beam quality of the oscillator. Furthermore it was shown experimentally that this parameter must be known for optimum transmission and energy extraction from the amplifier chain, and an

efficient Raman conversion in the Raman cell (see Section 5.22).

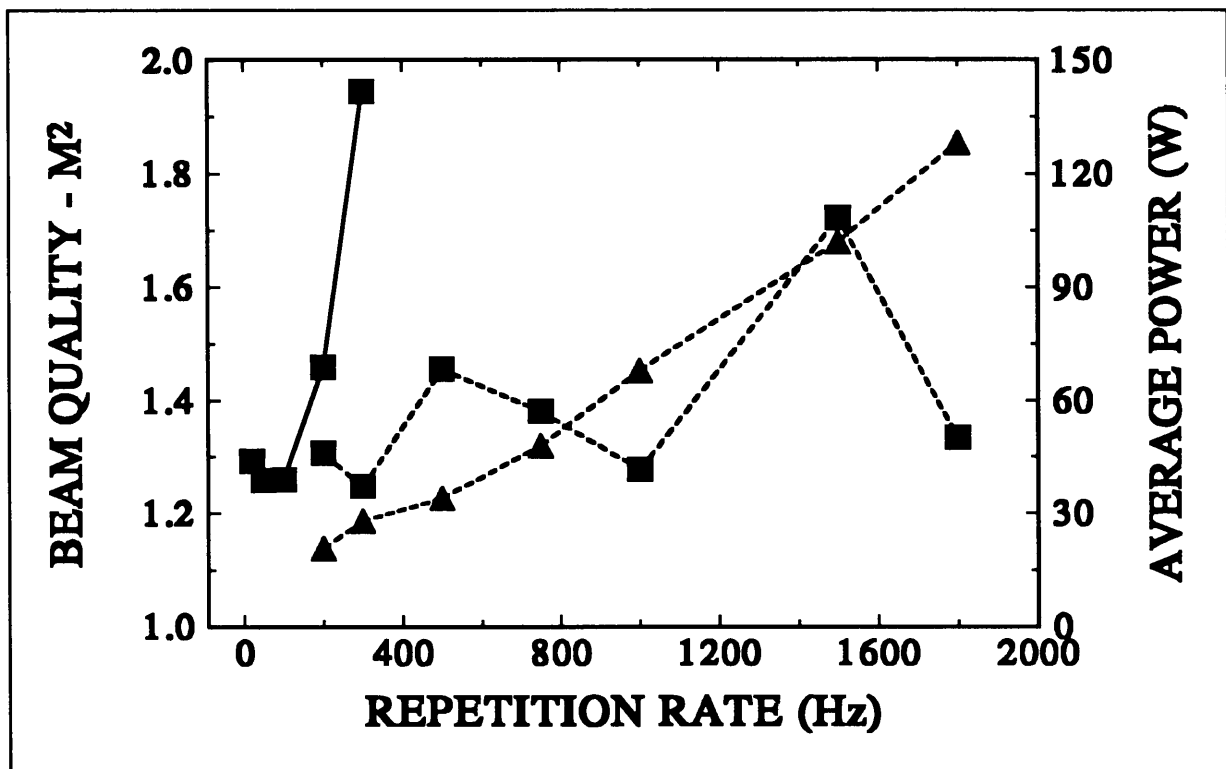


Figure 5.28  $M^2$  (■) for the rich (solid line) and the lean (broken line) mixtures with the average output power (▲) for the lean mix shown

## 5.12      **REFERENCES: CHAPTER 5**

1.      Defining and measuring laser beam parameters  
A.E. Siegman  
Workshop on Laser Beam Characterization, 14-16 June 1993, Madrid, Spain
2.      M<sup>2</sup> concept characterizes beam quality  
T.F. Johnston Jr.  
Laser Focus World, 173, (May 1990)
3.      Measuring and handling general astigmatic beams  
G. Nemes  
Workshop on Laser Beam Characterization, 14-16 June 1993, Madrid, Spain
4.      LASERS  
A.E. Siegman  
University Science Books, Mill Valley California, (1986)
5.      Quantum electronics 3rd Edition  
A. Yariv  
John Wiley & Sons, New York, (1989)
6.      A summary of useful laser equations-an LIA report  
H. Weichel, L.S. Pedrotti  
EOSD - Unknown
7.      Numerical modelling of stimulated Raman scattering in an astigmatic focus  
J.C. van den Heuvel  
IEEE J of Quantum Electron **28**(1),378, (January 1992)
8.      The physics and technology of laser resonators  
D.R. Hall, P.E. Jackson  
Adam Hilger, Bristol & New York, (1989)
9.      Laser beams and resonators  
H. Kogelnik, T. Li  
Appl Opt **5**(10),1550, (October 1966)
10.     Advances in laser resonator design using variable reflectivity mirrors  
A.E. Siegman  
Tutorials in Optics , Editor: Duncan T Moore, Optical Society of America,  
Washington DC, 65,(1992)

11. Defining the effective radius of curvature for a non-ideal optical beam  
A.E. Siegman  
IEEE J of Quantum Electron **27**(5),1146, (May 1991)
12. The change of width for a partially coherent beam on paraxial propagation  
F. Gori, M. Santarsiero, A. Sona  
Opt Comm **82**(3,4), 197, (April 1991)
13. New developments in laser resonators  
A.E. Siegman  
SPIE Proceedings Vol 1224, 16-18 Jan 1990, Los Angeles, California
14. Definition and measurements of high power laser parameters  
N. Reng, B. Eppich  
Opt and Quantum Electron **24**,S973, (1992)
15. Optics and optical instruments; Test methods for laser beam parameters: beam widths, divergence angle and beam propagation factor  
Giesen, Gindele  
ISO/TC 172/SC9/WG1 N46 Report by International Standardization Organization)
16. Some historical and technical aspects of beam quality  
H. Weber  
Opt and Quantum Electron **24**,S861, (1992)
17. Beam propagation in a linear or nonlinear lens-like medium using ABCD ray matrices:  
The method of moments  
C. Paré, P,-A. Bélanger  
Opt and Quantum Electron **24**,S1051, (1992)
18. Reliability of beam parameters measurements with CCD cameras  
B. Eppich, R. Kostka, M.A. Porrás, N. Renge  
Workshop on Laser Beam Characterization, 14-16 June 1993, Madrid, Spain
19. High repetition rate TEA-CO<sub>2</sub> laser beam characterization  
S.P. van Heerden, T.I. Salamon, L.R. Botha, H.M. von Bergman  
Workshop on Laser Beam Characterization, 14-16 June 1993, Madrid, Spain
20. Laser beam width, divergence and beam propagation factor - an international standardization approach  
D. Wright, P. Greve, J. Fleischer, L. Austin  
Opt and Quantum Electron **24**, S993, (1992)

21. Laser beam characterization and measurement techniques  
P. Loosen, K. Du, C. Maier, O. Marten, M. Scholl  
Workshop on Laser Beam Characterization, 14-16 June 1993, Madrid, Spain
22. Measurement of Gaussian beam parameter  
R.L. McCally  
Appl Opt **24**(14), 2227, (July 1984)
23. Choice of clip levels for beam width measurements using knife-edge techniques.  
A.E. Siegman, M.W. Sasnett and T.F. Johnston, Jr.  
IEEE J Quantum Electron **27**(4),1098, (April 1991)
24. The stimulated Raman scattering threshold for a non-diffraction-limited pump beam  
J.C. van den Heuvel, F.J.M. van Putten, and R.J.L. Lerou  
IEEE J Quantum Electron **28**(9),1930, (Sept 1992)
25. Development of an infrared laser system for molecular isotope separation  
EG Rohwer  
PhD Dissertation, Stellenbosch University, South Africa, (1992)
26. Polarization coupling effect in transversely excited atmospheric CO<sub>2</sub> lasers: Application to single axial mode operation  
A.K. Kar, R.G. Harrison, D.M. Tratt and C.A. Emshary  
Appl Phys Lett **42** (1),12,(1983)
27. Beam characterization and measurement of propagation attributes  
M.W. Sasnett, T.F. Johnston Jr.  
SPIE Vol 1414, Laser Beam Diagnostics, 21, (1991)
28. Laser beam quality versus aperture size in a cw argon-ion laser  
T.F. Johnston Jr., M.W. Sasnett, J.L Doumont, and A.E. Siegman  
Opt Lett **17** (3), 198, (1992)

## **APPENDIX 5.A: ABCD MATRIX METHOD FOR BEAM PROPAGATION THROUGH AN OPTICAL SYSTEM**

The basic tools for analysing all possible elementary forms of paraxial optical systems are supplied by the paraxial optical ray matrices or the ABCD matrices. This is a very powerful technique of examining most of the optical systems. For example, an easy stability calculation is possible for a complex resonator. The total transformation of the optical ray coordinates through any cascaded multielement paraxial optical system can be calculated by elementary matrix multiplication. This matrix is then expressed in the ABCD-matrix for the optical system. A very important property of this matrix is that all ray matrices have unity determinant

$$AC - BD = 1$$

For astigmatic systems the 2x2 matrices are complicated by matrices for the x and y directions. For simple astigmatic systems, i.e. the major and minor axes can be identified, the matrices in the two directions are not coupled. However, for more general astigmatic beams there is coupling between these matrices.

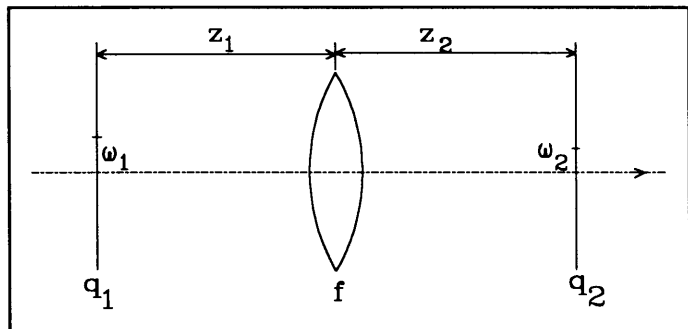


**Figure A.1 Thin-lens system**

Consider, for example, an optical ray that passes through a thin lens from a reference  $q_1$  at a distance  $z_1$  from a lens of focal length  $f$ . Then the transformation of the complex radius of curvature is given by<sup>[2]</sup>

$$q_2 = \frac{Aq_1 + B}{Cq_1 + D}, \tag{A.1}$$

where  $T = \begin{bmatrix} A & B \\ C & D \end{bmatrix}$  is the transformation matrix for the optical systems shown in Figure A.1.

The ray matrices for the free space propagation and lens transformation is shown in Figure A.2.<sup>[3]</sup>

<sup>[2]</sup> Laser beams and Resonators, H. Kogelnik, T. Li, Appl Optics 5(510),1550, (Oct 1966)

<sup>[3]</sup> Quantum Electronics 3rd ed, A. Yariv, John Wiley and Sons, New York, 1988



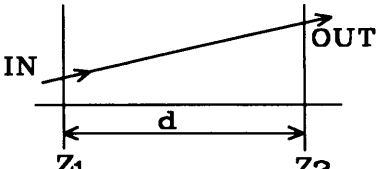
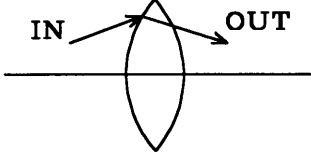
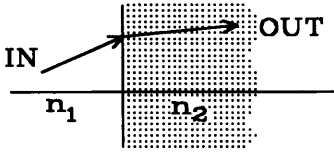
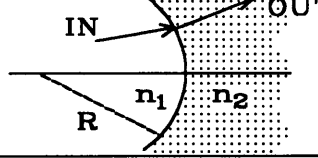
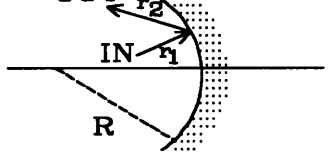
(1) Homogeneous Medium: Length $d$		$\begin{bmatrix} 1 & d \\ 0 & 1 \end{bmatrix}$
(2) Thin Lens: Focal length $f$ ( $f > 0$ , converging; $f < 0$ , diverging)		$\begin{bmatrix} 1 & 0 \\ \frac{-1}{f} & 1 \end{bmatrix}$
(3) Dielectric Interface: Refractive indices $n_1, n_2$		$\begin{bmatrix} 1 & 0 \\ 0 & \frac{n_1}{n_2} \end{bmatrix}$
(4) Spherical Dielectric Interface: Radius $R$		$\begin{bmatrix} 1 & 0 \\ \frac{n_2 - n_1}{n_2} \frac{1}{R} & \frac{n_1}{n_2} \end{bmatrix}$
(5) Spherical Mirror: Radius of curvature $R$		$\begin{bmatrix} 1 & 0 \\ \frac{-2}{R} & 1 \end{bmatrix}$

Figure A.2 Ray matrices for some common optical elements and media

It is important to note that the ray matrices must be cascaded in reverse order to the order in which the individual paraxial elements are encountered. Using the matrices in Figure A.2, the transmission matrix for the optical system depicted in Figure A.1 can be written as

$T = T_{z_2} T_f T_{z_1}$  which is

$$\begin{bmatrix} A & B \\ C & D \end{bmatrix} = \begin{bmatrix} 1 & z_2 \\ 0 & 1 \end{bmatrix} \begin{bmatrix} 1 & 0 \\ -\frac{1}{f} & 1 \end{bmatrix} \begin{bmatrix} 1 & z_1 \\ 0 & 1 \end{bmatrix} = \begin{bmatrix} 1 - \frac{z_2}{f} & z_1 + z_2 - \frac{z_1 z_2}{f} \\ -\frac{1}{f} & 1 - \frac{z_1}{f} \end{bmatrix}. \quad (\text{A.3})$$

Using these expression for the ABCD elements, equation (A.1) can be written as

$$q_2 = \frac{\left(1 - \frac{z_2}{f}\right) q_1 + z_1 + z_2 - \frac{z_1 z_2}{f}}{-\frac{q_1}{f} + \left(1 + \frac{z_1}{f}\right)} \quad (\text{A.4})$$

## APPENDIX 5.B: SECOND-ORDER LEAST-SQUARES FIT FOR THE EXTRACTION OF PROPAGATION PARAMETERS

Equations (5.29) and (5.30) can be written as  $Y = \sum_{i=0}^2 a_i z^i$ , where  $Y = W^2(z) = 4 \sigma_x^2(z)$ . Using

a second-order least-squares fit<sup>[4]</sup> the matrix equation below follows for a set of measurements  $(z_1, W_1), (z_2, W_2) \dots (z_n, W_n)$

$$\begin{bmatrix} n & \sum_i z_i & \sum_i z_i^2 \\ \sum_i z_i & \sum_i z_i^2 & \sum_i z_i^3 \\ \sum_i z_i^2 & \sum_i z_i^3 & \sum_i z_i^4 \end{bmatrix} \begin{bmatrix} a_0 \\ a_1 \\ a_2 \end{bmatrix} = \begin{bmatrix} \sum_i Y_i \\ \sum_i z_i Y_i \\ \sum_i z_i^2 Y_i \end{bmatrix}.$$

Solving the three equations for  $a_0$ ,  $a_1$  and  $a_2$ , the beam parameters  $W_0$ ,  $z_0$  and  $M^2$  can be calculated from the following relationships:

$$W_0 = \sqrt{\frac{(a_0 - a_1^2)}{4a_2}}, \quad z_0 = -\frac{1}{2} \frac{a_1}{a_2}, \quad M^2 = \frac{\pi W_0}{\lambda} \sqrt{a_2}.$$

## APPENDIX 5.C: ERROR CALCULATION FOR SCANNING SLIT METHOD

Assume a slit width  $d$  at a position  $x'$  on the irradiance profile. At this position the power transmitted by the slit is given by

$$P(x') = \sqrt{\frac{\pi}{2}} I_0 W \int_{x' - \frac{d}{2}}^{x' + \frac{d}{2}} e^{-2 \frac{x^2}{W^2}} dx. \quad (C.1)$$

Using the substitutions  $r = \frac{W}{\sqrt{2}}$ ,  $v = \frac{x}{r}$ ,  $\Delta = \frac{d}{2r}$ ,  $dx = r dv$  equation (C.1) can be written as

<sup>[4]</sup> Numerical Analysis 2nd Edition, R.L. Burden, J.D. Faires, A.C. Reynolds, Prindle, Weber & Schmidt, Boston, Massachusetts, 1981

$$P(rv') = \sqrt{\pi} I_0 r^2 \int_{v'-\Delta}^{v'+\Delta} e^{-v^2} dv . \quad (C.2)$$

This is exactly the equation used by McCally<sup>[5]</sup> to calculate the error for a slit  $d$  at a position  $v'$  on the irradiance profile. Note that  $r$  is the  $1/e$  radius of the intensity whereas  $W$  is the  $1/e^2$  radius of the intensity. It is shown by McCally (see footnote 5) that the deviation from the true Gaussian radius is given by

$$\Delta W = \frac{\Delta^2}{3} = \frac{2}{3} \left( \frac{d}{D} \right)^2 , \quad (C.3)$$

where  $D=2W$ . Clearly for  $d/D < 1/10$ , the measuring error on the true Gaussian radius is less than 0.67 %.

## ***APPENDIX 5.D: CLIP LEVEL CALCULATION FOR THE KNIFE-EDGE METHOD***

Assuming an intensity profile given by  $I(x,y)$ , then the clip width in the  $x$ -direction for a given level  $\epsilon$  is given by  $D_c = x_2 - x_1$  where  $x_1$  and  $x_2$  are the positions along the  $x$ -axis at which

$$\epsilon P_0 = \int_{-\infty}^{x_1} \int_{-\infty}^{\infty} I(x,y) dy dx, \quad (1-\epsilon) P_0 = \int_{x_2}^{\infty} \int_{-\infty}^{\infty} I(x,y) dy dx , \quad (D.1)$$

where  $P_0 = \int_{-\infty}^{\infty} \int_{-\infty}^{\infty} I(x,y) dy dx$  is the total power of the beam.

The knife-edge integrates over the  $y$ -variation automatically as the knife-edge moves in the  $x$ -direction. For a Gaussian beam ( $TEM_{00}$  beam)  $I(x,y)$  is separable in the form  $I(x,y) = I_x(x) I_y(y)$ . In this case the  $y$ -variation can be dropped from the evaluation of the clip levels. Consider only symmetric beam profiles with  $-x_1 = x_2 = D_c/2$  then the clip level  $\epsilon$  is related to the clip diameter by<sup>[6]</sup>

---

[5] Measurement of Gaussian beam parameter, R.L. McCally  
 Appl Optics 24(14), 2227, (July 1984)

[6] Choice of Clip levels for Beam Width Measurements using Knife-Edge Techniques.  
 A.E. Siegman, M.W. Sasnett and T.F. Johnston, Jr.  
 IEEE J Quantum Electron 27(4), 1098, April 1991

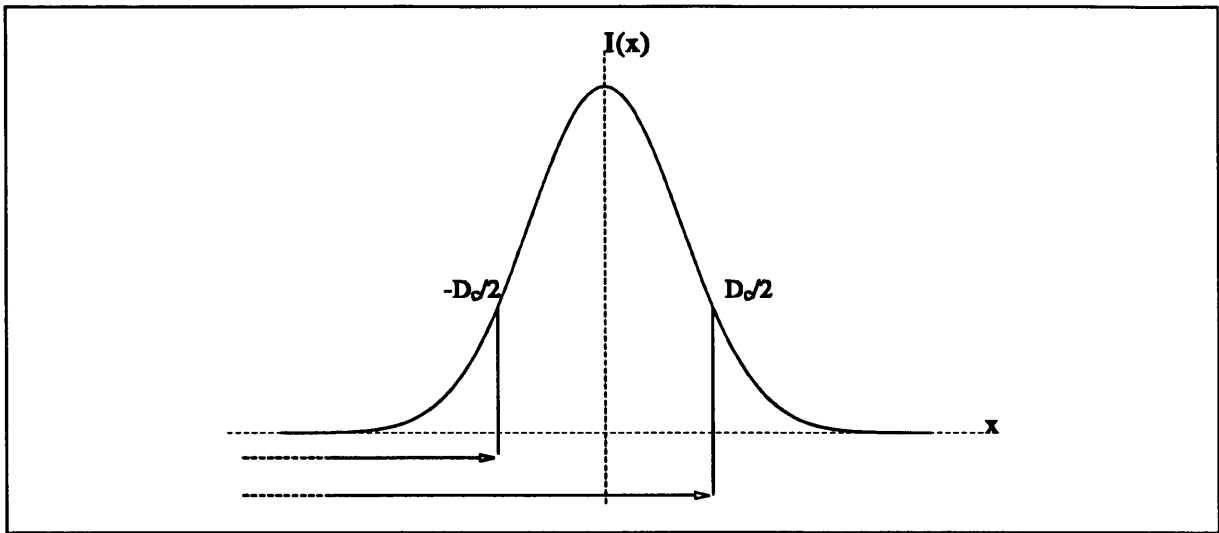


**Figure D.1** *Beam width calculation with symmetric clip positions for the knife-edge method*

$$(1-2\varepsilon)P_0 = \int_{-D_c/2}^{D_c/2} \int_{-\infty}^{\infty} I(x,y) dy dx . \quad (D.3)$$

The intensity profile of the lowest-order Hermite-Gaussian mode is given by

$$I(x,y) = I_0 e^{-\frac{2(x^2+y^2)}{W^2}} .$$

Then the clip level equation (D.3) can be written as

$$(1-2\varepsilon)P_0 = I_0 W^2 \frac{\sqrt{\pi}}{2} \left( \int_0^{u_1} e^{-u^2} du - \int_0^{-u_1} e^{-u^2} du \right) , \quad (D.4)$$

where  $u = \sqrt{2} \frac{x}{W}$ ;  $u_1 = \frac{D_c}{\sqrt{2}W}$ ;  $P_0 = I_0 \frac{\pi W^2}{2}$ .

Using the definition for the error function <sup>[7]</sup>

$$\text{erf}(x) = \frac{2}{\sqrt{\pi}} \int_0^x e^{-y^2} dy$$

equation (D.4) can be rewritten as

$$(1-2\varepsilon) = \text{erf} \left( \frac{D_c}{\sqrt{2}W} \right) \quad (D.5)$$

<sup>[7]</sup> Mathematical Handbook of Formulas and Tables  
 M.R. Spiegel  
 Schaum's Outline Series in Mathematics, McGraw-Hill Book Company, New York, 1968

This is exactly the result obtained by Siegman *et al.* (see footnote 6) for a TEM<sub>00</sub> beam. For a 10%-90% clip level, i.e.  $\epsilon = 0.1$ , it can be shown that  $\frac{D_c}{\sqrt{2}W} = 0.906$ , which means that

the scale factor for a 10%-90% clip level is given by  $2W = 1.561D_c$ . It can also be shown that for  $D_c = 2W$  the clip level is given by  $\epsilon = 0.023$  <sup>[8]</sup> which is the 2.3%-97.7% clip level. Clearly for these clip levels the scale factor is equal to unity.

## APPENDIX 5.E: POWER CONTENT CALCULATIONS FOR THE VARIABLE-APERTURE METHOD

The relationship between the real beam width and the power enclosed in a radius  $r_c$  will be found. Using a scaling factor, in analogy to knife-edge scaling factor, the beam width can be calculated. Assuming a Gaussian intensity profile in polar coordinates  $I(r, \theta) = I_0 e^{-2\frac{r^2}{W^2}}$

with  $I_0 = 2\frac{P_0}{\pi W^2}$ , where  $P_0$  is the total power of the beam. The power content enclosed in the

radius,  $r_c$ , is then given by

$$P_{r_c} = \epsilon P_0 = I_0 \int_0^{r_c} \int_0^{2\pi} e^{-2\frac{r^2}{W^2}} \theta r dr .$$

Performing the integration the power content is given by  $\epsilon = 1 - e^{-2\frac{r_c^2}{W^2}}$ .

---

[8] Handbook of Mathematical functions:ninth printing  
 M. Abramowitz, I.A. Stegun  
 Dover Publications Inc, New York, Dec 1972 (error function tables)

## ***LIST OF SYMBOLS: CHAPTER 5***

$c$	: speed of light
$d$	: slit width
$D$	: beam diameter
$D_c$	: clip level width of the beam
$E$	: electric field distribution as a function of $x$ , $y$ , $z$ and $t$
$f$	: focal length of a thin lens
$g_1, g_2$	: resonator parameters
$I_0$	: peak irradiance of a beam
$I(x,z)$	: irradiance distribution of a beam
$k$	: propagation constant
$L$	: length of the resonator
$M^2$	: laser beam quality parameter
$P$	: total power in a beam
$q(z)$	: complex beam parameter
$r_c$	: clip radius
$R(z)$	: radius of curvature of the beam
$R_1$	: radius of curvature of resonator mirror 1 or radius of curvature of a beam
$R_2$	: radius of curvature of resonator mirror 2 or radius of curvature of a beam
$s_c$	: angular beam centroid position
$T$	: transformation matrix
$W_0$	: minimum radius of a general beam
$W$	: beam radius of a general beam
$x_c$	: spatial beam centroid position
$z_R$	: Rayleigh range of an ideal Gaussian beam
$z_0$	: position of the minimum radius $\omega_0$ or $W_0$
$z_1$	: position of the beam radius $W_1$
$z_2$	: position of the beam radius $W_2$
$Z_R$	: Rayleigh range of a general beam
$\Delta W$	: error on beam radius measurement using a finite slit width
$\epsilon$	: clip level
$\theta_f$	: far-field half-angle divergence of a beam
$\lambda$	: free space wavelength
$\sigma_{x0}$	: minimum spatial beam variance

- $\sigma_x$  : spatial beam variance
- $\sigma_s$  : angular beam variance
- $\phi(z)$  : phase term
- $\omega_0$  : minimum beam radius of an ideal Gaussian beam
- $\omega_1$  : beam radius on resonator mirror 1
- $\omega_2$  : beam radius on resonator mirror 2
- $\omega_{1,2}$  : beam radius on the mirrors of a symmetric resonator
- $\omega(z)$  : beam radius as a function of the propagation distance

# 6. RAMAN CONVERSION RESULTS AND CONCLUSIONS

## 6.1 INTRODUCTION

In this chapter most of the experimental results are reported. The results were obtained on the high repetition rate Raman cell pumped with a CO<sub>2</sub> master oscillator power amplifier (MOPA) chain. This multipass cell consists of 34 individual 2 m mirrors, arranged in such a way that a transverse flow of the parahydrogen can be achieved (see Figure 6.1).

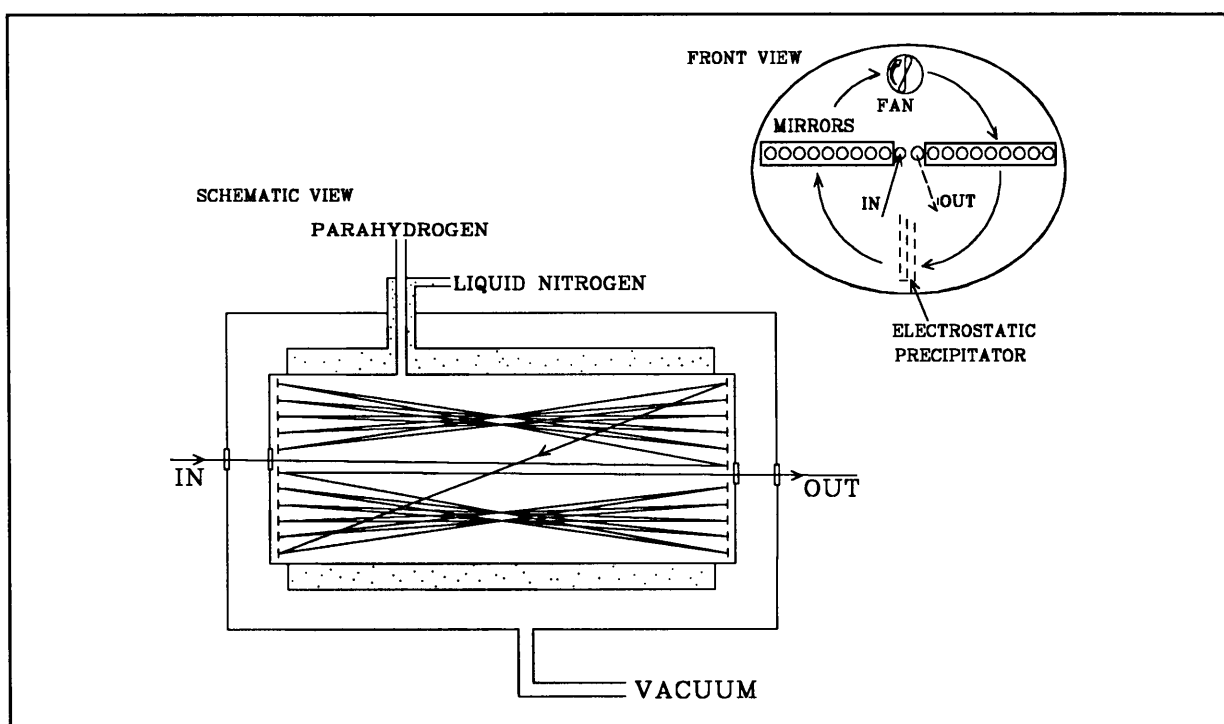


**Figure 6.1** High repetition rate multipass Raman cell

The parameters for the Raman conversion in this cell were measured. Although most of the measurements were performed at repetition rates lower than 300 Hz, outputs were measured up to 1000 Hz. For most of the tests the 10R18 CO<sub>2</sub> line was used. Single longitudinal mode operation was ensured using a low-pressure CO<sub>2</sub> seed laser.

The characterization of the Raman output for the 35 pass Raman cell includes the following:

- Raman threshold measurements as a function of parahydrogen content,
- Raman line-width measurement employing a wedge etalon and
- Raman output as a function of parahydrogen pressure for a constant CO<sub>2</sub> laser input.



### 6.1.1 MASTER OSCILLATOR POWER AMPLIFIER CHAIN DESCRIPTION

As discussed in Section 5.11, the chain consists of an oscillator and three power amplifiers with a total optical path of approximately 45 m. Most of the measurements were carried out using a pulse of 1.5 J in 60 ns or 1.8 - 2.1 J in 80 ns. Typical multimode and single-mode pulses are shown in Figure 6.2.

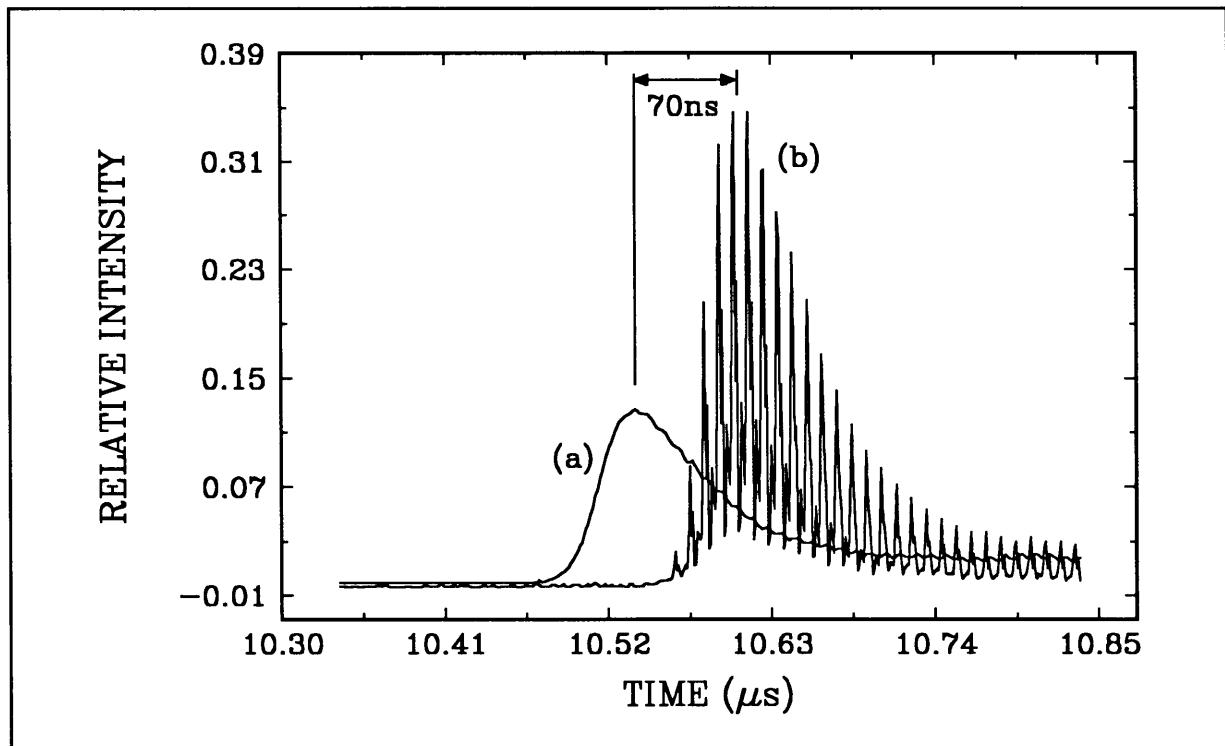


**Figure 6.2** Typical input  $CO_2$  pulse shapes with (a) the single-mode and (b) the multimode pulses. Note the difference in the pulse onset time.

The master-oscillator-power-amplifier chain (Figure 6.5) was characterized with respect to the output beam quality (Section 5.11) and the output temporal quality of the pulses (Figures 6.2 and 6.3). The temporal quality characterization includes the development of a system that uses an active feedback to ensure single longitudinal mode operation from the oscillator. This system is depicted in Figure 6.3 and uses a fast pyroelectric detector as the optical feedback (see Section 6.1.3). It operates on the principle that the onset time for the single-mode pulse is much shorter than that of the multimode pulse [1] (see Figure 6.2). Figure 6.3(b) shows the operational result of the mode-locking device (procedure shown in Figure 6.3a). The vertical axis is the time delay from the discharge, which is detected using a fast Si-pin detector, to the optical output. The low-pressure seeding of the TEA laser is shown in Figure 6.4. This technique was thoroughly investigated by Rohwer [2].

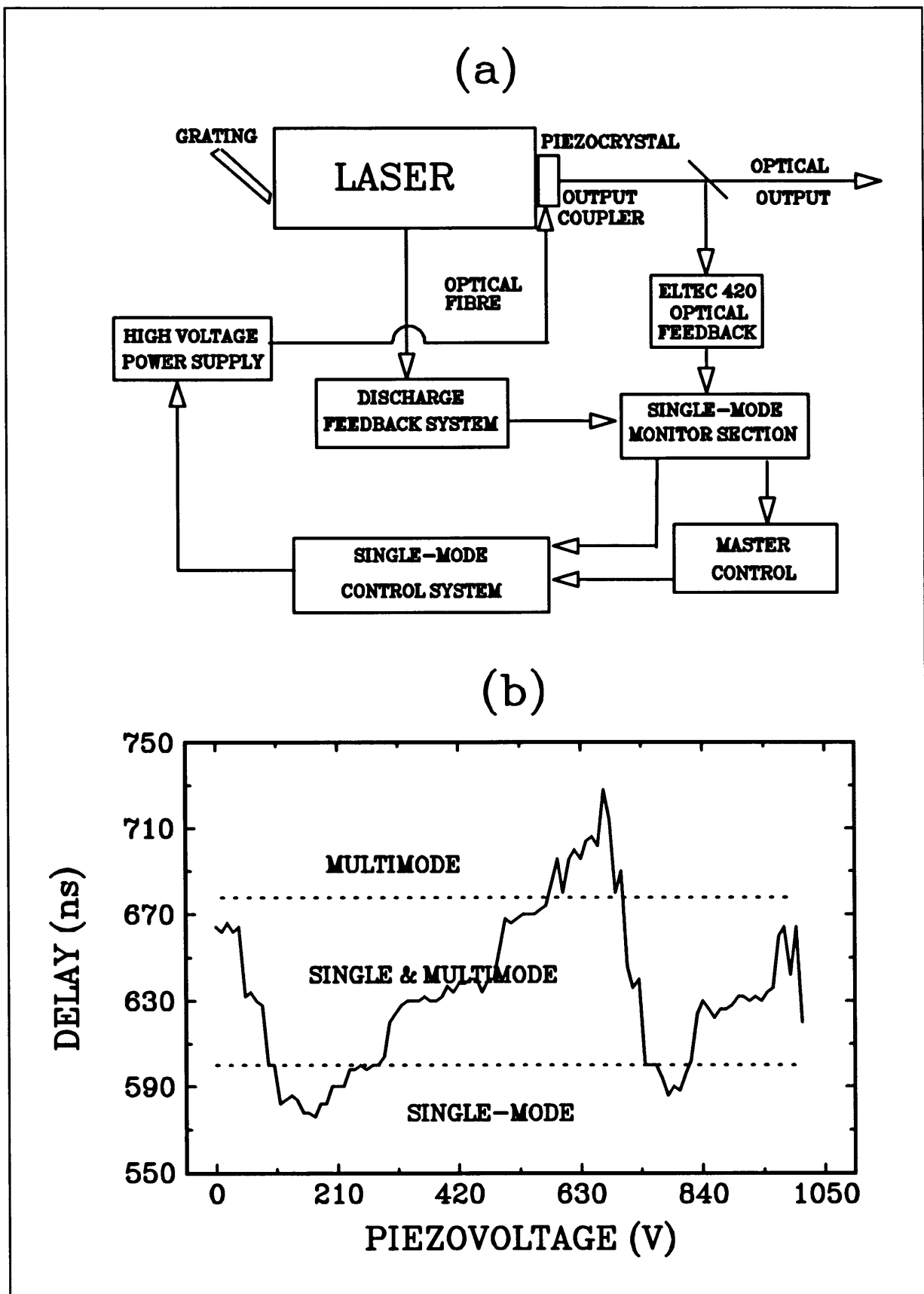
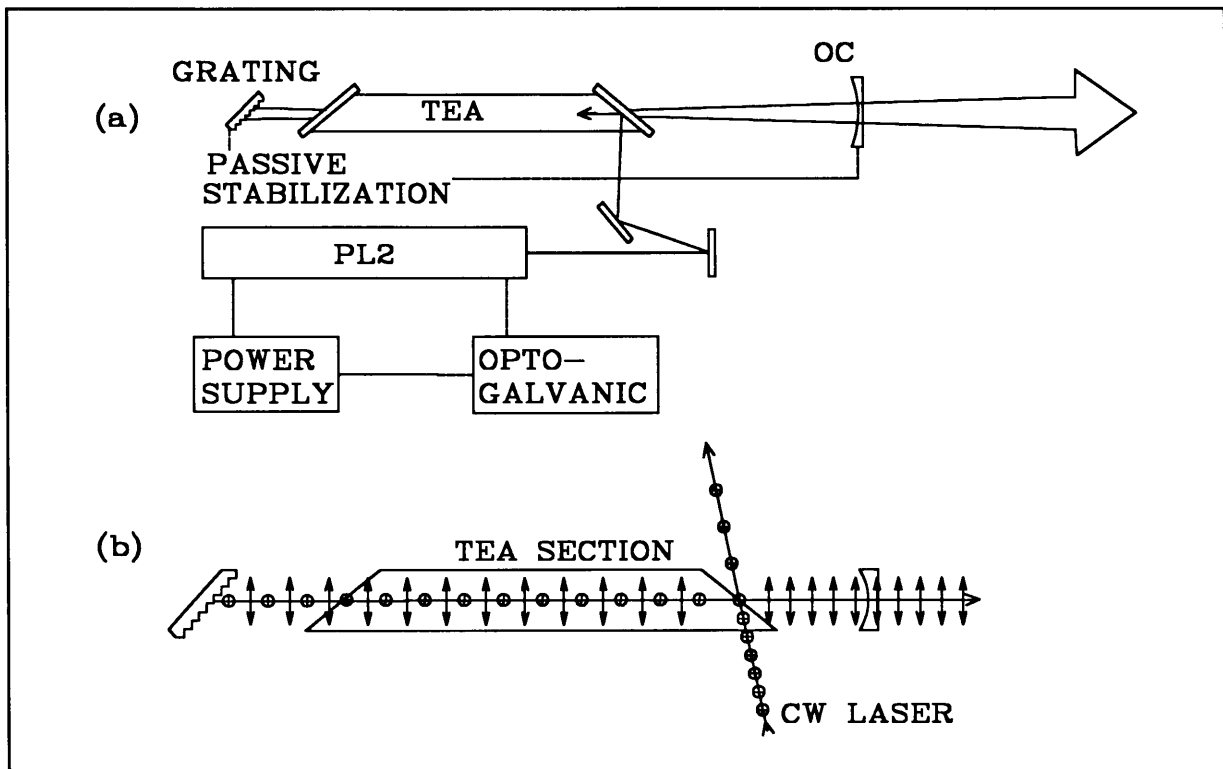


Figure 6.3 (a) Schematic of the active single-mode system and (b) the minimum delayed position that will ensure single-mode operation



**Figure 6.4** (a) Oscillator layout with CW seeding for single mode operation and (b) principle of operation

The amplifier chain consists of three amplifiers with a double pass through the first amplifier (see Figure 6.5). The double pass had to employ a cross alignment as shown in Figure 6.5. Using this alignment procedure we were able to misalign any parasitic resonator and so avoid parasitic output. The remaining amplifiers are used as single-pass systems. The unsaturated single-pass amplification for each of the amplifiers is shown in Table 6.1.

<i>Amplifier no</i>	<i>Small signal single-pass amplification</i>
1	3.0
2	3.3
3	3.4

**Table 6.1** Amplifier single-pass unsaturated amplification

The saturable gain from the amplifiers is a function of the mode-matching through the amplifiers. It is obvious that optimum amplification can be achieved if the gain volume is fully utilized. This can only be possible if the oscillator output beam parameters are known. The parameters were measured using the procedures described in Section 5.11. All the lasers in the chain can run at pulse rates up to 1 kHz from an electrical point of view. However,

this limit cannot be reached if a rich gas mixture ( $\text{CO}_2 > 40\%$ ) is used. It was shown that the limit could be achieved if leaner gas mixtures ( $\text{CO}_2 < 20\%$ ) were used. The higher repetition rate can be achieved if a reduction of 25% in chain output energy is tolerated due to the leaner gas mixture.

In conclusion, Figure 6.6 is a photograph of the master-oscillator-power-amplifier chain which emphasizes the path-length problem in achieving optimum beam propagation and amplifier extraction.

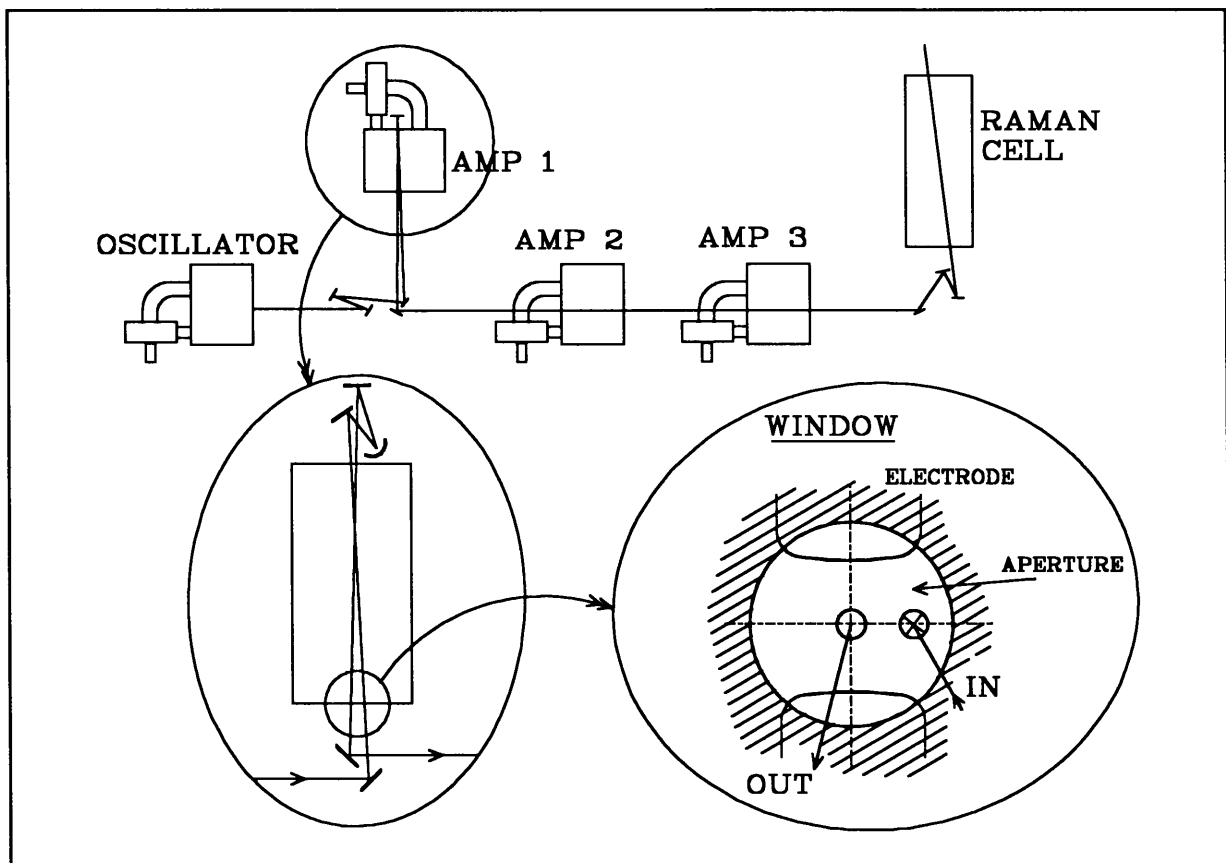


**Figure 6.5** Master-oscillator-power-amplifier chain layout with double-pass configuration shown



**Figure 6.6** *High repetition rate master-oscillator-power-amplifier chain [6]*

## 6.1.2 WAVELENGTH CALIBRATION

Due to the Raman conversion a number of wavelengths can emerge from the Raman cell. For measuring the 16  $\mu\text{m}$  output ( $354\text{ cm}^{-1}$  shift of  $10.2\ \mu\text{m}$  in parahydrogen) an 0.5 m monochromator, employing a 90 lines/mm grating, was used. The monochromator was originally calibrated for use in the visible part of the EM spectrum using a 1200 lines/mm grating. It was then recalibrated for the 90 lines/mm (Figure 6.7). Figure 6.8 shows the experimental layout on the exit aperture of the Raman cell, utilizing the 0.5 m monochromator.

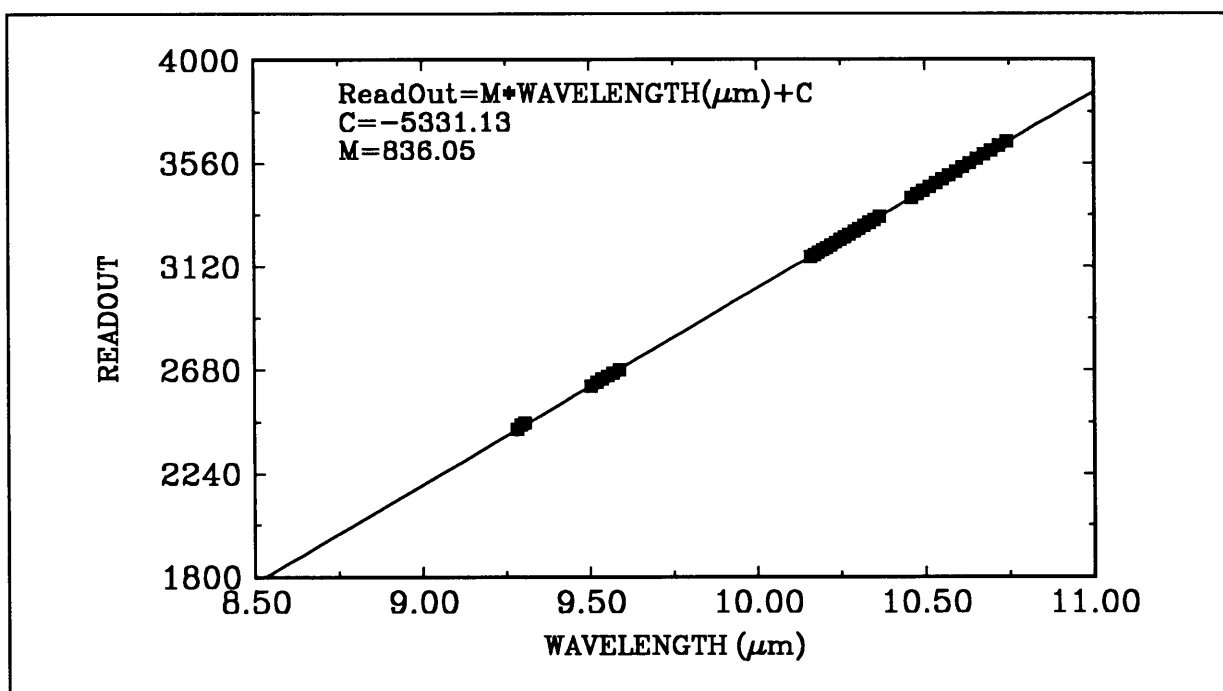


*Figure 6.7 Calibration of the 0.5 m monochromator employing a 90 lines/mm grating*

A second technique used for the  $10.2\ \mu\text{m}$  and  $16\ \mu\text{m}$  wavelength separation is a set of two band-pass filters. The optics have two specifically designed coatings, (a) a  $16\ \mu\text{m}$  reflection layer on one surface and (b)  $10.2\ \mu\text{m}$  anti-reflection coatings on both surfaces. The advantage of this method is that simultaneous measurements can be made of the  $16\ \mu\text{m}$  and the depleted  $10.2\ \mu\text{m}$ . The band-pass method is shown in Figure 6.9. This is also the technique used for the high repetition rate, pulse-to-pulse characterization of the  $16\ \mu\text{m}$  output.

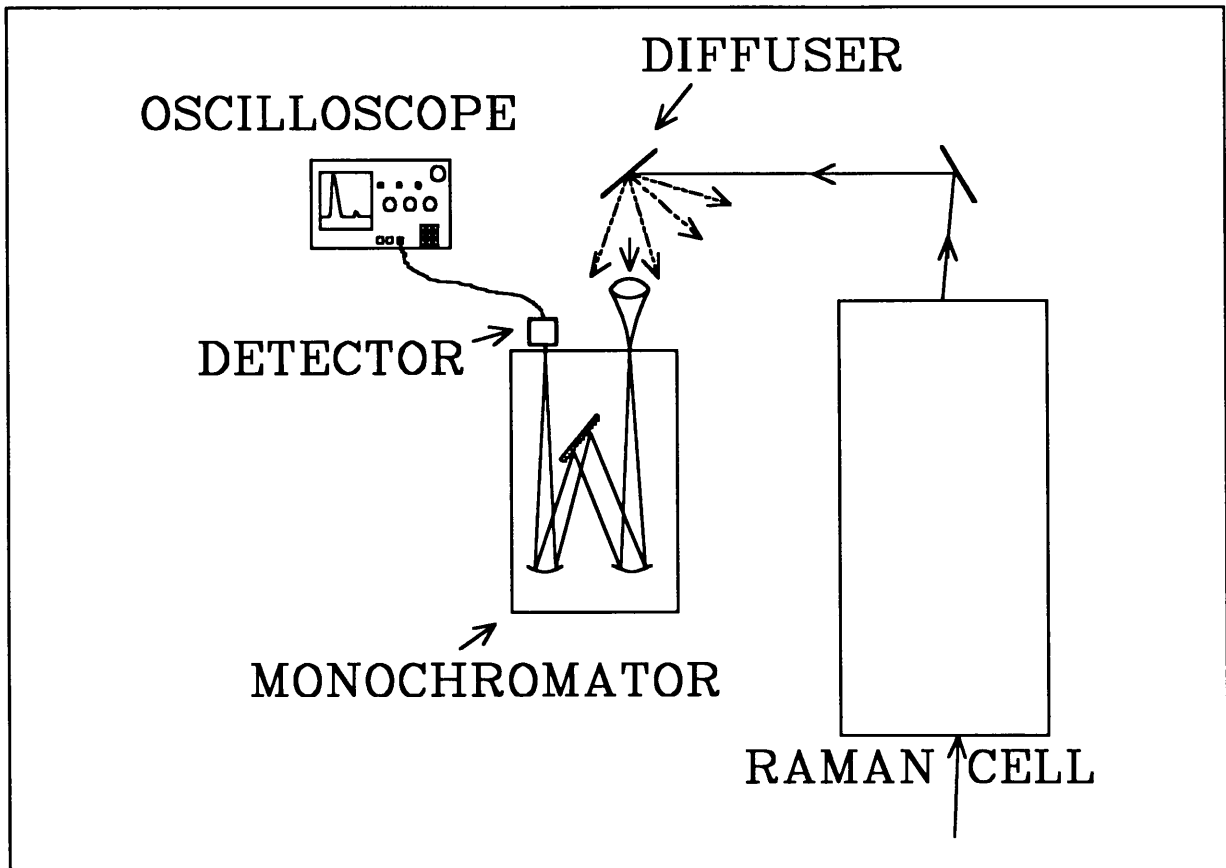


Figure 6.8 Monochromator configuration for wavelength measurement

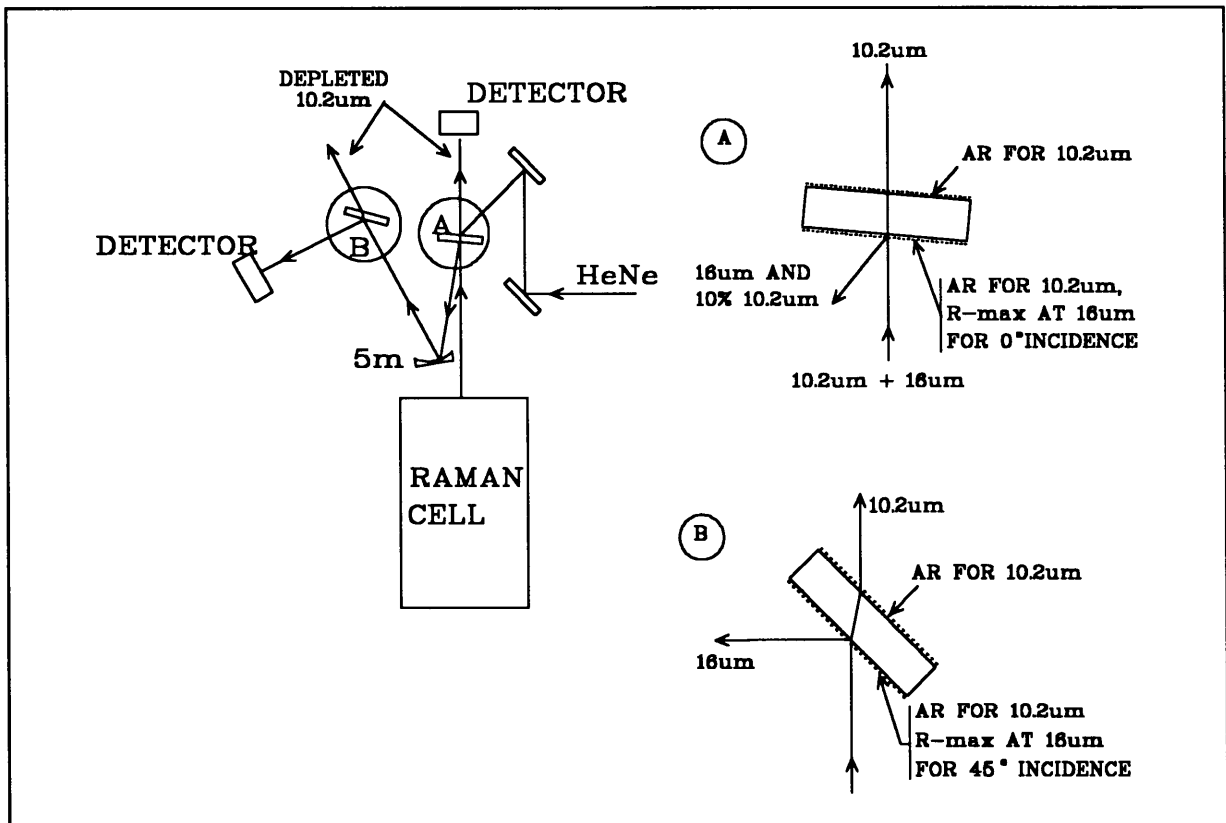
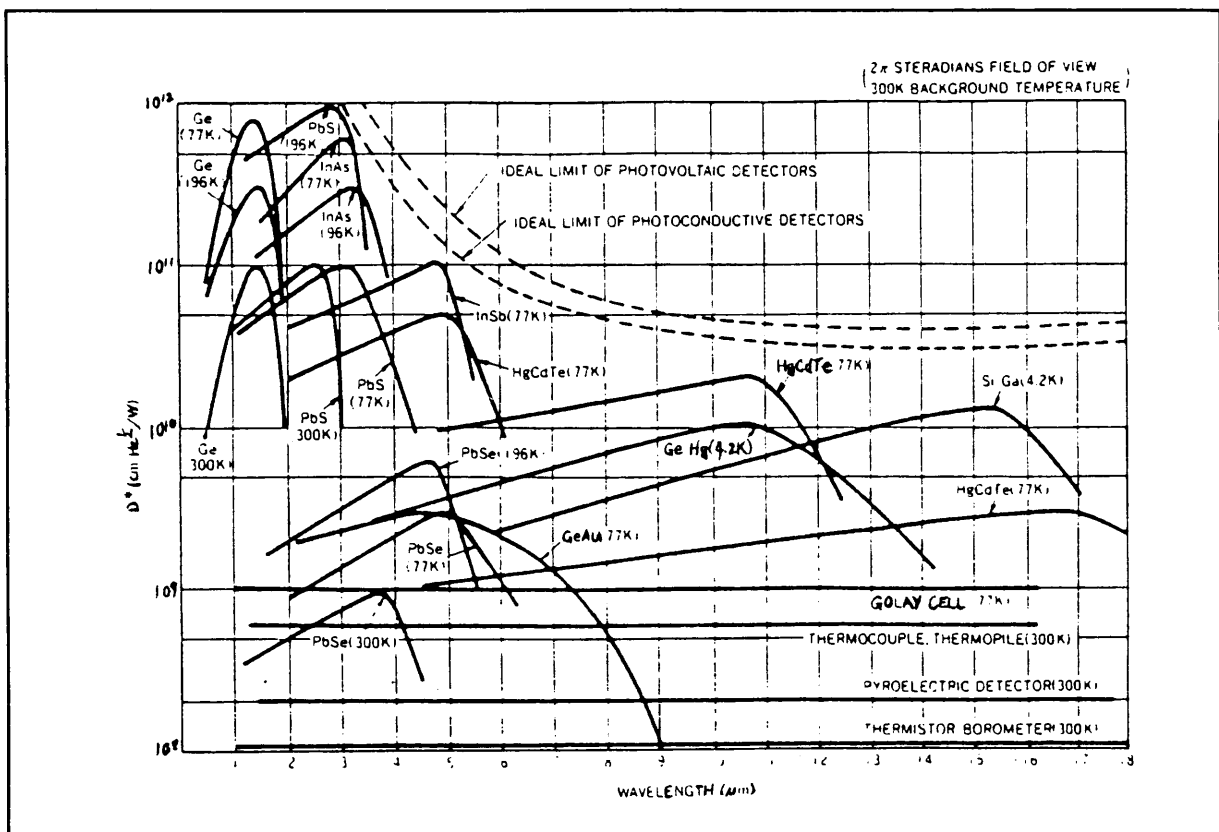


Figure 6.9 Band-pass filter configuration

### 6.1.3 DETECTORS

Detectors designed for high-repetition rate ( $> 1$  kHz) laser operation, at  $10\ \mu\text{m}$ , are nonexistent, especially detectors that can follow the  $\text{CO}_2$  pulse in time (i.e. photon-drag detectors). At low repetition rates a germanium photon drag detector is used for a time-resolved laser pulse. This detector cannot be used at high repetition because of the thermal run-away effect that takes place in germanium. This happens due to increased absorption as the temperature increases in the germanium material.

The only useful IR ( $10\ \mu\text{m}$ ) detectors are pyro-electric and MCT (Hg-CdTe) detectors. Figure 6.10 shows the detector sensitivity as a function of wavelength. The cryogenically cooled MCT detectors are extremely sensitive. However, these detectors are too slow to resolve the  $\text{CO}_2$  pulse in time (time response  $< 1$  MHz).



**Figure 6.10** *Detector sensitivity as a function of wavelength*

At low repetition rates two types of detectors were used: large surface pyro-electric detectors for energy measurements, and a germanium photon drag detector for peak power measurements (pulse shape). The detector selected for high repetition characterization is the ELTEC 420 [3] pyroelectric detector. This detector comes in two models, the 420 and 420-M3. The model 420 can be used as photon drag detector as shown in Figure 6.11. It is



clear that this detector will follow the CO<sub>2</sub> pulse. The only disadvantage is the slightly slower decay visible in the tail of the pulse. For the characterization of the beam this error can be tolerated as long as a calibration standard is used.

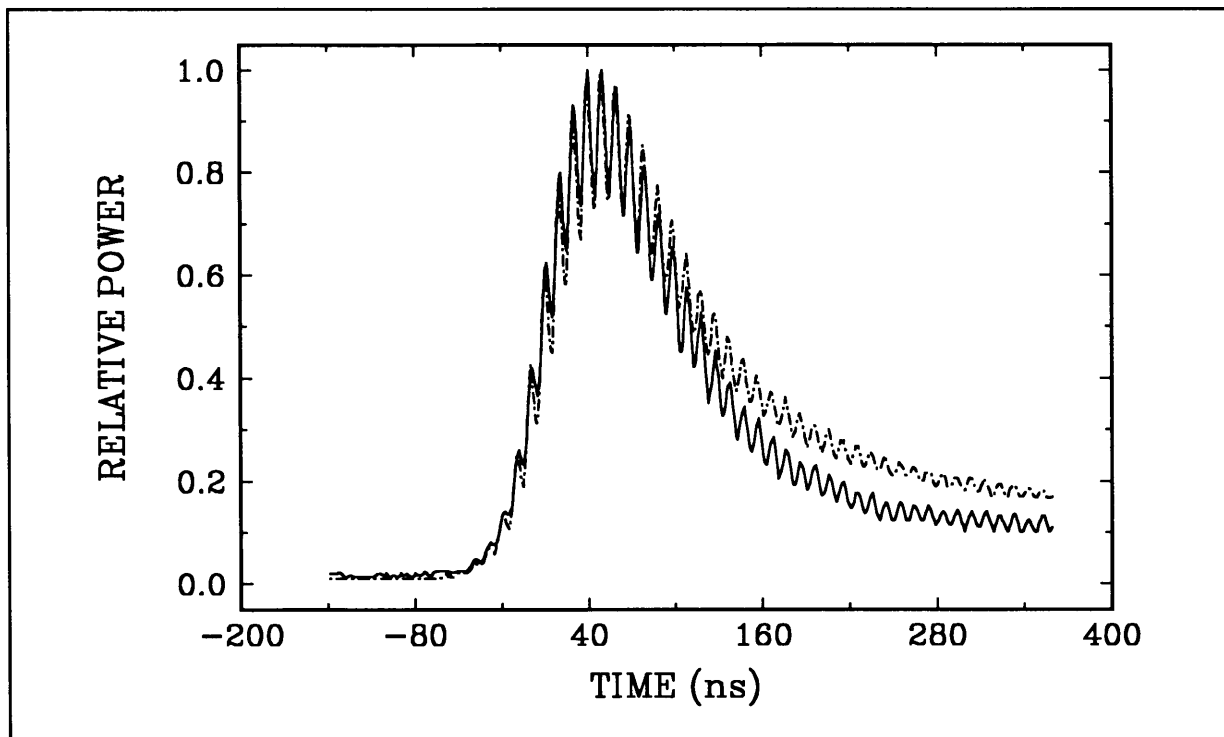


Figure 6.11 Germanium photon drag (solid) trace vs 420 detector (dashed) ( $R_L=50 \Omega$ )

The 420 detector was used in the voltage output mode (Figure 6.12). For the appropriate load resistor  $R_L=50\Omega$  the detector has a time response of less than 2 ns. In this mode it is quite clear that the detector will temporally resolve any pulse longer than 4 ns. Indeed this detector can resolve the mode beating for a multi-mode pulse which is clearly seen in Figure 6.11. A drawback of the 420 detector in the "photon drag" mode, is reduced sensitivity. It is thus necessary to expose the detector to large peak power. At high repetition rates the average power will then exceed the 5 W average power damage threshold for the detector.

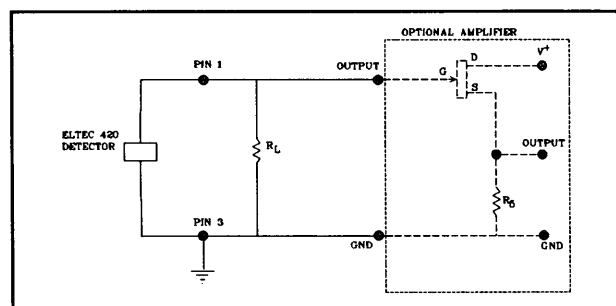
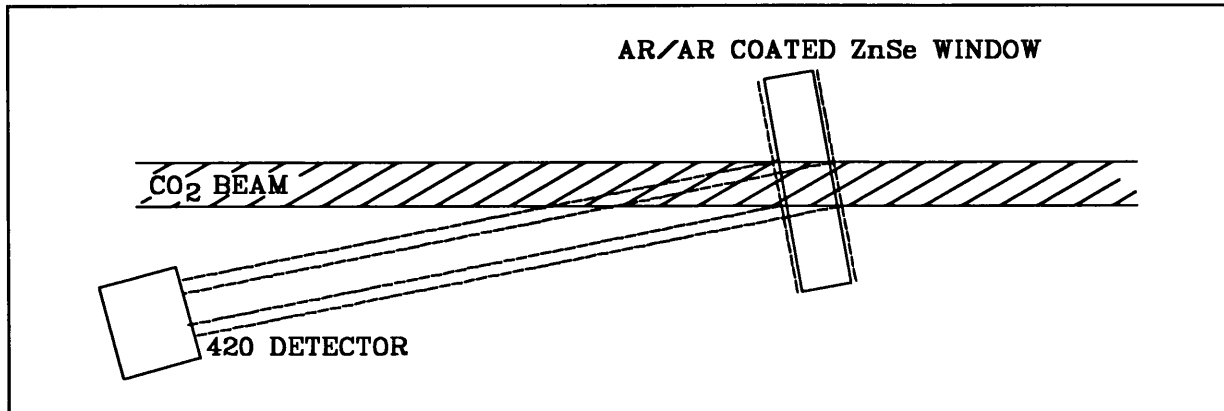


Figure 6.12 The 420 detector in voltage output mode

A costly room temperature MCT detector can also be used. It is less sensitive than the cryogenic version, but better than the model 420. Its time response is below 1 ns [4].

The advantage of the model 420 is its usefulness as an energy detector - the mode in which it was used. With  $R_L > 1 \text{ M}\Omega$  the detector will integrate the incoming  $\text{CO}_2$  laser pulse with an output signal FWHM in the order of  $40 \mu\text{s}$ . In this mode the 0.1% reflection off an AR/AR coated ZnSe window is sufficient for signal detection, with a signal-to-noise ratio of better than 100:1.



**Figure 6.13** The 420 detector in a relative energy output mode ( $R_L > 1 \text{ M}\Omega$ )

For the configuration shown in Figure 6.13, it is extremely difficult to calibrate the output signal for an absolute energy measurement due to the spatial wandering of the beam across the small detector area. Using focusing optics the average power exceeds the detector damage threshold. An integrating sphere (Figure 6.14) can be used to solve this problem.

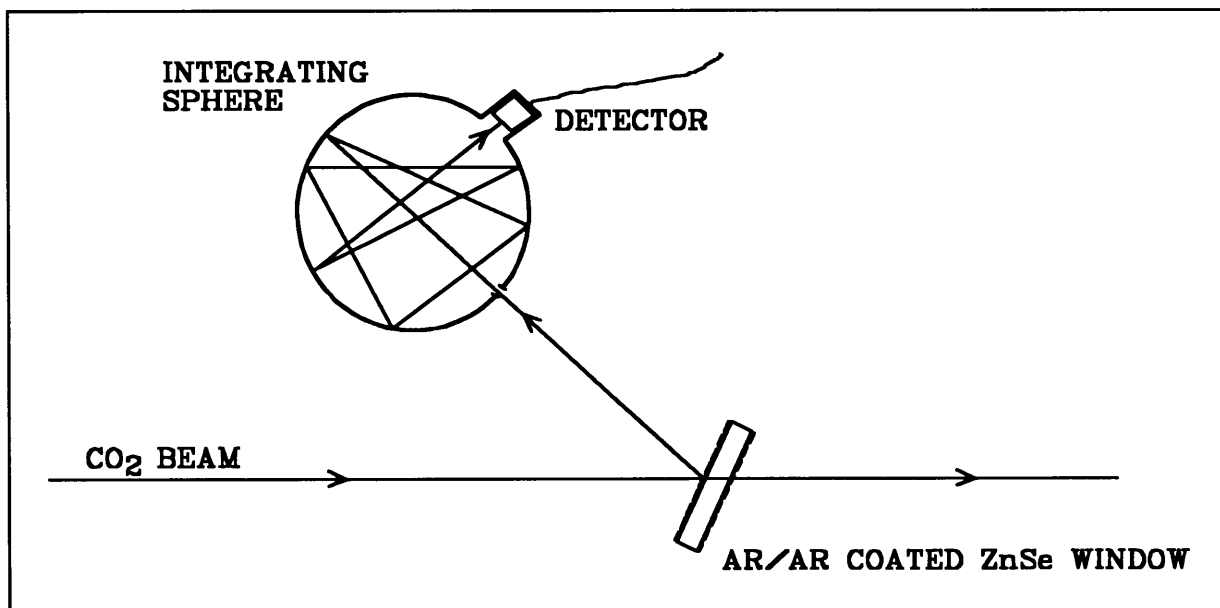


**Figure 6.14** Absolute energy measurement using the 420 detectors in energy mode ( $R_L > 1 \text{ M}\Omega$ ) employing an integrating sphere

To conclude, the evaluation and integration of detectors in a high repetition rate laser chain needs more investigation. This will allow real-time characterization of the beam on a pulse-to-pulse basis.

## 6.2 RESULTS

The Raman output characterization includes the 16  $\mu\text{m}$  bandwidth and output energy measurement. The Raman output is measured as a function of input power and parahydrogen pressure (for a constant  $\text{CO}_2$  laser input).

### 6.2.1 BANDWIDTH MEASUREMENT

The aim of this measurement is to establish the relationship between single longitudinal mode input bandwidth and the 16  $\mu\text{m}$  output bandwidth. This aim is clear from the flow-cooled  $\text{UF}_6$  spectra (Figure 6.15) [5]. If the bandwidth of the selective excitation step is not narrow enough, non-selective excitation of the R(6)  $^{238}\text{UF}_6$  line occurs which lies close ( $< 0.8$  GHz) to the Q-Branch of the  $^{235}\text{UF}_6$ .

A wedge etalon used in conjunction with a pyroelectric linear array detector provides an effective method of measuring the line width of a high repetition rate  $\text{CO}_2$  laser on a shot-to-shot basis [5]. The limitation of this method is the low resolution of the linear array detector (128 elements in 50 mm) and the wedge etalon. The wedge-etalon system fulfils the requirements necessary to determine the bandwidth of the  $\text{CO}_2$  lasers and 16  $\mu\text{m}$  output for the molecular laser isotope separation (MLIS) process. This system was chosen owing to its ease of use which is an improvement on the conventional scanning Fabry-Perot interferometer.

Although the Fabry-Perot has a very high resolution it is an averaging method and a large number of shots are needed to analyze the bandwidth structure. Furthermore, it is extremely difficult to align.

The wedge etalon is shown in Figure 6.16. When the etalon is illuminated by a monochromatic plane wave, the light transmitted through the etalon consists of a set of plane waves propagating in different directions as a result of multiple reflections at the surface. If a wave is approaching the surface at an angle  $\theta$  the  $n$ -th order of the transmitted waves

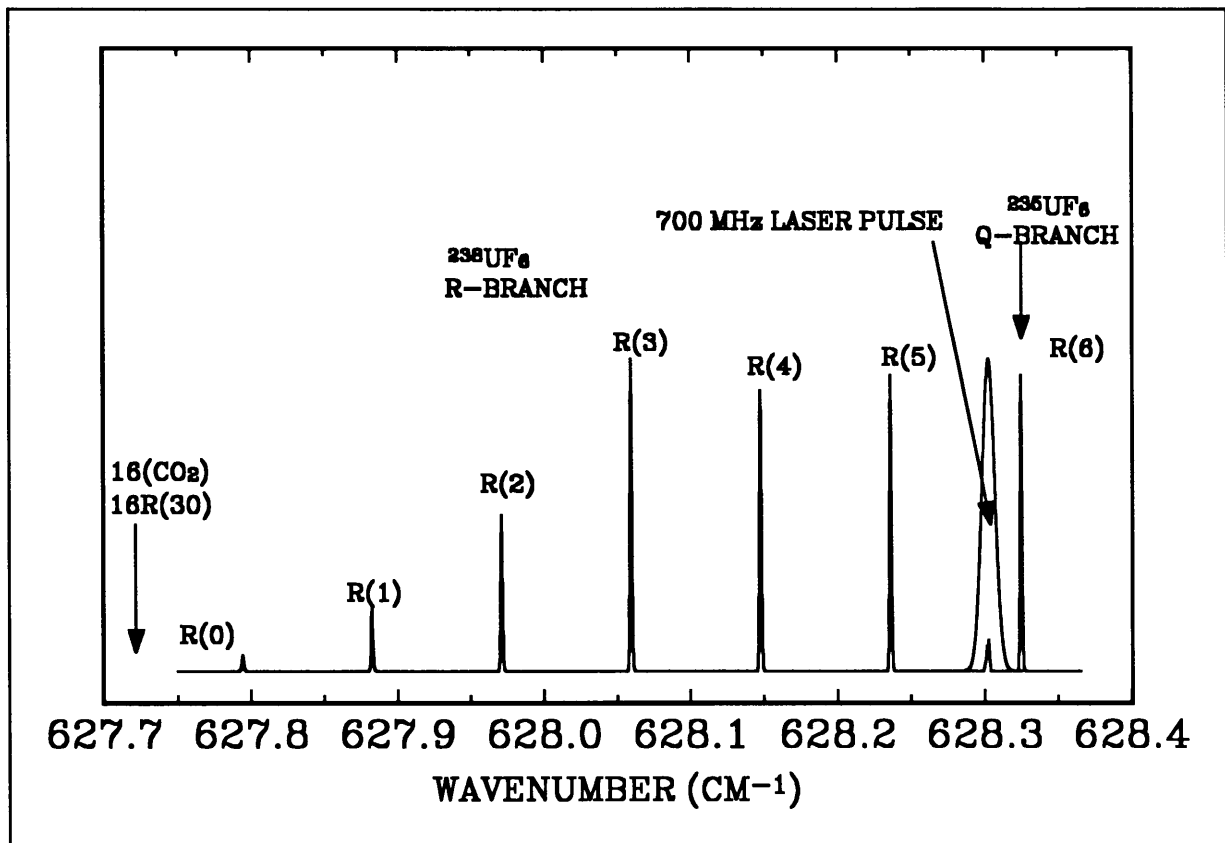


Figure 6.15 Calculated high resolution infrared spectrum of flow-cooled  $UF_6$

emerges at an angle  $\theta_N$ , using Snell's law

$$n_i \sin \theta_N = n \sin[\theta + 2(N-1)\alpha],$$

where  $n$  and  $n_i$  are the refractive index of the etalon and surrounding medium respectively.

The total path difference  $\Lambda_N$  is then given by [5]

$$\Lambda_N = 2nd \cos \theta_i \frac{\sin(N-1)\alpha}{\tan \alpha} [\cos(N-1)\alpha - \tan \theta_i \sin(N-1)\alpha],$$

where  $d = x \tan \alpha$  (see Figure 6.16) is the thickness of the etalon at point P. Assuming  $\theta_i = 0^\circ$  (normal incidence) the phase difference can be written as

$$\delta_N = \frac{4\pi}{\lambda} nx \sin[(N-1)\alpha] \cos[(N-1)\alpha] + 2(N-1)\phi,$$

where  $\phi$  is the phase difference introduced at each reflection.

The transmittance of the wedge etalon with absorption  $\gamma$  is given by [5]

$$T = (1-R)^2 \left( \left[ \sum_{N=1}^{\infty} R^{N-1} \cos \delta_N \exp\left(-\frac{\gamma \lambda \delta_N}{2\pi}\right) \right]^2 + \left[ \sum_{N=1}^{\infty} R^{N-1} \sin \delta_N \exp\left(-\frac{\gamma \lambda \delta_N}{2\pi}\right) \right]^2 \right). \quad (6.1)$$

This equation is used to calculate the etalon bandwidth.

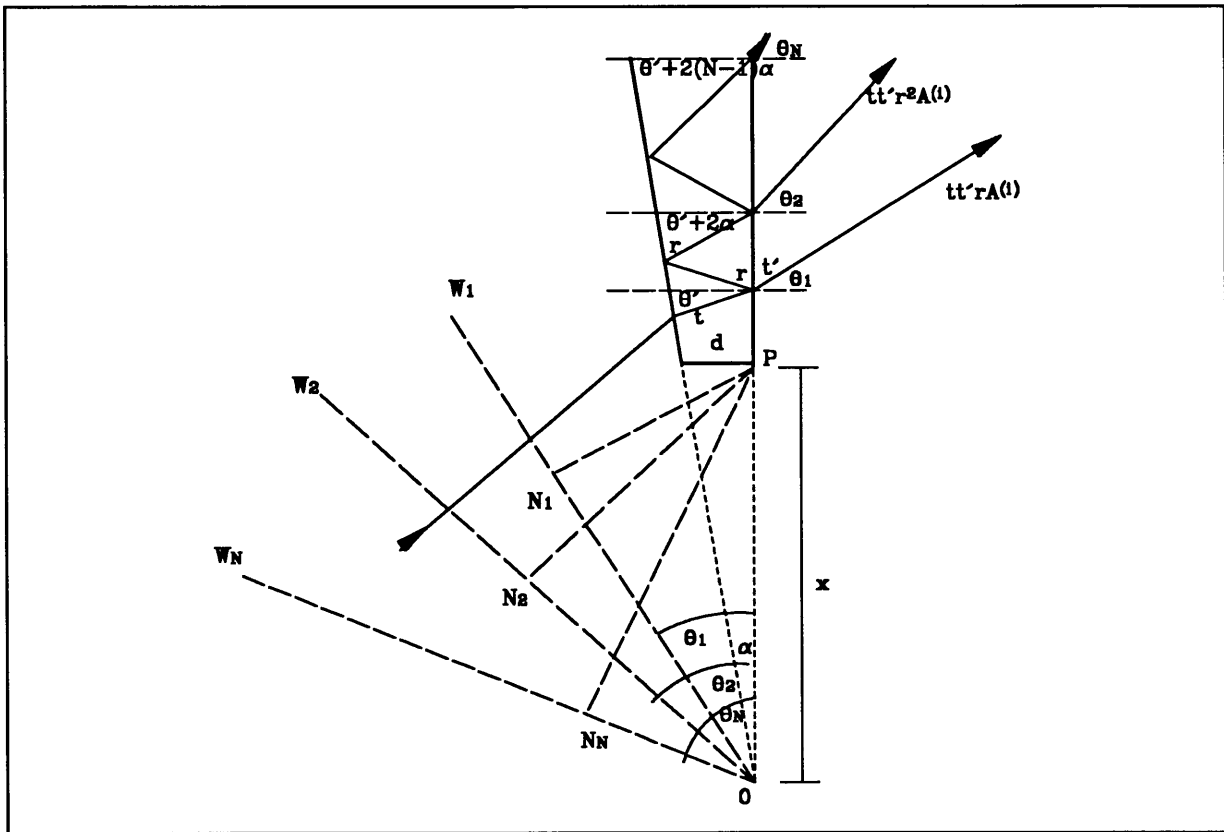


Figure 6.16 Optical path through a wedge etalon of width  $d$

The actual instrument bandwidth is, however, a convolution of the wedge etalon bandwidth (determined with the aid of equation 6.1) and the detector resolution. The finesse  $F$  of the wedge-etalon/linear-array system is given by

$$F = \frac{\Delta \nu}{\delta \nu_T},$$

where  $\Delta \nu$  is the free spectral range of the etalon and  $\delta \nu_T$  the FWHM of the total instrument function. The free spectral range is determined in the same manner as that of a conventional Fabry-Perot interferometer. This is possible since the thickness of the etalon does not change appreciably owing to the small wedge, thus  $\Delta \nu = c / (2nd)$ .

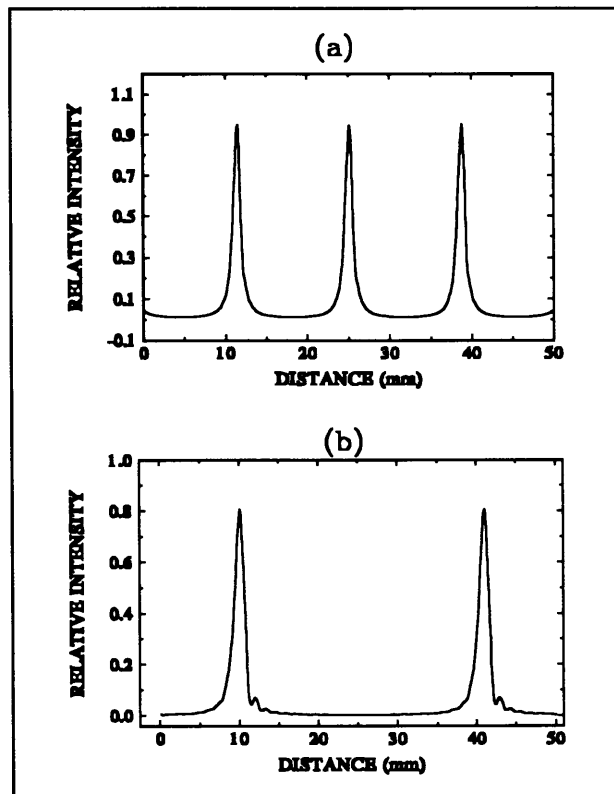


Figure 6.17 Computed transmission for (a) germanium 10 mm etalon at  $10.2 \mu\text{m}$  and (b) CdTe 15 mm etalon at  $16 \mu\text{m}$

Figure 6.17 shows the calculated transmittance function for the Ge and CdTe wedge etalons, which are the etalons used for 10.2  $\mu\text{m}$  and 16  $\mu\text{m}$  measurements respectively. From this figure (for  $\theta = 0^\circ$ ) the FWHM of the etalon can be determined and is given in Table 6.2.

The bandwidth of the TEA lasers is expected to be in the range of 80 MHz to 250 MHz, which is the single longitudinal mode width and multi-mode (three mode competition) width respectively. These values are clearly much smaller than the total instrument function  $\delta v_T$  in Table 6.2. The measured function ( $\delta v_M$ ) will be a convolution of the wedge-etalon bandwidth ( $\delta v$ ), the laser bandwidth ( $\delta v_L$ ) and obviously the linear array resolution function ( $\delta v_D$ ).

Assuming that the three functions can be approximated by a Gaussian profile, the convolution is given by

$$(\delta v_M)^2 = (\delta v_L)^2 + (\delta v)^2 + (\delta v_D)^2 = (\delta v_L)^2 + (\delta v_T)^2, \quad (6.2)$$

where  $(\delta v_T)^2 = (\delta v)^2 + (\delta v_D)^2$ .

<i>MATERIAL</i>	<i>WAVELENGTH</i> ( $\mu\text{m}$ )	<i>d</i> (mm)	$\alpha$	<i>n</i>	$\Delta v$ (GHz)	$\delta v$ (MHz)
Ge	10.2	10	20"	4	3.75	408
CdTe	16	15	20"	2.67	3.74	330

**Table 6.2** Wedge-etalon parameters for 10.2  $\mu\text{m}$  and 16  $\mu\text{m}$  bandwidth measurements

From this relationship the laser line width  $\delta v_L$  can be calculated, if the detector resolution function is known. The detector resolution function can be determined from the interference fringe spacing  $\lambda/2nd$  and if it is assumed that at least three elements are necessary to resolve a fringe (see Figure 6.18).

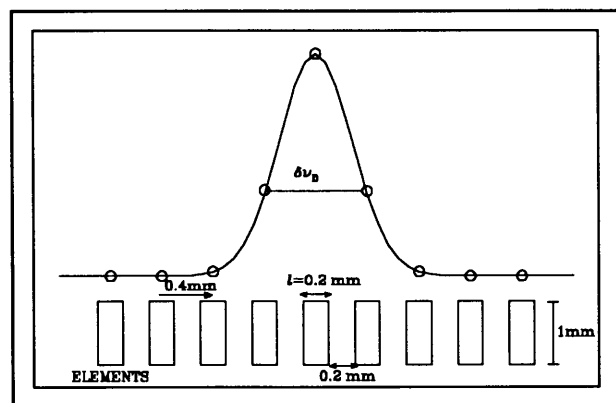


**Figure 6.18** Determination of the array profile for a linear array detector consisting of 128 elements with a length of 50 mm

The finesse of this linear array can then be written as

$$F_D = \frac{\lambda}{5 \alpha n l},$$

where  $\alpha$  and  $n$  are etalon parameters previously defined. Taking into consideration that the

free spectral range of a wedge etalon is given by  $\Delta\nu = c/2nd$ , the FWHM of the linear array is given by

$$\delta\nu_D = \frac{\Delta\nu}{F_D} = \frac{5\alpha nl \Delta\nu}{\lambda}$$

The FWHM for the two etalons under consideration (Table 6.2) is given in Table 6.3. The detector used in this case is a 50 mm array as shown in Figure 6.18.

<i>MATERIAL</i>	$\alpha$	$n$	$l$ (mm)	$\Delta\nu$ (GHz)	$\lambda$ ( $\mu\text{m}$ )	$\delta\nu_D$ (MHz)
Ge	20"	4	0.2	3.75	10.2	285
CdTe	20"	2.67	0.2	3.74	16	121

**Table 6.3** *Detector bandwidth ( $\delta\nu_D$ )*

Figures 6.19 and 6.20 show the pump CO<sub>2</sub> laser bandwidth measurements. In Figure 6.19 a typical measurement is shown and in Figure 6.20 the bandwidth distribution of 128 sequential pulses is shown. For this analysis a rich CO<sub>2</sub> mixture (CO<sub>2</sub> > 40%) was used at a total pressure of 750 mBar. The measurements were taken at a low repetition rate of 5 Hz. For this measurement no beam wandering was experienced.

A slightly different picture is shown for the 16  $\mu\text{m}$  bandwidth analysis shown in Figures 6.21 and 6.22. For this analysis a lean CO<sub>2</sub> mixture (CO<sub>2</sub> < 20%), at a total pressure of 1050 mBar, was used for the pump laser system. The first reaction analysing the data shown in Figure 6.22b, is to assume that more than four longitudinal modes can exist in the cavity. This is not true as only three to four modes (without mode seeding) are possible for this cavity.

In the multimode case a much larger bandwidth spread is measured. The measurements were taken at a higher repetition rate (>20 Hz). In this case a larger beam wandering was experienced due to the long path length in the Raman cell and heating effects in the parahydrogen as a static parahydrogen gas fill was used. Figure 6.23 shows the fringe structure for a number of different incidence angles  $\theta_i$ . It is clear that for small deviation from normal incidence the instrument bandwidth increases dramatically. This is most

probably the reason for these exceptionally larger  $\delta v_M$  measurements. The single longitudinal mode pump appears to be much more favourable from a beam pointing stability point of view as very little beam wandering was experienced in this case. This is also confirmed by Figure 6.22(a). However, some beam wandering was experienced, which is shown as a larger variation in the single mode bandwidth distribution compared to the  $\text{CO}_2$  bandwidth measurements.

The single longitudinal mode distribution compares well with the single longitudinal mode  $\text{CO}_2$  bandwidth measurements. This result confirms the expected  $16 \mu\text{m}$  bandwidth, which is the convolution of the  $\text{CO}_2$  bandwidth and the Raman transition. In the cold Raman cell,  $\Delta v_R \sim 50 \text{ MHz}$  with the result that  $\delta v_{16 \mu\text{m}}$  is of the order of  $\delta v_{10 \mu\text{m}}$ .

<i>CO<sub>2</sub> pump (<math>\lambda=10.2 \mu\text{m}</math>)</i>		<i>16 <math>\mu\text{m}</math> Output</i>	
<i>Single mode (MHz)</i>	<i>Multimode (MHz)</i>	<i>Single mode (MHz)</i>	<i>Multimode (MHz)</i>
$40 \pm 50$	$130 \pm 50$	$90 \pm 150$	$383 \pm 150$

**Table 6.4** *Bandwidth comparisons for 10.2  $\mu\text{m}$  and 16  $\mu\text{m}$  measurements with  $\delta v_T=408 \text{ MHz}$  for the Ge etalon and  $\delta v_T=399 \text{ MHz}$  for the CdTe etalon with an angle of incidence variation of one degree for the 16  $\mu\text{m}$  bandwidth measurement*

Table 6.4 shows the comparison in bandwidth measurements. The results were deconvoluted, using the relationship in equation (6.2) and the measured instrument ( $\delta v$ ) and detector ( $\delta v_D$ ) bandwidths. For the  $16 \mu\text{m}$  measurement an angle of incidence of one degree was used for calculating the  $16 \mu\text{m}$  measurement bandwidth. This instrument has a minimum standard deviation of approximately 100 MHz for no beam wandering on the wedge etalon. However, if beam wandering occurs (as is the case with the  $16 \mu\text{m}$  bandwidth measurements) the minimum standard deviation is the sum of the detector standard deviation and the bandwidth error caused by the pulse-to-pulse variation. In the case of the  $16 \mu\text{m}$  bandwidth measurement a standard deviation of approximately 300 MHz was calculated. For this reason accurate single longitudinal mode bandwidth measurements cannot be made. This instrument is however still capable of discriminating between single mode and various multimode behaviour.

It is also clear that the bandwidth of the  $16 \mu\text{m}$  output is well within the accepted range for the selective excitation of  $^{235}\text{UF}_6$  (see Figure 6.15).



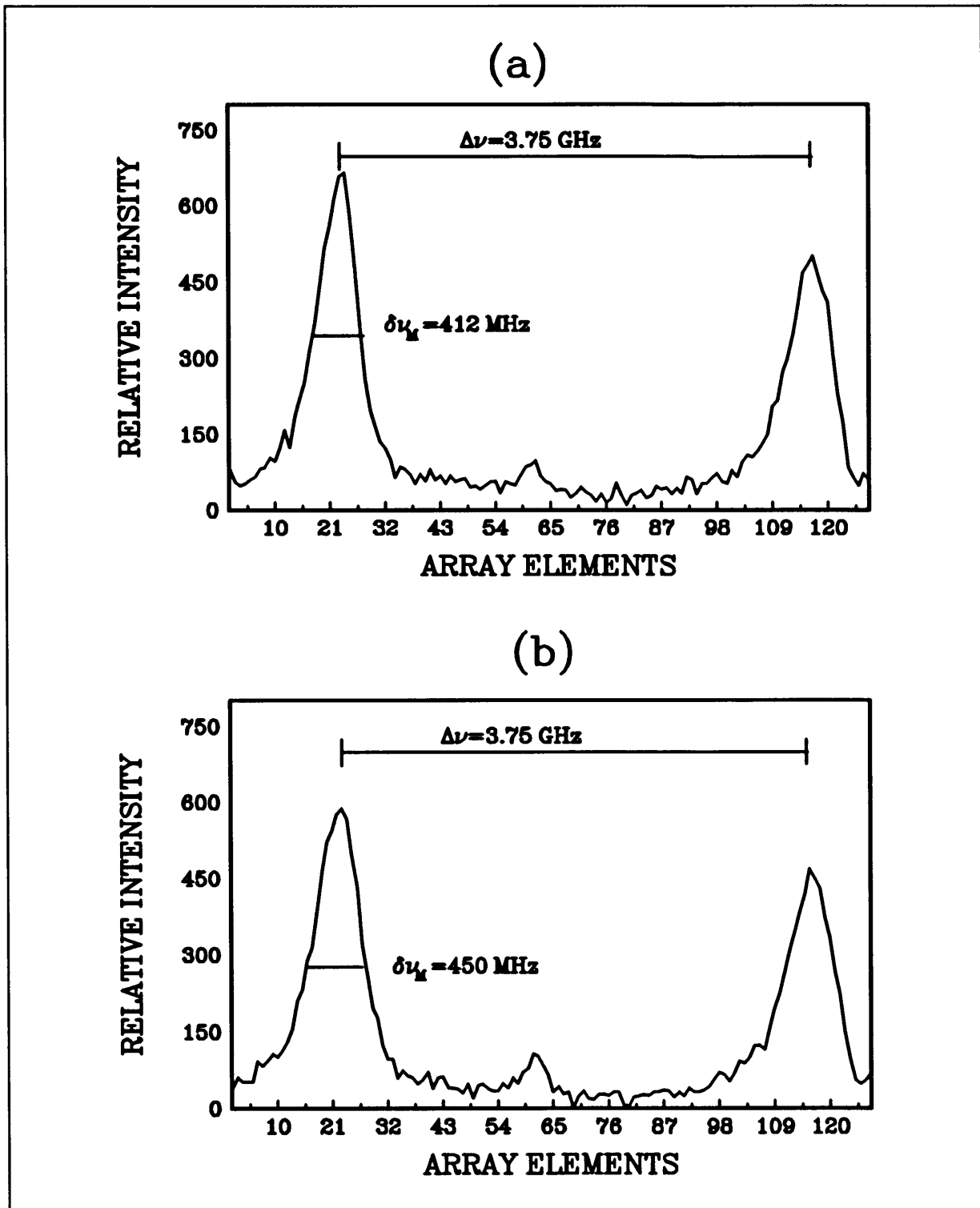


Figure 6.19 Typical CO<sub>2</sub> output fringes produced by a 10 mm Ge etalon for (a) single longitudinal mode and (b) multimode laser operation

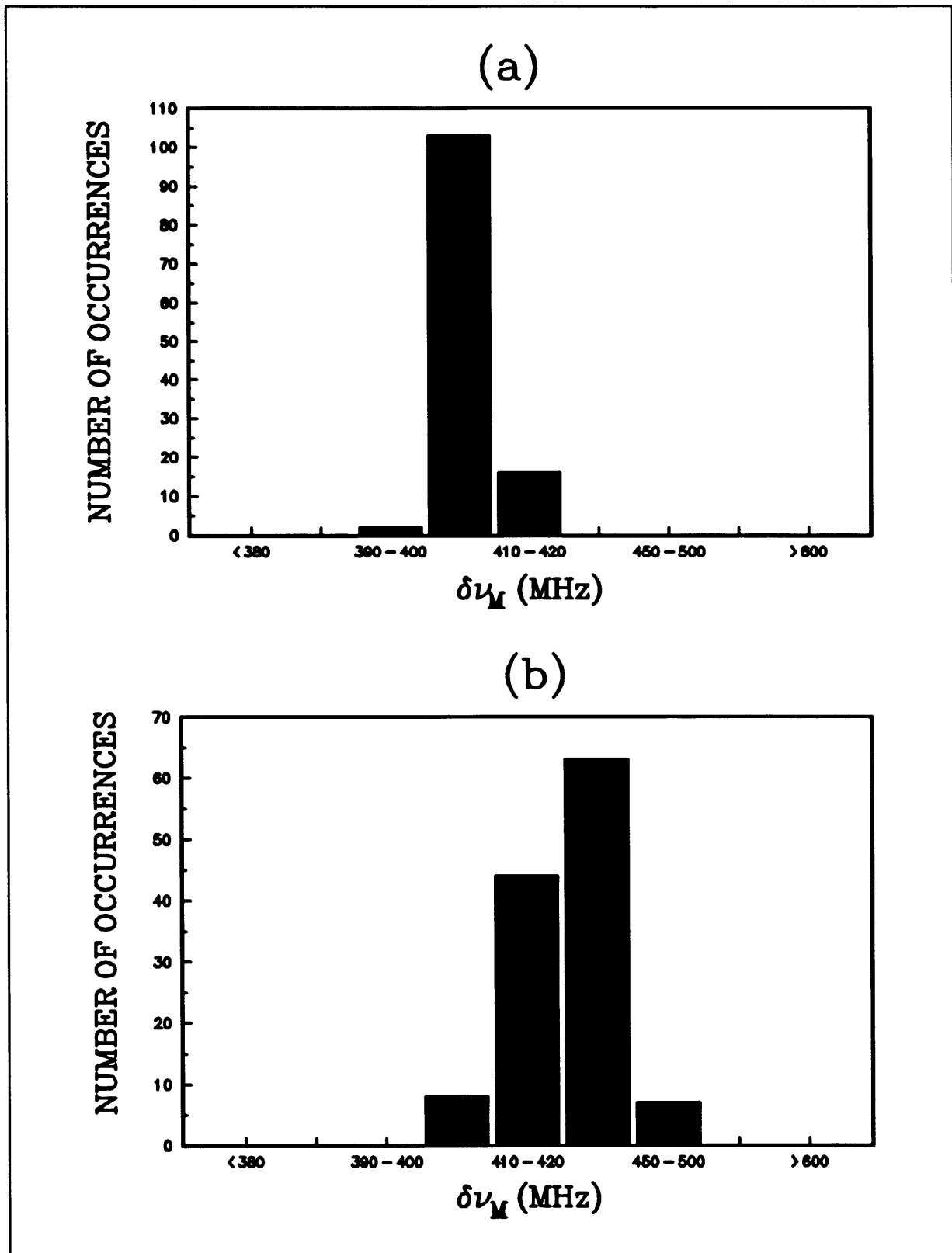


Figure 6.20 Bandwidth distribution for 128 sequential  $\text{CO}_2$  pulses for (a) single longitudinal mode and (b) multimode laser operation

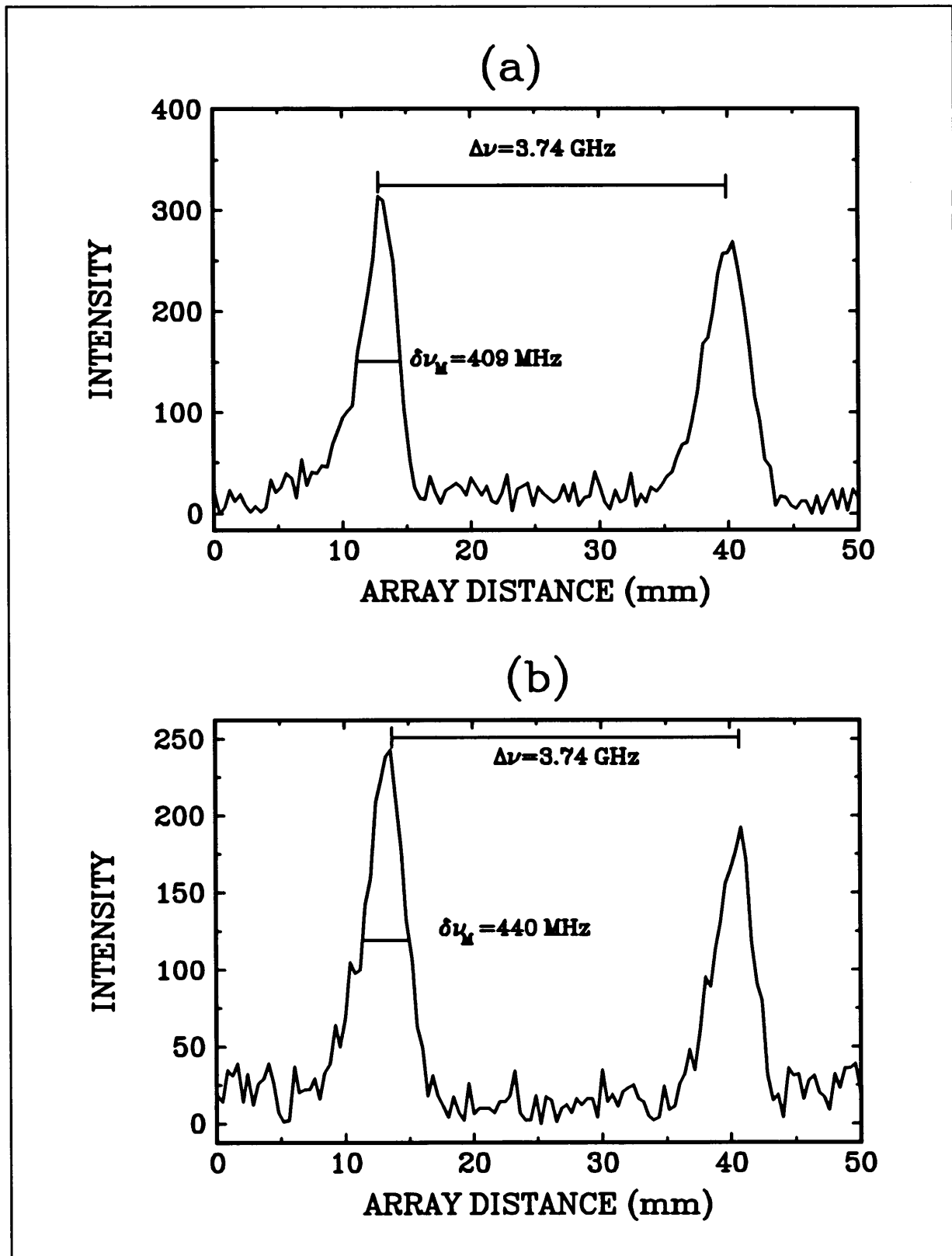


Figure 6.21 Typical  $16\ \mu\text{m}$  output fringes produced by a 15 mm CdTe etalon for (a) single longitudinal mode and (b) multimode laser operation

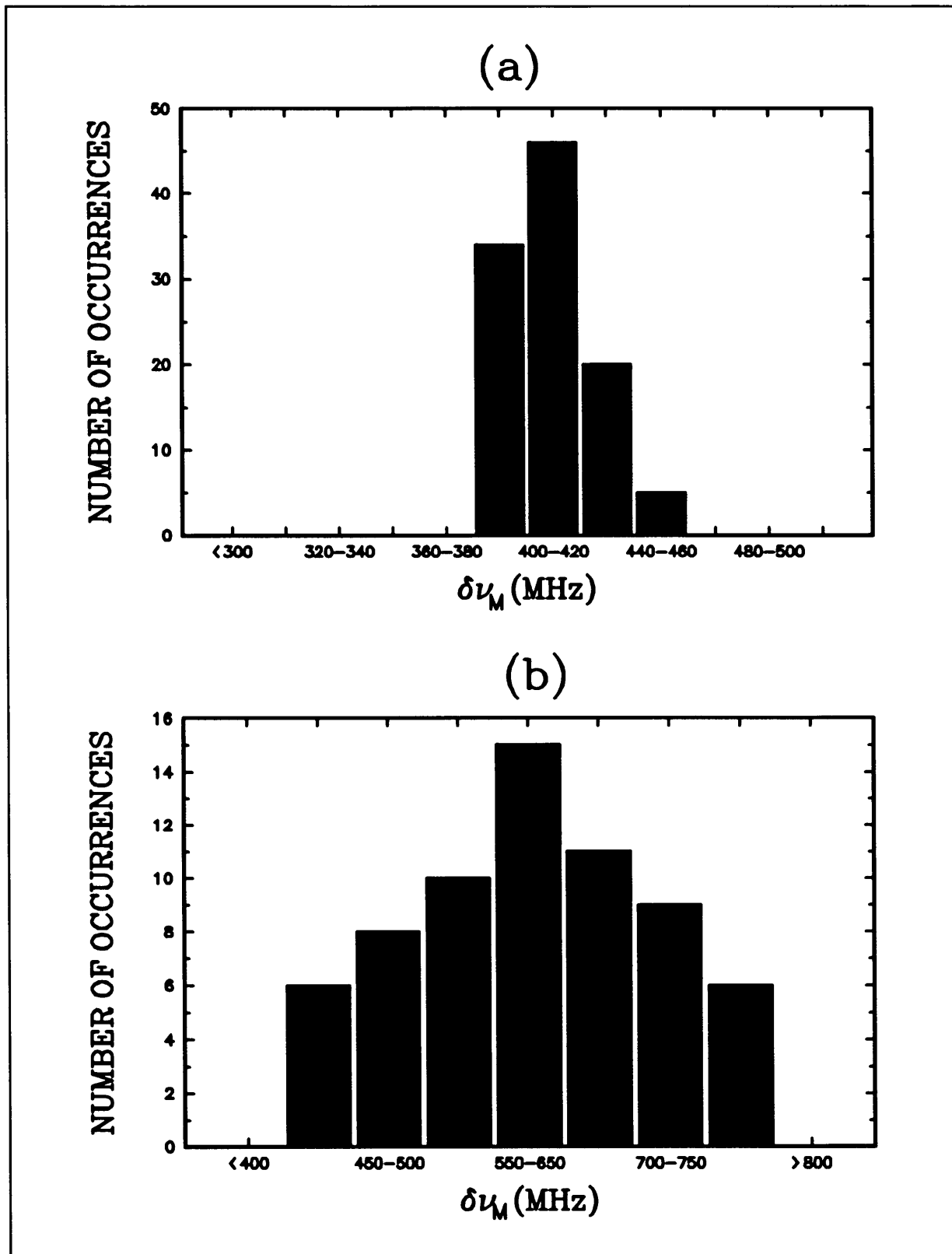
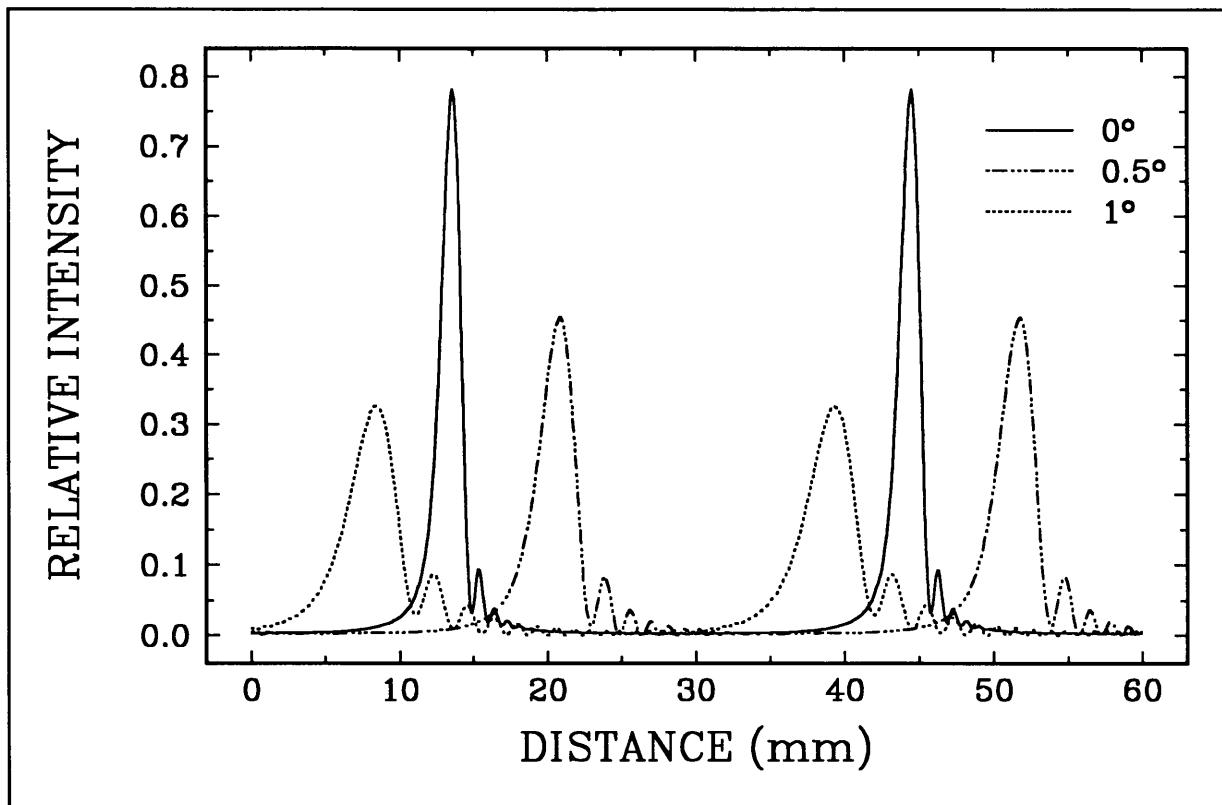


Figure 6.22 Bandwidth distribution for 128 sequential 16  $\mu\text{m}$  pulses for (a) single longitudinal mode and (b) multimode laser operation



**Figure 6.23** Calculated CdTe etalon transmission function for a number of angles of incidence  $\theta_i$

### 6.2.2 RAMAN THRESHOLD MEASUREMENTS

For these measurement the scheme shown in Figure 6.8 was used. Two sets of threshold measurements were performed, using a 60 ns pulse on the 10R18 line and a 67 ns pulse on the 10P20 line. Figure 6.24 shows the threshold measurements. These threshold measurements compare well with values published in the literature [7].

Figure 6.25 shows the Raman threshold calculation versus the Raman threshold measurement. In this case an  $M^2 = 1.45$  (Section 5.11) was measured for the input  $\text{CO}_2$  beam with the parahydrogen/orthohydrogen ratio of 70:30. It is clear from the figure that the modelled threshold compares well with the measured value.

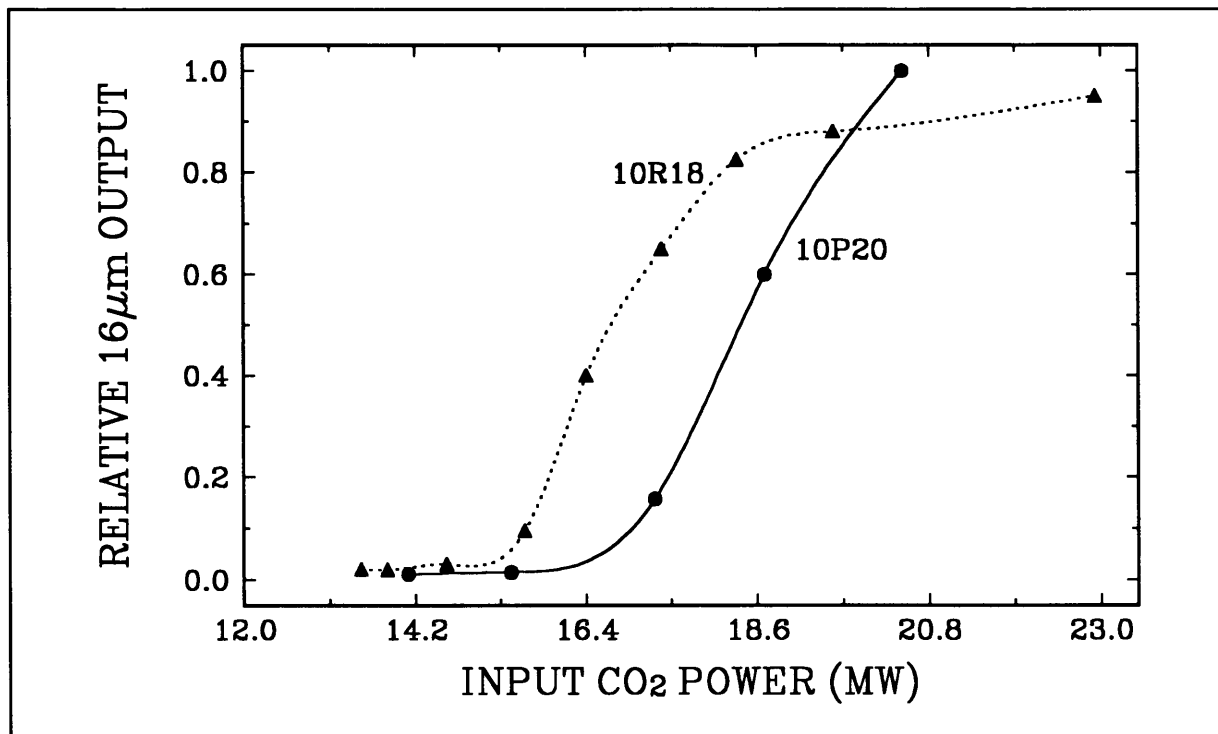


**Figure 6.24** Output Stokes measurements for a cold 35 passes Raman cell for the 10P20 and 10R18 lines with a 70% parahydrogen content

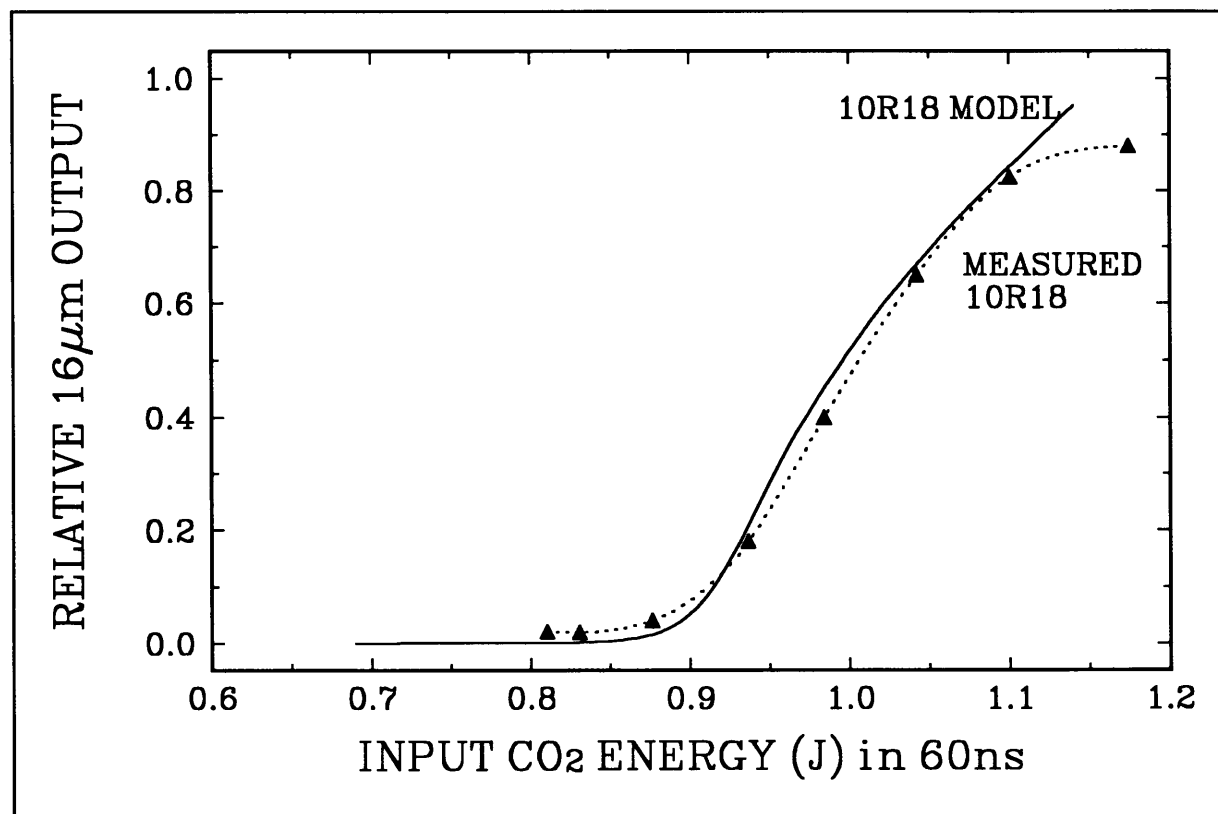


**Figure 6.25** Output Stokes calculation compares to the output Stokes measurement for a cold 35 passes Raman cell ( $M^2=1.45$  and 70% parahydrogen)

### 6.2.3 RAMAN OUTPUT AS A FUNCTION OF PARAHYDROGEN PRESSURE

With reference to Figure 3.5, the aim of this measurement was to establish the pressure above which the Raman output is a constant for a constant CO<sub>2</sub> laser input. It was found that the minimum pressure is ~30 kPa as shown in Figure 6.26. At this value the Raman output ceases to increase with an increase in parahydrogen pressure. Again referring to Figure 3.5, this suggests a Raman cell at a temperature of 200 K for 100% parahydrogen. In reality the temperature of the cell was kept at a constant 77 K with the aid of a liquid nitrogen jacket (see Figure 6.1) around the Raman amplifier. By comparison with Figure 3.2, this then suggests that the parahydrogen content deteriorated to about 68 % for this Raman experiment. This value is consistent with the measured parahydrogen content of 70 %.

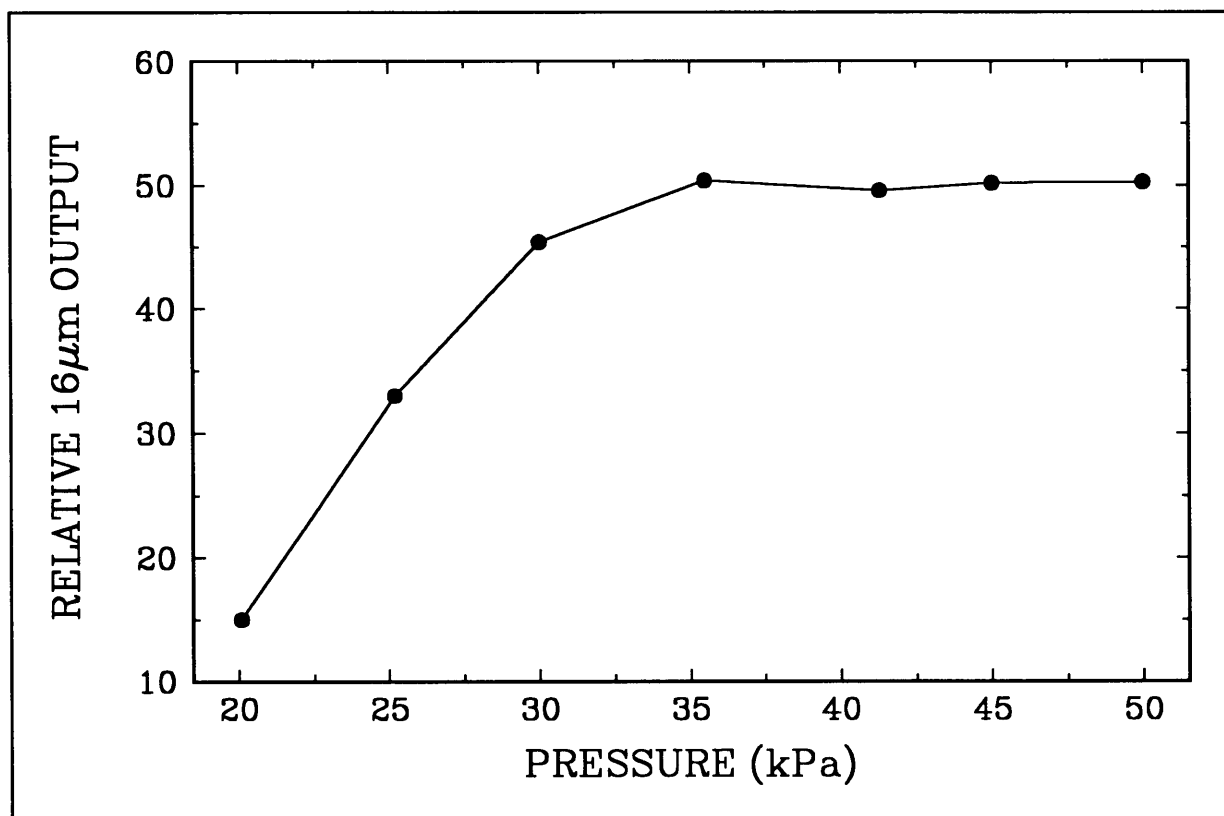


**Figure 6.26** Output Stokes as a function of the parahydrogen pressure for CO<sub>2</sub> laser on the 10R18 line. ( Input: 1.3 J in 60 ns)

It is advantageous to operate the Raman cell at 30 kPa, because a much higher gas breakdown threshold [9] is expected for this pressure condition. The parahydrogen density is about half that of the 50 kPa gas fill. This means that the gas breakdown threshold can be minimized.

## 6.3 CONCLUSIONS AND FUTURE PROJECTS

The aim of the dissertation was the characterization of the Raman conversion in parahydrogen with a CO<sub>2</sub> laser as the pump. To achieve high power (> 150 mJ in 40 ns pulsed), high repetition rate (> 1 kHz) 16 μm output, two beam confinement schemes filled with cold (77 K) parahydrogen were investigated: A novel multimirror multipass (35 passes) Raman cell and a hollow metal waveguide. A rate equation model was developed and verified using experimental results obtained from the conventional multipass (25 passes) Raman experiments.

In Chapter 2 a number waveguide parameters were investigated. Hollow metal waveguides with an inner germanium layer showed very promising theoretical results. However, some manufacturing difficulties have to be solved before these waveguides can be used as Raman amplifiers. An optimal  $\omega_0/a=0.644$  ratio was calculated for the effective coupling of the free space laser mode (TEM<sub>00</sub>) to the minimum loss HE<sub>11</sub> waveguide mode. This ratio was experimentally verified with a 13% discrepancy in the measured spot size probably due to the Gaussian approximation used for the measurement. It is clear from the results in Chapter 2 that a waveguide can be used as a Raman cell for the Raman conversion. However, a number of technical difficulties still exist, namely:

- manufacture of long (> 10 m) waveguides,
- uniform Ge-plating, and
- the lack of optical finish.

The idea of waveguides filled with parahydrogen as Raman converters can still be used as long as these technical difficulties are solved.

Comparing the measured Raman output with the calculated Raman output the validity of the laser beam quality parameter ( $M^2$ ) included in the rate equation model is demonstrated. It was shown that the beam propagation parameters are the most important information needed for optimum laser-beam propagation and amplifier extraction. The increased Raman thresholds, measured for the multipass Raman cell, can also be linked to this parameter. It was also shown in Chapter 5 that laser beam quality parameter ( $M^2$ ) is a function of the size and position of the intracavity aperture, gas lifetime and high pulse rates.

The characterization of the laser beam is a time-consuming and error-prone exercise owing



to the detectors available and the electromagnetic noise (EMI) generated by the lasers during operation. Using single-shot detectors (infrared vidicons and two-dimensional pyroelectric array detectors) this measurement can be extremely fast. A problem in using these detectors is their high sensitivity which is influenced by the EMI. Better screening techniques are needed in order to use these detectors to their full capabilities.

Beam characterization of the CO<sub>2</sub> laser beam and 16 μm output at high repetition rates is a problem that needs some in-depth investigations. A number of sampling schemes (i.e. synchronized rotating mirrors)[8] can be used. With these techniques the detectors currently available can be used as a low effective repetition rate can be generated. This is probably sufficient for the plant operation of the CO<sub>2</sub> pump Raman amplifier (multipass cell). However, for the initial investigation a pulse-to-pulse characterization is needed which emphasises the need for detectors that can operate at high power high repetition rates.

Finally, it was shown that the output frequency bandwidth of the 16 μm compares reasonably well with the measured CO<sub>2</sub> laser bandwidths. It is also important to note that even in multimode the output bandwidth is still within the limits of the <sup>235</sup>UF<sub>6</sub> selective excitation limits [5]. It was found that single longitudinal mode operation is needed for a higher gas-breakdown threshold if no or very little cleaning of the parahydrogen gas is performed, using electrostatic precipitators (ESP's) [9].

## 6.4 REFERENCES: CHAPTER 6

1. Report on single mode control (Afrikaans)  
N. Hugo  
Informal AEC report, (1993)
2. Development of an Infrared laser system for molecular isotope separation  
E.G. Rohwer  
PhD Dissertation, Stellenbosh University, (Jan 1992)
3. Choosing and using pyroelectric detectors  
H. Keller, D. Cima  
ELTEC Instruments Inc, (1993)
4. Boston Electronic Catalog
5. Bandwidth determination of CO<sub>2</sub> lasers with a wedged etalon  
F.J. Prinsloo, L.R. Botha  
AEC Report LT110-000000-155-008, (Febr 1993)
6. Photo supplied by AEC
7. Output performance of a liquid-N<sub>2</sub> cooled, para-H<sub>2</sub> Raman laser  
K. Midorikawa, H. Tashiro, Y. Aoki, K. Ohashi, K. Nagasaka, K. Toyoda,  
S. Namba  
J. Appl Phys **57**(5),1504,(March 1985)
8. Rotating mirror beam samplers  
D. Louwrens  
Private discussions, (1993)
9. CO<sub>2</sub> laser induced gas-breakdown in hydrogen  
F.J. Prinsloo, S.P. van Heerden, L.R. Botha  
Submitted for publication Opt Eng, (1994)

## ***LIST OF SYMBOLS: CHAPTER 6***

$c$	: speed of light
$d$	: thickness of the wedge etalon
$F$	: wedge etalon finesse
$F_D$	: linear array detector finesse
FWHM	: full width at half the maximum
$l$	: detector element size and interelement spacing
$n$	: refractive index of the wedge etalon
$n_i$	: refractive index of the medium surrounding the wedge etalon
$N$	: number of passes through the wedge etalon
$R$	: reflectivity of the wedge etalon
$T$	: transmittance of the wedge etalon
$x$	: lateral distance between the apex of the wedge and the point where $d$ is equal to the width of the etalon
$\alpha$	: the wedge angle
$\gamma$	: absorption of the wedge etalon material
$\Lambda_N$	: the total path length of a ray travelling through a wedge etalon
$\delta_N$	: total phase difference
$\delta v_T$	: FWHM of the total instrument function (etalon bandwidth and detector resolution width)
$\delta v$	: etalon bandwidth
$\delta v_M$	: measured bandwidth
$\delta v_L$	: laser bandwidth
$\delta v_D$	: detector bandwidth
$\Delta v$	: free spectral range of the wedge etalon
$\theta$	: angle of incidence
$\theta_N$	: exit angle of the $N$ -th order of the transmitted waves
$\lambda$	: free space wavelength
$\phi$	: phase difference introduced at a reflection